DISS. ETH NO. 20490

MODELLING HOLOCENE GEOMAGNETIC FIELD EVOLUTION

A dissertation submitted to

ETH ZURICH

for the degree of

Doctor of Sciences

presented by

SANJA PANOVSKA

MEng, Ss. Cyril and Methodius University, Skopje

Born September 13, 1980

citizen of Republic of Macedonia

accepted on the recommendation of

Prof. Dr. Andrew Jackson, examiner
Dr. Christopher C. Finlay, co-examiner
Prof. Dr. Ann M. Hirt, co-examiner
Dr. Monika Korte, co-examiner

2012

Abstract

Sediment and archeomagnetic data spanning the Holocene allow the reconstruction of the evolution of the geomagnetic field on centennial to millennial time scales. In this thesis new Holocene geomagnetic models are built utilizing newly derived lake sediment uncertainty estimates and directly incorporating relative declination and paleointensity. It also includes a study on periodicity and power spectrum of paleomagnetic data derived from Holocene sediment magnetic records.

Uncertainty estimates are important prior information for global field modelling because they ensure proper weighting of different data sources. New uncertainty estimates for the Holocene magnetic records are derived considering both comparisons with archeomagnetic estimates and the variance about robust smoothing spline models. The latter are determined using a cross validation approach along with the use of a minimum smoothing time inferred from the sedimentation rate and an assumed lock-in depth. The obtained uncertainties span a wide range of values, demonstrating the diversity in quality of the records. These range from 2.5° to 11.2° (median: 5.9°; interquartile range: 5.4° to 7.2°) for inclination, 4.1° to 46.9° (median: 13.4°; interquartile range: 11.4° to 18.9°) for relative declination, and 0.59 to 1.32 (median: 0.93; interquartile range: 0.86 to 1.01) for standardized relative paleointensity. These results suggest that uncertainties may have been underestimated in previous studies. Inclination records are shown to be the most reliable field component. No evidence is found for systematic inclination shallowing. Study of the temporal resolution of the resulting spline models indicates an interquartile range of between 80 and 250 years.

Investigation for periodicities in Holocene sediment magnetic records is carried out by applying three techniques: multitaper spectral estimation, wavelet analysis and empirical mode decomposition. No compelling evidence is found for the existence of discrete periods on a global scale. Consistency amongst the observed periods is however found when records are grouped according to their geographical location with best agreement obtained for inclination records. A continuous broadband spectrum spanning periods between 300 and 4000 years is found, with a slope corresponding to a power law with exponent of -2.3 ± 0.6. This is consistent with the hypothesis that chaotic convection in the outer core drives the majority of the observed secular variation.

Two new records, Lake Soppen and Lake Baldegg, are analysed in order to produce a paleomagnetic composite master curve for Holocene geomagnetic field evolution in Switzerland. The method for uncertainty estimates and the periodicity analysis implemented on the global data compilation is applied as a case study for these two records. Furthermore, a search for 'archeomagnetic jerks' is carried out both in the individual records and the composite curve. Two well constrained events at 700 BC and 450 AD, and three less defined at 4650 BC, 3150 BC, and 2450 BC are identified. These findings are compared to sudden changes of the Earth's magnetic field previously proposed in other studies of archeomagnetic data and lake sediment records from Fennoscandia.

Finally, four new Holocene geomagnetic field models are constructed. These directly incorporate relative declination and paleointensity and utilize the new uncertainty estimates derived in previous chapters of the thesis. They also explore new possibilities regarding the measures of misfit and spatial regularization. An absolute deviation (L_1) measure of misfit is found to aid the construction of converged models without the need to impose very stringent data rejection. A model based on an entropy norm is found to have a spherical harmonic spectrum closest to that of the present field, while retaining low temporal complexity. Comparisons are made with the state-of-the-art CALS10k.1b model, similar fit to the observation is achieved and the dipole and quadrupole variations are found to be compatible, with the exception of the g_2^2 coefficient. Changes of the averaged field morphology at the CMB are analysed for two epochs (50 BC and 850 AD) in order to probe the mechanism underlying the start of the present episode of dipole moment decay. This is found to be associated primarily with a weakening of the strong high latitude flux patch beneath North America. An analysis of predicted directional variations in Europe reveals that models based primarily on lake sediments are capable of capturing archeomagnetic jerk events, provided these are of sufficiently large amplitude and of duration 200 years or more.

Zusammenfassung

Magnetische Aufzeichnungen in holozänen Sedimenten und archäomagnetischen Objekten erlauben die Rekonstruktion der Erdmagnetfeldveränderungen auf hundertjährigen bis tausendjährigen Zeitskalen. In dieser Arbeit wurden Erdmagnetfeldmodelle erstellt, die auf neuen Unsicherheitsabschätzungen von Seesedimenten beruhen, unter direktem Einbezug von relativen Deklinationsdaten und Paläointensitäten. Zusätzlich wurden Periodizitäten und Leistungsspektren von paläomagnetischen Aufzeichnungen in holozänen Sedimenten untersucht.

Unsicherheitsabschätzungen sind wichtige Vorraussetzung für die globale Erdmagnetfeldmodellierung, denn diese ermöglichen eine angemessene Gewichtung der verschiedenen Datensätze. Neue Unsicherheitsabschätzungen für holozäne Paläosäkulardatensätze wurden festgelegt unter der Berücksichtigung von Vergleichen mit archäomagnetischen Schätzungen und den Abweichungen von robusten geglätteten Splines. Letztere wurden basiert auf einer Vergleichsprüfung, kombiniert mit Annahmen für minimale Glättungszeiten aufgrund der Sedimentationsrate und der angenommenen Lock-in-Tiefe, ermittelt. Die hohe Spannbreite der Unsicherheitsabschätzungen demonstriert die Mannigfaltigkeit der Datenqualität. Die Werte sind im Bereich zwischen 2.5° und 11.2° (Median: 5.9°; Interquartilbereich: 5.4° bis 7.2°) für Inklination, 4.1° bis 46.9° (Median: 13.4°; Interquartilbereich: 11.4° bis 18.9°) für relative Deklination und 0.59 bis 1.32 (Median: 0.93; Interquartilbereich: 0.86 bis 1.01) für die standardisierte relative Paläointensität. Diese Werte lassen vermuten, dass die Unsicherheiten in vorausgegangenen Studien möglicherweise unterschätzt wurden. Es wird gezeigt, dass die Inklinationsdatensätze die zuverlässigste der Erdmagnetfeldkomponenten darstellen. Weiterhin gab es keinen Hinweis auf ein systematisches Abflachen der Inklinationswerte. Die Untersuchung der zeitlichen Auflösung der resultierenden Splinemodelle zeigte, dass der Interquartilbereich der zeitlichen Auflösung zwischen 80 und 250 Jahren liegt.

Für die Untersuchung der Periodizität holozäner Paläosäkularvariationsdaten wurden drei verschiedene Techniken angewendet: die Multitaper Spektralschätzung, eine Wavelet Analyse und Empirical Mode Decomposition. Es wurde kein eindeutiger Hinweis auf diskrete Perioden im globalen Massstab gefunden. Allerdings wurden Übereinstimmungen der Periodizität gefunden, wenn die Datensätze anhand der geographischen Position gruppiert wurden, vor allem für die Inklinationsdaten: Ein kontinuierliches Breitbandspektrum mit Perioden zwischen 300 und 4000 Jahren wurde ermittelt, wobei das Spektrum einem Potenzgesetz mit Exponent -2.3 ± 0.6 folgt. Dies ist im Einklang mit der Hypothese, dass chaotische Konvektion im äusseren Kern für den Grossteil der beobachteten Säkularvariationen verantwortlich ist.

Zwei neue Paläosäkularvariationsdatensätze vom Soppensee und Baldeggersee wurden analysiert, um eine neue Paläosäkularvariationsmasterkurve

für das Holozän in der Schweiz zu erstellen. Die oben erwähnten Methoden der Unsicherheitsabschätzung und der Periodizitätsanalyse wurden im Rahmen einer Fallstudie auf die zwei Paläosäkularvariationsdatensätze angewendet. Des Weiteren wurde sowohl in den einzelnen Datensätzen als auch in der kombinierten Paläosäkularvariations-Masterkurve nach dem Auftreten archäomagnetischer Jerks gesucht. Zwei solcher Ereignisse um 700 Jahre v. Chr. und 450 Jahre n. Chr. sind gut definiert, und drei weitere um 4650, 3150 und 2450 Jahre v. Chr. sind weniger gut definiert. Diese Events wurden mit Vermutungen über sprunghafte Veränderungen des Magnetfelds in Skandinavien aus früheren archäomagnetischen und lakustrinen Studien verglichen.

Schliesslich wurden vier neue Erdmagnetfeldmodelle für das Holozän entwickelt, welche sowohl die relativen Deklinationsdaten und die Paläointensität als auch die vorher durchgeführten Unsicherheitsabschätzungen einbeziehen. Mit den Modellen wurden auch die unterschiedlichen Möglichkeiten der Beschreibung der Modellgenauigkeit und der räumlichen Regulierung berücksichtigt. Eine Art, die Abweichung des Modells von den Messdaten zu bestimmen, ist die absolute Abweichung (L_1 Norm). Es hat sich gezeigt, dass diese der Konstruktion konvergierender Modelle förderlich ist, ohne dass eine strenge Rückweisung von Daten nötig ist. Ein Modell basierend auf der Entropienorm wurde generiert, dessen Kugelflächenfunktionsspektrum dem gegenwärtigen Erdmagnetfeld stark gleicht, wobei die zeitliche Komplexität tief bleibt. Vergleiche mit dem aktuellsten CALS10k1.b Modell zeigen eine ähnlich gute Übereinstimmung mit den Messdaten; auch die Dipol- und Quadrupol-Variationen sind ähnlich, mit Ausnahme der g_2^2 Koeffizienten. Veränderungen der gemittelten Feldmorphologie an der Kern-Mantel Grenze wurden für zwei Epochen (50 v. Chr. and 850 n. Chr.) untersucht, um den Mechanismus zu erforschen, der für den Beginn des gegenwärtigen Dipolmomentabfalls verantwortlich gemacht wird. Dieser wurde vorwiegend mit dem Schwächer-Werden der Flux Patches unterhalb Nordamerikas assoziiert. Eine Analyse der vorhergesagten Änderungen der Feldrichtung in Europa zeigt, dass Modelle, die auf Daten aus Seesedimenten basieren, archäomagnetische Jerks abbilden können, sofern diese Ereignisse eine genügend grosse Amplitude haben und 200 Jahre oder länger dauern.

Contents

List of Figures

List of Tables

List of Abbreviations

AD Anno Domini (denotes year after 0 in the Christian calender)

ARCH3k.1 Geomagnetic field model based on archeomagnetic data for the past 3 kyr.

ARM Anhysteretic remanent magnetisation

ATRM Anisotropy of thermoremanent magnetisation

BC Before Christ (denotes years prior to 0 in the Christian calender)

CALS10k.1b Geomagnetic field model: 8000 BC to 1990 AD

CALS7k.1 Geomagnetic field model: 5000 BC to 1950 AD

ChRM Characteristic remanent magnetisation

CMB Core - mantle boundary

CV Cross validation

D Declination, magnetic field component

DRM Depositional (detrital) remanent magnetisation

EMD Empirical Mode Decomposition

GAD Geocentric axial dipole

gufm1 Geomagnetic field model: 1590 to 1990 AD

I Inclination, magnetic field component

IGRF International geomagnetic reference field

IMF Intrinsic Mode Function

IQR Interquartile range

IRM Isothermal remanent magnetisation

MAD	Maximum angular deviation
MD	Multi domain grain size
NRM	Natural remanent magnetisation
PCA	Principal component analysis
PDRM	Postdepositional remanent magnetisation
PSD	Power spectral density
PSV	Paleosecular variation
pTRM	Partial thermoremanent magnetisation
RMS	Root mean squares value
RPI	Relative paleointensity
SCHA	Spherical cap harmonic analysis
SD	Single domain grain size
SIRM	Saturation isothermal remanent magnetisation
TRM	Thermoremanent magnetisation
VADM	Virtual axial dipole moment

Chapter 1

Introduction

1.1 Overview

The Earth possesses a magnetic field. This arises from a superposition of different sources: (a) the main field generated in the Earth's fluid core by a dynamo (see Fig. 1.1), (b) the crustal field, generated by magnetized rocks in the crust, (c) the external field, produced by electric currents in the ionosphere and magnetosphere, (d) magnetic field in the crust and the upper mantle induced by the external magnetic field variations (e.g. Backus et al., 1996). Furthermore, Earth's magnetic field undergoes continuous variations in time and space (Courtillot and Le Mouël, 1988; Bloxham et al., 1989). The geomagnetic field is a fascinating and challenging scientific topic because of the variety of processes and underlying mechanisms that contribute to its spatial morphology and temporal variation.

Fluctuations in the geomagnetic field due to the changes occurring in the core of the Earth, with time scales of years to millennia, are referred to as geomagnetic secular variation. The study of temporal variations with periods of hundreds to thousands of years requires very long records. Archeomagnetic and lake sediment magnetic records are important archives of geomagnetic field behaviour on these time scales, particularly in the Holocene (i.e., the past 11.5 kyr) for which a large number of records exist. Such observations can be combined together into models representing the global field evolution (e.g. Constable, 2007a; Jackson and Finlay, 2007). The aim of this thesis is to derive global, time-dependent, geomagnetic field models spanning the Holocene based on appropriately treated lake sediment and archeomagnetic data. Such models are needed in order to test hypotheses regarding processes in the core driving the secular variation on centennial to millennial time scales. The reliability of these models depends on the spatial and temporal distribution of the contributing observations and their quality, as encoded via uncertainty estimates during the modelling. This thesis investigates methods of handling the subtleties of the paleomagnetic data during field modelling. In particular

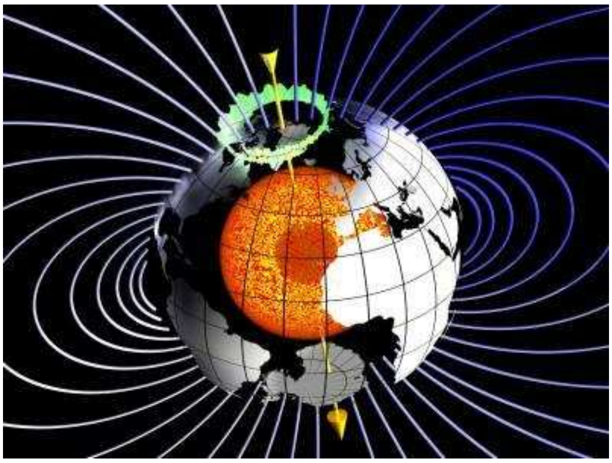

Figure 1.1: The Earth's magnetic field is mainly produced by a self-sustaining dynamo in the fluid outer-core. Picture credit: GeoForschungsZentrum Potsdam (GFZ).

it involves the derivation of consistent and independent uncertainty estimates for sediment magnetic records prior to their use in field modelling. A guiding principle is the use of a robust (absolute deviation) measure of the goodness of fit during the modelling carried out. The methods developed here had the benefit of testing undertaken as part of ETH CHIRP project (CH1-02-08-2) that involved the collection and magnetic analysis of new cores from Lake Soppen and Lake Baldegg in Switzerland.

1.2 Modelling the geomagnetic field

Observations in paleomagnetic and archeomagnetic archives involve recovery of one or more geomagnetic elements (declination, D, inclination, I or geomagnetic field intensity, F (Fig. 1.2). These three components completely determine the Earth's vector magnetic field at one location. The most commonly used method for combining such observations into a global geomagnetic field model is spherical harmonic analysis, originally developed by Gauss in 1839 (Chapman and Bartels, 1940; Backus et al., 1996). The magnetic field **B** is described by the following Maxwell's equations

$$\nabla \cdot \mathbf{B} = 0; \quad \nabla \times \mathbf{B} = \mu \left(\mathbf{J} + \frac{\partial \mathbf{D}}{\partial t} \right) \tag{1.1}$$

where $\mathbf{J}$ is the electric current density, $\mathbf{D}$ is the dielectric field and μ is the magnetic permeability. The magnetic field $\mathbf{B}$ in a source free region (where $\mathbf{J} = 0$) and ignoring very rapid time variations can be written as the negative

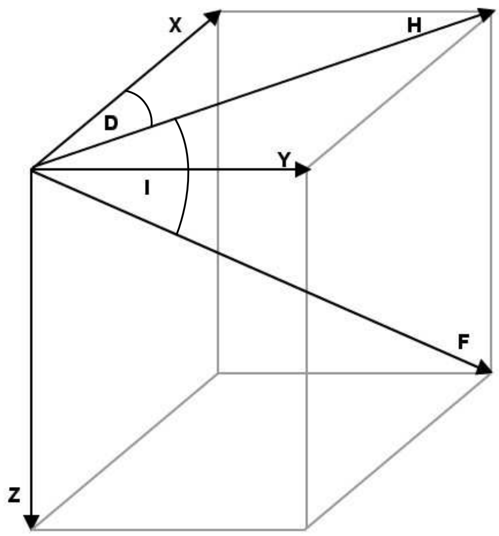

Figure 1.2: Elements of the Earth's magnetic field. The total magnetic field F can be projected along the three axes and three magnetic components are obtained: X (north), Y (east) and Z (vertical). H is horizontal projection of F. Inclination (I) is the angle between the horizontal plane and F. Declination (D) is the angle between H and X.

gradient of a scalar potential V:

$$\nabla \times \mathbf{B} = 0; \quad \mathbf{B} = -\nabla V \tag{1.2}$$

which satisfies Laplace's equation:

$$\Delta V = 0 \tag{1.3}$$

In a spherical coordinate system this may be written as

$$\Delta V = \frac{1}{r^2}\frac{\partial}{\partial r}\left(r^2\frac{\partial V}{\partial r}\right) + \frac{1}{r^2\sin\theta}\frac{\partial}{\partial\theta}\left(\sin\theta\frac{\partial V}{\partial\theta}\right) + \frac{1}{r^2\sin^2\theta}\frac{\partial^2 V}{\partial\varphi^2} = 0 \tag{1.4}$$

where r is the distance from Earth's center, θ is the colatitude and φ is the longitude. A general solution of this equation may be obtained via the technique of separation of variables (Riley et al., 2002). With the first variable, r, the internal and external origins of geomagnetic field can be taken in consideration. For φ, Fourier series are used because of its periodic behaviour from 0 to 2π. In the case of θ, Schmidt quasi-normalized associated Legendre functions are used:

$$\begin{aligned} P_l^m(\theta) &= (2l+1)^{\frac{1}{2}} P_{l,m}(\theta) \quad \text{for m=0;} \\ P_l^m(\theta) &= \left((2l+1)\tfrac{(l-m)!}{(l+m)!}\right)^{\frac{1}{2}} P_{l,m}(\theta) \quad \text{for m>0;} \end{aligned} \tag{1.5}$$

where l is the degree, m is the order and

$$P_{l,m} = \sin^m \theta \frac{d^m P_l(\theta)}{d(\cos\theta)^m} \tag{1.6}$$

This leads to the following spherical harmonic representation of V for internal sources

$$V(r,\theta,\varphi) = a \sum_{l=1}^{L} \sum_{m=0}^{l} \left(\frac{a}{r}\right)^{l+1} \left[g_l^m \cos\ m\varphi + h_l^m \sin\ m\varphi\right] P_l^m(\theta) \tag{1.7}$$

where g_l^m and h_l^m are model parameters, known as Gauss coefficients, to be determined from the observations (Langel, 1987) and a is the Earth's radius. L is the maximum spherical harmonic degree of the expansion, or truncation level. The Cartesian components of geomagnetic field are obtained as partial derivatives of scalar potential V with respect to r, θ and φ:

$$X = -B_\theta = \frac{1}{r}\frac{\partial V}{\partial \theta} \tag{1.8}$$

$$Y = B_\varphi = \left(-\frac{1}{r\ \sin\ \theta}\right)\frac{\partial V}{\partial \varphi} \tag{1.9}$$

$$Z = -B_r = \frac{\partial V}{\partial r} \tag{1.10}$$

Elements (H, F, D and I) are nonlinearly related to the Gauss coefficients and can be derived using their relations to the X, Y and Z elements:

$$H^2 = X^2 + Y^2 \tag{1.11}$$

$$F^2 = X^2 + Y^2 + Z^2 \tag{1.12}$$

$$D = \tan^{-1}\left(\frac{Y}{X}\right) \tag{1.13}$$

$$I = \tan^{-1}\left(\frac{Z}{H}\right) \tag{1.14}$$

1.3 Millennial time scale field models

Global geomagnetic field models spanning the past four hundred years based on direct historical measurements (Bloxham et al., 1989; Jackson et al., 2000) have proved to be a powerful tool for studying the evolving field structure both at the Earth's surface and at the core mantle boundary (CMB), and have also being widely used for analyses of global and regional field variations. Such models have also been constructed on millennial time scales using compilations of indirect field measurements obtained from archaeological artefacts, lavas

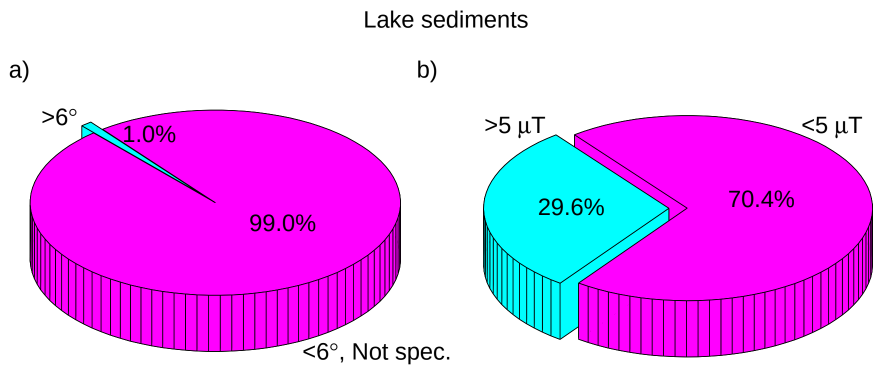

Figure 1.3: Pie charts presenting the fractions of lake sediment data belonging to a particular class of uncertainty. Blue indicates data for which the uncertainties available with the data were above the pre-define threshold value and used for field modelling. Pink indicates that no estimate was available, or estimates were below the threshold, so that threshold uncertainty values were allocated for use in field modelling. Thresholds of 6° for the α_{95} of directions (defined in Section 3.2) (a) and 5 μT for the intensities (b) were applied. Figure adapted from Donadini et al. (2009).

and sediments. Hongre et al. (1998) derived one of the first global geomagnetic model that was valid for 2000 years, and contained spherical harmonics up to degree 2 plus the degree 3 and order 3 on the basis of archeomagnetic data, 14 composite directional and 5 intensity time series. Constable et al. (2000) produced a global geomagnetic model spanning 3000 years on the basis of the PSVMOD1.0 dataset. Pavón-Carrasco et al. (2008) developed a regional archeomagnetic field model (SCHA-DI-00) covering Europe of the past 2000 years using a Spherical Cap Harmonic Analysis (SCHA) technique applied to European Palaeosecular Variation Curves (PSVC) only with directional information. The improved regional geomagnetic model for Europe for the last 3 kyrs. and 8 kyrs., SCHA.DIF.3K and SCHA.DIF.8K (Pavón-Carrasco et al., 2009, 2010) include intensity in addition to directional data. Global field models are generally smoother than regional models, but they also describe the long-wavelength global component of geomagnetic field and allow downward continuation to the CMB.

The state-of-the-art in this discipline is the rapidly improving CALSx series of continuous, time-dependent, global geomagnetic models (Korte and Constable, 2003, 2005a; Korte et al., 2009; Korte and Constable, 2011; Korte et al., 2011) covering the past 3, 7 and 10 kyr, respectively, and providing an extremely valuable representation of the evolution of the large-scale field at the CMB on these time scales.

To determine variations of the ancient geomagnetic field, we have to study the paleofield recorded in geological archives, such as lavas, archeological material and sediments. Remanent magnetisation can be acquired in several ways (e.g., Dunlop and Özdemir, 1997; Butler, 1992). When lava and clay are heated they acquire a magnetization parallel to the Earth's magnetic field. The cooling below the Curie temperature preserves the magnetization information, while the heating first destroys any permanent magnetization in the material. This process is called thermoremanent magnetization. In sedimentary environments, there is a strong tendency for magnetic moments of grains to align with the magnetic field and the acquired remanence is depositional or detrital remanent magnetization (e.g., Tauxe, 2002). These two mechanisms manifest different influence on the stability and reliability of the recorded geomagnetic signals and therefore, we have to take them in to account when assessing data uncertainty estimates. More details of how Holocene magnetic records acquire a stable magnetization, and how the data are processed and error estimates assigned are discussed in Chapter 2.

When field models are constructed, the reliability of underlying data is taken into consideration by weighting the data according to uncertainty estimates. Therefore, a pertinent question for attempts to accurately recover geomagnetic field behaviour on time scales of centuries to millennia, is how to assign appropriate and consistent estimates of data uncertainty for lake sediment records. Korte et al. (2005) assigned minimum uncertainties for sediment records of 3.5° in inclination, 5.0° in declination and 5 μT in intensity, based on the comparisons with the historical model *gufm1* (Jackson et al., 2000). Age uncertainties contributed to the total error as did possible location errors (Korte et al., 2005). Minimum uncertainties have been expressed in terms of an α_{95} of 6° (see Section 3.2), which could later be converted to uncertainty estimates for the field modelling (Donadini et al., 2009; Korte et al., 2009). Most of the lake sediment records were found to have α_{95} less than 6° or values were not available in the original studies, so 99% of the directional data were effectively allocated the same weights, regardless of the quality of the record (Fig. 1.3a). The situation is slightly better for the paleointensity where 30% of the records kept the originally assigned uncertainties (Fig. 1.3b). In this thesis a different approach to this issue is taken. Statistical uncertainty estimates are derived for each lake sediment record individually, taking into account the variance in the record and where possible comparisons to independent archeomagnetic estimates.

A further complication of using lake sediment data for field modelling is the problem that intensity and declination records are usually relative in nature, rather than absolute. Relative paleointensity used in the CALS3k models (Korte et al., 2009; Donadini et al., 2009) were calibrated prior to being used for modelling via the technique described by Korte and Constable (2006). That involves comparison with the ARCH3k.1 model or with archeomagnetic data from nearby locations. Relative declination records have been compared to the predictions from the previous models (e.g., CALS3K.1), and unoriented records have been adjusted before construction of the CALS7k model (Korte and Constable, 2005a). In the most recent models CALS3K.4b and CALS10k.1b (Korte and Constable, 2011; Korte et al., 2011), the calibration strategy has been improved with the implementation of iterative re-calibration of RPI. Initial calibration is based on the CALS3k.3 model, and after each iteration step, a clean dataset is created from the data which misfits lie in the 99% confidence interval. The sediment records are then re-calibrated and the procedure is repeated. In this thesis calibration factors are instead directly inverted for, as an integral part of the field modelling procedure.

Obtaining stable field models that are valid at the CMB also requires a measures of field complexity to be minimized during the modelling procedure. Several choices for the measures of complexity are possible, and their impact on Holocene time scale field models has been little studied. The choice of measure of misfit between model predictions and observations is also important, particularly as the noise inherent in the measurements is not Gaussian. Most previous time-dependent field models implicitly assume a Gaussian noise model and adopt a least-squares measure of misfit (e.g., Jackson et al., 2000; Korte and Constable, 2005a; Korte et al., 2009). When distributions possess longer tails than a Gaussian (more outliers), then a Laplacian distribution is known to be a useful alternative that leads to an absolute deviation measure of misfit (Claerbout and Muir, 1973; Farquharson and Oldenburg, 1998; Walker and Jackson, 2000). Rather than construct only one Holocene field model, issues related to the choice of complexity and misfit measures are explored in this thesis by constructing and comparing four models involving different combinations of norms and misfit measures.

1.4 Operation of the Holocene geodynamo and the nature of secular variation

In order to understand mechanisms that maintain and drive the evolution of the Earth's magnetic field, a characterisation of its behaviour on time scales of centuries to millennia is required. Previous millennial time scale field reconstructions show complex patterns of geomagnetic field change, including fluctuations of the dipole field (Constable, 2007b; Nilsson et al., 2010), regional non-dipole field changes (Constable, 2007c; Amit et al., 2011), westward (or eastwards) drift of field structures (Dumberry and Bloxham, 2006; Dumberry and Finlay, 2007; Wardinski and Korte, 2008), and suggestions for a continuous spectrum of variability (Constable and Johnson, 2005). Fig. 1.4 taken from Barton (1982) nicely summarizes what are thought to be the main manifestations of such temporal variations and basic ideas concerning the origin of these changes.

Significant progress in our understanding of the geodynamo has been possible thanks to the advent of numerical simulations of the geodynamo over

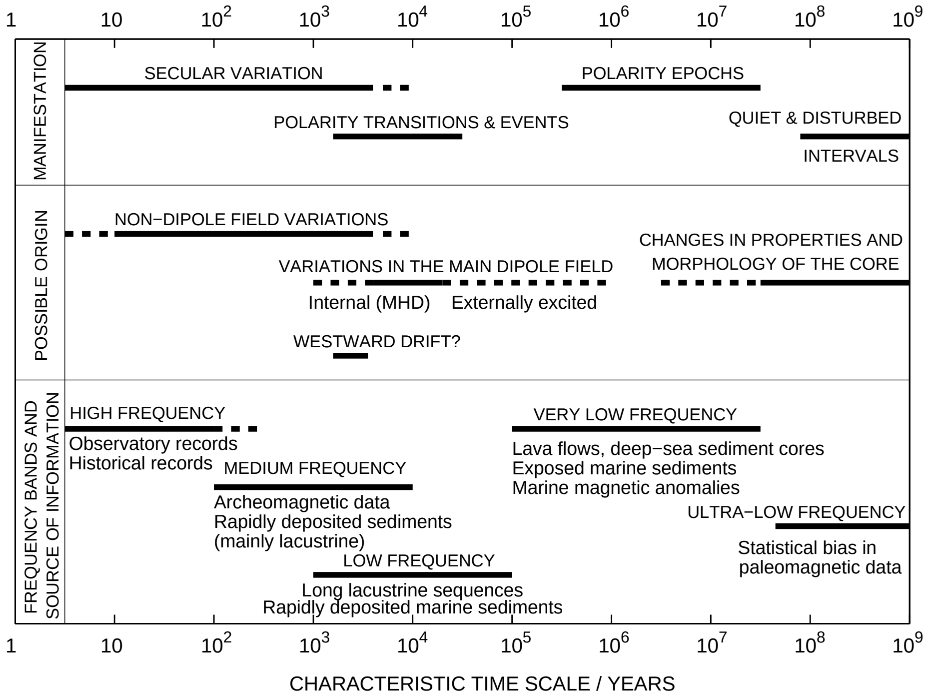

Figure 1.4: Principal frequency bands of the geomagnetic spectrum of internal origin, showing how the variations are manifested, hypothesized origins, and frequency band classification and sources of observational data. Dividing lines between frequency bands are only intended to be approximate. After Barton (1982).

the past two decades (e.g., Roberts and Glatzmaier, 2000; Busse, 2002; Kono and Roberts, 2002). These simulations successfully capture the gross characteristics of the core-generated field, including its dipole-dominated nature and reversals. Paleomagnetic model reconstructions are however vital for the testing such numerical simulations through comparisons of the field behaviour (e.g., McMillan et al., 2001; Bouligand et al., 2005) and also help to drive future research directions by pinpointing deficiencies in the simulations.

1.4.1 The temporal spectrum of field variations

In this thesis, an example of how output of geodynamo simulations and paleomagnetic observations can supplement each other is given through study of the power spectrum of geomagnetic field variations on time scales of 10^2-10^4 years. Relative paleointensity or directional components from sediment cores are obvious candidates for time series analyses, especially the use of spectral estimation techniques. Several previous studies of secular variation in sediment records have reported evidence for periodicities. For example, Barton

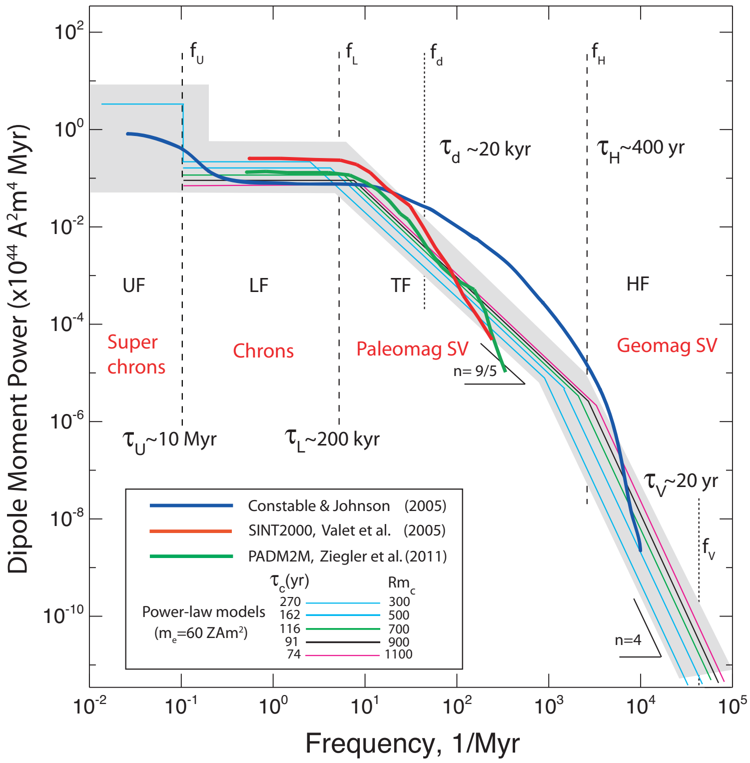

Figure 1.5: Comparison of observed geomagnetic dipole moment frequency spectra (thick solid lines) with the composite power-law model converted to dipole moment (thin solid lines) using results from numerical dynamos, for various outer core advection times τ_c. Rm_c is the corresponding magnetic Reynolds number and the grey bar shows the range of plausible τ_c values. Spectral slopes (n) corresponding to exponents of the power-law model (f^{-n}) are shown for reference. Figure from Olson et al. (2012).

(1983) carried out spectral analysis of paleomagnetic time series, concluding that there was no evidence for discrete periods but rather for wide frequency bands of preferred periods. Constable and Johnson (2005) later produced a composite paleomagnetic power spectrum for the dipole moment, including a contribution from the CALS7k.2 field model (Korte and Constable, 2005a). Currie (1968) has argued that temporal power spectra of geomagnetic field observations obtained at worldwide observatories is governed by a power law.

Recently a power spectrum derived by Olson et al. (2012) from numerical dynamo simulations (Fig. 1.5), showed different spectral slopes for different frequency bands. Their broadband spectrum agrees well with the spectra of geomagnetic variations discussed by Constable (2011), the observed geomagnetic dipole moment frequency spectrum from the SINT2000 relative paleointensity record by Valet et al. (2005), the composite paleomagnetic spectrum by Constable and Johnson (2005), and PADM2M composite spectrum by Ziegler et al. (2011). Such a broadband spectrum has deep implications for our understanding of secular variation, because it implies chaotic forcing (due to turbulent core convection), with power distributed over all times scales, rather than simple, well organized modes of field evolution. In this thesis, we use the global compilation of Holocene lake sediment observations to study in more detail the temporal spectrum on time scales of 100 to 10,000 years. Attention is not restricted to dipole field variations and care is taken to search for preferred periodicities, taking into account that these may be non-stationary or quasi-periodic.

1.4.2 Holocene dipole moment evolution

All available absolute paleointensity data from the GEOMAGIA50 database have been used used to reconstruct the variations of the dipole moment over the last 50 kyrs (Knudsen et al., 2008). In Fig. 1.6, the GEOMAGIA50 virtual axial dipole moment VADM (Eq. 1.15) for the Holocene period is plotted together with the dipole moment estimates from the CALS10k.1b global field model.

$$\mathrm{VADM} = \frac{4\pi a^3}{\mu_0} \frac{F}{\sqrt{1 + 3\cos^2\theta}} \tag{1.15}$$

where F is an intensity measurement, $\mu_0 = 4\pi \cdot 10^{-7}$ Vs/(Am) is the permeability of free space and θ is geographic colatitude.

The two reconstructions agree fairly well in the recent millennia and reproduce the historically observed decay of the dipole moment. Although, the CALS10k.1b dipole moment follows the trend in the GEOMAGIA50 VADMs, there is a notable offset in the magnitude with the CALS10k.1b reconstruction exhibiting lower values than the direct estimates from archeomagnetic intensity data that effectively ignore non-dipolar fields (Korte and Constable, 2005b). The general trend of relatively higher dipole moment in the recent 3 millennia and lower values before, with a minimum Holocene dipole moment between 6000 BC and 4000 BC is observed in both reconstructions. In this thesis, dipole moment predictions are estimated from four new Holocene field models and compared with the CALS10k.1b estimates. Moreover, the averaged field morphology at the CMB is investigated in order to see what changes occur that may help to explain the current dipole moment decay.

1.4.3 Time-averaged field structure at the CMB

The time-averaged radial field structure at the CMB from the *gufm1* historical field model, spanning the past 400 years, and the CALS7K.2 model covering the past 7000 years are presented in Fig. 1.7. It is obvious that averaging over longer time scales somewhat smooths out the intense magnetic flux patches

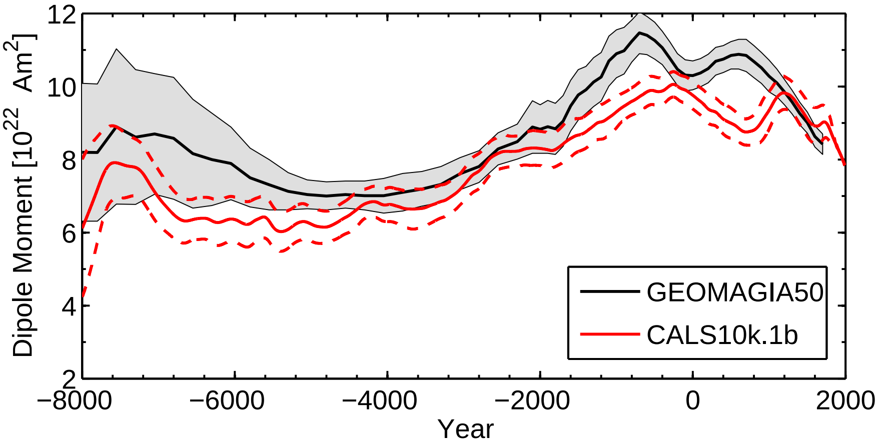

Figure 1.6: Evolution of the Holocene dipole moment from the CALS10k.1b model (Korte et al., 2011) (red curve) compared to the dipole moment reconstruction of Knudsen et al. (2008) (black curve) based on the GEOMAGIA50 database (Korhonen et al., 2008). Dashed red lines are the error bounds of the CALS10k.1b dipole moment obtained by bootstrap sampling. The grey area shows the associated error estimates (2σ) obtained using a bootstrap approach of reconstructing the GEOMAGIA50 dipole moment.

seen over the historical era. While two strong flux lobes in both, the Northern and Southern hemispheres are seen in the *gufm1* model (under North America and Siberia, and South America and Australia, respectively) they can not be clearly distinguished in CALS7K.2 model. Another difference is the reversed flux patches in the Southern hemisphere from the *gufm1* model, which are not present in the CALS7K.2 model. In this thesis, the time-averaged field morphologies from four new Holocene field models are investigated to test the existence of persistent flux patches over the Holocene period. The influence on the inferred field structures of the form of spatial regularization and measure of misfit employed during the modelling is discussed.

1.4.4 Abrupt changes on centennial time scales: Archeomagnetic jerks

Studying the directional and intensity variation from high-resolution (well dated), archeomagnetic data in Western Europe during the last 3 kyr, Gallet et al. (2003) defined a new feature of geomagnetic secular variation they christened as 'archeomagnetic jerks'. These events involve sharp changes in directions and maxima in intensity on a time scale of about hundred years. Two clear events were identified ∼200 AD and 1400 AD; two less well constrained at ∼800 BC and 800 AD (Fig. 1.8) were also discussed. An investigation of

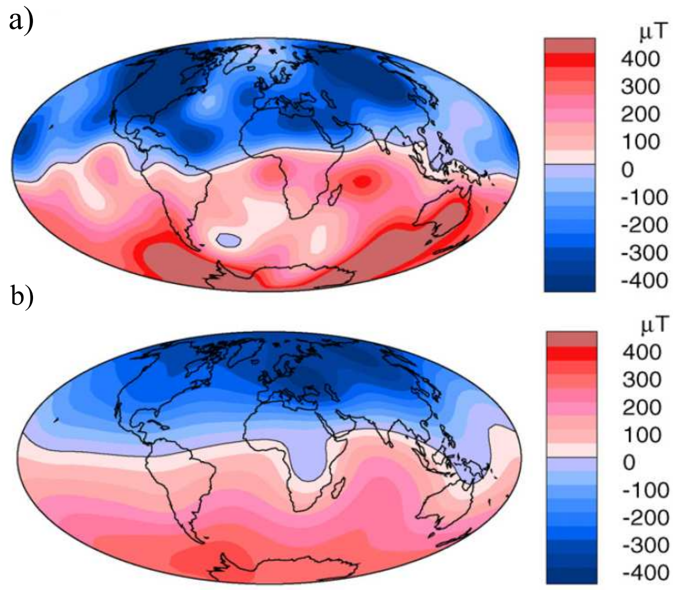

Figure 1.7: Time-averaged radial field component at the CMB from the historical field model *gufm1* (Jackson et al., 2000) (a) and the 7000 years CALS7K.2 model (Korte and Constable, 2005a) (b) over the past 400 years and 7 kyrs, respectively. Figure adapted from Korte and Holme (2010).

samples from an archeometallurigal excavation in the Middle East (Ben-Yozef et al., 2009) also displays a remarkable spike in field strength, with sample mean values of over 120 μT in around 1000 BC.

It is important to know whether these events are global or local in extent and to determine what changes in the core surface underlies them (Dumberry and Finlay, 2007; Gallet et al., 2009). Recent studies on Peruvian potsherds (Stark et al., 2009) and kilns/hearths in Korea (Yu et al., 2010) implied an occurrence of archeomagnetic jerks outside European continent whose findings fit well with those suggested in French archeomagnetic data. Apart from archeomagnetic data, Snowball and Sandgren (2004) reported that these features can be recorded in lake sediment records from Fennoscandia. Pavón-Carrasco et al. (2009, 2010) used the regional geomagnetic field models SCHA.DIF.3K and SCHA.DIF.8K to identify six archeomagnetic jerks for the last 3000 years and several prior to 1000 BC in Europe.

The origin of these jerks is still not completely understood, although there are some suggestions related to the dynamics of the core surface. Dumberry and Finlay (2007) showed that rapid changes in the direction of the azimuthal flow at the core mantle boundary cause sharp directional changes. Gallet et al. (2009) found that the occurrence of archeomagnetic jerks coincide with a strong quadrupole field component and strong eccentric dipole. This finding has lead them to connect archeomagnetic jerks and times of maximum

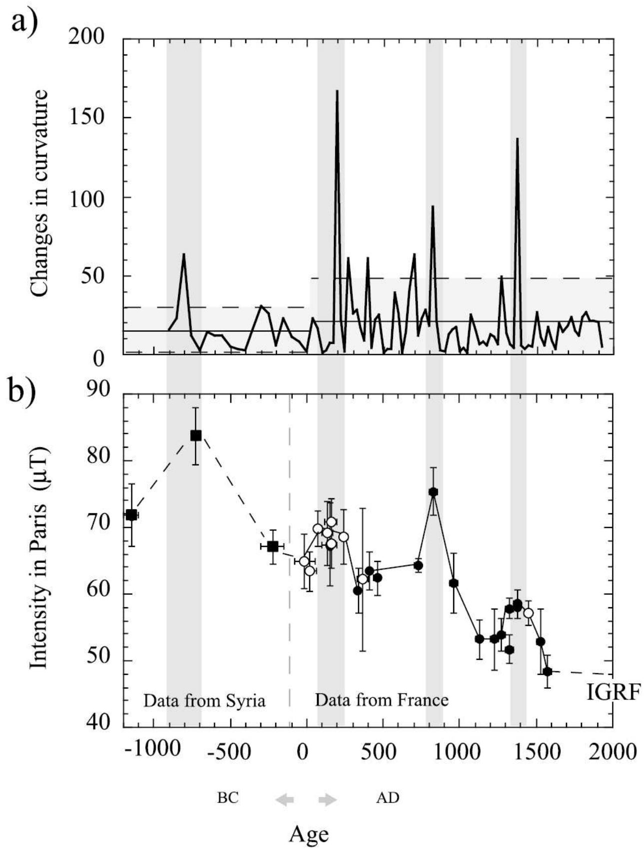

Figure 1.8: (a) Changes in curvature of the smoothed directional variations curve of the geomagnetic field in Western Europe during the last 3 kyr inferred from archeomagnetic data; (b) Archaeointensity variation curve in Europe and the Middle East; Shaded bands indicate the proposed times of occurrence of archeomagnetic jerks, i.e., cusps in magnetic field directional drift and sharp intensity maxima. Figure adapted from Gallet et al. (2003).

hemispheric asymmetry of the geomagnetic field. In this thesis investigations are carried out to determine whether lake sediments and field models derived primarily from them are capable of capturing archeomagnetic jerk type events during the Holocene.

1.4.5 Link to paleoclimate

An important application of knowledge of the geomagnetic field evolution on centennial to millennial time scales is the information given to workers studying the production rate of cosmogenic isotopes (Beer et al., 2002; Knudsen et al., 2008). It is known that Earth's magnetic field shields our planet from charged particles of cosmic origin. Cosmogenic nuclides, such as ^{14}C, ^{10}Be, and ^{36}Cl, are produced in the Earth's upper atmosphere by nuclear interactions between energetic cosmic ray particles with target elements. This cosmogenic isotope production is also modulated by the geomagnetic field as was initially inferred from archeomagnetic absolute paleointensities (Elsasser et al., 1956). Reconstructions of millennial time scale geomagnetic field behaviour now provide the basis for assessing variations in these production rates (e.g., Masarik and Beer, 1999; Snowball and Sandgren, 2002; Solanki et al., 2004). Usoskin et al. (2006) reconstructed the solar activity using the paleomagnetic dipole moment over the last 7000 years from the CALS7k.2 model (Korte and Constable, 2005a,b). More recently, Usoskin et al. (2008) and Usoskin et al. (2010) have used both dipole and quadrupole terms from geomagnetic field models in studies of centennial variations of cosmic ray induced atmospheric ionisation. The new Holocene field models constructed in this thesis will contribute to an improved understanding how geomagnetic field modelling choices influence the diagnostics required in cosmogenic isotope studies.

1.5 Thesis outline

The objectives of this thesis are 1) to derive new appropriate and consistent uncertainty estimates for lake sediment records; 2) to implement the method developed on a case study of new lakes sediment records from Switzerland; 3) to search for evidence of periodicities in Holocene lake sediment magnetic records, and 4) to build on new models of Holocene geomagnetic field evolution based on a global compilation of paleomagnetic and archeomagnetic data directly including relative declination and paleointensity and also making use of the new uncertainty estimates for lake sediment records.

The structure of the thesis is as follows. Chapter 2 gives an introduction to the available data compilation of sediment magnetic records and archeomagnetic data (Korte et al., 2011). The manner in which materials acquire magnetization are discussed, as well as the advantages and disadvantages of both types of data. Details concerning the spatial and temporal distribution of observations, age ranges, dating techniques, and sedimentation rate of lake sediments are provided.

Chapter 3 presents a new statistical analysis technique developed as part of this thesis to provide improved uncertainty estimates for sediment magnetic records. The approach combines robust smoothing spline models for capturing the random variability in the records and comparisons with the archeomagnetic data and global field models predictions. An output of the analysis is the inherent smoothing time of these paleomagnetic records, i.e., the time scale that they can resolve. Furthermore, a test for the occurrence of systematic inclination shallowing is carried out. The analysis also emphasises some important recommendations for future paleomagnetic studies and for allocating errors to this type of data. Chapter 3 is essentially the published study of Panovska et al. (2012).

In Chapter 4, we search for global periodicities in Holocene sediment magnetic records and characterize of the power spectrum in the period range of $10^2 - 10^4$ years. Three techniques, multitaper spectral estimation, wavelet analysis and empirical mode decomposition, are applied to the robust smoothing spline models of each sediment record derived in Chapter 3. Findings concerning the temporal power spectrum and its slope are linked with the hypothesis of chaotic convection in the outer core and compared with previous results (e.g., Barton, 1982; Constable and Johnson, 2005; Olson et al., 2012).

New lake sediment records, from Lake Soppen and Lake Baldegg in Switzerland, are analysed in Chapter 5. These serve as a case study of the methods for deriving uncertainty estimates and the periodicity analysis. A Holocene paleosecular variation curve for Switzerland is derived by combining the data from the two lakes. Additionally, the occurrence of archeomagnetic jerks is tested on the Swiss records because of their vicinity to the location where these sudden changes of the Earth's magnetic field were originally observed (Gallet et al., 2003).

Chapter 6 presents a series of new time-dependent spherical harmonic field models for the Holocene. These explore different possibilities for the choice for the measures of data misfit and field complexity. The direct implementation of relative declination and relative paleointensity, i.e., calibration of these components during the inversion is described and the new lake sediment uncertainty estimates described in Chapter 3 are used. The field models are compared in terms of the norms, misfits and spherical harmonic spectra. Millennial time scale secular variation in the Holocene is discussed in terms of the evolution of flux features at the CMB. Dipole moments and time average fields are analysed and compared amongst themselves and with the CALS10k.1b (Korte et al., 2011), the only existing model covering the same era.

Chapter 7 collates the results of all analyses: uncertainty analyses, periodicity determinations and Holocene geomagnetic field modelling. It also presents the conclusions and the outlook for future studies. Two appendices are included in the thesis. Appendix A includes three tables with details of the archeomagnetic directional and archeointensity data used, as well as the sediment magnetic records with their codes, coordinates, age ranges, number of data and references. Appendix B discusses the influence of the default parameter used to build field model using maximum entropy regularization. Appendix C summarizes the L_2 misfits of the four models in Chapter 6 to all the lake sediment records. Spatial distributions of residuals from the four models are presented in Appendix D. Comparison plots of field model predictions to all lake sediment records, as well as the CALS10k.1b model predictions, are shown in Appendix E.

Chapter 2

Holocene magnetic data compilation

2.1 Overview

A number of paleomagnetic databases (McElhinny and Lock, 1996; McElhinny and McFadden, 1997), as well as a notable collections of archeomagnetic data (Daly and Le Goff, 1996) are stored at the World Data Center in Boulder. In addition to these, the more recent archeomagnetic directional database Archeo00 by D. Tarling, the ArcheoInt database of intensity measurements spanning the past 10 millennia (Genevey et al., 2008), and comprehensive GEOMAGIA50 database (Donadini et al., 2006; Korhonen et al., 2008) are available. These contain archeomagnetic data collected from original literature or directly from authors. In particular, the GEOMAGIA50 database is useful because it has the possibility for querying some metadata, e.g., material, paleointensity method, dating technique, number of samples, number of specimens, and permits the construction of constrained datasets.

Constable et al. (2000), in one of the first attempts to construct regularized field models spanning the past few thousand years, developed the PSVMOD1.0 compilation consisting of 24 globally distributed paleosecular variation curves. This compilation has been greatly expanded and successively updated (Korte et al., 2005; Donadini et al., 2009; Korte et al., 2011), resulting in the most complete assemblage of paleomagnetic data that has been used to construct a series of time-dependent field models spanning the Holocene (e.g., Korte and Constable, 2005a; Korte et al., 2009, 2011). This compilation forms the basis for the work performed in the present thesis. In the remainder of this section the characteristics of archeomagnetic data and sediment magnetic records are presented. The mechanism by which these materials acquire magnetization, associated laboratory procedures, and the assessment and treatment that should be employed on these data, are described.

2.2 Archeomagnetic data

Lava flows and archaeological artifacts, such as pottery, kilns or ceramics provide very important isolated records for studying geomagnetic secular variation. When igneous rocks and archeological artifacts cool down, they acquire a thermoremanent magnetisation (TRM) (Constable, 2007a). Above the Curie temperature (T_c) of the ferromagnetic minerals, individual magnetic moments are free to fluctuate (Fig. 2.1). When cooling through the (T_c) magnetic moments statistically align in the geomagnetic field and a spontaneous magnetisation arises (Lowrie, 2007). The magnetisation becomes blocked along an easy direction of magnetisation of the grain when the thermal energy is no longer greater than the magnetic anisotropy energy. The blocking temperature of TRM depends on factors, including the grain size, grain shape, spontaneous magnetisation and magnetic anisotropy of the ferrimagnetic mineral. Therefore a broad spectrum of blocking temperatures can happen, and a partial TRM (pTRM) is acquired while a rock is cooling down. It is important to observe the pTRM steps in order to check the thermal stability of ferromagnetic minerals and chemical alterations, which can produce new minerals.

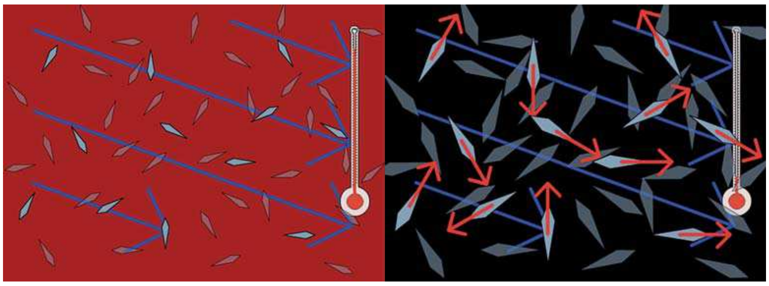

Figure 2.1: Acquisition of a thermoremanent magnetisation (TRM) in lava flow. Domains within the magnetic mineral statistically align with the ambient Earth's magnetic field when the lava cooled below the Curie temperature. Figure from Tauxe and Yamazaki (2007).

One specific characteristic of archeomagnetic data is that they are not a continuous series in time for one particular location, but the data are often grouped in regions where a considerable quantity of suitable artifacts are available and studies have been carried out (Fig. 2.2). The number of available archeomagnetic data is rather small on the global scale, especially in the Southern hemisphere. For example, there are no directional archeomagnetic data from South American continent, only archeointensity data from Peru and Bolivia. The European continent has the highest concentration of archeomagnetic data (Fig. 2.3a, where the markers shown indicate the average locations of the archeomagnetic regions). Tables A.1 and A.2 in Appendix A

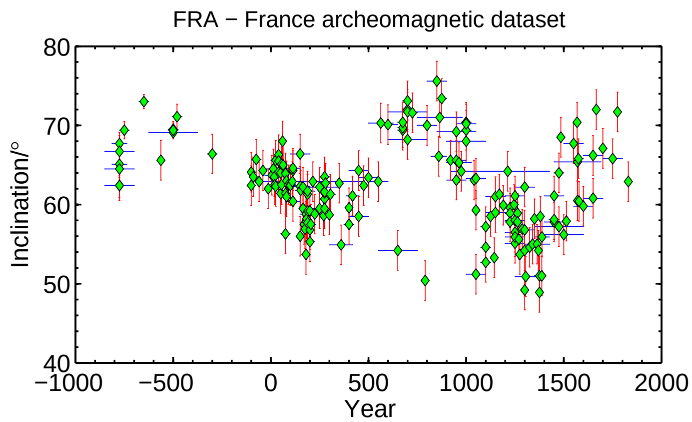

Figure 2.2: An example of inclination archeomagnetic data from France (Korhonen et al., 2008), FRA in Table A.1. Green diamonds represent original data, error bars for age estimates (blue) and uncertainties in inclination (red) are shown.

list the names, regions, geographic locations, time span and number of data available in the archeomagnetic compilations of Korte et al. (2005); Donadini et al. (2006); Korte and Constable (2011), documenting the directional and intensity data, respectively. Aside from data obtained from lava flows and archeological artifacts, some data from Mexican stalagmites (Latham et al., 1986) have been added to Southwest USA (SWU dataset in Table A.1). Note that the data are not evenly distributed in time (Fig. 2.3b). It is evident that the quantity of archeomagnetic data is increasing with time.

2.3 Lacustrine and marine sediment dataset

Sediments acquire their magnetisation in a process known as depositional or detrital remanent magnetization (DRM) (Johnson et al., 1948; Griffiths, 1955; King, 1955; Tauxe, 2002), which involves the magnetic moments of grains aligning statistically with the ambient magnetic field (Fig. 2.4). However, DRM is not final magnetization until the sediment has been compacted and locked. The original DRM is often destroyed by sediment compaction, bioturbation, and diagenesis, and the remanent magnetisation that eventually locks-in is then refereed to as post-depositional remanent magnetization (pDRM) (Irving and Major, 1964). When assessing reliability of sediment magnetic records, the process by which the sediments become magnetized must be considered.

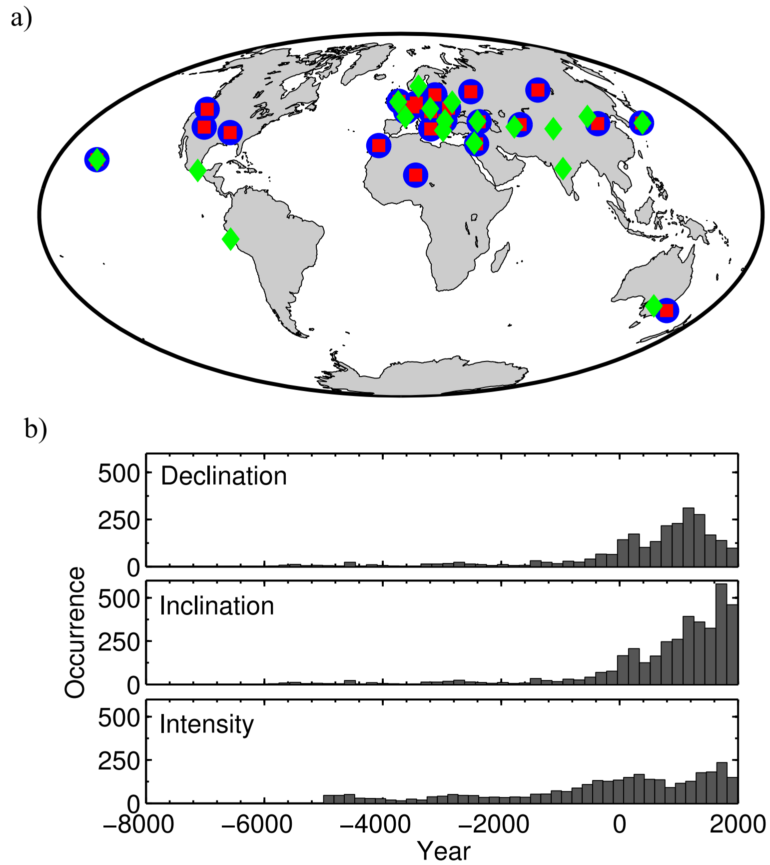

Figure 2.3: (a) The global spatial distribution of archeomagnetic data, declination (red squares), inclination (blue circles) and intensity (green diamonds). Archeomagnetic data are grouped in regions and they do not come from the exact same locations. Markers are plotted on the average location for the given region. (b) Temporal distribution of declination, inclination, and intensity. The time scale is in units of years (AD/BC), following the convention used in the field modelling community.

Sedimentary sequences provide long and continuous records of the variations of the geomagnetic field and also provide a reasonably global distribution. In the thesis I make use of the most comprehensive existing database of Holocene sediment records. This was originally compiled by Korte et al. (2005), updated by Donadini et al. (2009), and expanded with new records from 13 additional locations by Korte et al. (2011). Most of the records come from lakes (90%), the remainder are marine sediment records from a limited catchment basin. Table A.3 in Appendix A lists the codes, names, location, latitude, longitude, mean sedimentation rate (SR), age range, number of data and references for the individual sediment records. The Finnish lake record

(FIN) contains multiple lake sediment cores, with the Lake Lehmilampi and Lake Kortejärvi stacked and smoothed together (Haltia-Hovi et al., 2010). Three marine sediment records from the Ionian Sea, Adriatic Sea (core AD2) and Tyrrhenian Sea were excluded from further analysis due to their very low sedimentation rate (approximately 0.1 mm/yr), or questions concerning disturbances in the Tyrrhenian cores due to their high water content (Vigliotti, 2006). A further two records from Byestadsjön, Sweden (Snowball and Sandgren, 2004; Snowball et al., 2007) and the Larsen Ice Shelf, Antarctic Peninsula (Brachfeld et al., 2003) were also omitted, because their ages were determined by paleomagnetic method rather than by independent dating.

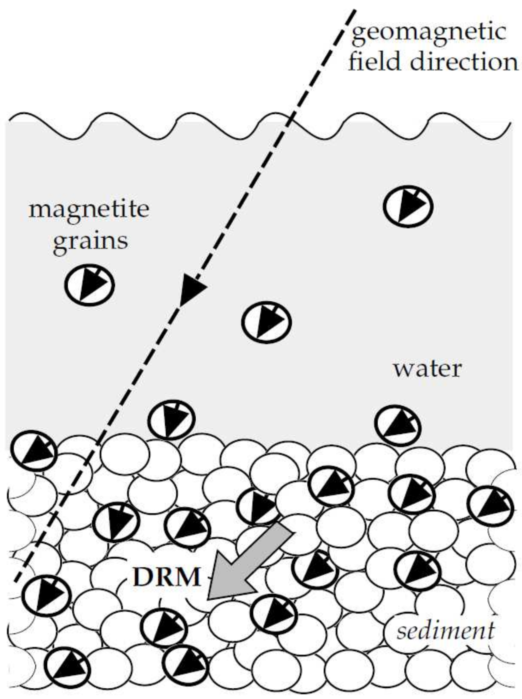

Figure 2.4: Simplified sketch showing the acquisition of a detrital remanent magnetisation (DRM) in a sediment. Orientation of the sediment magnetic grains is driven by the geomagnetic field. Figure adapted from Lowrie (2007).

The spatial and temporal distribution of the geomagnetic field elements declination (D), inclination (I), and relative paleointensity (RPI) from this dataset are illustrated in Fig. 2.5 for the Holocene (i.e., last 11.5 kyr). The southern hemisphere is poorly represented for both directional and intensity data, while there is a high concentration of observations in the European region. Histograms of the temporal distribution show that the number of data records increases toward more recent times, and that intensity data constitute

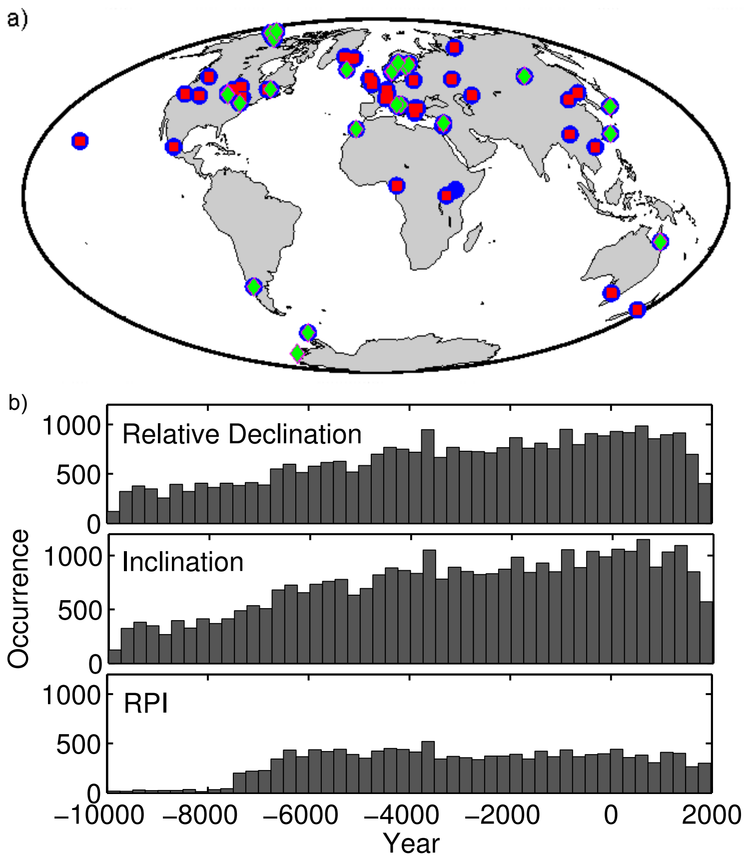

Figure 2.5: (a) The global spatial distribution of Holocene sediment magnetic records, relative declination (red squares), inclination (blue circles) and relative paleointensity (green diamonds). (b) Temporal distribution of relative declination, inclination, and relative paleointensity.

a rather small fraction of the total dataset. The length of the records range from 1150 to 11,855 years, taking into consideration only the data from the Holocene. Age ranges are shown in Fig. 2.6, where at least one component of the magnetic field is available for a given site. In general, the recent half of the Holocene has good data coverage, while coverage is very sparse for the earliest times. This point should be keep in mind when evaluating the global field models.

Radiocarbon (^{14}C) dating is the age determination method most commonly used (Fig. 2.7); it is only possible when organic material is present in the sediments. Some sediments, in particular the Fennoscandian records (Snowball et al., 2007), are varved and can be dated by varve counting, which gives more precise age scales and smaller age uncertainties. Almost half of

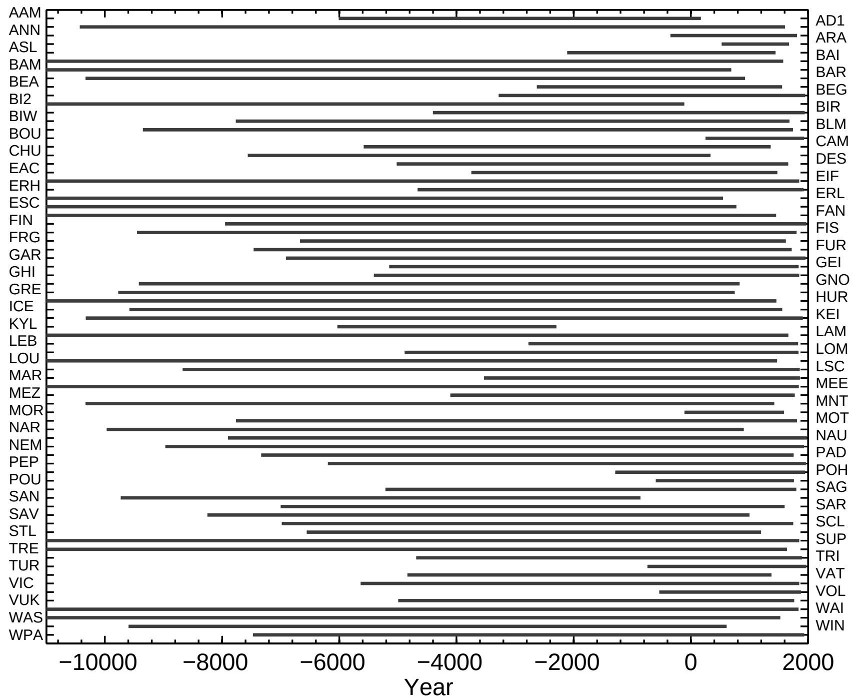

Figure 2.6: Age range at each site location from the database of Holocene sediment magnetic records, where at least one component is available.

the radiocarbon dated records have independent dating points (tephra, varves or pollen) to improve their age-depth model. Korte et al. (2005) used recent calibration curves (e.g., Stuiver and Reimer, 1993) in order to re-calibrate the radiocarbon ages.

An important factor influencing recording fidelity of sediments is the sedimentation rate. The true geomagnetic signal becomes significantly smoothed when the sedimentation rate is low (cf. Roberts and Winklhofer, 2004). Usually, an assumption of constant (or partially constant) sedimentation rate is made in order to obtain an age model for the entire sediment sequence, with linear interpolation based on only a few tie point ages. In most of the original magnetic sediment publications only average sedimentation rates are reported. A mean value for the sedimentation rate is calculated using the age model if more information has been provided. A histogram of the average sedimentation rates for the records used in this thesis is plotted in Fig. 2.8. Lake Aral is a notable outlier with an exceptionally high mean sedimentation of 10.2 mm/yr, due to the tectonic activity, and for clarity of presentation it is

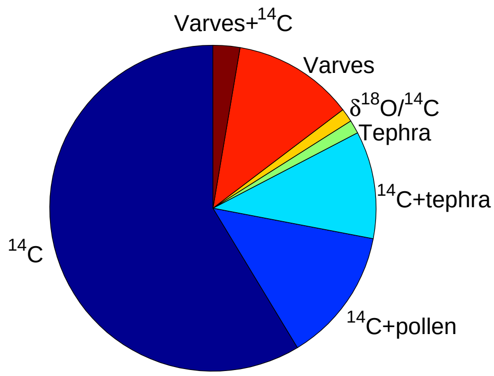

Figure 2.7: Pie chart presenting the different dating techniques used for age determinations of the global Holocene sediment records.

excluded from the Fig. 2.8. The remainder of the sediment sequences have accumulation rates between 0.14 to 3.9 mm/yr.

In order to obtain directional and relative paleointensity data, a range of different sampling strategies, tests and normalisation techniques have been used. Only 12% of the results in the entire database were acquired by U-channel measurements; most studies use discrete samples, which allows for higher temporal resolution. Directional information from the majority of the records has been recovered by selecting pilot samples from different lithological sections and conducting stepwise alternating field (AF) demagnetization to establish the characteristic remanent magnetisation (ChRM). AF demagnetization vector plots for typical pilot samples reveal the optimum AF field which removes any viscous component that may overprint the ChRM.

Sedimentary sequences give only RPI, because there is no definitive theoretical model for how a sediment acquires its magnetisation. The intensity of the natural remanent magnetisation must be therefore normalized by a magnetic parameter that accounts for variations in the concentration of ferromagnetic minerals. Different normalization parameters, such as, anhysteretic remanent magnetisation (ARM), magnetic susceptibility, isothermal remanent magnetisation (IRM), or saturation isothermal remanent magnetisation (SIRM) are employed in various studies. For the majority of the records considered, RPI is determined by the ratio NRM/ARM after some AF demagnetisation (generally between 10 mT-20 mT) or over several demagnetization steps. King et al. (1983) and Tauxe (1993) suggested criteria that paleointensity determinations should meet in order to be considered as reliable. These criteria include consistency between the records from a given region, internal agreement between

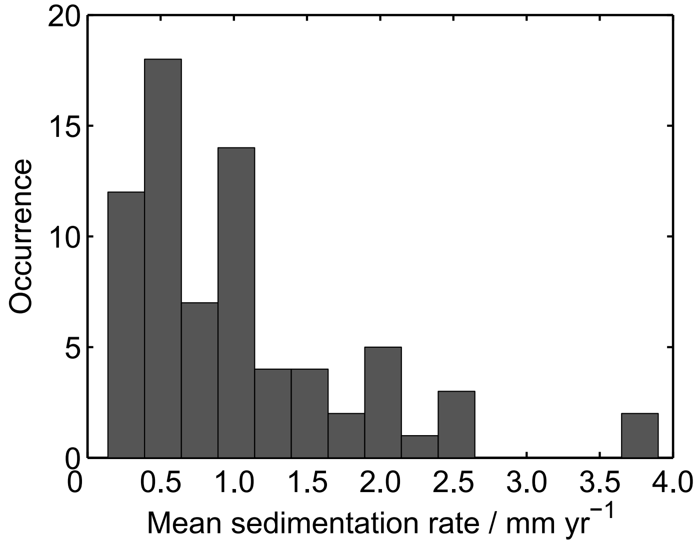

Figure 2.8: Histogram of the mean sedimentation rate in the Holocene sediment records. The mean sedimentation rate of Lake Aral is omitted from this histogram due to its exceptionally high value of 10.2 mm/yr.

cores, uniform magnetic mineralogy, i.e., concentration variations should be less than an order of magnitude, stable magnetic carriers, same ferromagnetic (s.l.) mineralogy, and agreement among different normalization methods.

In Chapter 3 the sediment datasets described above are examined by deriving robust spline models and uncertainty estimates record by record. This data is also the basis for the search for periodicities and the determination of the spectrum of Holocene field variations reported in Chapter 4, Finally, new Holocene geomagnetic field models (Chapter 6) are derived based on both the archeomagnetic and lake sediment data.

Chapter 3

Uncertainty estimates for Holocene magnetic records

3.1 Overview

The goal of many paleomagnetic study is to recover the behaviour of the core geomagnetic field. Unfortunately, volcanic rocks are usually extruded in areas of large magnetic anomaly, while archeological artifacts are often fired in regions with developed industry nearby. In both of these cases the local magnetic field deviates from the field of the surface of the core, due to these local magnetic disturbances, so that these materials can only be considered at best to be an approximation of the core geomagnetic field. In practise, this problem is further complicated by the fact that uncertainties in archeomagnetic and paleomagnetic records are much higher than in direct field measurements.

Many factors can influence the accuracy of Holocene magnetic records, and unfortunately there is no simple theory of how uncertainties should be assigned. Previous attempts to estimate uncertainties in paleomagnetic data have taken a variety of approaches. For example, sediment records have been compared with the historical field model *gufm1* (Jackson et al., 2000) in overlapping time intervals (Constable et al., 2000), or by assigning minimum uncertainties for different classes of data. Errors in the ages of paleomagnetic samples are another important source of uncertainty. In most cases, the age uncertainties range from a few decades to a few centuries, depending on the dating method. Radiocarbon (^{14}C) dating is commonly used, but some sediments are varved and ages can then be determined with close to annual accuracy, however some uncertainty is still associated with these methods (Stuiver and Reimer, 1993; Oldfield et al., 1997; Stuiver et al., 1998; Stanton et al., 2010). Ideally, all these sources of uncertainty should be taken into account during any field modelling procedure. In the geomagnetic field model of the Holocene presented in Chapter 6 of this thesis, we adopted uncertainty estimates for archeomagnetic data used by other workers (Korte and Constable, 2011; Korte et al., 2011). Note that these studies avoid the problem of assigning larger uncertainty estimates to intensity data where the field is strong (Suttie et al., 2011), which occurs when intensity errors are defined as a percentage of the observed value (Korte et al., 2005). However, new uncertainty estimates for sediment magnetic records are derived in this chapter and employed later for the field modelling.

3.2 Uncertainty estimates for archeomagnetic data

Determination of the absolute intensity is based on comparison of the natural remanent magnetisation (NRM) of the sample with a laboratory acquired thermoremanence. The commonly used techniques are Thellier-type methods (Thellier and Thellier, 1959; Coe, 1967; Aitken et al., 1988; Yu et al., 2004), Shaw-type methods (Wilson, 1961; Shaw, 1974; Senanayake et al., 1982) and several other techniques (Kono and Ueno, 1977; Walton et al., 1992; Cottrell and Tarduno, 1999; Hoffman and Biggin, 2005; Dekkers and Böhnel, 2006; Weiss et al., 2007). Several studies discuss the problems concerning the paleointensity determination using different procedures (e.g. Thellier and Thellier, pseudo-Thellier, Wilson, Shaw, microwave), including TRM anisotropy, cooling rate effects, mineralogy alteration during heating and grain size effects of MD and PSD (Genevey and Gallet, 2002; Valet, 2003; Genevey et al., 2008). In order to obtain directional data, progressive demagnetization (AF or thermal) is done and results are plotted using orthogonal vector component diagrams (Zijderveld, 1967). This data is then analysed with help of principal component analysis (PCA) to obtain magnetisation components (Kirschvink, 1980).

Due to the process of TRM acquisition (see Section 2.2), corrections for magnetic anisotropy of the TRM, cooling rate, and alteration are often applied (e.g., Genevey et al., 2008). Strong magnetic anisotropy can introduce an over- or underestimation of intensity if the laboratory field is applied in a different direction than the natural magnetic field. Therefore, the laboratory field should be applied in a direction parallel to NRM, in order to minimise the anisotropy effect, alternatively corrections based on anisotropy tensor of TRM (ATRM) should be applied (Selkin and Tauxe, 2000; Leonhardt, 2006). The cooling rate in the laboratory should ideally be similar to the natural one in order to obtain unbiased paleointensity, otherwise a cooling rate correction based on relaxation geospeedometry can be applied (Leonhardt et al., 2006).

To summarize, potential sources of the uncertainty in archeomagnetic data include: 1) dating errors; 2) cooling rate differences; 3) magnetic anisotropy (Lanos et al., 2005); as well as 4) uncertainties related to the thermal remanence acquisition, local magnetic field anomalies, and errors during sampling (Constable et al., 2000). For artifacts from regions with well-constrained archeological data, the ages can be accurate to within few years. Radiocarbon dating is also commonly used for both sediments and archeomagnetic data.

When no age uncertainties were given for archeomagnetic data, Korte et al. (2005) assigned dating uncertainties depending on age, 250 years for data older than 0 AD, and 10 years, 50 years or 100 years for younger data based on the archaeological knowledge available for the particular location. These data uncertainties were taken into consideration in time-dependent global field modelling in combination with measurement uncertainties (Korte et al., 2005). In this way, magnetic uncertainty estimates were increased depending on the age uncertainty categories (cf. Table 5 in Korte et al., 2005). Moreover, extra uncertainties were added to the magnetic uncertainties if the precise coordinates of the archeomagnetic data were unknown. The associated uncertainties were determined from average spatial gradients from previous global model predictions assuming the location was unknown within an accuracy of 0.1 degrees (cf. Table 6 in Korte et al., 2005). A different approach to account for age uncertainties is used in the more recent global models of the geomagnetic field CALS3k.3, CALS3k.4 and CALS10k (Korte and Constable, 2008; Korte et al., 2009; Korte and Constable, 2011; Korte et al., 2011). In these studies, age errors are not explicitly taken into account, instead multiple possible solutions were obtained by bootstrap resampling with each sample obtained from a normal distribution centered on the age estimate with a standard deviation corresponding to the age uncertainty estimate. An age uncertainty of 100 years was allocated in the case of no uncertainty, and no minimum value was implemented as some archeological artifacts and lava flows are dated precisely by historical means.

Data from archeomagnetic and lava flows are often obtained by averaging several measurements from individual samples. The most frequently reported values for directional data are 95% confidence cones about the mean (α_{95}) from site directional specimen results or from a smaller number of independent samples (Schnepp et al., 2004). These α_{95} values can be converted to standard deviation errors of declination and inclination using the Fisher statistics (Fisher, 1953) in the following way (Piper, 1989)

$$\alpha_{95} = 140(kN)^{-1/2} \tag{3.1}$$

where N is the number of directions of magnetisation ($N \geq 10$), and k is the precision parameter:

$$k = \frac{N-1}{N-R} \tag{3.2}$$

where R is the resultant vector (Butler, 1992). Uncertainties of site mean inclination and declination are related to α_{95} by

$$\alpha_{95} = \delta I = \delta D \cos I \tag{3.3}$$

The angle α_{63}, often called the angular standard deviation, is analogues to one standard deviation (σ) of a Normal distribution. While 68% of observations in a Normal distribution lie within σ of the mean value, only 63% of directions are within α_{63} of the true mean direction.

$$\alpha_{63} = 81(kN)^{-1/2} \tag{3.4}$$

Combining 3.1, 3.3 and 3.4, declination and inclination uncertainties are:

$$\sigma_I = \frac{81}{140}\alpha_{95} \quad \text{and} \quad \sigma_D = \frac{81}{140\ \cos I}\alpha_{95} \tag{3.5}$$

Korte et al. (2005) converted the α_{95} to standard deviation errors for declination and inclination in cases where α_{95} is provided by the authors of the archeomagnetic studies. If only one sample per site is measured (no α_{95} is available) or α_{95} is calculated using the number of specimens rather than the number of independent samples, then minimum uncertainty estimates were allocated. Constable et al. (2000) estimated 2.5° and 3.5° as minimum uncertainty for inclination and declination respectively, based on a comparison between archeomagnetic data and the historical geomagnetic field model *gufm1* (Jackson et al., 2000) for overlapping times. All archeomagnetic data whose estimated uncertainties from α_{95} are smaller than these threshold values were assigned with minimum uncertainty estimates in the construction of the CALS7k.2 model (Korte et al., 2005). A similar approach is used for the more recent global models (Korte et al., 2009; Korte and Constable, 2011; Korte et al., 2011) but a minimum α_{95} of 4.3° is implemented instead. Conversion of α_{95} to σ_I and σ_D is achieved with help of (3.5); this means that the minimum declination uncertainty varies with local inclination. Archeomagnetic data often have a priori uncertainties (from the original studies) lower than the estimated threshold, and only 10% to 15% of the original data uncertainties are typically retained (Donadini et al., 2009).

Accurate archeointensity data are more difficult to obtain and there are a wide range of experimental protocols used to derive the results. However, most of the archeointensities ($\sim$ 90%) in the database that we consider are obtained by classical thermal methods (Korte et al., 2005). Coe et al. (1978) proposed a protocol for deriving uncertainty estimates for paleointensity measurements as a standard error of the weighted mean. Often, the mean and standard deviation are calculated according to the number of available specimens. If the standard error (s) has been given, then the standard deviation is calculated according to $\sigma = s \cdot \sqrt{n}$, where n is the number of specimens (Donadini et al., 2009). Comparison with the historical field model *gufm1* revels that minimum uncertainty estimates lie in the range of 5% to 10%. Korte et al. (2005) categorise archeointensity data in three classes according to the following criteria: experimental procedure, dispersion of the mean, TRM anisotropy, number of samples per site and samples per fragment. A relative dispersion between 6% and 10% in the first category, and 10% and 20% in the second and third category, respectively, were assigned to the data.

Suttie et al. (2011) recently found that systematic error is a main contributor to the uncertainty in archeointensity measurements, showing that the experimental protocol or the number of samples do not greatly influence the uncertainty. This implies that uncertainty can not be reduced by averaging and that the use of standard deviation as uncertainty estimate is a questionable approach. Based on the average deviation of archeomagnetic data and historical *g*ufm model, minimum uncertainty estimates of 5 μT are applied to archeomagnetic data, as well as sediment magnetic data, in the more recent models CALS3k.3, CALS3k.4 and CALS10k.1b (Korte et al., 2009; Korte and Constable, 2011; Korte et al., 2011). Such absolute thresholds avoid the criticism of Suttie et al. (2011), using percentages of intensities as error thresholds that later results in a biased inference of global intensity. An alternative treatment of measurement uncertainties has recently been employed in the construction of the CALS3k.4 and CALS10k.1b models, with the bootstrap archeomagnetic samples obtained from a normal distribution centered on the magnetic field value with a standard deviation equal to the data uncertainty estimate. In this thesis, conventional error estimates on the input archeomagnetic data are used for uncertainties, mapping age errors in together with measurement errors and using the errors estimates of Korte et al. (2009) and Donadini et al. (2009).

3.3 Uncertainties in sediment magnetic records

Due to the magnetization process of sediments via DRM and pDRM (see Chapter 2), some additional source of error may enter when considering sediment magnetic records. Inclination flattening caused by sediment compaction has been proposed to affect lake sediment records (cf. Tauxe, 2005; Tauxe et al., 2008). This hypothesis will be tested later in this chapter. Furthermore, because the acquisition process occurs over a significant period of time, this leads to a smoothed record of the actual field behaviour. The amount of smoothing depends on factors including sample size, porosity, sedimentation rate, grain size, bioturbation and the lock-in depth. Bioturbation occurs in the surface mixed layer that has an estimated mean value of 9.8 cm for marine sediments (Boudreau, 1994, 1998), which causes a time lag between the sediment deposition and magnetization ages. The ambient magnetic field vector only starts to lock below the mixed layer when the sediment becomes consolidated. Estimates of the lock-in depth vary over a range of values on the order of 10-20 cm in the deep-sea sediments (Hyodo, 1984; Yamazaki, 1984; Lund and Keigwin, 1994; Channell and Guyodo, 2004; Suganuma et al., 2011). An average lock-in depth of 24 cm, corresponding to 150 yr, has been determined in the sediments from three maar lakes from the West Eifel (Germany) by Stockhausen (1998) from comparison of stacked sediment data with archeomagnetic data. Roberts and Winklhofer (2004) have produced models of the

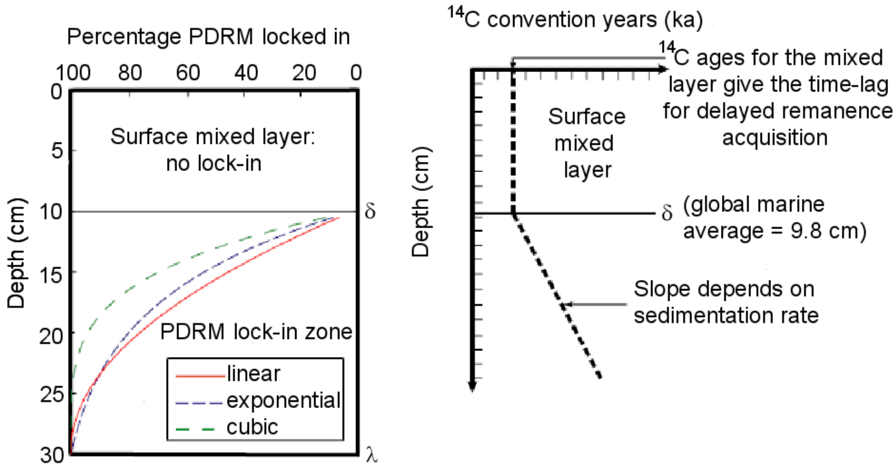

Figure 3.1: Illustration of post-depositional remanent magnetisation (PDRM). The cumulative percentage PDRM locked-in with depth for linear, exponential, and cubic lock-in functions. Surface mixed layer causes a delay in PDRM acquisition and no lock-in occurs within this layer. Adapted from Roberts and Winklhofer (2004).

lock-in process that display a lock-in depth of 10 cm (below the surface mixed layer), with 95% of the pDRM being locked-in within the first 5 cm (Fig. 3.1). This depth is important because together with the sedimentation rate it provides an estimate of the minimum smoothing time (T_s) expected due to the sediment magnetization process.

$$\mathrm{T_S} = \frac{\text{lock-in depth [mm]}}{\text{sedimentation rate [mm/yr]}} \tag{3.6}$$

In this chapter, new uncertainty estimates for Holocene sediment magnetic records, arising from a combination of the effects discussed above, are derived via statistical modelling and comparisons with other sources. The approach is designed to account for the diversity among the records, for example, the measurement procedures, paleomagnetic component determination, or dating techniques. Smoothing spline models are used to separately investigate the random variability present in each record at each location. The degree of smoothing is determined using the technique of cross validation (Green and Silverman, 1994), with a lower limit defined based on an assumed lock-in depth and the mean sedimentation rate for each record. The variance in each record is estimated from the scatter of the data about the spline model. Further tests to evaluate the accuracy of the sediment records are performed by comparing each record to neighbouring sediment records, archeomagnetic data within a 5° area of latitude and longitude, and global field models *gufm1* and ARCH3k.1

(Korte et al., 2009), if nearby archeomagnetic data exist. This allows us to investigate both systematic and random uncertainties that may be present in the records. Further details of this analysis are given in the remainder of this chapter (see also Panovska et al. (2012)).

3.3.1 Spline smoothing methodology

For a given record (t_i, y_i), where t_i is the age and y_i is an observation, a model function $f(t_i)$ is defined, such that:

$$y_i = f(t_i) + \varepsilon_i; \quad i = 1, 2, ..., N \tag{3.7}$$

where ε_i is assumed to be a random, uncorrelated noise. The aim is to find the smoothest possible function $f(t)$ that satisfactorily fits the observations y_i.

The quality of each individual component, i.e., declination, inclination and RPI, can exhibit different uncertainties due to peculiarities of the coring and acquisition processes. For example, due to possible rotations during the coring, inclination records are often found to be more reliable than the declination records. For this reason, each individual field component is studied separately.

Cubic splines

Cubic spline interpolation is a very useful technique to provide an interpolation curve between known data points that possesses desirable stable and smoothness characteristics (Wahba, 1990). It involves constructing a polynomial of low degree between each pair of chosen support points (knots), and gives better results than global interpolation, when a single function is used to fit all the data points. The knot points can be identical with the measurement points, but in general this need not be the case. When degree three (fourth order) polynomials are used, we are considering cubic splines. Splines of degree m have continuous derivatives up to degree $m-1$ at the knot points, thus a cubic spline possesses continuous second derivatives.

Consider a set of known points $t_0, t_1, ..., t_{i-1}, t_i, t_{i+1}, ..., t_n$. To interpolate between these data points using cubic splines, a degree three polynomial is constructed between each pair of knot points. The equation to the left of point (t_i) is indicated as f_i with value $y = f_i(t_i)$ and the equation to the right of point f_i is indicated as f_{i+1} with a value $y = f_{i+1}(t_i)$. The cubic spline function is constructed based on the following criteria (Green and Silverman, 1994):

$$f(t) = \alpha_3(t - t_i)^3 + \alpha_2(t - t_i)^2 + \alpha_1(t - t_i) + \alpha_0 \ \text{ for } \ t_i \leq t \leq t_{i+1} \tag{3.8}$$

The continuity conditions on f and its first two derivatives imply the relations between the coefficients:

$$f_i(t_i) = f_{i+1}(t_i) = y_i \tag{3.9}$$

$$f_i^{'}(t_i) = f_{i+1}^{'}(t_i) \tag{3.10}$$

where the first derivative or the slope $f^{'}$ is the same for the functions on the both sides of a knot, and

$$f_i^{''}(t_i) = f_{i+1}^{''}(t_i) \tag{3.11}$$

where the second derivative $f^{''}$ is the same for the functions on both sides of a knot. One special type of the cubic spline are natural splines where the second derivatives of the splines at the end points are zero.

$$f_1^{''}(t_0) = f_n^{''}(t_n) = 0 \tag{3.12}$$

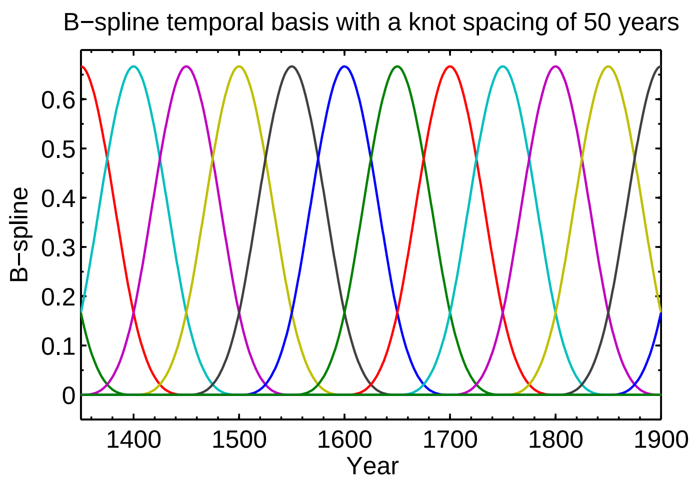

Figure 3.2: Example of a cubic B-spline temporal basis with a knot spacing of 50 years, over the interval $[1350, 1900]$.

B-splines

A B-spline (short for **B**asis spline) curve $f(t)$ can also be defined by

$$f(t) = \sum_{i=1}^{N_K} \alpha_i B_{i,k}(t) \tag{3.13}$$

where N_K is the number of knots, α_j are the spline coefficients, k is the order of polynomial segments and $B_{i,k}(t)$ are the basis functions of the B-splines defined in (3.14). Order k means that the spline is made up of piecewise polynomial segments of degree $k-1$, it follows that the cubic spline is order 4. Below is the Cox-De Boor algorithm (De Boor, 2001) for recursive computations of the basis functions for any B-spline curve of degree n with the knot points t_i:

$$\begin{aligned} B_{i,1}(t) &= 1 \text{ if } t_i \leq t \leq t_{i+1} \text{ , else } 0 \\ B_{i,n}(t) &= \tfrac{t-t_i}{t_{i+n-1}-t_i} B_{i,n-1}(t) + \tfrac{t_{i+n}-t}{t_{i+n}-t_{i+1}} B_{i+1,n-1}(t) \end{aligned} \tag{3.14}$$

B-splines are preferred to polynomial interpolation because they are more accurate, can be easily integrated and differentiated, and do not exhibit spurious oscillations that often accompany polynomial interpolation. For knots that are equally spaced at distances δ, see for example Fig. 3.2, the cubic B-spline function has the following form:

$$f_i(t) = \begin{cases} \frac{1}{6}\left(\frac{t-t_i}{\delta} - 2\right)^3 & t \in [x_i, x_{i+1}], \\ \frac{2}{3} - \frac{1}{2}\left(\frac{t-t_i}{\delta}\right)^3 - \left(\frac{t-t_i}{\delta}\right)^2 & t \in [x_{i+1}, x_{i+2}], \\ \frac{2}{3} + \frac{1}{2}\left(\frac{t-t_i}{\delta}\right)^3 - \left(\frac{t-t_i}{\delta}\right)^2 & t \in [x_{i+2}, x_{i+3}], \\ \frac{1}{6}\left(2 - \frac{t-t_i}{\delta}\right)^3 & t \in [x_{i+3}, x_{i+4}], \\ 0 & \text{otherwise} \end{cases} \tag{3.15}$$

For the analysis of Holocene sediment magnetic records, a regular array of knot points with a fixed 50 year spacing was employed, except for a small number of records with a very small a priori smoothing time, in which case a knot spacing of 25 years was adopted.

Robust smoothing splines

A standard penalized smoothing spline estimation involves minimization of the following objective functional Θ (e.g., Constable and Parker, 1988; Parker, 1994), consisting of the L_2 misfit to the data and a roughness measure chosen to be the quadratic norm of the second time derivative

$$\Theta = \sum_{i=1}^{N} [y_i - f(t_i)]^2 + \lambda \int_{t_1}^{t_N} \left[\partial_t^2 f(t)\right]^2 dt \tag{3.16}$$

where $\lambda > 0$ is a smoothing parameter controlling the trade off between the smoothness and the goodness of fit to the data. This parameter is not specified directly but can be chosen using the method of cross-validation (CV) (cf. Section 3.3.2). t_1 is the start time of the model and t_N is the end time. Due to the presence of non-Gaussian noise and suspected outliers in sediment magnetic records, a 'robust' formulation of the smoothing spline is adopted, replacing the functional (3.16) by

$$\Theta = \sum_{i=1}^{N} |y_i - f(t_i)| + \lambda \int_{t_1}^{t_N} \left[\partial_t^2 f(t)\right]^2 dt \tag{3.17}$$

where the first term is now an L_1 norm of the residuals (e.g., Menke, 1989; Parker, 1994; Gubbins, 2004; Aster et al., 2005; Tarantola, 2005). Using the L_1 norm criterion, i.e., least-absolute deviation, has been shown to reduce the influence of spurious data points, giving them less weight than the L_2 norm (Claerbout and Muir, 1973; Walker and Jackson, 2000). (3.17) can be written in matrix notation as follows:

$$\Theta = \|\mathbf{y} - \mathbf{Bm}\|_1 + \lambda \mathbf{m}^T \mathbf{Dm} \tag{3.18}$$

where $\mathbf{B}$ is a matrix of B-spline construction factors, $\mathbf{m}$ is a vector of the spline coefficients, $\mathbf{D}$ a matrix of inner products of second derivatives of B-splines and $\mathbf{r} = \mathbf{y} - \mathbf{Bm}$ is the residual vector. Minimization of the L_1 norm is carried out by solving a sequence of weighted least squares problems. The solution is obtained by an iterative procedure that involves repeatedly solving the following system (Schlossmacher, 1973; Farquharson and Oldenburg, 1998)

$$(\mathbf{B}^T \mathbf{WB} + \lambda \mathbf{D})\mathbf{m} = \mathbf{B}^T \mathbf{Wy} \tag{3.19}$$

where $\mathbf{W}$ is a diagonal weighting matrix, whose elements are determined from the residuals at the previous iteration as $\mathbf{W} = \mathrm{diag}\,(\sqrt{2}/\mathrm{r}_i)$ (e.g., Walker and Jackson, 2000), starting with $\mathbf{W}_0 = \mathbf{I}$, where $\mathbf{I}$ is the identity matrix. After solving the normal equations via Cholesky decomposition and determining an appropriate smoothing parameter, where possible using the CV method, the residuals are calculated from the final spline model. Following Bard (1974), appropriate L_1 and L_2 measures of the misfit for each of the elements, declination, inclination or RPI, are

$$\sigma_1 = \frac{\sqrt{2}}{N} \sum_{i=1}^{N} |y_i - f(t_i)| \tag{3.20}$$

and respectively

$$\sigma_2 = \sqrt{\frac{1}{N} \sum_{i=1}^{N} [y_i - f(t_i)]^2} \tag{3.21}$$

Cholesky Decomposition

To solve the normal equations (3.19), I used a fast numerical method known as the Cholesky decomposition. If a given matrix $\mathbf{G}$ is symmetric (means $G_{ij} = G_{ji}$) and positive-definite ($\mathbf{xGx} > 0$ for all vectors $\mathbf{x}$), one can implement Cholesky factorization to construct the lower triangular matrix $\mathbf{L}$ and its transpose $\mathbf{L}^T$ which serves as a upper triangular matrix (e.g., Trefethen and Bau, 1997)

$$\mathbf{G} = \mathbf{LL}^T \tag{3.22}$$

or writing in terms of the components:

$$L_{ii} = \left(G_{ii} - \sum_{k=1}^{i-1} L_{ik}^2 \right)^{1/2} \tag{3.23}$$

and

$$L_{ji} = \frac{1}{L_{ii}} \left(G_{ij} - \sum_{k=1}^{i-1} L_{ik} L_{jk} \right) \quad j = i+1, i+2, ..., N \tag{3.24}$$

The Cholesky solving algorithm which is used for determining the cubic B-spline coefficients proceeds as follows:

1. Computation of $\mathbf{B}^T\mathbf{B}$, the damping matrix $\mathbf{D}$ and the right hand side $\mathbf{RHS} = \mathbf{B}^T\mathbf{y}$
2. Cholesky decomposition of $\mathbf{G} = \mathbf{L}^T\mathbf{L} = (\mathbf{B}^T\mathbf{B} + \lambda\mathbf{D})$
3. Solve the lower triangular system $\mathbf{L}^T\mathbf{w} = \mathbf{RHS}$ by back substitution
4. Solve the upper triangular system $\mathbf{L}\boldsymbol{\alpha_o} = \mathbf{w}$ by forward substitution

3.3.2 Selection of the smoothing parameter

The smoothing parameter λ should, where possible, be chosen in an objective fashion. One well known automatic procedure for estimation of the smoothing parameter is the method of cross validation (CV) (cf. Green and Silverman, 1994; Wahba, 1990, for a description and applications). The idea behind this method is the prediction of each data point in turn, using all the remaining data points to find a model that best reproduces the omitted point. It involves making one inversion for each data point, with that data point omitted and then computing the prediction misfit while varying λ. Finally, the λ with the smallest value of cumulative misfit for all inversions (called the CV score) is adopted. The following L_1 version of the cross validation method is used for determination of λ in order to be consistent with the L_1 objective function used in the construction of the smoothing splines

$$CV(\lambda) = \frac{1}{N} \sum_{i=1}^{N} \left| \frac{y_i - f(t_i)}{1 - A_{ii}(\lambda)} \right| \tag{3.25}$$

where A_{ii} is the diagonal element of the so-called hat matrix which maps the vector of observed values to their predicted values, i.e., $f = \mathbf{A}(\lambda)\mathbf{y}$ (Green and Silverman, 1994). This robust CV score is the sum of the absolute values of the residuals corrected by a factor $(1 - \mathbf{A}_{ii})$. A drawback of the method is that this function does not always have a unique minimum, so one must be careful to explore a wide range of λ. In practise, it was evident that a constraint on the minimum degree of smoothing should be implemented in order to avoid underestimating the smoothing parameter. Therefore, a minimum smoothing time (3.6) estimated from the mean sedimentation rates, which are inferred from the original studies of each record, and an assumed minimum lock-in depth (below the mixed layer) of 10 cm, following Roberts and Winklhofer (2004) and Lund and Keigwin (1994), is used. The search over λ is performed across a wide range of values, starting at an upper limit of 10^{10}, and decreasing until a minimum of CV is found or the smoothing time, as deduced by a resolution analysis of the spline model, reaches the minimum a priori smoothing time derived from the sedimentation rate (3.6). In 21% of the records studied the smoothing parameter was objectively determined by the CV method. In the remainder it was set by the a priori threshold smoothing time T_s; the unexpectedly low number of objective determinations of λ was partly because a number of the records had already been pre-smoothed, and partly due to the existence of inconsistent cores in some records.

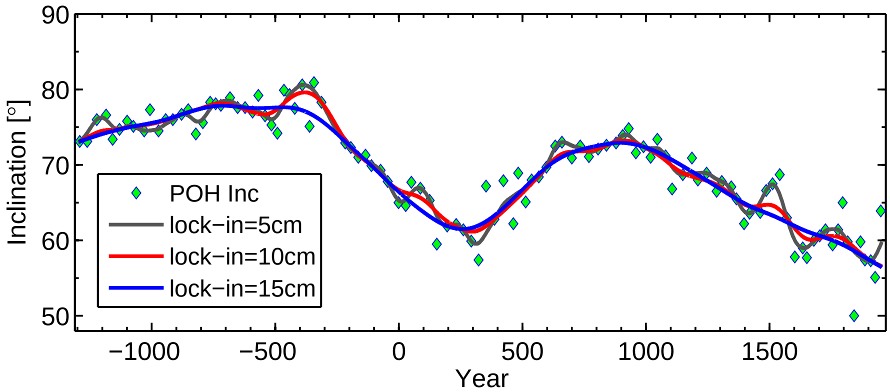

Figure 3.3: Example of the robust spline analysis of inclination data from Pohjajärvi, Finland (POH) (Saarinen, 1998) for assumed a priori lock-in depths of 5 cm, 10 cm and 15 cm.

In order to test the influence of the a priori assumed lock-in depth, an example robust smoothing spline modelling was performed using different possible lock-in depths of 5 cm, 10 cm and 15 cm. The result for the inclination record from Pohjajärvi, Finland (POH) presented in Fig. 3.3 shows that σ_2 for the inclination varied by less than one degree, i.e., 2.66°, 2.47° and 2.50° for 5 cm, 10 cm and 15 cm depths, respectively. The effect is similar for declination records, with variations of the order of degree. Given the weak sensitivity of the variance estimates to the a priori smoothing time, a constraint based on an assumed lock-in depth of 10 cm is implemented in the remainder of the records. This is sufficient to prevent gross underestimation of the smoothing parameter.

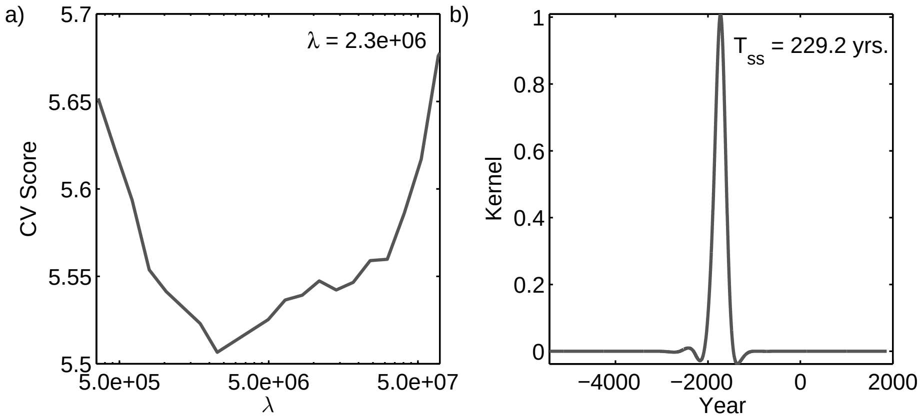

Figure 3.4: (a) Example of the method of cross validation (CV) for choosing the smoothing parameter (λ) for the relative declination record from Cape Ghir, NW African Margin (GHI). The minimum of the CV score determines the choice of λ. The x-axis is given in logarithmic scale. (b) An example of the kernel function on the central point of the same record, which diagnoses a temporal resolution of 229.2 years. The width refers to a full width at half maximum of this kernel function. The robust smoothing spline model for this record is presented in Fig. 3.6 (upper sub-figure).

3.3.3 Results from robust spline modelling

The robust smoothing spline modelling technique was applied to the Holocene sediments records listed in Table 3.2. In each case the original dataset was used without rejection of data. An example of the CV score as a function of the smoothing parameter λ is presented in Fig. 3.4 for the relative declination record of Cape Ghir, NW African Margin (GHI). The minimum of the CV function with respect to λ determines the smoothness of the spline model fit to the data. Also shown in Fig. 3.4 is the temporal resolution kernel, i.e., the response obtained from the spline model to a delta input, in this case placed on the central data point.

For illustration, robust smoothing spline analysis is demonstrated here on two typical examples, where the three components are available, Lago di Mezzano, Italy and Cape Ghir, NW African Margin in Fig. 3.5 and Fig. 3.6, respectively. Similar plots for all records are available online from the EarthRef Digital Archive (ERDA) at http://earthref.org/ERDA/1383. If the CV score is used then a label 'not constrained' is added, otherwise the threshold time value determined from the sedimentation rate is stated. The sub-plots show the data in units of degrees and the robust smoothing spline fit, together with the associated histogram of residuals (normalized to the unit area). To allow comparisons across the records, we consider standardized version of RPI record is defined as

$$RPI_{stand} = \frac{RPI}{\sqrt{\frac{1}{N}\sum_{i=1}^{N}(RPI_i - \mu)^2}} \tag{3.26}$$

where $\mu = 1/N \sum_{i=1}^{N} RPI_i$ is the mean value.

Overall, the robust spline modelling technique performs well, producing smooth models that explain the most coherent signals in the magnetic records. Outliers do not greatly distort the spline model, while the data gaps are handled in a parsimonious manner without spurious oscillations (e.g., Fig. 3.5 and Fig. 3.6). The histograms of the residuals are typically well-explained by a Laplacian distribution, though due to the rather small number of data points it is difficult to rigorously favour either a Gaussian or Laplacian uncertainty model. In the forthcoming sections the L_2 measure of variance σ_2 (henceforth σ_{rss}, where 'rss' stands for the random error determined from the robust smoothing splines) is used to characterize the spread in the residuals, since this is easier to combine with other uncertainty estimates. For the records studied, σ_{rss} ranges from 0.5° to 11.6° (median value: 2.7°; interquartile range: 1.8° to 4.4°) for inclination, 1.2° to 45.6° (median value: 7.5°; interquartile range: 5.1° to 13.2°) for declination, and 0.2 to 1.0 (median value: 0.5; interquartile range: 0.3 to 0.6) for standardised RPI.

Once a spline model is constructed, it is useful to analyse the model's temporal resolution (e.g., Constable and Parker, 1988; Korte and Constable, 2008). This procedure involves inverting a delta function input at various locations with the same smoothing parameter used to create the model (e.g., Parker, 1994). The output is effectively a resolving kernel that diagnoses the amount of smoothing inherent in the spline model. The width at half maximum height of the resolving kernel is thus a measure of the time scale that can be resolved in the record (i.e., it provides the a posteriori estimate of the smoothing time derived from the spline models) and is denoted as T_{ss} in the remainder of the thesis. It is calculated on the internal points of the record, but Table 3.2 only lists its mean and this is used for the comparisons in Section 3.3.2. The smoothing time is difficult to derive directly because it depends on the smoothing parameter, the uneven distribution of data, and different weights that are applied to individual points (due to the L_1 measure of misfit). The smoothing times T_{ss} inferred from the spline modelling range from 27 to 980 years with a median value of 130 years and an interquartile range from 80 to 250 years.

The distribution of the a posteriori smoothing times T_{ss} is presented in Fig. 3.7. Results for σ_{rss} and T_{ss} for all lakes are reported in Table 3.2. The large spread of values obtained for σ_{rss} and T_{ss}, and the significant differences between components, demonstrates the importance of considering each component of each record separately when deriving uncertainty estimates.

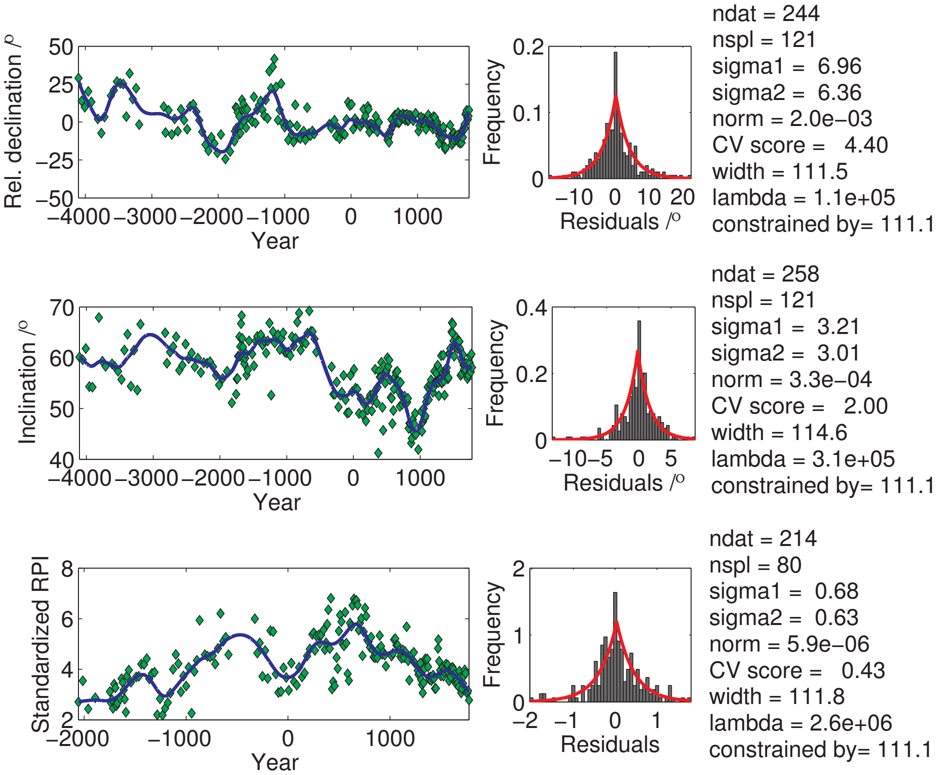

Figure 3.5: Example of the robust spline analysis of relative declination (upper), inclination (middle) and standardized relative paleointensity data (lower) from Lago di Mezzano, Italy. Also shown are the histograms of the residuals (normalized to the unit area) with a Laplacian distribution with mean and deviation calculated from the residuals. Information about the number of data (ndat), the number of splines functions used (nspl), the L_1 measure of misfit σ_1 (sigma1), the L_2 measure of misfit σ_2 (sigma2), the norm measuring the model roughness (norm), the value of the CV minimum (CV score), the width of the resolving kernel or T_{ss} (width), the corresponding smoothing parameter λ (lambda) and a priori smoothing time T_s (constrained) are provided in the label on the right of each sub-figure.

3.3.4 Comparison with existing field models

In addition to the spline modelling analysis, comparisons are carried out between the database of Holocene sediment magnetic records and nearby archeomagnetic data, other nearby sediment records, the historical field model *gufm1* in the time periods of overlap, and the archeomagnetic field model ARCH3k.1 when nearby archeomagnetic data are available. Where possible, these comparisons enable an independent assessment of the fidelity of sediment records

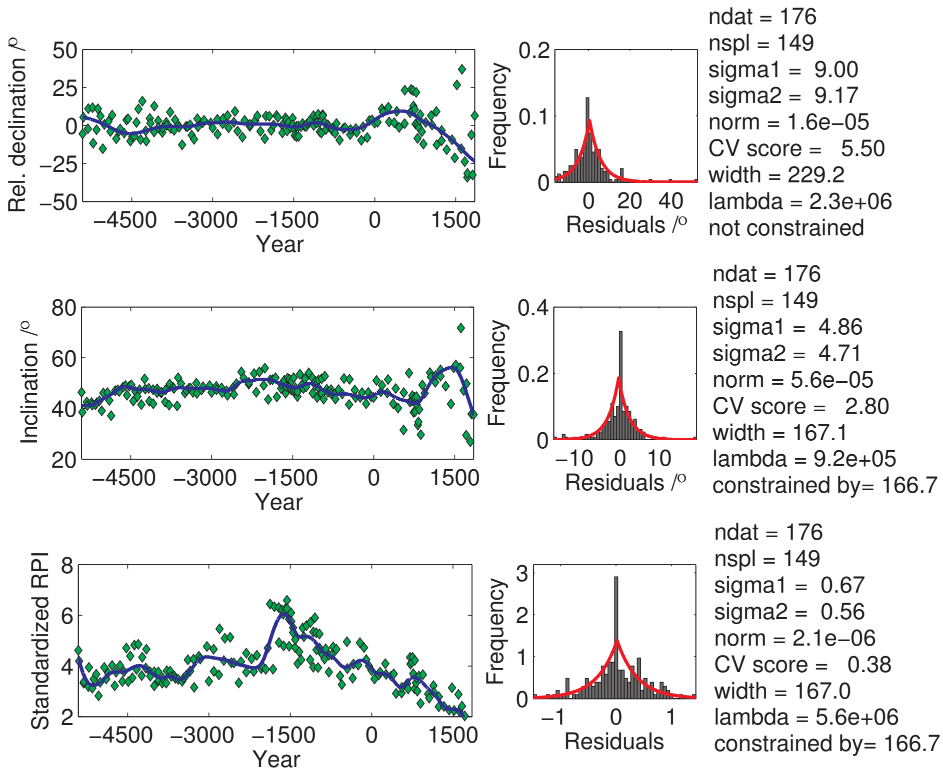

Figure 3.6: Example of the robust spline analysis of relative declination (upper), inclination (middle) and standardized relative paleointensity data (lower) from Cape Ghir, NW African Margin. Also shown are the histograms of the residuals (normalized to the unit area) with a Laplacian distribution with mean and deviation calculated from the residuals. An explanation of the labels is given in the caption of Fig. 3.5.

that include the effects of both random and also systematic uncertainties that could not be assessed by the spline modelling. In order to assess the difference between the compared quantities for each record, the following L_2 measure is used

$$\sigma_c = \sqrt{\frac{1}{N_c}\sum_{i=1}^{N_c}[y_i - \hat{y}(t_i)]^2} \tag{3.27}$$

where $\hat{y}$ are either 'neighbouring' archeomagnetic or lake records, or else global model predictions and N_c is the number of the compared data points. 'Neighbouring' is defined as within 5° latitude and longitude from the record location; such neighbours were then relocated to the lake location using the CALS7k.2 model (Korte and Constable, 2005a), which is a minor correction of at most

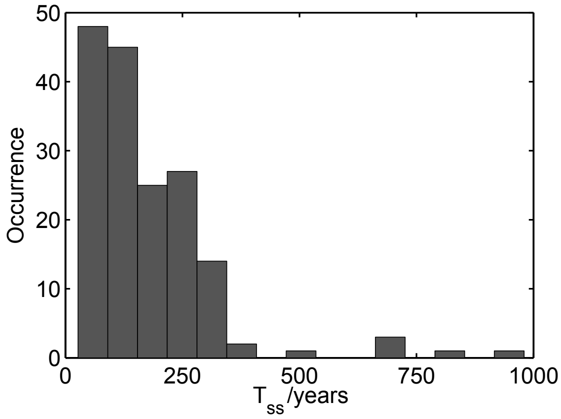

Figure 3.7: Histogram of the a posteriori smoothing time T_{ss} obtained from the smoothing spline modelling for relative declination, inclination and RPI of the Holocene sediment records.

2%. In some cases, the compared values are not of exactly the same age. In this case the mean value of sediment record within an interval of ±50 years was used for the comparison. In the case of neighbouring records, σ_c is computed as a mean over all the data available for comparison with a particular record. In order to obtain statistically reliable estimates, only comparisons with ≥ 30 data are considered. The quantity of comparisons with the historical field model *gufm1* is unfortunately small because of the short period of overlap. Moreover, the magnetization of the top of sediment cores may be not locked-in, which may result in inconsistency when attempting to compare magnetic sediment records with the *gufm1*.

The standardized form of RPI defined in (3.26) is used in the comparisons. Furthermore, due to the fact that many cores may not have been oriented to a known azimuth, declination values are compared in terms of the deviation from the average value of the record, i.e., $D_{rel} = D_{obs} - 1/N \sum_{i=1}^{N} D_{iobs}$. Absolute inclination values are however considered. The lack of absolute measurements of declination and paleointensity from the sediment records requires a special calibration technique. Calibration involves addition of a constant for relative declination and a multiplication by a scaling factor for RPI respectively. Each absolute datum, i.e., field model prediction or archeomagnetic datum, is, in turn, considered to be the true absolute value of the field, and I then calibrate the entire sediment record by assuming the sediment estimate and the selected datum agree at that time. The remaining absolute data can then be compared to the calibrated sediment record. This process is repeated for all the available data M and the total number of comparisons in this case is $N_c = M(M-1)$. The variance σ_c is then obtained from all the comparisons using (3.27). Examples of such comparisons are presented in Fig. 3.8, where the relative declination, inclination and standardized RPI time series from Lago di Mezzano (Italy), the *gufm1* and ARCH3k.1 predictions, and archeomagnetic data are also presented.

The *gufm1* and ARCH3k.1 field models are used for the comparisons since they are truly independent of the sediment magnetic data. Their predictions do not always provide a good fit to the sediment records, and offsets in magnitude and time shifts are observed (e.g., Fig. 3.8). Residuals from the comparisons exhibit in some cases positive or negative mean biases, indicating systematic shifts between the compared quantities. The offsets in inclination obtained by the comparison with the archeomagnetic data and ARCH3k.1 field model (when archeomagnetic data exist) however show no conclusive evidence for systematic inclination shallowing across the compilation of records studied here. For instance, the offsets obtained in the comparisons with the ARCH3k.1 model (when nearby archeomagnetic data were available) range from -6.4° to 6.3° (interquartile range: -4.0° to 2.3°) with a median of -0.9°. The range (minimum and maximum value) together with the median and interquartile values from the four types of comparisons are summarised in Table 3.1. Considering all comparisons, a much better agreement is found for inclination than for declination data. Comparison of inclination estimates yields similar results in all four cases, with median values of σ_c of between 5° and 8°. Encouragingly, good results are obtained for the inclination comparisons between nearby records, indicating the strong inter-lake consistency of inclination. The best comparison results for declination are achieved when lake sediments data are compared with the ARCH3k.1 model when nearby archeomagnetic data are available, see Table 3.1. The maximum value for relative declination comparison with nearby records is obtained between the two coring sites in Arctic Ocean (Alaskan margin and Chukchi Sea), where sharp declination changes with very high amplitudes occur in both records. Overall, these comparisons again indicate the wide range of fidelities that occur in Holocene sediment records and how it is essential to have individual uncertainty estimates for each component of each record.

These test results illustrate that the comparison of sediment magnetic records with the ARCH3k.1 model (at times when archeomagnetic data are available within ±5° latitude and longitude of the record location) is the most useful assessment. Comparison with *gufm1* is limited by the short period of overlap and by atypical behaviour at the top of many sediment cores. Comparison with other sediment records is complicated by the fact that there are no independent a priori estimates of the accuracy of the other sediment records. Direct comparisons with archeomagnetic data are also difficult due to the considerable scatter that is sometimes present in these measurements. In contrast, the ARCH3k.1 model provides a parsimonious estimate of the field at the location of interest that is compatible with nearby archeomagnetic samples. Because the records span several thousand years they enable many

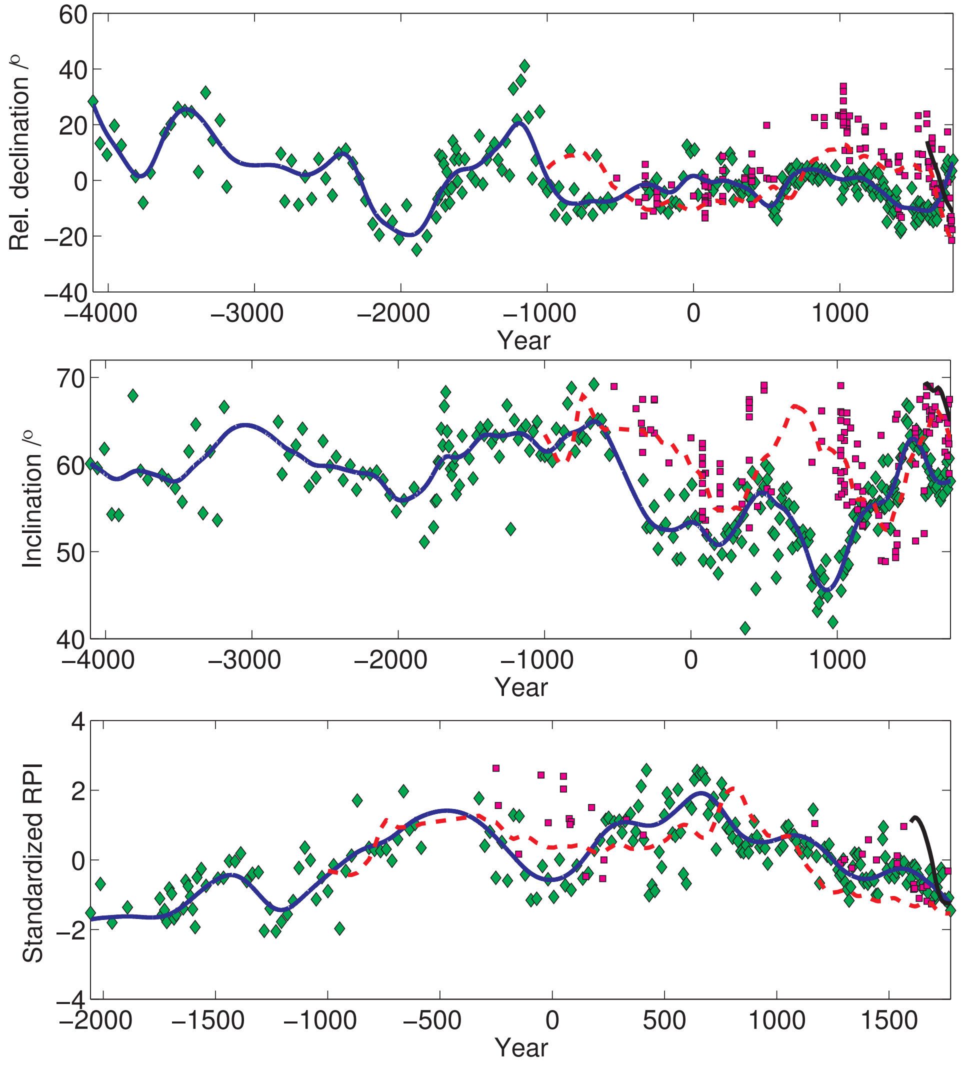

Figure 3.8: Examples of the comparisons between lake sediment data from Lago di Mezzano, Italy (green diamonds), global field models *gufm1* (black curve), ARCH3k.1 (red dashed curve) and archeomagnetic data (magenta squares). Robust smoothing spline fit (blue curve) is shown for reference. Declinations are presented as deviations from their mean value, while RPI are standardized according to the mean and the standard deviation.

Table 3.1: Minimum, maximum and median values, and interquartile ranges (IQR) from comparison between Holocene sediment database with the historical geomagnetic field model *gufm1*, the ARCH3k.1 global model (only when nearby archeomagnetic data are available), archeomagnetic data and nearby sediment records. σ_c is obtained using (3.27), and β_c is systematic bias, which can only be assessed for inclination. n is the number of comparisons considered, each of which has more than 30 contributing data. Last three rows are the final uncertainty estimates σ_l for sediment magnetic records obtained by combination of errors (Section 3.3.5).

Comparison	Component		n	min	max	median	IQR	
gufm1	I [°]	σ_c	8	2.2	17.1	7.0	6.3	9.8
	D [°]	σ_c	6	12.7	34.2	21.8	18.0	27.5
	RPI	σ_c	1	1.4	1.4	1.4	1.4	1.4
	I [°]	β_c	8	-8.3	16.2	-3.1	-5.9	-0.5
ARCH3k.1	I [°]	σ_c	17	3.2	8.1	5.7	5.0	6.8
	D [°]	σ_c	15	5.2	24.6	9.6	7.6	21.7
	RPI	σ_c	3	0.7	1.4	1.3	0.7	1.4
	I [°]	β_c	17	-6.4	6.3	-0.9	-4.0	2.3
Archeomagnetic data	I [°]	σ_c	18	5.0	9.9	7.6	6.6	8.2
	D [°]	σ_c	16	10.0	27.8	17.7	13.6	23.8
	RPI	σ_c	5	1.2	2.8	1.5	1.3	2.7
	I [°]	β_c	18	-7.3	6.1	0.1	-4.4	3.6
Nearby lakes	I [°]	σ_c	49	3.1	14.7	7.6	6.5	10.8
	D [°]	σ_c	45	8.0	151.2	18.4	14.4	27.9
	RPI	σ_c	17	1.0	3.8	1.7	1.4	2.5
Uncertainty estimates	I [°]	σ_l	72	2.5	11.2	5.9	5.4	7.2
	D [°]	σ_l	68	4.1	46.9	13.4	11.4	18.9
	RPI	σ_l	27	0.59	1.32	0.93	0.86	1.01

comparisons. A further advantage of this approach is that uncertainty estimates are available for the model predictions (Korte et al., 2009), which is useful for the combination of uncertainties considered in Section 3.3.5. Henceforth, the terminology 'archeomagnetic estimate' (X_a) is used to mean the ARCH3k.1 model prediction estimated at the record location.

3.3.5 Uncertainty estimates for global field modelling

In order to construct reliable models of the geomagnetic field, consistent and independent uncertainty estimates are required. The nature of an uncertainty may generally be divided into random and systematic. Random uncertainties are assumed to involve fluctuations around the true value while systematic uncertainties deviate from the truth in a predictable manner. It is important when considering the uncertainty in sediment records to use estimates that encompass both random and possible systematic contributions. The random variability present in each record is obtained by fitting a robust smoothing spline model and looking at the variance of the data away from the resulting smooth curve. The comparative analysis (e.g., with archeomagnetic estimates), on the other hand provides a means to assess the total uncertainty, including both random and also any systematic uncertainty that may be present.

Following Rice (1995), the true value of a quantity X can be written as a sum of a measurement x_0, the systematic β and the random ε components of the uncertainty, with an expected value $E(\varepsilon) = 0$ and a variance $Var(\varepsilon) = \sigma^2$

$$\begin{aligned} &X = x_0 + \beta + \varepsilon \\ &E(X) = x_0 + \beta \\ &Var(X) = \sigma^2 \end{aligned} \tag{3.28}$$

The estimated uncertainty is then the expected squared deviation of the true value from the measurement

$$E[(X - x_0)^2] = \sigma^2 + \beta^2 \tag{3.29}$$

which represents the sum of the systematic bias and the random variance. The following related model is adopted for the sediment records

$$X_l = x_l^{true} + \beta_l + \varepsilon_l^{rss} + \varepsilon_l^{add} \tag{3.30}$$

where β_l is any systematic bias present in the sediment record and the random uncertainty ε_l is separated into two components. The ε_l^{rss} which is a random uncertainty that is estimated from the variance of sediment data about the robust spline models, which have variance $Var(\varepsilon_l^{rss}) = \sigma_{rss}^2$. The term ε_l^{add} then represents additional random uncertainty which cannot be assessed by looking at deviations from a spline fit, e.g., due to uncertainties in the age model; this component is allocated a variance $Var(\varepsilon_l^{add}) = \sigma_{add}^2$. Using this model, the estimated uncertainty for a sediment record is:

$$\sigma_l^2 = \beta_l^2 + \sigma_{rss}^2 + \sigma_{add}^2 \tag{3.31}$$

Comparisons X_c between the sediment data X_l and archeomagnetic estimates X_a, where $X_c = X_l - X_a$, involve uncertainties of both contributing quantities $Var(X_c) = Var(X_l - X_a) = Var(X_l) + Var(X_a)$, i.e.,

$$\beta_c^2 + \sigma_c^2 = \beta_l^2 + \sigma_{rss}^2 + \sigma_{add}^2 + \beta_a^2 + \sigma_a^2 \tag{3.32}$$

where β_c and σ_c are now the systematic bias and variance of the comparison residuals respectively, and β_a and σ_a are the bias and variance of the archeomagnetic estimates. σ_a is estimated as the root mean square of the uncertainties predicted by the ARCH3k.1 model for each comparison; these uncertainties are based on parametric bootstrap resampling techniques (Korte et al., 2009). The systematic bias β_a of the archeomagnetic estimates are neglected, since its magnitude is found to be small based on direct comparisons between archeomagnetic data and *gufm1* model (the median values are -1° for inclination, 0.3° for declination and -0.8 μT for the intensity). The systematic bias of the comparison for inclination can then be ascribed only to the bias of sediment records, i.e., $\beta_l = \beta_c$. On the other hand the bias cannot be determined from the comparisons of relative declination and RPI.

There are two possible cases:

- For sediment records with sufficient comparisons to archeomagnetic estimates (i.e., there is sufficient nearby archeomagnetic data), the final uncertainty estimate is based on the uncertainty estimates from the comparisons and the archeomagnetic estimates (Eq. 3.32), i.e., $\sigma_l^2 = \sigma_c^2 - \sigma_a^2 + \beta_c^2$ for inclination, $\sigma_l^2 = \sigma_c^2 - \sigma_a^2$ for the declination, and standardized RPI.
- When no or few (< 30) archeomagnetic estimates are available for comparison, mean values for σ_{add} and β_l are used as calculated from cases when comparisons were possible, utilizing the expression $\sigma_{add}^2 = \sigma_c^2 - \sigma_{rss}^2 - \sigma_a^2$. Then, following (3.31), these are combined with σ_{rss}^2 for the particular record to obtain the required uncertainty estimates. In cases when the term $(\sigma_c^2 - \sigma_a^2)$ is smaller than σ_{rss}^2 then no additional uncertainty is assigned, i.e., $\sigma_{add}^2 = 0$. This approach thus combines information specific to each record derived from the spline analysis, with mean values obtain from comparisons with archeomagnetic estimates.

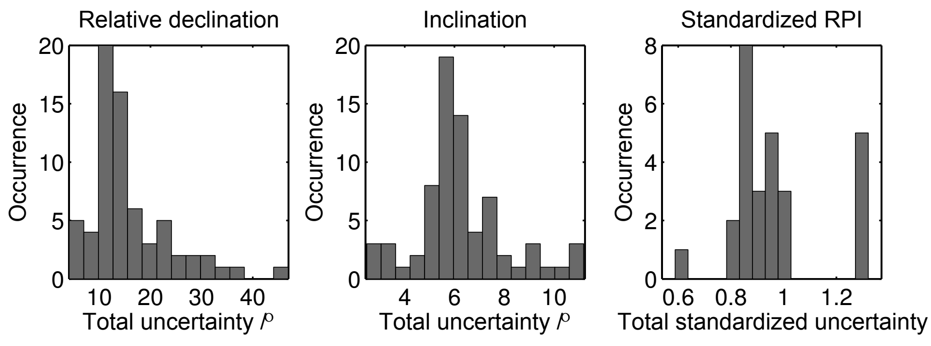

Figure 3.9: Histograms summarizing the uncertainty estimates for Holocene sediment magnetic records.

Final uncertainty estimates σ_l for each record are listed in Table 3.2. To convert the standardized RPI uncertainty estimates to absolute intensity uncertainty estimates, they can be multiplied by the standard deviation of the

RPI and a preferred scaling factor for the record of interest (cf. Korte and Constable, 2006). Histograms of the uncertainty estimates obtained for all records are plotted in Fig. 3.9. They show a wide range of uncertainty estimates across the lakes studied, spanning 2.5° to 11.2° for inclination (interquartile range: 5.4° to 7.2°), 4.1° to 46.9° for relative declination (interquartile range: 11.4° to 18.9°) and 0.59 to 1.32 (interquartile range: 0.86 to 1.01) for the standardized RPI.

Table 3.2: Summary of uncertainty estimates and smoothing times for Holocene sediment records. Dash stands for the absence of a particular component. σ_{rss} refers to the random uncertainty component obtained from the robust smoothing spline fit. σ_c is an uncertainty from the comparison with archeomagnetic estimates. Empty space in the columns for σ_c means no comparison is possible. σ_l is the overall estimated uncertainty for the sediment records. T_{ss} is the smoothing time obtained from the robust smoothing spline analysis.

Code	σ_{rss}			σ_c			σ_l			T_{ss} [yrs.]		
	D[°]	I[°]	RPI	D[°]	I[°]	RPI	D[°]	I[°]	RPI	D	I	RPI
AAM	27.8	2.2	0.43				29.9	5.7	0.81	52.2	52.0	52.0
AD1	-	1.6	0.24	-	8.1		-	7.4	0.84	-	185.4	186.9
ANN	9.7	3.6	-	21.7	8.0	-	21.5	9.1	-	56.8	84.6	-
ARA	1.6	0.5	-			-	11.0	5.3	-	34.0	37.4	-
ASL	1.3	0.6	-			-	11.0	5.3	-	134.1	133.4	-
BAI	10.3	3.5	0.53			1.32	15.0	6.3	1.27	719.4	717.9	717.6
BAM	1.7	1.5	-			-	11.1	5.6	-	79.7	84.3	-
BAR	20.4	9.5	1.05				23.1	10.9	1.32	134.1	134.8	136.6
BEA	22.2	2.3	0.22				24.8	5.9	0.84	76.0	74.1	74.9
BEG	5.4	2.3	-	10.0	3.7	-	9.4	2.5	-	101.9	100.3	-
BI2	1.8	1.2	0.61				11.1	5.5	1.01	252.0	252.9	251.0
BIR	7.3	5.1	0.34			1.34	13.1	7.4	1.30	64.4	66.4	68.9
BIW	1.2	0.7	-	5.2	5.0	-	4.1	3.5	-	82.9	83.0	-
BLM	4.9	3.3	-			-	12.0	6.3	-	179.5	186.7	-
BOU	8.2	2.8	-	14.6	3.2	-	14.3	2.9	-	36.5	93.6	-
CAM	5.3	2.1	-			-	12.2	5.8	-	130.4	130.7	-
CHU	14.0	2.3	0.18				17.7	5.9	0.83	78.5	78.6	77.0
DES	12.5	7.0	-			-	16.6	8.8	-	50.2	50.2	-
EAC	27.4	8.9	0.99				29.5	10.4	1.28	91.1	100.7	91.4
EIF	4.3	1.8	-	8.7	5.4	-	8.3	4.3	-	126.0	113.9	-
ERH	9.0	7.8	-			-	14.2	9.4	-	111.2	132.8	-
ERL	5.8	3.1	-			-	12.4	6.2	-	370.6	377.0	-
ESC	11.5	2.9	0.62				15.8	6.1	1.02	335.0	333.6	333.7
FAN	6.5	9.8	-			-	12.7	11.2	-	201.5	201.2	-
FIN	2.7	0.9	-			-	11.3	5.5	-	158.0	158.2	-
FIS	5.0	3.3	-			-	12.0	6.3	-	125.8	125.2	-
FRG	9.2	2.4	0.49				14.3	5.9	0.94	255.7	253.5	254.1
FUR	10.5	2.6	0.22				15.2	6.0	0.83	250.7	244.7	245.8
GAR	17.4	3.3	0.32				20.5	6.3	0.87	341.7	333.6	334.7
GEI	3.5	1.4	-	9.2	5.7	-	8.8	5.2	-	328.0	323.1	-
GHI	9.2	4.7	0.56				14.3	7.2	0.98	229.2	167.1	167.0
GNO	6.9	5.2	-			-	12.9	7.5	-	257.9	257.1	-
GRE	16.9	2.1	-			-	20.1	5.8	-	102.8	102.5	-
HUR	26.3	5.7	-			-	28.5	7.9	-	159.1	164.5	-
ICE	18.3	3.0	-			-	21.3	6.1	-	50.1	50.1	-
KEI	7.9	3.6	-			-	13.5	6.5	-	326.0	329.3	-
KYL	7.0	2.0	-			-	12.9	5.8	-	125.1	125.6	-
LAM	30.7	5.3	-			-	32.6	7.6	-	170.1	173.5	-
LEB	3.8	1.0	0.47				11.6	5.5	0.93	163.1	170.3	52.2
LOM	3.4	1.5	-	9.6	3.2	-	9.3	3.2	-	325.7	322.6	-
LOU	45.6	5.4	-			-	46.9	7.6	-	503.0	980.0	-
LSC	5.2	2.7	0.29				12.1	6.0	0.86	77.4	79.7	54.8
MAR	1.7	0.7	-			-	11.1	5.4	-	82.0	82.1	-
MEE	27.2	11.6	-	24.6	6.7	-	24.5	6.1	-	100.0	102.9	-
MEZ	6.4	3.0	0.63	21.8	6.8	0.65	21.6	7.4	0.59	111.5	114.6	111.8
MNT	6.4	3.5	-			-	12.7	6.4	-	334.3	335.9	-
MOR	9.9	2.1	-	6.2	5.6	-	5.4	4.4	-	113.5	112.1	-
MOT	10.9	4.0	0.47				15.4	6.7	0.93	245.8	254.9	247.1
NAR	2.2	0.8	-			-	11.2	5.4	-	156.9	156.7	-
NAU	5.6	1.8	0.50		6.7		12.3	8.2	0.95	167.1	174.4	167.2
NEM	4.4	2.6	-	23.3	8.1	-	23.2	9.8	-	91.4	92.8	-
PAD	33.4	4.4	0.30				35.1	7.0	0.86	40.3	40.1	40.3

Continued on next page

Table 3.2 – continued from previous page

Code	σ_{rss}			σ_c			σ_l			T_{ss} [yrs.]		
	D[°]	I[°]	RPI	D[°]	I[°]	RPI	D[°]	I[°]	RPI	D	I	RPI
PEP	-	2.9	0.33	-			-	6.1	0.87	-	66.8	68.0
POH	6.4	2.5	0.46				12.7	5.9	0.93	103.1	96.6	96.4
POU	2.2	1.2	-			-	11.2	5.5	-	111.0	127.2	-
SAG	5.8	2.2	-			-	12.4	5.8	-	67.0	67.1	-
SAN	12.2	9.9	-			-	16.4	11.3	-	268.7	264.7	-
SAR	34.9	2.1	0.38				36.6	5.8	0.89	252.9	250.4	250.6
SAV	11.8	2.1	-			-	16.1	5.8	-	238.7	242.1	-
SCL	7.8	5.4	-			-	13.4	7.7	-	45.5	45.6	-
STL	5.3	1.9	0.29				12.2	5.7	0.86	67.3	67.4	67.5
SUP	14.3	1.9	-			-	18.0	5.7	-	93.4	93.3	-
TRE	5.9	1.6	0.50				12.4	5.6	0.95	252.3	252.3	252.1
TRI	5.4	4.4	-	7.6	5.2	-	6.8	3.3	-	100.2	100.7	-
TUR	-	7.6	-	-		-	-	9.3	-	-	59.7	-
VAT	16.6	3.4	-			-	19.9	6.4	-	129.9	129.3	-
VIC	7.7	4.5	-			-	13.3	7.0	-	100.5	103.8	-
VOL	13.8	6.7	-	14.6	5.8	-	14.3	4.0	-	40.6	40.6	-
VUK	10.7	3.4	-			-	15.3	6.4	-	200.4	201.1	-
WAI	5.3	3.1	-	8.1	6.1	-	6.5	6.2	-	250.6	251.1	-
WAS	-	-	1.00	-	-		-	-	1.29	-	-	803.2
WIN	1.6	0.5	-	6.4	5.0	-	5.8	2.5	-	204.2	202.1	-
WPA	-	1.7	0.15	-			-	5.6	0.82	-	27.0	28.9

3.4 Discussion and conclusions

The primary goal of this analysis was to assess the quality of Holocene sediment magnetic records and to provide individual weightings to be used in future geomagnetic field model construction. Nilsson et al. (2010) previously found that poor quality paleomagnetic data and large dating uncertainties force complex models to place too much power into higher degrees. With reliable and consistent errors allocated to individual datasets it may therefore be possible for simpler models to adequately explain the variance in many of the records.

In the study of Korte et al. (2005), minimum uncertainties for sediment records based on comparisons with *gufm1* were predominantly used. Default uncertainties of 3.5° in inclination, 5.0° in declination and 5 μT in intensity were allocated. Donadini et al. (2009) expressed their minimum uncertainty estimate in terms of a minimum α_{95} of 6°, which corresponds to a 3.5° uncertainty in inclination, with declination uncertainties depending on the inclination at the location. In contrast, the new uncertainties derived in this thesis have a wide range of values that differ greatly between inclination and declination. Inclination uncertainties show a median value of 5.9° and an interquartile range of 5.4° to 7.2°; thus the allocated uncertainties at most records are considerably larger than the threshold values used by Korte et al. (2009) and Donadini et al. (2009). The uncertainty estimates for relative declination have a median value of 13.4° and an interquartile range of 11.4° to 18.9°, much larger than the previously considered uncertainties. For comparisons with previous studies the standardized RPI uncertainty estimates first need to be calibrated to an absolute scale, multiplying by the standard deviation and a rescaling factor specific for each record. Performing such a calibration using the CALS7k.2 field model, the absolute uncertainty estimates for the paleointensity have a median value of 11 μT and an interquartile range of 9 to 14 μT. For all three components, derived uncertainty estimates are much larger than those used previously. These uncertainty estimates implicitly include the effect of age uncertainties while the uncertainties quoted from the previous studies (Korte et al., 2005) do not. However if the age uncertainties proposed by Korte et al. (2005) are mapped into measurement uncertainties they equate to a relatively small contribution (see Table 5 in Korte et al. (2005)).

A different approach to account for age uncertainties is used in the more recent global models of the geomagnetic field CALS3k.3, CALS3k.4 and CALS10k (Korte and Constable, 2008; Korte et al., 2009; Korte and Constable, 2011; Korte et al., 2011). They created multiple possible solutions by bootstrap resampling of a statistical model for age uncertainties, in such a way that the record can be shifted in time by up to ±300 years. A similar approach is applied to the uncertainties of magnetic components, where each bootstrap sample is obtained from a normal distribution centred on the magnetic component with a standard deviation equal to the data uncertainty estimate. Thus, an average of all bootstraps hopefully provides a robust picture of the field structure. Nevertheless, this technique relies on the error estimates being allocated to each record (Donadini et al., 2009); In particular the results presented here suggest this should be done on a lake by lake basis, which has not previously been the case.

The largest uncertainties in inclination are obtained in cases where there is much scatter in the data or many outliers are present, e.g., Lake Barrine, Australia ($\sigma_l = 10.9°$), Lake Fangshan, China ($\sigma_l = 11.2°$), Hoya de San Nicolas, Mexico ($\sigma_l = 11.3°$) and Lake Eacham, Australia ($\sigma_l = 10.4°$). The smallest uncertainties in inclination are observed in consistent records, usually when uncertainties are estimated via comparison with archeomagnetic estimates, e.g., Lake Begoritis, Greece ($\sigma_l = 2.5°$) and Lac du Bourget, France ($\sigma_l = 2.9°$). The Lake Biwa record showed the smallest uncertainty estimate for declination ($\sigma_l = 4.1°$) but this is probably an artifact due to pre-smoothing of the record, which yields not only an unrealistically small random uncertainty, but also limits the uncertainties derived from comparisons. Declination uncertainty estimates tend to increase with latitude (Fig. 3.10). The approach used by Donadini et al. (2009) also allows a similar dependence of the declination uncertainty with location, i.e., local inclination. The new uncertainty estimates follow the trend expected with their technique (see Fig. 3.10), the few exceptions are declination records with anomalously large data scatter.

In general, there are no obvious geographical regions with characteristically smaller or larger uncertainty estimates found across all components. An exception is that many of the best declination records come from Europe, for example, Lake Windermere ($\sigma_l = 5.8°$), Loch Lomond ($\sigma_l = 9.3°$) and Llyn Geirionydd ($\sigma_l = 8.8°$) in UK; Lake Trikhonis ($\sigma_l = 6.8°$) and Lake Begori-

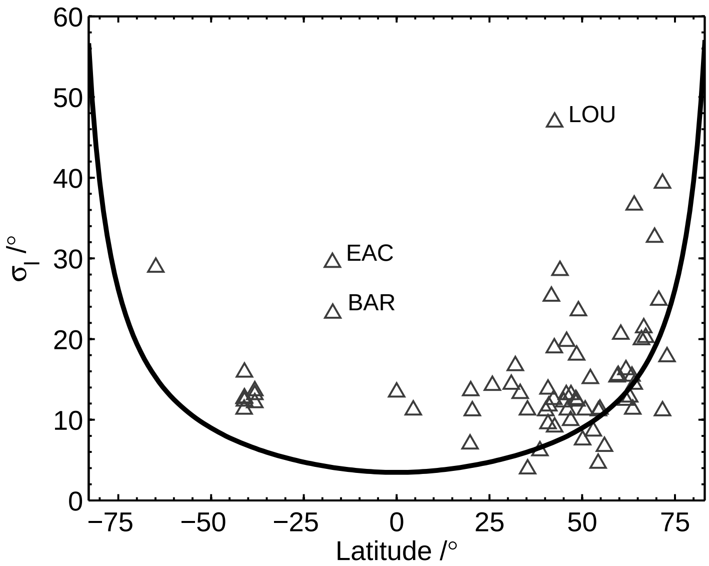

Figure 3.10: Dependence of uncertainty estimates for declination σ_l on latitude. Triangles are the uncertainty estimates for relative declination. The solid line represent the values estimated using the equation (2) from Donadini et al. (2009), where σ_l depends on the local inclination. Here, the inclination is obtained from the Geocentric Axial Dipole hypothesis and $\alpha_{95} = 6°$, the threshold value used for the uncertainty estimates in the lake sediment records by Donadini et al. (2009). The outliers (EAC, BAR, LOU) are declination records with anomalously large data scatter.

tis ($\sigma_l = 9.4°$) in Greece; Eifel maars, Germany ($\sigma_l = 8.3°$), but there are also lakes with larger uncertainty estimates in this region, for example, Lac d' Annecy, France ($\sigma_l = 21.5°$), Meerfelder Maar, Germany ($\sigma_l = 24.5°$) and Sarsjön, Sweden ($\sigma_l = 36.6°$). In general, the results imply that the uncertainties have not reduced over time, in fact one of the best studies (in terms of the uncertainty estimates) remains the early study that by Turner and Thompson (1981). In spite of the development of equipment and instrumentation, recent records are not necessarily more reliable than older records. While in the past, the studies were focused on obtaining paleosecular variation data, today paleomagnetic studies are not always the first priority, i.e., the sites are usually not selected exclusively for secular variation purposes.

During this analysis, several difficulties were encountered related to the heterogeneous form in which lake sediment data are available.

- Records whose data was provided in pre-smoothed form (e.g., Aral Sea, Kazakhstan, Lake Aslikul, Russia, Lake Biwa, Japan, Lake LeBoeuf, USA, Lake Windermere, UK, Gardar Drift, N. Atlantic, Finnish Lakes) resulted in unrealistically small estimates of σ_{rss}. In the future, I recommend that all records should be published and contributed to databases in raw, unsmoothed form. Smoothed versions can still be presented as well, but the raw form is essential for further modelling. In this way information about the inherent reliability of records is preserved.

- Records consisting of multiple cores that are subsequently mixed or stacked together (e.g., Lac d' Annecy, France; Lake Huron, USA) produced much larger, and probably more realistic, uncertainty estimates. However, before using such records for field modelling, it may be preferable to reject cores that are incompatible with data from other sources (e.g., archeomagnetic data, nearby lake records or other cores from the same lake). This requires that data from individual cores are separately included in databases along with their depth-age model.

- High latitude records, such as those from Arctic and Antarctic seas, are found to possess a large random variance of declination due to rapid, large amplitude directional changes in these regions; it is essential that these records are given dedicated, suitably large, uncertainty estimates in field modelling.

- Results from the comparisons show no evidence for systematic shifts between lake sediment inclination data and archeomagnetic estimates. Caution should be exercised when automatically correcting the inclination shallowing without having any direct evidence for it in the records.

- Cores oriented to an azimuth should be collected whenever possible, or at least the upper sediments should be matched to measured local declination. Oriented data would help improve future geomagnetic field models, particularly at high latitudes.

This analysis does not take separately into account age uncertainties; instead, these are included within the comparison uncertainties, in particular contributing to the factor σ_{add}. Future studies may wish to use a more sophisticated approach that treats age uncertainties separately or try to determine shift factors associated with age problems during the field modelling procedure.

Chapter 4

Observed periodicities and the spectrum of field variations in Holocene magnetic records

4.1 Overview

In this chapter, an investigation into whether there is any evidence for persistent, globally observed, periodicities in Holocene sediment magnetic records is performed. Such periodicities may be indicative of specific global modes of core dynamics; they are therefore of great importance in understanding the mechanisms underlying geomagnetic secular variation. Recently, Nilsson et al. (2011) identified a period of 1350 years in the tilt of a dipole field model derived from five high quality records from lake sediments. This study has provided fresh impetus to early ideas by Braginsky (1972, 1974), and more recent suggestions by Dumberry and Bloxham (2006) and Wardinski and Korte (2008) that there may be important global modes of core dynamics on millennial time scales. On the other hand, studies of rotating magneto-convection and self-consistent geodynamo simulations suggest that secular variation may simply be an outcome of chaotic convection in the outer core, giving rise to localised oscillations and episodic drifts of flux patches (Sakuraba and Hamano, 2007; Amit et al., 2010, 2011). Such models predict a broadband continuous spectrum of field variability (Tanriverdi and Tilgner, 2011; Olson et al., 2012). By searching for periodicities in the global database of Holocene magnetic records we are able to distinguish between these scenarios.

Several previous studies of secular variation in sediment records, have reported evidence for periodicities, but no global analysis of the contemporary Holocene compilation (Korte et al., 2011) has yet been carried out. For example, Barton (1983) performed spectral analysis of declination and inclination time series, concluding that there is no evidence for discrete periods, but rather for bands of preferred periods, i.e., 60-70, 400-600, 1000-3000 and 5000-8000 years. Constable and Johnson (2005) later produced a composite paleomagnetic power spectrum for the dipole moment, including a contribution from the CALS7k.2 field model (Korte and Constable, 2005a); they found no evidence for discrete periodic dipole variations on time scales of 100 to 10000 years. Periodicities have, however, been reported in the studies of individual sediment records with identified periods spanning 200 to 8000 years (e.g. Turner and Thompson, 1981; Brown, 1991; Peng and King, 1992; Zhu et al., 1994; Nourgaliev et al., 1996, 2003; Peck et al., 1996; Gogorza et al., 1999; St-Onge et al., 2003).

Currie (1968) has argued that the temporal power spectra of geomagnetic field observations is governed by a power law, i.e., f^{-n}, where f is the frequency. More recently, Olson et al. (2012) have made a detailed study of the frequency spectrum of dipole field variations from numerical geodynamo simulations and also find broadband variability well described by power laws. Their results agree well with the composite paleomagnetic dipole spectrum of Constable and Johnson (2005), the PADM2M spectrum of Ziegler et al. (2011) and long-standing estimates of the spectral slope on millennial time scales (Barton, 1982; Courtillot and Le Mouël, 1988). In principle, the slope of the spectrum of magnetic variations may also provide information on the kinetic energy spectrum of the underlying core flow (Tanriverdi and Tilgner, 2011). In this chapter, we undertake a new observation-based characterisation of millennial time scale periodicities of Earth's magnetic field, and the associated spectrum of temporal variations, taking advantage of robust models of Holocene lake sediment magnetic records derived in Chapter 3.

For this purpose we employ three different signal analysis techniques: multitaper spectral estimation, wavelet analysis and empirical mode decomposition (EMD). Multitaper methods (Thomson, 1982; Riedel and Sidorenko, 1995; Percival and Walden, 1998) provide reduced variance and minimum bias spectral estimates compared to the conventional periodogram. Due to the short lengths of the time series compared to the time scales of interest, as well as the fact that geophysical systems are rarely exactly periodic and likely nonstationary, we also explore two alternative methods. Wavelet analysis, a spectrum analysis method developed in the 1990s (e.g., Chui, 1992), provides further complementary information, enabling the study of the nonstationary nature of signals, and providing access to the time-frequency distribution, i.e., how the power is distributed over time (e.g., Strang and Nguyen, 1996). Previously, wavelet analysis has proved useful in the study of relative paleointensity records and archaeomagnetic field intensity in order to search for significant frequencies (Guyodo et al., 2000; Gurarii and Aleksyutin, 2009) as well as in studies of geomagnetic jerks (Alexandrescu et al., 1996). The EMD method was introduced by Huang et al. (1998) with the purpose of analysing nonlinear and nonstationary data by decomposition into so-called 'intrinsic mode functions' possessing characteristic frequencies. Roberts et al. (2007) have successfully used this method to study both geomagnetic secular variation in the observatory era and decadal changes in the length of day, in particular detecting the existence of an approximately 60-year period. Jackson and Mound (2010) later succeeded in identifying periods of 11.5 years, corresponding to the solar cycle, 30.5 and 81 years by applying the same method to a larger database of observatory annual means. By investigating Holocene lake and marine sediment records with these three techniques, we are able to characterize possible modes of variability, even if these are nonstationary and quasi-periodic.

4.2 Multitaper spectrum, wavelet and EMD

The basis for these analyses is the compilation of Holocene sediment magnetic records of Korte et al. (2011), described in Chapter 2, in which the majority of the records are from lakes, with only 10% from marine sediments. Previously derived individual spline models from Chapter 3 that capture the most robust aspects of each of these records provide a convenient means by which to search for periodicities and carry out spectral analysis.

These investigations are illustrated using the following examples: a declination record from Eifel Maars, Germany (Stockhausen, 1998) (Fig. 4.3) and an inclination record from Lake Waiau, Hawaii (Peng and King, 1992) (Fig. 4.4). Similar plots for all the other records where periods were identified are available online at http://earthref.org/ERDA/1737.

We first applied the multitaper spectral analysis method. This involves multiplication of the data by several orthogonal tapers, Fourier-transforming and then averaging the independent spectral estimates (cf. Prieto et al., 2007, 2009; Smith-Boughner et al., 2011; Smith-Boughner and Constable, 2012).

The power spectrum is defined as a square of the absolute value of the Fourier coefficients for a given frequency (e.g., Press et al., 1992). This estimate is often biased due to spectral leakage, i.e. the power from strong peaks leak into neighbouring frequency intervals of lower power. Therefore, it is important to use a method of tapering to reduce this bias. The direct spectral estimate $S(f)$ at frequency f is:

$$S(f) = \frac{1}{N} \left| \sum_{t=0}^{N-1} v(t) d(t) e^{-i2\pi f t} \right|^2 \tag{4.1}$$

where $d(t)$ is a data series with N points ($t = 0, 1, ..., N-1$) and $v(t)$ is the vector of weights named taper (Percival and Walden, 1998). If $v(t)$ is a boxcar function, then the classical periodogram is obtained. The taper function $v(t)$ is normalized by

$$\sum_{t=0}^{N-1} |v(t)|^2 = 1 \tag{4.2}$$

Properties of the taper in frequency domain can be analysed from the Fourier transform:

$$V(f) = \sum_{t=0}^{N-1} v(t)e^{-2\pi ift} \tag{4.3}$$

The function $V(f)$ is called a spectral window associated with $v(t)$. For conventional tapers, the spectral window has a broad main lobe and smaller sidelobes (e.g., Percival and Walden, 1998). Thomson (1982) introduced the multitaper spectral method in which the data series is multiplied by a set of tapers $v_k(t)$ in the time domain and then Fourier transformed. The multitaper spectrum is produced by taking a linear combination (a_k) of the individually tapered estimates:

$$S(f) = \frac{1}{K}\sum_{k=1}^{K} a_k \left|\sum_{t=0}^{N-1} v_k(t)d(t)e^{-i2\pi ft}\right|^2 \tag{4.4}$$

where K is the number of tapers. Thus, the approach reduces the variance of the spectral estimate. Various functions can be used as data tapers, and two types are discussed here, prolate and minimum bias tapers.

Prolate tapers. For these tapers, the energy is concentrated within the frequency range $[-w, w]$ and the bandwidth of interest is set by the parameter NW, called time-bandwidth product (Slepian, 1978; Thomson, 1982). NW is a product of the number of samples N and the frequency resolution $W = 2w$. The prolate tapers are calculated by solving the following eigenvalue problem:

$$\sum_{s=0}^{N-1} \frac{\sin\left[2\pi w(s-t)\right]}{\pi(s-t)} v(s) = \lambda v(t) \tag{4.5}$$

The eigenvector solutions $v(t)$ are known as the prolate spheroidal sequences or the Slepian functions (Slepian, 1978). The corresponding eigenvalues λ are related to the energy within the desired frequency range. The first $2NW - 1$ eigenvalues are close to unity and then fall to zero. Therefore, $K \approx NN - 1$ is the number of tapers with good spectral leakage reduction and this is typical value for the multitaper spectral estimates. Prolate tapers are proven to be valuable when the spectrum varies rapidly with a large dynamic range (Walden et al., 1995).

Minimum bias tapers. These tapers minimize the local bias in the spectral estimate, which bandwidth is defined by the number of tapers K. The minimum bias tapers (Riedel and Sidorenko, 1995) are the solution of the following optimization problem, defined as an eigenvalue problem:

$$\sum_{s=0}^{N-1} \frac{(-1)^{t-s+1}}{2\pi^2(t-s)^2} v(s) = \lambda v(t) \tag{4.6}$$

The eigenfunctions $v(t)$ can be approximated by the sinusoidal tapers, which are discrete version of the continuous time minimum bias tapers

$$v_k(t) = \sqrt{\frac{2}{N+1}} \sin\left(\frac{\pi k t}{N+1}\right) \tag{4.7}$$

where $k = 1, 2, ..., N$, and N is the sequence length. The amplitude term on the right in Eq. 4.7 is the normalization factor that ensures orthogonality of the tapers. The kth taper has its spectral energy concentrated in the frequency bands

$$\frac{k-1}{2(N+1)} \leq |f| \leq \frac{k+1}{2(N+1)} \tag{4.8}$$

These tapers have a much narrower main lobe and much higher sidelobes. In this way, they achieve a smaller bias due to smoothing by the main lobe, at the expense of sidelobe suppression. This behaviour is suitable for slowly varying spectra.

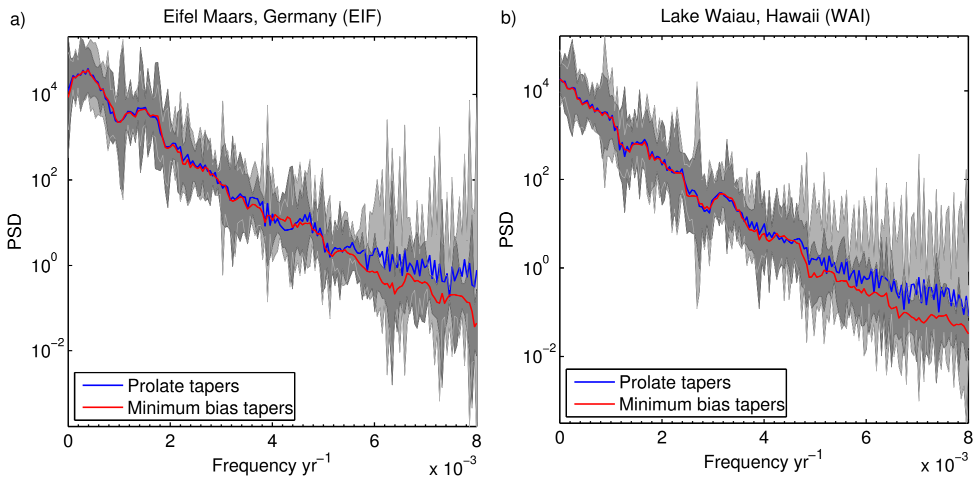

Figure 4.1: Multitaper spectra using 5 prolate and 5 minimum bias tapers of an example declination record from Eifel Maars, Germany (a) and inclination record from Lake Waiau, Hawaii (b). Confidence intervals for both types of spectral estimates are calculated using the jackknife method of Thomson and Chave (1991).

For all records we computed power spectral estimates using both prolate tapers and minimum bias tapers (two examples in Fig. 4.1), varying the number of tapers between 5 and 9. We found that the spectral estimates obtained with different tapers agreed well for a subset of frequencies that were well constrained by the data. Figs. 4.3a and 4.4a show two examples of the spectral estimates obtained with the minimum bias tapers computed with 5 tapers. The well defined frequency ranges in this case are noted in the figure captions. The best fitting power law slope is then calculated for the well determined range of each spectrum. These results are summarized in Fig. 4.6a. Only records whose slopes are estimated for a range > 1000 yr on a period scale were considered for the spectral slope analysis. In addition, records with a relative difference between the spectral slopes < 10%, based on prolate and minimum bias tapers, are only included.

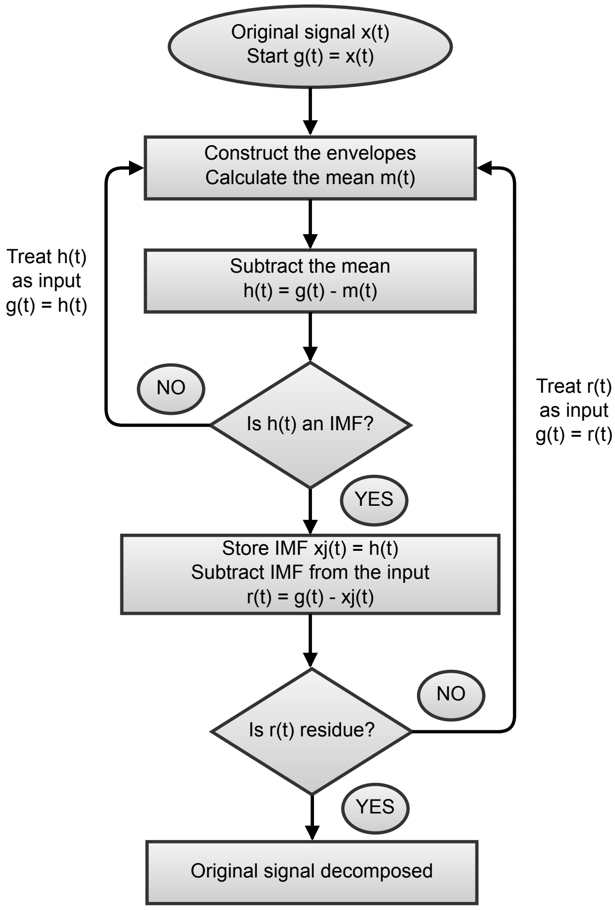

Figure 4.2: Flow chart of the EMD algorithm. After Zeiler et al. (2010).

In a second step, a 'Mexican hat' wavelet transform is carried out in order to map the temporal evolution of the spectral power in the records (e.g., Foufoula-Georgiou and Kumar, 1994). To analyse variability at different periods, the number of scales used in the wavelet analysis was chosen to be 90, these were later converted into frequencies (10^{-4} to 10^{-2} Hz) (Trauth, 2010). Absolute values of the wavelet coefficients are plotted as contour maps constituting the wavelet power spectrum (Figs. 4.3b and 4.4b) with the frequency/period (right/left) axis plotted using a logarithmic scale.

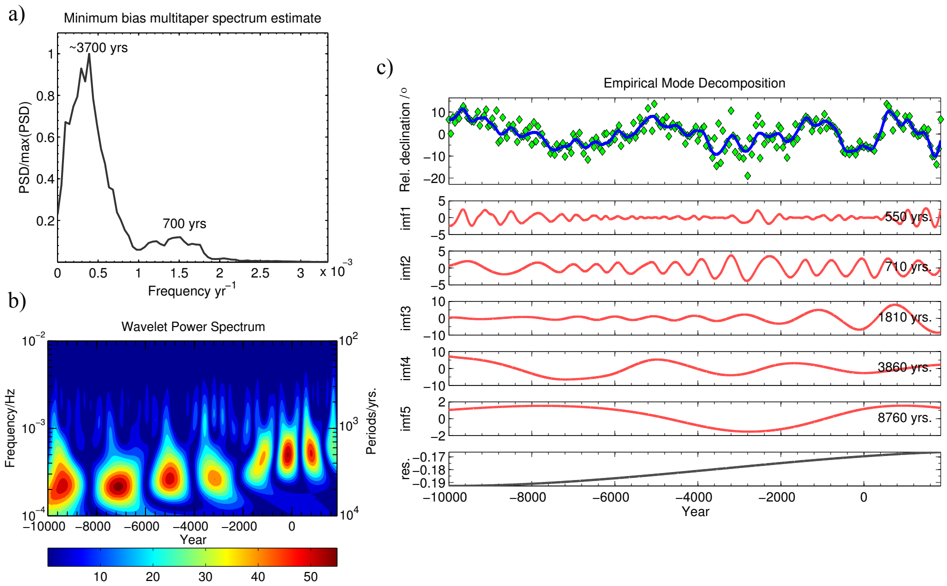

Figure 4.3: Comparison of techniques for periodicity analysis for an example declination record from Eifel Maars, Germany (EIF): a) Multitaper spectrum using 5 minimum bias tapers, b) 'Mexican hat' wavelet analysis and c) Empirical Mode Decomposition. Peaks in the multitaper spectrum are noted along with the corresponding periods. The spectral slope is calculated in the period range from 300 to 2500 years. The wavelet power spectrum is given as a function of frequency (left axis) and associated periods (right axis). The colour scale denotes contours of the absolute value of the wavelet coefficients. Green diamonds denote the sediment magnetic data while the robust smoothing spline model is plotted as a blue curve. The EMD method decomposes the record into five IMFs (red curves) and a residual (grey curve).

Finally, the EMD implementation of Flandrin (2009) is used to decompose each record into a small number of oscillation modes known as intrinsic mode functions (IMF) together with a residual (cf. Rilling et al., 2003). An IMF satisfies two requirements: (i) the number of extrema and the number of zero-crossings are equal or differ at most by one; (ii) the mean value of the envelopes defined by the local maxima and local minima is zero across the whole record (see Fig. 2 in Roberts et al. (2007)). The method works iteratively, extracting the highest frequency mode first, then forming a new signal by subtracting the first mode from the original signal and then repeating the procedure (a flow chart showing the EMD analysis procedure is presented in Fig. 4.2).

Usually, the first IMF separated out by EMD is noise; this is not the case

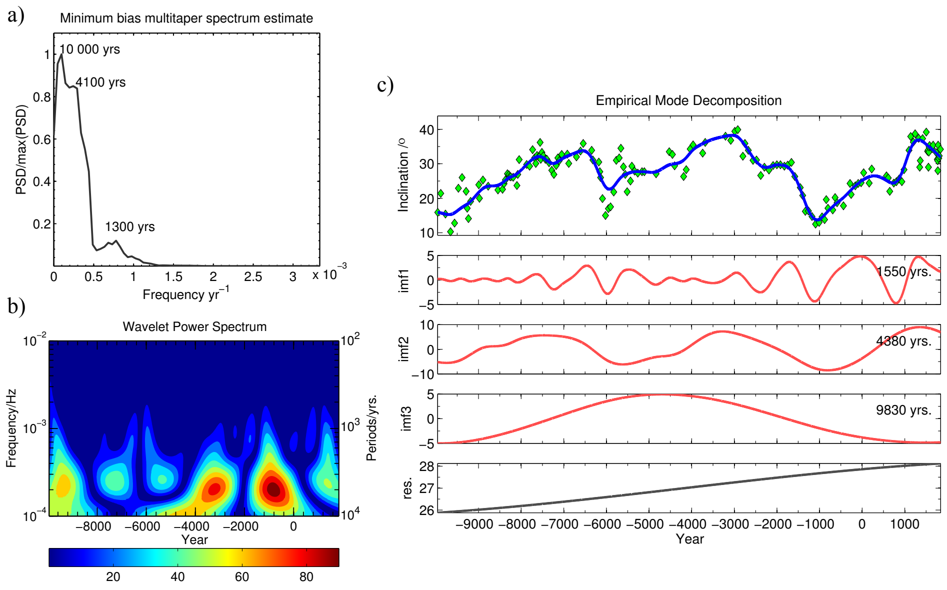

Figure 4.4: Comparison of techniques for periodicity analysis for an example inclination record from Lake Waiau, Hawaii: a) Multitaper spectrum using 5 minimum bias tapers, b) 'Mexican hat' wavelet analysis and c) Empirical Mode Decomposition. The spectral slope is calculated in the period range from 600 to 3500 years. Details are given in the caption of Fig. 4.3.

in the present study because the input signals derived from the robust spline models are already smooth. Using the spline model predictions as the input enables us to avoid problems in the analysis associated with the presence of outliers and gaps in the original time series.

Two examples of the EMD analyses are presented in Figs. 4.3c and 4.4c. The top plot is always the input signal, our robust spline model, with the original data also shown for reference. The number of IMFs obtained differs from record to record, depending on the number of coherent oscillations that can be extracted. The residual trend can be a monotonic function or an incomplete cycle with a period longer than the length of the record. Two methods suggested by Roberts et al. (2007) have been used to estimate the periods of the IMFs: the autocorrelation function (ACF) based on identifying peaks that exceed the 95% confidence level, and averaging of time interval lengths between successive maxima, successive minima, and successive ascending and descending zero crossing points (visual method). These two methods are demonstrated in Fig. 4.5 for the IMF4 of the declination record from Eifel Maars, Germany (EIF). Periods of 3860 years and 3730 years are obtained from the two methods with a 3.4% difference. Periods with a difference larger than 10% between these two estimates are omitted from further analysis as they are considered unreliable. In the remainder only the ACF periodicity results are reported.

In order to determine errors in the estimated periods, the EMD analysis is performed on artificially shortened time series (Jackson and Mound, 2010). For example, the obtained periods for the IMF4 of declination record from the Eifel maars (Table 4.1) are 3860, 4090, 3920, 3950 and 4080 years when the length of the record is 11850 (full), 11260, 10670, 10100 and 9480 years, respectively. The corresponding maximum changes obtained from the ACF method are 9.8%, 5.4%, 23.6% and 5.6%, with an average of 10%. Thus, in this case, the IMF4 is accompanied by an estimated uncertainty of 10% of the estimated period. To assess the mode significance, the average power of each mode compared to the power of the signal minus the residual was estimated. Only modes that explain more than 10% of the power of the decomposed signal were considered in the subsequent analysis and included in the summary plot shown in Fig. 4.6b.

Additionally, periods obtained from records with uncertainty estimates from Chapter 3 greater than 20° for D, 7° for I and 1 in standardized units of RPI are omitted. According to tests performed by Jackson and Mound (2010), the longest meaningful period will not exceed 75% of the time series length. Consequently the longest retrieved periods are about 9000 years. The shortest periods are bounded by a record's intrinsic smoothing time (due to the sedimentation process - see Section 2.3), which has an estimated mean value of 160 years for these records (Chapter 3).

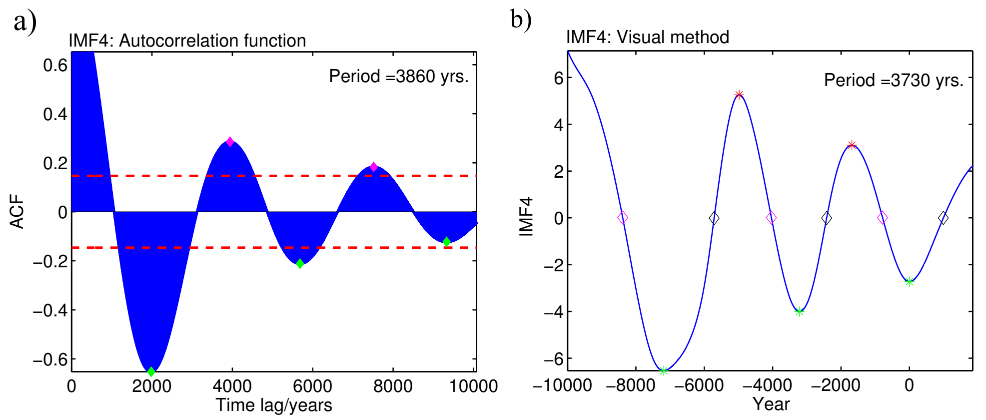

Figure 4.5: Comparison between the two methods used for period estimation. This example is for IMF4 of the declination record from Eifel Maars, Germany (EIF). (a) Autocorrelation function (ACF). The horizontal read dashed lines are the 95% confidence levels. (b) Visual method. Diamonds and stars showed a consecutive points of maxima, minima, up and down zero-crossing.

Table 4.1: Changes in the periods of IMFs (in years) derived from EMD for the declination record of the Eifel Maars, Germany (EIF) as the length of the time series is shortened. Periods of IMFs are estimated using the autocorrelation function (ACF) and the visual method (VIS). The EMD decomposition of this record is given in Fig. 4.3. IMF5 is obtained only when the full length of the record is decomposed.

Length (yrs.)	IMF1 (ACF)	IMF1 (VIS)	IMF2 (ACF)	IMF2 (VIS)	IMF3 (ACF)	IMF3 (VIS)	IMF4 (ACF)	IMF4 (VIS)
11850	550	550	710	700	1810	1820	3860	3730
11260	570	570	740	730	1860	1890	4090	3770
10670	580	580	720	720	1740	1740	3920	3710
10100	580	580	700	700	1710	1740	3950	3840
9480	610	610	700	700	1420	1390	4080	3900
$m$ax % change	9.8	9.8	5.4	4.1	23.6	26.5	5.6	6.1

4.3 Results for the power spectrum and periodicities

As illustrated by the examples in Figs. 4.3 and 4.4, the periods extracted by EMD analysis generally agree well with the periods obtained by the multitaper spectral estimates, although in some instances periods obtained with one method do not obviously correspond to periods obtained with the other method.

A summary plot of the minimum bias multitaper spectra of all D, I and RPI records satisfying the criteria discussed above is presented in Fig. 4.6a. Considering power law fits to all the spectra a mean power law exponent of -2.3 and a standard deviation of 0.6 is obtained. Slopes were calculated by a least squares fit on logarithmic axes for each considered record and component. Similar mean slopes are obtained when D, I and RPI are considered separately. The mean slope was estimated for the best constrained period range of 300 to 4000 years. Very similar results were obtained when the number of tapers (5, 7 and 9), the time-bandwidth product (3, 4 and 5) and choice of taper (minimum bias and prolate) were varied. The spectral slope for periods longer than 4000 years appears shallower, whereas the high frequency end of the spectrum appears to possess a steeper slope but these portions of the spectrum are less well constrained in the records considered here.

The wavelet analysis demonstrates the nonstationary nature of the analysed records with peaks observed in the time-frequency spectrum not persisting throughout the full length of the record. This non-stationarity motivated the need to apply the EMD technique in order to characterize the quasi-periodic and transient oscillations embedded in the records.

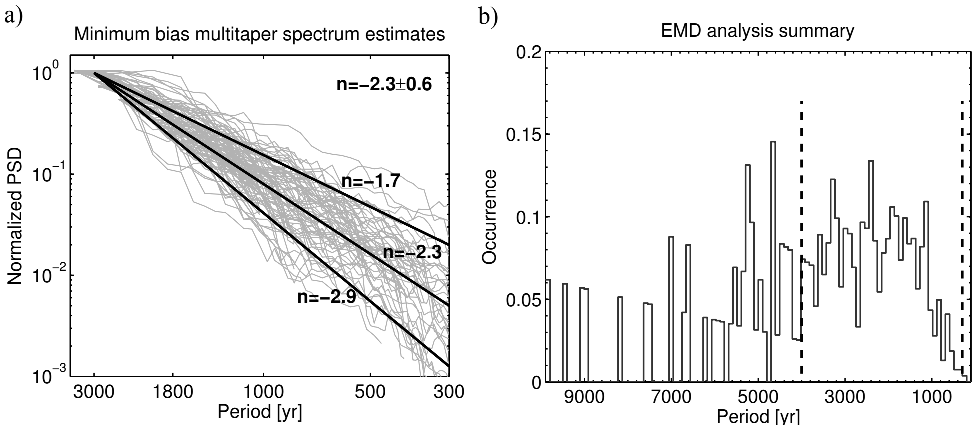

Figure 4.6: (a) Multitaper spectra (individually normalized to their maximum) computed using 5 minimum bias tapers. A power law exponent (spectral slope) of -2.3 ± 0.6 is estimated for the best constrained part of the spectrum [300 to 4000 years]. (b) Histogram of periodicities obtained from the EMD analysis of all components from all records. Occurrence of periods is normalized by the number of records occurring in each period bin. The period range used for the spectral slope estimation in (a) is indicated by the dashed lines.

Fig. 4.6b presents an alternative summary of the periodicities present in these records in terms of a histogram, collecting all the periods identified by the EMD analysis. The periods obtained for each lake sediment record are also presented in Table 4.2. This analysis also indicates broadband variability across the entire period range to which these records are sensitive. The number of retrieved modes drops at the ends of the period range where only a few lakes, with either high sedimentation rate, or very long records, contribute. A similar broadband result is obtained when periods are grouped by individual components, i.e. inclination, declination or RPI.

Fig. 4.7 presents the periodicity distribution as a function of latitude and longitude. There are no periods universally present at all latitude and longitudes, but rather there are a wide range of periods present at all latitudes and longitudes. However, periods grouped according to geographical regions show notable consistency, for example, with periods of 1100, 1300, 1700, 2100, 2400 and 2800 commonly observed in Europe, including in the Eifel maars, Germany (Stockhausen, 1998), Finnish Lakes (Haltia-Hovi et al., 2010), Lago di Mezzano, Italy (Brandt et al., 1999) and Lake Windermere, UK (Turner and Thompson, 1981). This demonstrates that independent, high quality, sediment records that are geographically close, are capable of recording the same secular variation signal.

Table 4.2: Periodicities (in years) obtained by EMD analysis for the Holocene sediment magnetic records

Record	Declination	Inclination	RPI
AAM	1500	1100	1140, 1300, 3070
AD1	/	1010, 1680, 4160	1250, 2170, 2820, 5990
ANN	380, 1050	410, 720, 1380	/
ARA	250, 790	250, 630	/
ASL	800, 1280	1600	/
BAI	8090	3280	/
BAM	1120, 2350, 5050	2440	/
BAR	970, 1620	790, 1410, 6750	450, 1030, 1830
BEA	850, 2170	1020, 2000, 3500	1040, 2560
BEG	610, 1180, 1730	850, 1100, 2870	/
BI2	3010, 4350	2820, 4470	1490, 3720, 5200
BIR	200, 440, 1060	360, 650, 1190, 3320	730, 1350, 3700
BIW	1640, 2420, 5300	2100	/
BLM	1310, 1940, 3520	950, 1700, 2860	/
BOU	150, 330, 610	1000	/
CAM	560, 1530, 5080	880, 5790	/
CHU	1750, 5180	920, 6570	1820, 4870
DES	360, 540, 1060, 2230	380, 2320	/
EAC	690, 1580	510, 970, 3270	610, 1280
EIF	550, 710, 1810, 3860, 8760	600, 1050, 2450, 3650, 9940	/
ERH	460, 910, 3180	770, 1470, 2320	/
ERL	2490, 6940	1810, 3900, 8870	/
ESC	2200, 4800, 9030	1550, 2780	1070, 1820, 2630
FAN	1210, 2700, 4960	1080, 1730, 340, 6290	/
FIN	1110, 1840, 3450, 7510	1230, 2340, 4640	/
FIS	1380, 3190, 6550	1250, 1950, 4270, 8340	/
FRG	1860, 4010	2230, 4300	2310, 4920
FUR	1820, 1960, 3800	2520, 4370	/
GAR	1330, 2400, 3390	1410, 2950	2040
GEI	1780, 2960	3740	/
GHI	3060	1280, 2680	1420, 2210
GNO	1760, 2860, 5230	3140	/
GRE	1600, 4170	1300, 2590,	/
HUR	2210, 3220, 8580	980, 1960	/
ICE	1480, 2970	1170, 2330	/
KEI	3930, 7500	2410, 3780	/
KYL	550, 940, 1670	1430	/
LAM	1100, 1540, 2770	830, 1570, 5210	/
LEB	1150, 2060, 3300	1070, 1830, 2470	1630, 3600
LOM	1810	1050, 3920	/
LOU	1950, 3640, 5120	/	/
LSC	970, 1450, 3150	1260, 2100, 4570	/
MAR	590, 1200, 1730	830, 1390, 3510	/
MEE	760, 1620, 3410	450, 1380, 3260	/
MEZ	580, 1090, 2310	400, 990, 2530	690, 1360, 3140
MNT	4420, 9380	3320	/
MOR	530	830	/
MOT	1130, 3380	2580, 4630	/
NAR	1410, 3730, 6920	1870, 2600, 5530	/
NAU	2330, 2940, 5580	1620, 2280, 5100	1180, 2000, 3550
NEM	1030, 2000, 3580, 5170	970, 3770	/
PAD	1070, 3800	400, 1340, 2250, 5170	460, 1000, 1970
PEP	/	460, 1360, 2900, 4310	610, 1770, 3100
POH	960, 1810	1530	1030, 1570
SAG	1630, 4530	790, 2320, 5400	/
SAN	1560, 2660, 4640	810, 1630, 2640	/
SAR	1820, 3100, 7180	1680, 2560, 4560	/
SAV	2020, 3200, 7480	1320, 2560, 4140	/
SCL	640, 1470, 1930, 5480	520, 740, 1860	/
STL	1050, 1440, 3590	560, 1040, 1900, 3090	990, 1270, 2450
SUP	2100, 3120, 5060	1930, 2740, 5320	/
TRE	1410, 2110, 3390, 6190	1760, 3250	1730, 4580
TRI	790, 1190, 2050, 4190	740, 1510, 2290	/
TUR	/	630, 1200	/
VAT	790, 2310, 3100	1050, 2130, 3720	/
VIC	470, 770, 1700	790, 960, 1550	/
VOL	1100, 1680	620, 770, 1550	/
VUK	870, 1510	980, 1490, 2290, 4220	/
WAI	1190, 1960, 3340	1550, 4380, 9830	/
WAS	/	/	3920, 7280
WIN	2210, 3480	1910, 2780, 6700	/
WPA	/	1010, 1200, 3270, 5870	1630, 3000

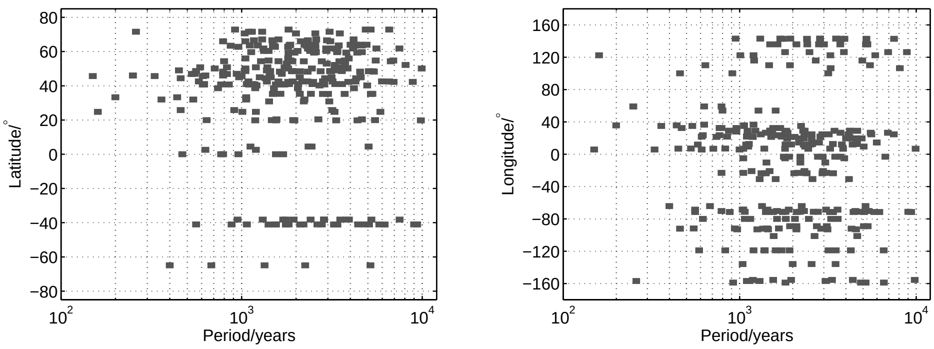

Figure 4.7: Periodicities dependence on latitude and longitude. Horizontal bars represent periods with their 10% uncertainty. The longer the period is, the larger the uncertainty is. Note the logarithmic scale on x-axis.

4.4 Discussion and conclusions

The application of three different time series analysis techniques to the contemporary database of Holocene sediment magnetic records demonstrates that millennial time scale geomagnetic field variability should be understood as a superposition of broadband variations. This conclusion is compatible with previous studies of periodicities in sediment magnetic records, based on a less comprehensive data collection (Barton, 1982, 1983) and with recent findings regarding the spectrum of the geomagnetic dipole (Constable and Johnson, 2005; Ziegler et al., 2011; Olson et al., 2012). No evidence is found for discrete, globally observed, periodic signals capable of accounting for large portions of the secular variation. Nilsson et al. (2011) have recently identified a 1350 years cycle in modelled dipole tilt variations for the past 9000 years based on five high quality sediment records. Although power is present at this period when considering the global database of records, it does not dominate the observed secular variation spectrum. Changes in the dipole tilt are a very specific aspect of the geomagnetic field evolution (e.g. Amit and Olson, 2008) and the field variations associated with it constitute only a small part of the observed secular variation.

A mean power law exponent of -2.3 ± 0.6 is found for the period range from $300 - 4000$ years (Fig. 4.6a). This is in good agreement with a previous observation-based estimate by Barton (1982) of -2 using a much smaller data collection and compares well with values of $-5/3$ for the range 500 to 50000 years and $-11/3$ for shorter periods obtained by Constable and Johnson (2005) for their composite spectrum for the dipole moment. Furthermore it is in remarkably good agreement with the exponent of $-9/5$ recently obtained from geodynamo simulations by Olson et al. (2012) for the band of periods between 500 yrs and 200 kyrs and similar to the exponent of $-5/3$ obtained in a high resolution rotating magneto-convection simulation by Sakuraba and Hamano (2007), considering frequencies up to 3 kyr^{-1}. Tanriverdi and Tilgner (2011) have demonstrated that, for small amplitude fluctuations, a power law exponent of -2 for the magnetic energy indicates an underlying, bandlimited, white spectrum of temporal fluctuations in the core flow. These results therefore suggest that the present (Holocene) mode of operation of the geodynamo, with no excursions or reversals and a power law exponent of approximately -2 for its magnetic fluctuations, is a consequence of chaotic convection producing a white spectrum of flow fluctuations and broadband variations in magnetic induction.

It should be remembered that the analyses presented here cannot rigorously distinguish between geomagnetic and environmental sources of variability. Consequently, the possibility of some contamination from environmental sources cannot be excluded. For example, the recovery of the paleointensity variation in sediments requires a normalisation to reduce the environmental effects, and any inadequately treated records may remain biased with respect to non-geomagnetic signals (Constable and Johnson, 2005). It is also noteworthy that the same periods are not always seen in different components at the same site. This may partly be due to sensitivity kernels for D, I and RPI (Johnson and Constable, 1997) sampling different regions of the core-mantle boundary (Figs. 6.1 and 6.2), but may also reflect differences in the recording fidelity of the different components. Inaccuracies in dating of the sediment magnetic records also contribute to uncertainties in the reported periodicities.

The conclusion is that Holocene sediment magnetic records possess a continuous spectrum of variations on time scales from $300-4000$ years, with some local variability. This is compatible with the hypothesis of chaotic convection in the Earth's core driving secular variation as suggested by recent numerical simulations of the geodynamo (Sakuraba and Hamano, 2007; Amit et al., 2010; Tanriverdi and Tilgner, 2011; Olson et al., 2012). On the other hand, our findings are more difficult to reconcile with models of secular variation consisting of only a small number of global modes possessing very simple space and time dependence.

Chapter 5

Case study of Swiss lakes: Soppen and Baldegg

5.1 Overview

Paleomagnetic studies carried out on Swiss lake sediments have shown that these sediments can be good recorders of the Earth's magnetic field. For example, paleomagnetic data obtained from Lake Geneva (Creer et al., 1975) and Lac de Joux (Creer et al., 1980) exhibit good correlation with archeomagnetic data and nearby UK records (Turner and Thompson, 1979, 1981). The work by Hirt et al. (2003) shows that in the sediments of Lake Baldegg and Lake Hallwil, both in Switzerland, the primary carriers of the remanent magnetization are magnetotactic bacteria, which are ideal recorders of the Earth's magnetic field. Unfortunately, only incomplete information is available from the previous studies on Lake Zug and Lake Zurich (Thompson and Kelts, 1974), and Lac de Joux (Creer et al., 1980), which have only depth dependent PSV records, with no age model provided. In addition, there are short time interval records from the last 2000 years from Lake Morat (Hogg, 1978) and a 400 years record from Lake Geneva (Creer et al., 1975). A PSV record covering the entire Holocene on Swiss territory is lacking, despite the good recorders available. Therefore, within the framework of the ETH CHIRP project (Hirt et al., 2008) two Swiss lakes have recently been sampled: Lake Soppen and Lake Baldegg.

Complete and continuous paleosecular variation records are obtained from the Lake Soppen and Baldegg that fulfil the criteria of King et al. (1983) and Tauxe (1993). A detailed description of the magnetic methods used to obtain the records may be found in Kind (2012). A case study of the application of the robust spline modelling technique (cf. Chapter 3) to the Swiss records in order to test their fidelity and obtain error estimates for field modelling is presented in this chapter. We also apply the methods described in Section 4.2 to search for the presence of periodicities in these records. The degree of smoothing in the case of the Lake Soppen and Baldegg records is determined, based on an assumed lock-in depth (10 cm) and the average sedimentation rate. A Holocene PSV composite curve for Switzerland for the last 7000 years is also produced by combining the paleomagnetic data from these two lakes.

An important use for these continuous central European PSV records is to test their compatibility with 'archeomagnetic jerks' (Gallet et al., 2003). Analysis of the intensity maxima and directional curvature changes in Swiss records is therefore carried out in order to study the evidence of these sudden changes of the Earth's magnetic field in a location close to France where they were originally inferred from archeomagnetic studies.

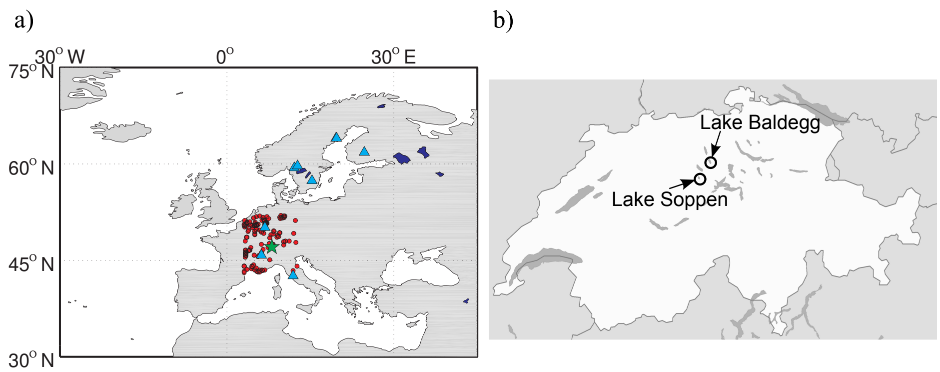

Figure 5.1: (a) Location of the Swiss lakes - Soppen and Baldegg (green star) on the map of Europe. Nearby archeomagnetic data (red circles) and neighbouring lake sediment records (blue triangles) from Italy (Lago di Mezzano), Germany (Eifel Maar), France (Lac d' Annecy and Lac du Bourget), and lake sediment records in Sweden and Finland that contribute to the Fennoscandian stack are also presented. (b) Position of the Lake Soppen and Lake Baldegg on a map of Switzerland.

5.2 Paleosecular variation and paleointensity records

Lake Soppen (8° 20′ 00″ E, 47° 05′ 30″ N) and Lake Baldegg (47° 11′ 55″ N, 8° 15′ 38″ E) are situated on the Central Swiss Plateau (Fig. 5.1). The location of these lakes allows us to compare with nearby archeomagnetic data and lake sediment records from Italy, Germany, France and Fennoscandia, as shown in Fig. 5.1a. Paleomagnetic data are obtained from a few parallel and overlapping sediment cores making use of the correlation between characteristic sedimentological features. Lake Soppen record I (SoI) consists of seven core sections and has a total length of 670 cm covering the past 14,000 years, while Lake Soppen record II ($SoII$) has a total length of 360 cm and consists of four core sections covering the past 7000 years and it is 3 m away from the SoI. The Lake Baldegg record (Ba) covers the past 11,000 years and it represents a composite of fifteen individual core sections. Samples that are not recording the Earth's field reliably, based on their demagnetization behaviour, were not used in the paleomagnetic evaluation. Therefore, Lake Soppen is limited to the last 6000 years and Lake Baldegg to the last 7000 years.

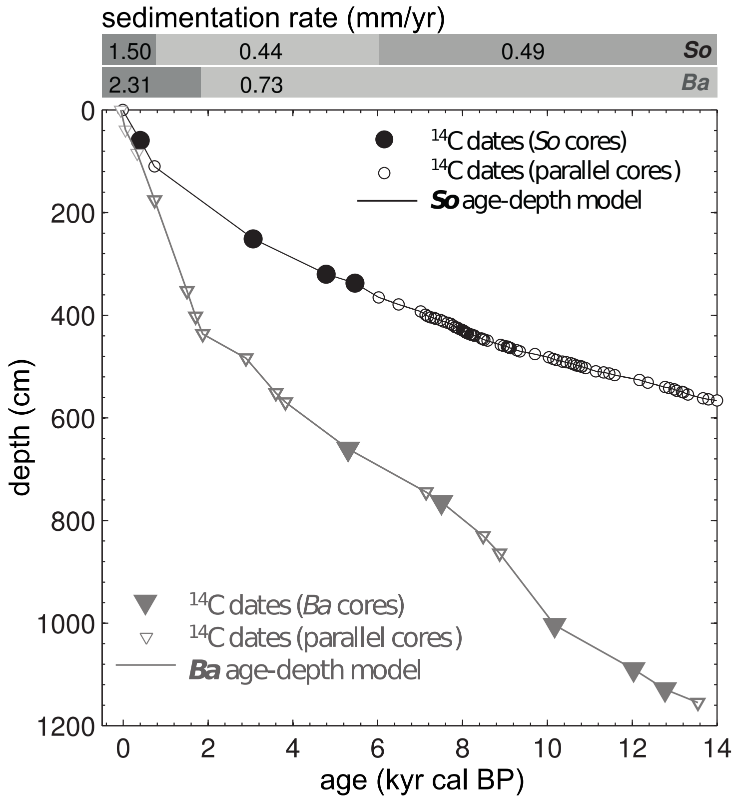

Figure 5.2: Age-depth correlation for Lake Soppen (black line) and Lake Baldegg (gray lines) based on ^{14}C dates. Filled symbols represent the new dates that are listed in Tab. 5.1. Open symbols represent cal ^{14}C dates from previous studies for Lake Soppen: Hajdas et al. (1993); Hajdas and Michczyński (2010) and for Lake Baldegg: Monecke et al. (2004). Figure from Kind (2012).

The age-depth models for both lakes are obtained from radiocarbon (^{14}C) dating and correlation of lithological information to previous sediment records from the same lakes (van Raden, pers. comm., Hajdas et al., 1993; Hajdas and Michczyński, 2010). Lake Soppen sediments contain one tephra layer (Laacher see tephra) dated at 10,900 years BC (Hajdas et al., 2000), whereas the Lake Baldegg sediments contain two thin tephra layers, the Laacher see tephra (Blockley et al., 2008; Hajdas et al., 2000) and the Vedde ash (Birks

Table 5.1: New ^{14}C dates from Lake Soppens and Lake Baldegg covering the Holocene period. Table adapted from Kind (2012).

	Lab code	Composite depth (cm)	^{14}C dates
Lake Soppen	ETH-39582	59.0	400±40
	ETH-39583	250.9	2835±40
	ETH-39584	319.8	4230±40
	ETH-39585	337.1	4825±40
Lake Baldegg	ETH-38958	660.5	4540±35
	ETH-43950	764.0	6615±40
	ETH-38959	1003.7	8935±45

et al., 1996). In addition to correlation, four new radiocarbon dates (Tab. 5.1) were obtained in order to better constrain the age model for the mid- to late Holocene (van Raden, pers. comm.). The age-depth model for Lake Soppen reveals a relatively high sedimentation rate (1.5 mm/yr) for the last 730 years and a nearly constant sedimentation rate of 0.44 mm/yr for the older sediment. Lake Baldegg exhibits a higher sedimentation rate than those from Lake Soppen and it therefore possesses the potential for better temporal resolution. It contains turbidite sequences (Monecke et al., 2004), however, these were removed prior to the construction of the age model (van Raden, pers. comm.). The final age model displays two sedimentation rates of 2.31 mm/yr for the past 1800 years and 0.73 mm/yr between 1800 and 14,000 years ago (Fig. 5.2).

Both lakes possess a uniform lithology throughout the Holocene with magnetite as the major magnetic carrier (e.g. Lotter, 1989, 1991; Hajdas et al., 1993; Egli, 2004; Kind et al., 2011). They are of single domain grain size (between $30-80$ nm), varying no more than one order of magnitude in concentration throughout the sediment record (cf., Tauxe, 1993). The paleomagnetic analysis was performed on about 500 samples in total (Kind, 2012). Both lake sediments carry stable remanent magnetisation and the characteristic direction of the remanent magnetisation was isolated using alternating field demagnetization. Principle component analysis (Kirschvink, 1980) was then used to define the direction. The low average values of 1.08° (SoI), 0.88° ($SoII$), and 0.62° (Ba) for the maximum angular deviation (MAD) indicate well-defined directions. Declination values for the individual cores are reported as relative deviations with respect to the average core directions, because all cores are azimuthally unoriented. The geocentric axial dipole (GAD) inclination at the lake's location is 65°, which is in a good agreement with the average inclination value for Lake Baldegg (61°), but there is an unexplained offset of about 20° with respect to the SoI (45°) and $SoII$ (49°) cores. Therefore, relative

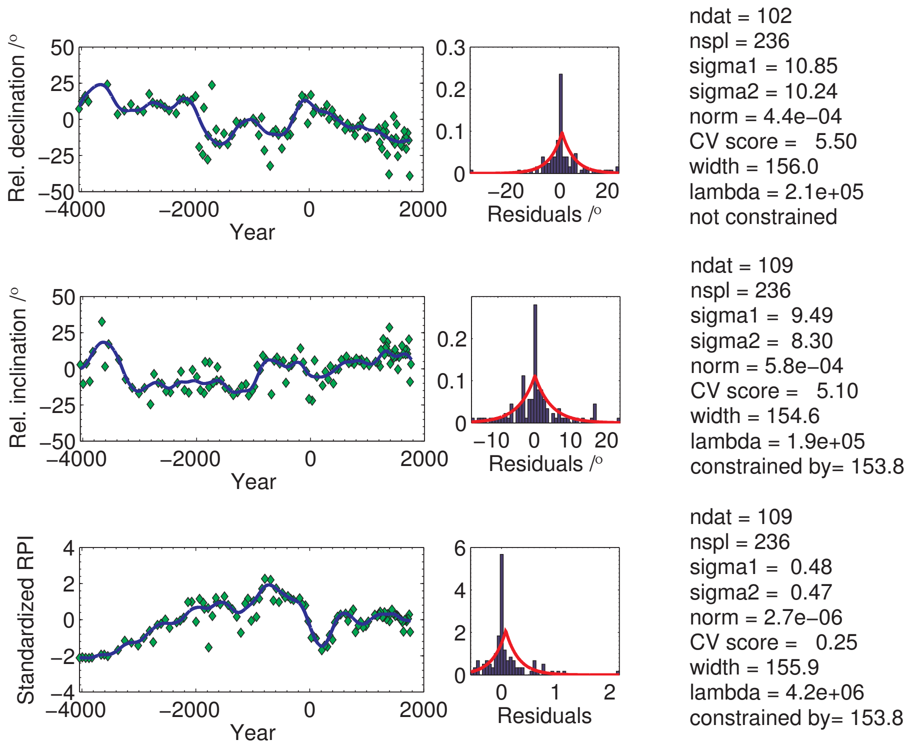

Figure 5.3: Robust spline analysis of relative declination (top), relative inclination (middle), and standardized relative paleointensity data (bottom) from the SoI record. Also shown are the histograms of the residuals (normalized to the unit area) with a Laplacian distribution with mean and deviation calculated from the residuals. Information about the number of data (ndat), the number of splines functions used (nspl), the L_1 measure of misfit σ_1 (sigma1), the L_2 measure of misfit σ_2 (sigma2), the norm measuring the model roughness (norm), the value of the CV minimum (CV score), the width of the resolving kernel or T_{ss} (width), the corresponding smoothing parameter λ (lambda) and a priori smoothing time T_s (constrained) are provided in the label on the right of each sub-figure.

inclination values were used to construct the final composite record described in Section 5.4.

The relative paleointensity was determined by three normalization parameters: anhysteretic remanent magnetization (ARM), saturation isothermal remanent magnetization ($SIRM$) and low-field magnetic susceptibility (χ). Although all three normalised records exhibited similar variations, ARM was found to give best results based on the correlation of normalization parameters and RPI records. Furthermore, RPI is standardized according to the mean and standard deviation estimated for the same time interval.

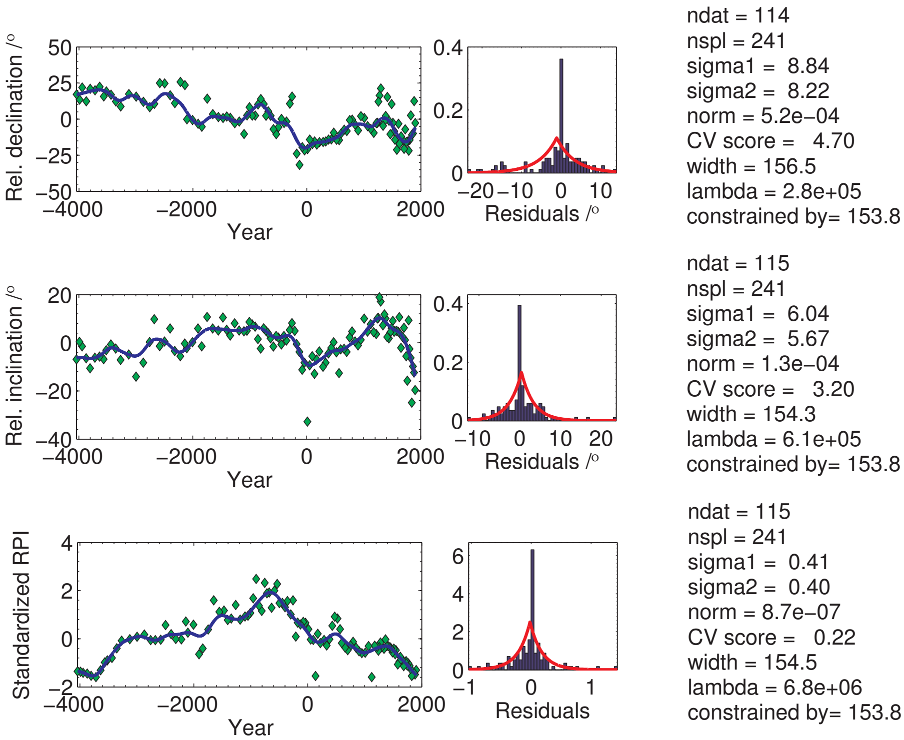

Figure 5.4: Robust spline analysis of relative declination (top), relative inclination (middle), and standardized relative paleointensity data (bottom) from the $SoII$ record. An explanation of the labels is given in Fig. 5.3.

5.3 Robust spline modelling of the Swiss lake sediment records

The technique for obtaining uncertainty estimates for sediment magnetic records (Panovska et al., 2012) (Chapter 3), is now employed to analyze records from Lake Soppen and Lake Baldegg. Robust smoothing spline models fits to the three cores are presented in Figs. 5.3, 5.4 and 5.5. The degree of smoothing is determined, based on an assumed lock-in depth (10 cm) and the mean sedimentation rate for each record. A statistical rejection of outliers is applied after the initial spline inversion and data points deviating more than three standard deviations from the spline model. Eleven points have been rejected in the final analysis.

The variance of the record away from the spline model σ_{rss} (Eq. 3.21) was computed for each record. This was for Lake Soppen I, II and Lake Baldegg, 0.47, 0.40 and 0.65 for the standardized RPI; 8.3°, 5.7° and 4.6° for the relative inclination; and 10.2°, 8.2° and 9.1° for the relative declination, respectively. The three records thus show similar variability away from the spline models

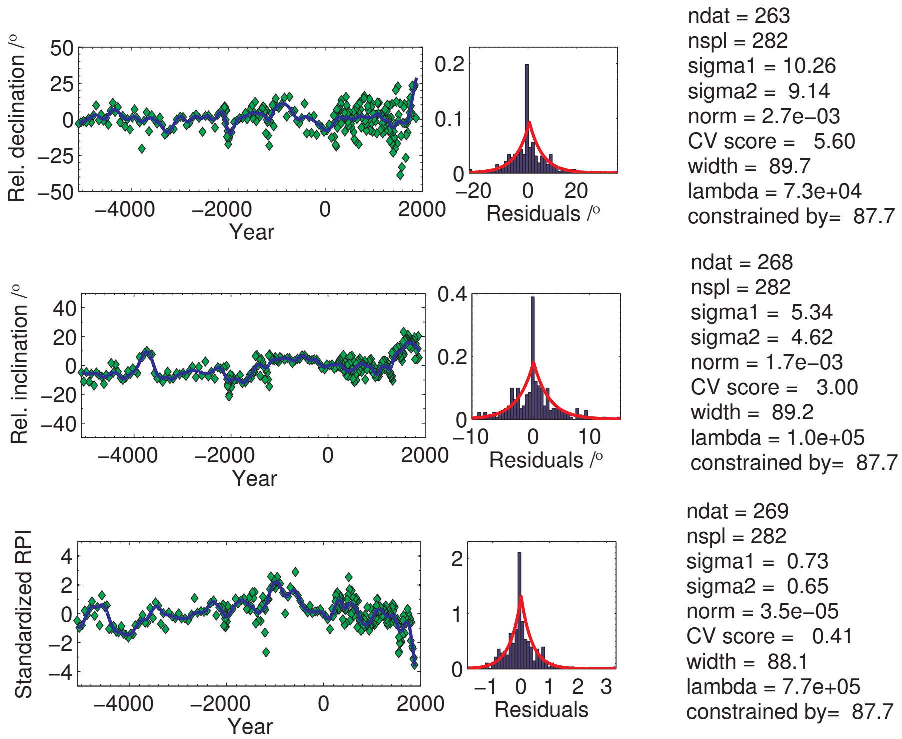

Figure 5.5: Robust spline analysis of relative declination (top), relative inclination (middle), and standardized relative paleointensity data (bottom) from Lake Baldegg (*Ba*) record. An explanation of the labels is given in Fig. 5.3.

for declination and RPI, while the Lake Baldegg record shows considerably less variability about the spline fit in the case of inclination. Final uncertainty estimates to be used for field modelling require comparison to archeomagnetic estimates; these are derived and discussed in Section 5.5. The smoothing times that are inferred from the analysis, as define in Section 3.3, are 155 years for *SoI* and *SoII*, and 90 years *Ba*. These are constrained by the assumed a priori smoothing time based on the sedimentation rate (Section 3.3.2).

5.4 Composite paleomagnetic secular variation record

The robust spline models of the three individual records (*SoI*, *SoII*, and *Ba*) show broadly similar trends within their overlapping time interval, though slight variations in time and amplitude can be observed when comparing (Figs. 5.3, 5.4 and 5.5). A composite record (*SoBa*) has therefore been derived by combining the data on the same time scale and fitting a robust smoothing

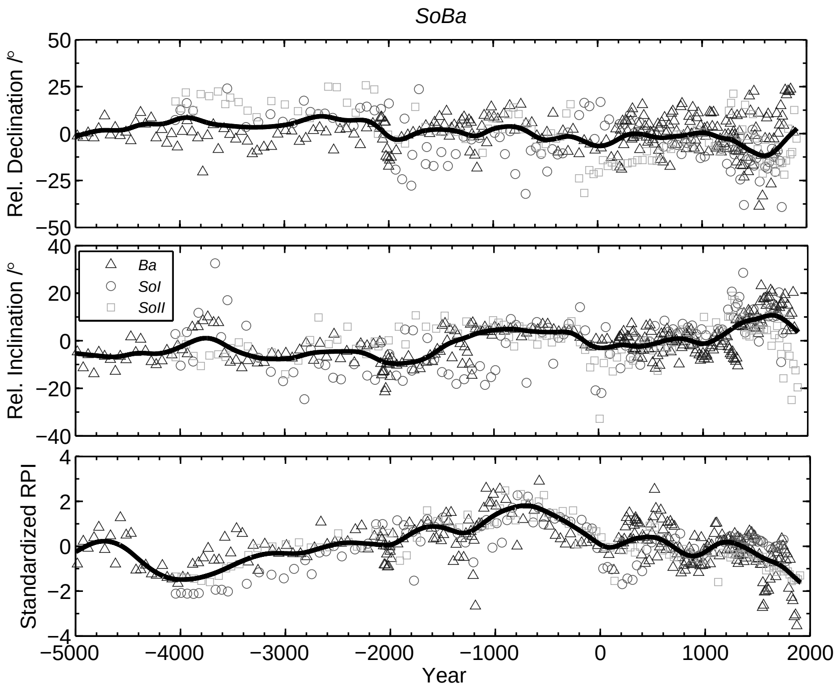

Figure 5.6: A composite record *SoBa* for relative declination, relative inclination and standardized RPI (solid lines) calculated from the *SoI* (circles), *SoII* (squares) and *Ba* (triangles) data.

spline to each component (Fig. 5.6). Due to the age models of the individual sediment records not being definitive, an error may be introduced in the composite model. Incompatibilities between the age-depth models cause some features to mutually cancel out, so the composite record shows smoother variations with smaller amplitudes than the individual records. For example, additional smoothing can be seen in relative inclination values, which are around $\pm 10°$, while the individual records exhibits larger variations: $\pm 20°$ (*SoI*), $\pm 15°$ (*SoII*), and $\pm 12°$ (*Ba*).

The first pronounced peak in the *SoBa* record at $\sim$ 1680 AD is broader and less pronounced in amplitude than the peaks of the individual records, because the maxima differ in their age between $\sim$ 1680 for the *SoI* and $\sim$ 1620 AD for *SoII*. Shallower inclination values between 3500 BC and 1500 BC are observed in the records *SoI* and *Ba*. The slightly steeper inclination ($\sim 10°$) in the *SoII* gives a less pronounced trough in the composite *SoBa* record. In general, good agreement in relative inclination is found for peaks around 1680 AD, 750 AD, 850 BC, 2450 BC, and 3750 BC years and troughs around 150 AD and 3500 BC - 1500 BC years, so these features appear prominently in the composite record. Relative declination variations exhibit similar values to those of the relative inclination of about ±20° for *SoI* and *SoII*, and ±10° for *Ba*. The robust smoothing spline model of the relative paleointensity yield best agreement between the records. The general trend of increasing the intensity towards a distinct maximum at around 700 BC and a continuous decrease towards recent times is present in all the records and in the composite model. The quality of the records is next further tested by comparing them with other geomagnetic field recorders and global field models.

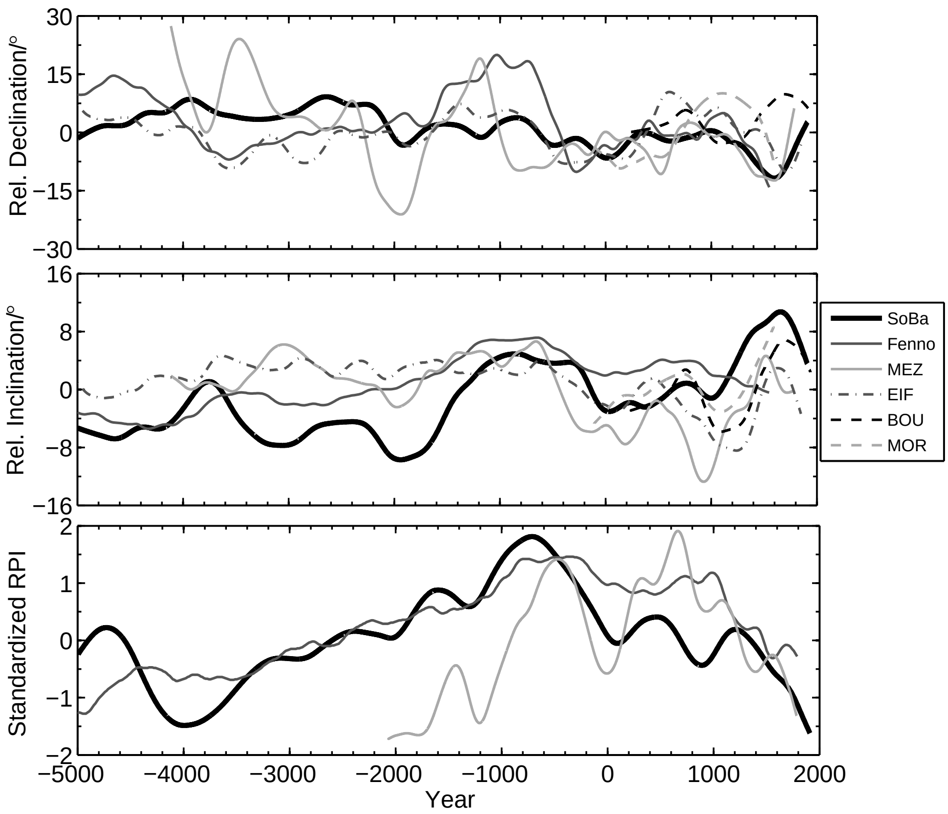

Figure 5.7: A comparison of the *SoBa* composite record (black solid lines) to the smoothing spline fits of the data from neighbouring lakes - FEN (the stack record from Fennoscandia), MEZ (Lago di Mezzano, Italy), EIF (Eifel Maar, Germany), BOU (Lac du Bourget, France) and MOR (Lac Morat, Switzerland) for the relative declination, relative inclination and standardized RPI.

5.5 Comparison with other magnetic recorders and global field models

5.5.1 Comparison of the individual records

Quantitative comparison with model predictions from ARCH3k.1 enables independent assessment of the reliability of individual records. This comparison was performed when archeomagnetic data exist in the vicinity of the lake location in order to estimates the combined uncertainty σ_c (cf. Section 3.3.4). Using the Eq. 3.32, the total uncertainties σ_l were calculated, based on σ_c, and the estimated error of the archeomagnetic estimates σ_a. The results are summarized in Table 5.2.

Table 5.2: Uncertainty estimates for relative declination, relative inclination and standardized RPI for the composite and the three individual records. σ_{rss} refers to the random uncertainty component obtained from the robust smoothing spline fit. σ_c is an uncertainty from the comparison with archeomagnetic estimates. σ_a is the estimated error of the archeomagnetic estimates, while σ_l is the final uncertainty estimate for the lake record.

Record	Component	σ_{rss}	σ_c	σ_a	σ_l	Smoothing time [yr]
	D/°	10.2	22.5	2.9	22.3	
SoI	I/°	8.3	15.6	4.9	14.8	155
	RPI	0.47	0.90	0.30	0.85	
	D/°	8.2	11.1	2.9	10.7	
SoII	I/°	5.7	16.5	4.9	15.7	155
	RPI	0.40	0.52	0.14	0.50	
	D/°	9.1	11.9	2.9	11.5	
Ba	I/°	4.6	7.8	4.9	6.1	90
	RPI	0.40	0.65	0.40	0.45	
	D/°	10.7	11.1	2.9	10.7	
SoBa	I/°	7.5	8.4	4.8	6.9	155
	RPI	0.69	0.27	0.18	0.20	

The final uncertainty estimates for relative inclination for each record are 14.8° for *SoI*, 15.7° for *SoII*, and 6.1° for *Ba*. Larger uncertainty estimates for the *SoI* and *SoII* are obtained when absolute inclination values are considered due to larger systematic errors ($\sim$ 13°). Final relative declination uncertainties are 22.3° for *SoI*, 10.7° for *SoII*, and 11.5° for *Ba*. Standardized RPI uncertainties range from 0.85 for *SoI*, 0.50 for *SoII*, and 0.45 for *Ba*. The best results as quantified by the smallest uncertainty estimate are obtained for the inclination and standardized RPI of the *Ba* record. On the other hand, the *SoI* shows the largest relative declination uncertainty due to the highest comparison error ($\sigma_c = 22.5°$). The width of the resolving kernel for the composite spline model is constrained by the threshold estimated from the average sedimentation rate and an assumed lock-in depth of 10 cm. Consequently, the smoothing times are 155 years for Lake Soppen and 90 years for Lake Baldegg.

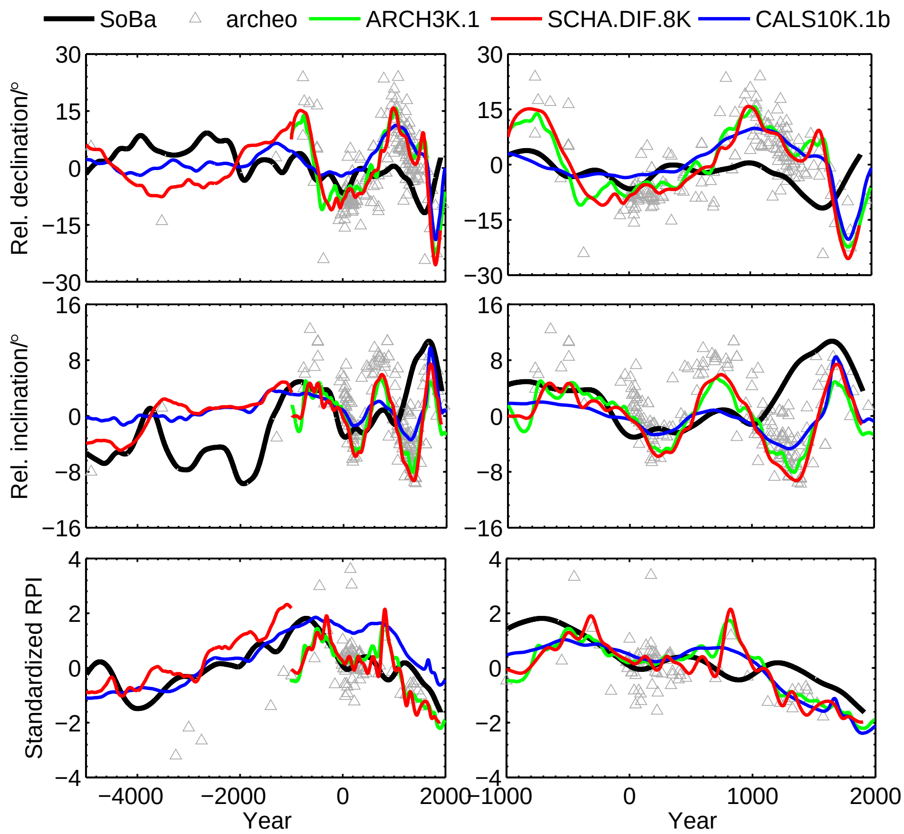

Figure 5.8: A comparison of the *SoBa* composite record with nearby archeomagnetic data (grey triangles) and the global geomagnetic field models ARCH3k.1 (green line), SCHA.DIFF.8k (red line), and CALS10k.1b (blue line) for the relative declination, relative inclination and standardized RPI. The archeomagnetic data are selected within an area of $\pm 5°$ from the lake locations and relocated using the CALS7k.2 model. Comparisons are given for the entire 7000 yr span of the *SoBa* composite record (left column subplots) and for the last 3000 yr (right column subplots).

5.5.2 Comparison of the *SoBa* composite record

The three components of the Swiss composite PSV curve *SoBa* are here compared first to nearby lakes from Europe, i.e. Lac Morat (MOR) in Switzerland (Hogg, 1978), Lac du Bourget (BOU) in France (Hogg, 1978), Lago di Mezzano (MEZ) in Italy (Brandt et al., 1999), the Eifel Maar (EIF) in Germany

(Stockhausen, 1998), and the PSV master curve from Fennoscandia (FEN) (Snowball et al., 2007). Next, comparisons are made to the archeomagnetic data (Korhonen et al., 2008; Donadini et al., 2009) available within a 5° area of latitude and longitude from the lake location (relocated to the study site using the CALS7k.2 global model produced by Korte and Constable (2005a)); and to global field model predictions from CALS10k.1b (Korte et al., 2011), ARCH3k.1 (Donadini et al., 2009; Korte et al., 2009), and SCHA.DIF.8k (Pavón-Carrasco et al., 2009, 2010).

The three components of the PSV from the *SoBa* composite record are shown with respect to nearby lakes in Fig. 5.7. For relative declination, the variations in the *SoBa* record are less pronounced in general, compared to the other lakes, but the minimum around 1650 AD is visible in all lakes. The low inclination values between 3500 BC and 1500 BC agrees with the FEN record. Better agreement is obtained for the more recent times (last 2000 years), although the *SoBa* record shows a shift of about 200 years with respect to BOU, MOR and EIF. The major trend of increasing RPI towards 550 BC agrees well with the FEN and MEZ records. The other nearby records have only directional components.

Comparison of the *SoBa* composite record with the global field model predictions in Fig. 5.8 yields similar agreement, i.e, features produced by the global models in the three components are observed in the *SoBa* record. The most striking difference is between 3500 BC and 1500 BC where the inclination values indicate an offset of about 10° with respect to the global model predictions.

5.6 Periodicity analysis of Swiss PSV records

The techniques employed on the global database in Chapter 4 to search for periodicities are now implemented on robust smoothing spline models of the *SoI*, *SoII*, *Ba* and the composite master curve *SoBa*. Table 5.3 summarized the periodicities obtained by the EMD technique. The results are found to be approximately consistent with the periods often seen in European region records: 700, 1100, 1800, 2400 and 3200 years (Section 4.3), taking into account the uncertainty of 10% typically associated with each determination.

Table 5.3: Periodicities (in years) obtained by EMD analysis for the SoI, $SoII$, Ba and the composite $SoBa$ record

Record	Declination	Inclination	RPI
SoI	1110, 2220, 3540	860, 1700, 4830	670, 1200, 1960
$SoII$	650, 1700, 2560	1380, 2330	1870, 3050
Ba	330, 770, 1510, 3310	810, 1760	550, 1180, 2130
$SoBa$	630, 1580, 1790	1230, 2570	1000, 4980

5.7 Archeomagnetic jerk analysis

Investigation for the possible occurrence of archeomagnetic jerks in the individual records and in the final composite record $SoBa$ was carried out. Archeomagnetic jerks are defined as significant peaks in geomagnetic field intensity, that occur simultaneously with abrupt changes in field direction, i.e., changes in the field's temporal curvature (Gallet et al., 2003). Several jerks have been inferred from French archeomagnetic data at 200 AD and 1400 AD, and two further less constrained events at $\sim$ 800 BC and 800 AD. Table 5.4 lists all studies that have reported archeomagnetic jerks in different types of data and models.

Unlike the archeomagnetic field intensity, the absolute rate of intensity change in sediment records cannot be determined. Snowball and Sandgren (2004) suggested that archeomagnetic jerks can be also identified in lake sediments and reported their findings for Fennoscandian records. SoI, $SoII$, Ba and $SoBa$ records were therefore analysed in order to infer the existence of archeomagnetic jerks in Swiss paleosecular variation (Fig. 5.9).

The curvature in directional data (C_D) and maximum intensity (M_F) as a function of time have been estimated via following equations (Pavón-Carrasco et al., 2010):

$$C_D(t) = \frac{\left|\dot{D}(t)\ddot{I}(t) - \dot{I}(t)\ddot{D}(t)\right|}{\left[\dot{D}(t)^2 + \dot{I}(t)^2\right]^{3/2}} \tag{5.1}$$

and

$$M_F(t) = -sign(\ddot{F}(t))\frac{1}{\left|\dot{F}(t)\right|} \tag{5.2}$$

where $\dot{D}$, $\dot{I}$ and $\dot{F}$ are the first time derivatives and $\ddot{D}$, $\ddot{I}$ and $\ddot{F}$ are the second time derivatives. The second time derivative is formally allowed to change in a discontinuous way only at the knot points of a cubic spline model (Lesur et al., 2008). Here, cubic spline models use a knot spacing which is much smaller than the temporal resolution in the records. Changes in the curvature and maximum intensity are presented in Fig. 5.9. Two well-defined archeomagnetic jerks at 450 AD and 700 BC, and three less constrained at 2450 BC, 3150 BC and 4650 BC are found based on the sharp cusps in geomagnetic field directions that occur simultaneously with peaks in RPI in the four analysed series. Since there are errors associated with dating, some archeomagnetic jerks are shifted within 200 yr for the individual records. Also some distinct changes in the curvature are associated with a minimum in geomagnetic field intensity Fig. 5.9. The occurrence of archeomagnetic jerks in the *SoBa* records support the previous findings based on archeomagnetic studies that these distinct changes in the geomagnetic field have occurred and moreover, strengthen the hypothesis that lake sedimentary data can resolve such sudden changes of the geomagnetic field (Turner and Thompson, 1981; Saarinen, 1998; Snowball and Sandgren, 2004).

Table 5.4: Summary of archeomagnetic jerks.

Reference	Location	Data Type or Model	Archeomagnetic jerks occurrence
Gallet et al. (2003)	France	archeomagnetic	800 BC 200 AD 800 AD 1400 AD
Snowball and Sandgren (2004)	Scandinavia	lake sediments	6450 BC 4450 BC 1950 BC 850 BC
Stark et al. (2009)	Peru	archeomagnetic	200 AD 620 AD - 820 AD 1000 AD - 1400 AD
Ben-Yozef et al. (2009)	Jordan	archeomagnetic	800 BC - 1000 BC
Yu et al. (2010)	Korea	archeomagnetic	745 BC 300 AD 1400 AD - 1700 AD
Pavón-Carrasco et al. (2009)	Europe	SCHA.DIF.3K	300 BC 300 AD 800 AD 1350 AD 1600 AD
Pavón-Carrasco et al. (2010)	Europe	SCHA.DIF.8K	5800 BC 4500 BC 4100 BC 3600 BC 3000 BC 2500 BC 1700 BC
This study	Switzerland	lake sediments	4650 BC 3150 BC 2450 BC 700 BC 450 AD

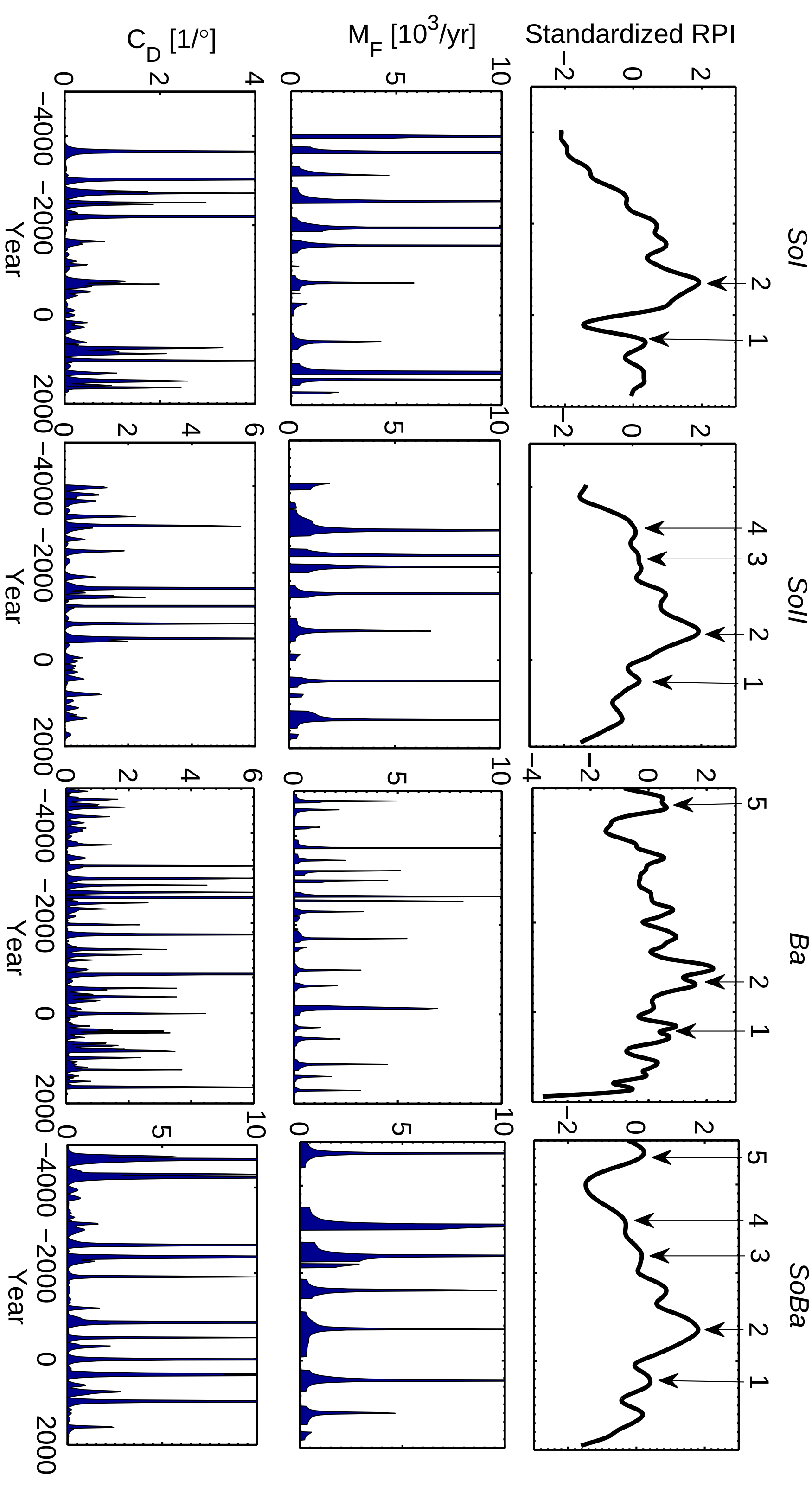

Figure 5.9: Standardized RPI, maximum intensity (M_F) and directional curvature (C_D) for the composite *SoBa* and the individual *SoI*, *SoII* and *Ba* records. Event are numbered as follows: 1) 450 AD, 2) 700 BC, 3) 2450 BC, 4) 3150 BC and 5) 4650 BC.

5.8 Discussion and conclusions

Paleomagnetic records have been obtained from the Swiss Lake Soppen and Baldegg. The three records SoI, $SoII$ and Ba show similar trends, in particular in the relative paleointensity, which suggest that the relative paleointensity is indeed related to geomagnetic field behaviour. The composite $SoBa$ record is obtained implementing a robust smoothing spline fit to the combined dataset. Additionally, a statistical analysis was performed in order to assign uncertainty estimates to each record. These data will later be used in the construction of the Holocene geomagnetic field model reported in Chapter 6.

Observed variations with opposite sign in the Soppen and Baldegg records contribute to the cancellation of some features in the composite $SoBa$ record (Fig. 5.6). For example, the minima around 100 AD in the $SoII$ and Ba records contrast with the maximum in the SoI record. According to the error estimates, the $SoII$ record exhibits better results for the Lake Soppen with $\sigma_l = 10.7°$, half as much as the SoI. However, the error estimate for the $SoBa$ of $\sigma_l = 10.7°$ lies within the range of declination uncertainties (4.1° to 46.9° with a median of 13.4°) for the sediment records in the global database (Panovska et al., 2012). The smoothness of the composite model can be observed by a variation of around 20 degrees, whereas the data vary by about 65°. Thus, the composite $SoBa$ record may not capture all features from the individual records, but it does not over-interpret spurious features of individual records. A possible reason for the observed inconsistency in declination may be that the cores have been not azimuthally oriented and individual core sections have been averaged to zero.

There is a good agreement of the directional and intensity features found in the $SoBa$ record and nearby lakes (EIF, MOR, BOU, FEN and MEZ), archeomagnetic data and global field models (ARCH3k.1, SCHA.DIF.8k and CALS10k.1b) for the past 3000 years. However, an offset of about $250 - 300$ years is observed for the first 3000 years with respect to the global models predictions in all three components (see Fig. 5.8). Considering that the $SoBa$ record consists of three individual records, it has been shown that all features in the Ba record occur earlier than in SoI and $SoII$ records (see Figs. 5.3, 5.4 and 5.5). Dating errors may therefore contribute to some discrepancies in the comparison between the cores. Lake Soppen and Lake Baldegg records are dated by radiocarbon dating of organic remains, two tephra layers (Laacher See Tephra and Vedde ash), and cross-correlation with previous well-dated cores (e.g. Hajdas and Michczyński, 2010). The FEN record has a good age-depth control based on the varve counting on six independent records (Snowball et al., 2007), while MEZ age model is based on radiocarbon dating of the bulk material and partly on varve counting (Brandt et al., 1999). Second, different lock-in times by means of different average sedimentation rate (0.65 mm/yr for So and 1.1 mm/yr for Ba) can contribute to the shift of some features.

The inclination shallowing of the *SoBa* record for the period between 3500 BC and 1500 BC is mainly caused by the shallower inclination values in the *SoI* and the *Ba* records (see Figs. 5.3 and 5.5). The flattening is also present in neighbouring lakes, but the amplitude is not so pronounced (e.g., FEN record) or its duration is shorter (in MEZ). The CALS10k.1b model predictions shows a similar trend between 4000 BC and 1000 BC, although the lowering is not distinct as in the *SoBa* composite record (Fig. 5.8). This flattening can be caused by various processes occurring during or after deposition of sediments, e.g. compaction and porosity (Anson and Kodama, 1987; Kodama and Sun, 1992; Arason and Levi, 1990; Tauxe, 2005). Several samples have been tested for anisotropy of the magnetic susceptibility (Kind, 2012). No anisotropy has been observed and therefore there is no obvious evidence for inclination flattening due to a sediment compaction. Verosub (1977) and Ojala and Saarinen (2002) suggested shallower inclination values in varved sediments, which is unlikely in the *SoBa* records. Except for the period 3500 BC - 1500 BC years, most of inclination features observed in the archeomagnetic data and neighbouring lakes are also recorded in the *SoBa* (Fig. 5.8).

Snowball and Sandgren (2004) showed that lake sediments are able to record strong and sudden departures from the geomagnetic axial dipolar field. Over a slightly longer timescales than the French archeomagnetic data, they claimed to see intensity peaks in Swedish lake sediment records at: 6450 BC, 4450 BC, 1950 BC and 850 BC. The analysis of the change in curvature and in field intensity in the *SoBa* records (Fig. 5.9) shows archeomagnetic jerks at 450 AD and 700 BC, and possibly at 2450 BC, 3150 BC, and 4650 BC. Except the 700 BC jerk, all others are related to the archeomagnetic jerks found in the SCHA European models by Pavón-Carrasco et al. (2009, 2010). Recent studies by Stark et al. (2009) and Yu et al. (2010) reported an occurrence of archeomagnetic jerks outside European continent. These showed the possibility of archeomagnetic jerks being of global significance, and not only regional as had initially been suggested (Gallet et al., 2003). Archeomagnetic jerks found in the *SoBa* records show good agreement with those in the Korean archeomagnetic data and the Peruvian potsherds (see Table 5.4) within the dating errors of *SoBa*.

Rapid changes in the direction of the azimuthal flow at the core mantle boundary have been suggested by Dumberry and Finlay (2007) as a possible origin of sharp changes in the field direction. Gallet et al. (2009) linked the occurrence of the archeomagnetic jerks detected in the French archeomagnetic data with a maximum of geomagnetic field hemispheric asymmetry, i.e., the strong movement of the eccentric dipole center away from the Earth's center. No complete answer for the source of these features can be found without evidence of their existence from a broader range of regions which requires global field modelling. The recovery in Swiss PSV records shows that there is potential for continuous sedimentary records to study sudden changes of geomagnetic field, provided the changes are of sufficiently large amplitude and take place over several hundred years. However, it should be noted that this is best done by having multiple independent records (cores) from a region.

Chapter 6

Time-dependent, spherical harmonic models of the Holocene geomagnetic field

6.1 Overview

New approaches to modelling the Holocene geomagnetic field using archeomagnetic and lake sediment data are tested in this chapter. In particular, it explores: 1) the use of relative intensity and declination observations; 2) the consistently allocated uncertainty estimates for lake sediments; 3) choice of measure of misfit; and 4) choice of regularization. Spherical harmonics up to degree and order 10 in space and cubic B-splines in time with a 40 years knot spacing are used as the parametrization of models of the geomagnetic field spanning the past 12 kyr with the final models considered trustworthy for the past 10 kyr.

The archeomagnetic dataset used is the same as that employed in the construction of CALS10k models by Korte et al. (2011). The lake sediment data are also those used by Korte et al. (2011), but using the uncertainty estimates derived in Chapter 3. When constructing field models it is often assumed that the noise inherent in the measurements maybe be described by a Gaussian distribution; consequently the L_2 norm of measure of misfit is employed. But in many geophysical scenarios, when more heavy tailed distributions are found empirically, a Laplacian distribution of residuals is a more suitable description and the L_1 norm measure of misfit may be more appropriate (Claerbout and Muir, 1973; Walker and Jackson, 2000). Here, models are constructed using both L_1 and L_2 misfit measures, in order to test the importance of this choice. The Ohmic heating (or dissipation) norm, the integral of B_r^2 and an entropy norm are possible choices for the measure of model spatial complexity, minimized during the inversion procedure; all three choices are explored in this chapter and comparisons are made. This is the first study in which an entropy norm measure of complexity has been applied to field modelling on millennial time scales. Four representative models: L_1 misfit and Ohmic heating norm (HFM-OL1), L_2 misfit and Ohmic heating norm (HFM-OL2), L_1 misfit and B_r^2 norm (HFM-BL1), and L_1 misfit and entropy norm (HFM-EL1) are presented to illustrate the influence of the various modelling choices.

Use of consistent error estimates for lake sediment data and the inclusion of relative intensity and declination directly in the inversion permits the construction of models that satisfactorily fit the data. These models are smoother in space and time than previously published field models covering this era. Use of the L_1 norm is found to aid the construction of robust, converged, models while use of the L_2 norm at the same level of data rejection leads to difficulties with convergence. Use of maximum entropy regularization can allow slightly higher amplitude, smaller scale field structures to be recovered at the CMB but requires the specification of an additional parameter. The HFM models show evidence of persistent non-axisymmetric field structure at high latitudes at the CMB, and a dipole moment that increases from about 6000 BC until around 250 BC before decaying to its present value. These models are suitable for interpreting geomagnetic field evolution on millennial time scales, but are only able to accurately capture field changes such as archeomagnetic jerks if these are of sufficiently high amplitude and long duration.

This chapter begins in Section 6.2 with a brief reminder of the data sources, then there is a description of the averaging kernels relevant for paleomagnetic data, that quantify the extent to which a measurement of D, I or F, both at one particular location and for the overall dataset, sample the CMB field (Section 6.3). Section 6.4 presents the technical details of the field modelling method. In Section 6.5 model results including comparisons with CALS10k.1b are presented, including an analysis of the geomagnetic dipole moment and time-averaged field structure. Maps of the time evolution of the radial component of the geomagnetic field at the CMB are presented in Section 6.5 and a discussion including implications of the results is give in Section 6.6.

6.2 Data sources for Holocene field modelling

The dataset spanning the last 12 kyr described in Chapter 2 along with the uncertainty estimates derived in Chapter 3, including the new lake sediment records from Switzerland, are the basis for the Holocene geomagnetic field models constructed in this chapter. The whole dataset comprises about 87,000 data, of which about 4% are archeomagnetic declination data, 6% are archeomagnetic inclination and 5% are absolute archeomagnetic intensity. The contribution of lake sediment data includes 35% relative declination, 37% inclination and 13% RPI (Table 6.1). Korte and Constable (2011) previously found that the RPI record from Lake Pepin, USA (Brachfeld and Banerjee, 2000) has a suspicious drop in amplitude from 1800 AD to 2000 AD and these unreliable data caused a reverse flux patch at the CMB over North America in the CALS3k.3 model. Therefore, this part of the Lake Pepin record was disregarded prior the modelling. Lake Biwa 2 (BIW2) has been used instead of the previous record from the same lake (BIW). Further, RPI and inclination of the West Pacific (WPA) record (Richter et al., 2006) were also excluded after the initial testing, due to the unrealistically large weight given to this record.

The HFM models were constructed using data rejection at the level of five standard deviations, which is less stringent than the three sigma rejection criteria applied by (Korte et al., 2011); this is justified by the use of the more robust L_1 measure of misfit for most of the HFM models. 3.4% of data were rejected considering all components and both archeomagnetic and lake sediment data.

All four models are built using data rejection of five standard deviations. This is reasonable, at least for the models constructed using the L_1 norm that is less sensitive to outliers, and is less rejection than the 99% confidence interval criteria used by Korte et al. (2011). Our models therefore make use of more of the original data set. The average number of rejected data from the lake sediment record for the three components is very small (0.4%), while for the archeomagnetic dataset, the percentages were 3% for the inclination, 2% for the intensity and surprisingly high percentage of declination data were rejected (45%). In general, 3.4% were rejected for all components from both types of data.

Table 6.1: Datasets used to construct the HFM models. Number of data in the initial and final datasets, using a 5 standard deviation rejection criteria are reported.

Model	Dataset	D/rel. D	I	F/RPI	Sum	Total
	Archeomagnetic	3612	5097	4121	12,830	86,802
	Sediment	30,639	31,955	11,378	73,972	
HFM-BL1	Archeomagnetic	1976	4952	4023	10,951	84,407
	Sediment	30,427	31,699	11,330	73,456	
HFM-OL1	Archeomagnetic	1976	4952	4026	10,954	84,572
	Sediment	30,502	31,786	11,330	73,618	
HFM-OL2	Archeomagnetic	1969	4905	3990	10,864	83,873
	Sediment	30,324	31,339	11,346	73,009	
HFM-EL1	Archeomagnetic	1977	4965	4037	10,979	84,683
	Sediment	30,524	31,837	11,343	73,704	

6.3 Data kernels describing sensitivity to the CMB field

The quality of the CMB field models is ultimately limited by geographical distribution and the different types of available data. To examine how a given dataset is sensitive to the CMB field, one may calculate appropriate data kernels (e.g., Gubbins and Roberts, 1983; Bloxham et al., 1989; Johnson and Constable, 1997). The magnetic field at the Earth's surface can be expressed in terms of the radial component of geomagnetic field at the core-mantle boundary $B_r(\hat{s})$ as follows

$$B(r) = \int_S G(r|\hat{s}) B_r(\hat{s}) d^2\hat{s} \tag{6.1}$$

where $G(r|\hat{s})$ is an appropriate Green's function, S is the CMB, and $\hat{s}$ is a unit vector ranging over the CMB. Its components describe how $B_r(\hat{s})$ influences the geomagnetic field elements measured at the Earth's surface. The relationship between the X, Y and Z field components and $B_r(\hat{s})$ is linear with the relevant Green's functions being

$$G_X = -\frac{\left(1 + 2R - \rho^2\right)}{R^3 T} \rho^3 \hat{s} \cdot \hat{x} \tag{6.2}$$

$$G_Y = -\frac{\left(1 + 2R - \rho^2\right)}{R^3 T} \rho^3 \hat{s} \cdot \hat{y} \tag{6.3}$$

$$G_Z = \rho^2 - \frac{\rho^2 \left(1 - \rho^2\right)}{R^3 T} \tag{6.4}$$

where $\rho = c/r$, $R = \sqrt{1 - 2\mu\rho + \rho^2}$, $\mu = \hat{r} \cdot \hat{s}$, $T = 1 + R - \mu\rho$, $\hat{r}$ is a unit vector in the direction of the measurement point, and c is the radius of the CMB. A detailed derivation of the Green's function for surface magnetic field from radial CMB field is given by Constable et al. (1993). The Z component of the field is most sensitive directly above the the source, while X and Y sensitivities are maximum at 23° away from the source. The other components of the field D, I, and F, most often measured in paleomagnetic studies, are related nonlinearly to $B_r(\hat{s})$, and the following versions of the kernels, linearized about the axial dipole field, are usually employed to study their sensitivity (Johnson and Constable, 1997):

$$G_D = \frac{1}{X^2 + Y^2} \left[X G_Y - Y G_X \right] \tag{6.5}$$

$$G_I = \frac{1}{H^2 + Z^2} \left[H G_Z - \frac{Z}{H} \left(X G_X + Y G_Y \right) \right] \tag{6.6}$$

$$G_F = \frac{1}{F} \left[X G_X + Y G_Y + Z G_Z \right] \tag{6.7}$$

Linearized data kernels for one observation of declination, inclination and intensity at the location of Lake Soppen, Switzerland are illustrated in Fig. 6.1. The kernels of inclination and intensity show that the models built with only inclination or intensity data are not influenced by $B_r(\hat{s})$ far from the measurement locations and are not sensitive to $B_r(\hat{s})$ at high latitudes. In

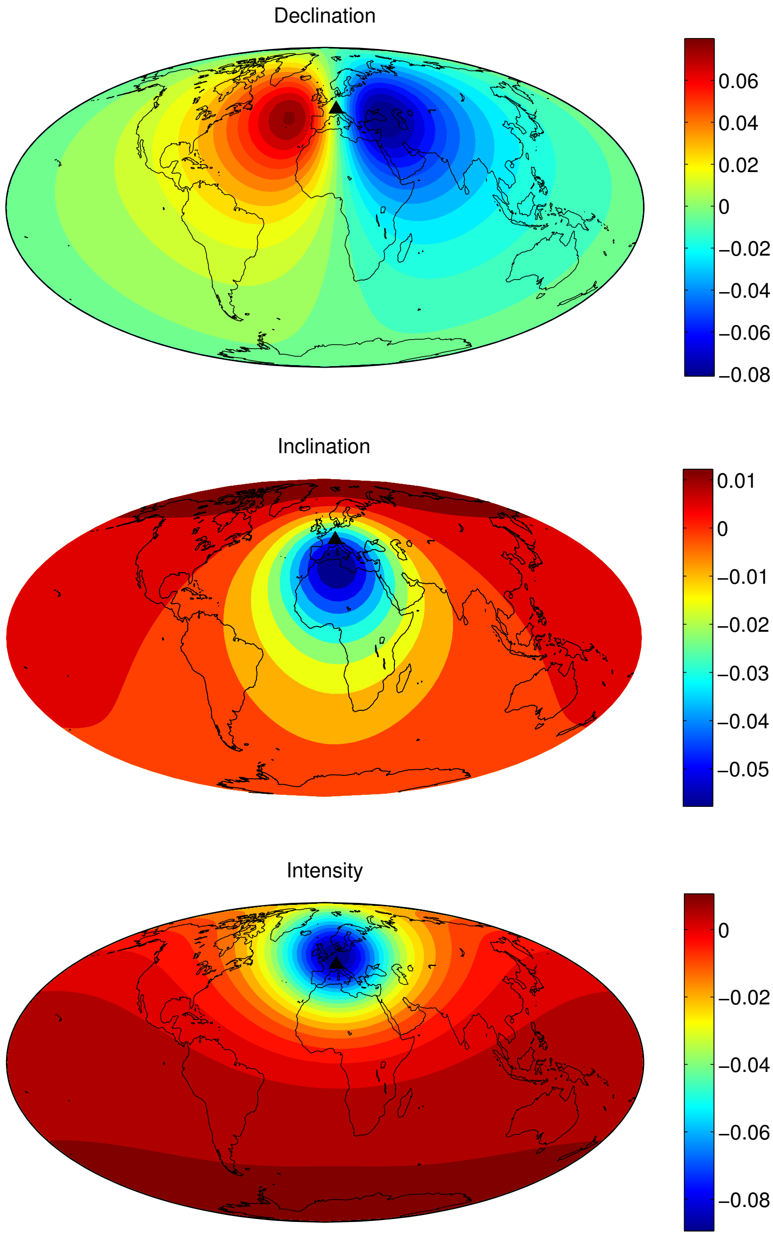

Figure 6.1: Linearized kernels, showing the sampling of the radial field at the CMB for one observation of declination, inclination and intensity at the location of Lake Soppen, Switzerland with latitude 47.09° and longitude 8.08° on Earth's surface (black triangle). Declination observations provide the best longitudinal coverage; inclination samples B_r at the CMB at lower latitudes than the observation site, while intensity samples higher latitudes than the observation site.

contrast, the declination kernel involves contributions from a broader area of CMB, and has low sensitivity directly beneath the sampling site.

It is also possible to look at a combined sensitivity kernel from all data in the compilation from which field models are constructed (e.g., Korte and Constable, 2011; Korte et al., 2011). If more than one site is considered, then absolute values of the kernels can be summed to obtain the following sampling function

$$S(\hat{s}) = \sum_{i}^{N_D} |G_{D(r_i|\hat{s})}| + \sum_{i}^{N_I} |G_{I(r_i|\hat{s})}| + \sum_{i}^{N_F} |G_{F(r_i|\hat{s})}| \tag{6.8}$$

where $G_{D(r_i|\hat{s})}$,$G_{I(r_i|\hat{s})}$ and $G_{F(r_i|\hat{s})}$ are the data kernels for declination (N_D data points), inclination (N_I data points) and intensity (N_F data points) at all locations. The summed absolute linearized data kernels describing the resulting sampling of the CMB are presented in the Fig. 6.2 taking into account the whole dataset. These functions show how Holocene observations of the geomagnetic field at the Earth's surface are sensitive to the CMB field. The maximum values of the combined kernels occur at northern mid- latitudes due to the highest concentration of the observations in the Northern hemisphere. The Southern hemisphere is however very poorly sampled, especially if only directional data are considered. Notsurprisingly, considering all three field components gives the best coverage of the CMB field. The coverage of the CMB field described here should be borne in mind as an important caveat when the results of the field models constructed below are interpreted.

6.4 Field modelling methodology

6.4.1 Forward modelling and parametrization

As discussed in Chapter 1, the solution of the forward problem of geomagnetic field modelling may be expressed in terms of spherical harmonics as

$$V(r,\theta,\varphi) = a \sum_{l=1}^{L} \sum_{m=0}^{l} \left(\frac{a}{r}\right)^{l+1} [g_l^m \cos\ m\varphi + h_l^m \sin\ m\varphi]\, P_l^m(\theta) \tag{6.9}$$

where $a = 6371.2$ km is the Earth's mean radius, r, θ, φ are the geocentric spherical coordinates, radius, colatitude and longitude, and P_l^m are the Schmidt quasi-normalized associated Legendre functions of degree l and order m (e.g., Chapman and Bartels, 1940; Langel, 1987). In the models presented here we use a maximum degree of $L = 10$.

Modelling of the temporal evolution of the geomagnetic field requires a further expansion of the Gauss coefficients g_l^m and h_l^m in time. For this purpose, a cubic B-splines basis is adopted

$$g_l^m(t) = \sum_{k}^{N_{spl}} g_l^{mk} B_k(t) \tag{6.10}$$

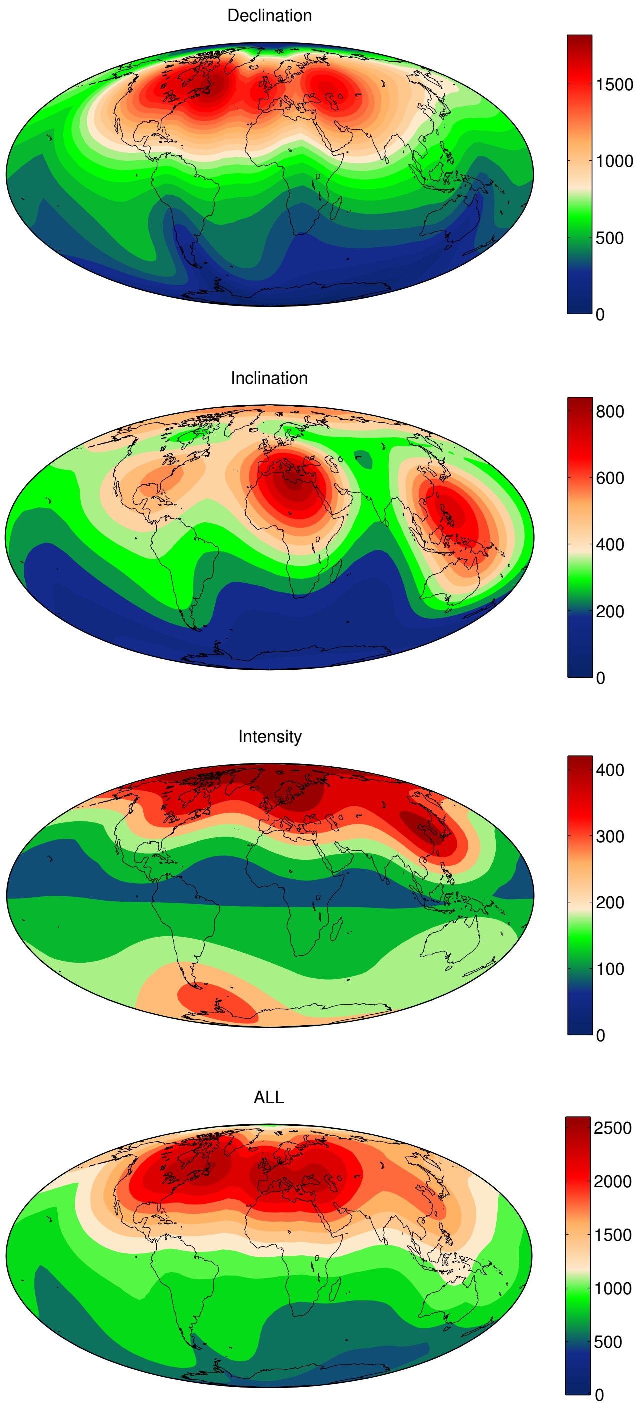

Figure 6.2: Linearized data kernels for the sampling of the CMB field by the global compilation of Holocene sediment and archeomagnetic records. Sampling of the CMB achieved by only declination, inclination, intensity, and sum of all three components. Kernels for declination and inclination are not scaled by horizontal and vertical field intensity.

The time-dependent Gauss coefficients are thus linear combinations of the spline coefficients and the piecewise polynomial functions $B_k(t)$ of order 4 and degree 3. Further properties of cubic B-splines have been described earlier in Section 3.3.1. The spline knot points are here chosen to be equally spaced with knot spacing of 40 years - this is the same spacing as is used by Korte et al. (2011) and much shorter than the expected temporal resolution of the model. In total 301 internal points spanning the time interval from 10,010 BC to 1990 AD are used. Three additional knot points at each end of the time interval give a total number of 307 knot points. The model is considered valid only for the past 10 kyrs, with the first 2000 years (10,010 BC to 8000 BC) included in an attempt to mitigate undesirable spline endpoint effects. No further endpoint constraints are applied to the models, in contrast to the CALSK10k models which are forced to agree with *gufm1* model in the recent epoch.

6.4.2 Inversion procedure

Finding the time-dependent field model coefficients from Holocene magnetic data is an example of a nonlinear inverse problem (e.g., Parker, 1994; Gubbins, 2004). The relation between the observed data $\mathbf{d}$ and model parameters $\mathbf{m}$ may be expressed in vector notation as

$$\mathbf{d} = f(\mathbf{m}) + \mathbf{e} \tag{6.11}$$

where f is the non-linear functional relating the data vector and the model vector, and $\mathbf{e}$ is a vector of the differences between the model predictions and the observations. The solution to such an inverse problem involving noisy observations is generally non-unique (Parker, 1994). It is, however, possible to find a suitable solution by minimization of an objective functional $\Phi(\mathbf{m})$ containing two terms, the first $Q(\mathbf{m})$ that corresponds to some measure of the misfit between the observations and the model predictions $(\mathbf{d} - f(\mathbf{m}))$, and the second $R(\mathbf{m})$ that measures the complexity of the model (e.g., Shure et al., 1982; Gubbins and Bloxham, 1985; Gubbins, 2004):

$$\Phi(\mathbf{m}) = Q(\mathbf{m}) + R(\mathbf{m}) \tag{6.12}$$

Two choices for the measure of misfits between the model predictions and the measured data can be considered, respectively the L_2 measure of misfit:

$$Q_2(\mathbf{m}) = \sqrt{\frac{1}{N}\sum_{i=1}^{N}\left[\frac{d_i - f(\mathbf{m})_i}{\sigma_i}\right]^2} \tag{6.13}$$

and the L_1 measure of misfit (Bard, 1974; Walker and Jackson, 2000)

$$Q_1(\mathbf{m}) = \frac{\sqrt{2}}{N}\sum_{i=1}^{N}\left|\frac{d_i - f(\mathbf{m})_i}{\sigma_i}\right| \tag{6.14}$$

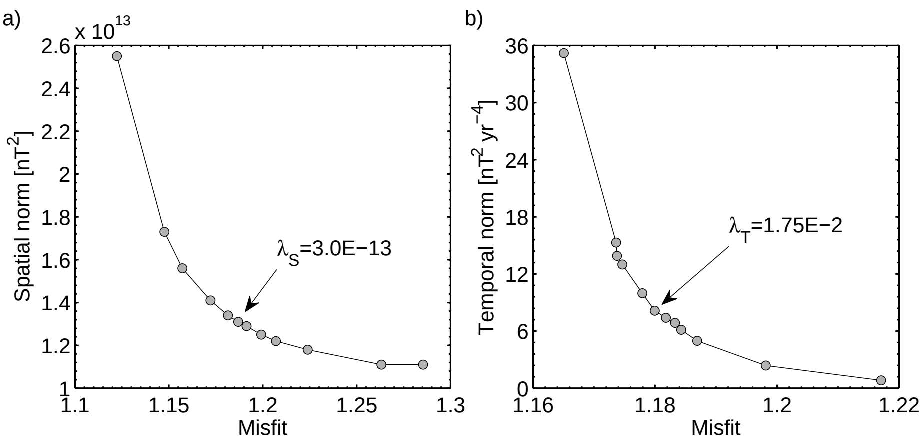

Figure 6.3: Trade-off curves used to select the spatial (λ_S) and temporal (λ_T) damping parameter for the model HFM-OL1. (a) Spatial Ohmic heating norm (R_S^O) vs. normalized misfit (L_1-norm measure); (b) Temporal norm (R_T) vs. normalized misfit (L_1-norm measure).

were σ_i are the a priori estimated errors on the data, derived in Chapter 3, and N is the total number of data. Use of the L_1 measure of misfits has proved useful in a number of geophysical applications as it is found to be less sensitive to the influence of outliers and yields more stable model estimates (e.g., Claerbout and Muir, 1973; Scales et al., 1988; Farquharson and Oldenburg, 1998; Tarantola, 2005). The L_1 norm measure of misfit has also previously been successfully employed in geomagnetic field modelling (Walker and Jackson, 2000; Lesur et al., 2008; Pavón-Carrasco et al., 2009; Finlay et al., 2012), but it has not previously been employed in the construction of global field models on millennial time scales. Here, the L_1 norm is implemented via the technique of iteratively reweighted least squares (IRLS) (e.g., Schlossmacher, 1973; Constable, 1988; Farquharson and Oldenburg, 1998; Walker and Jackson, 2000).

Measures of the spatial and temporal complexity of the model were combined in the regularization term of the Eq. 6.12. This can be expanded as

$$R(\mathbf{m}) = \lambda_S R_S(\mathbf{m}) + \lambda_T R_T(\mathbf{m}) \tag{6.15}$$

λ_S and λ_T are damping parameter which describes the trade-off between the misfit and the norms measuring the complexity of the model. These parameters are chosen on the basis of a trade-off curve (e.g., Gubbins, 2004). Fig. 6.3 gives an example of trade-off curves from the present study. Large values of damping parameters put more emphasis on model smoothness, while smaller values promote a better fit to the data. Various choices of regularization norm in time and space have been explored by different authors. For example, the ohmic heating (dissipation) norm (Gubbins and Bloxham, 1985; Bloxham and

Jackson, 1992; Jackson et al., 2000; Korte and Constable, 2005a; Korte et al., 2011), a B_r^2 norm (Shure et al., 1982; Jackson et al., 2007; Korte and Holme, 2010; Finlay et al., 2012), and the entropy norm (Jackson et al., 2007; Gillet et al., 2007; Finlay et al., 2012) have been explored with regard to the spatial norm. Further details of the choices explore here are given in Section 6.4.3.

To measure the temporal complexity of the model we follow Bloxham and Jackson (1992), Jackson et al. (2000) and Korte and Constable (2005a) and adopt a norm based on the second time derivative of the radial magnetic field integrated over the CMB and over the time span of the model:

$$R_T(\mathbf{m}) = \frac{1}{t_e - t_s} \int_{t_s}^{t_e} \int_{CMB} \left(\frac{\partial^2 B_r}{\partial t^2} \right)^2 d\Omega dt \tag{6.16}$$

where t_s is the model's start time, t_e is the model's end time and the integration is over the CMB. This choice is optimal if one wishes to reconstruct a smoothly varying function using a cubic spline basis (e.g., De Boor, 2001).

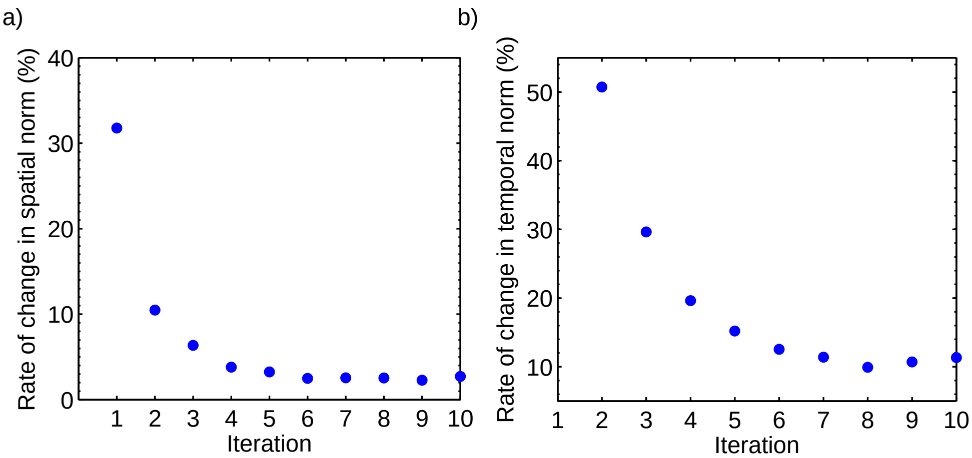

Figure 6.4: Rate of change in a) spatial (Ohmic heating norm) and b) temporal norm with iterations for the model HFM-OL1.

We carry out the minimization of the objective function (6.12), using an iterative a Newton type iteration algorithm (e.g., Gubbins and Bloxham, 1985; Tarantola, 2005). This algorithm requires knowledge of the Fréchet derivatives at the current model iterate $\mathbf{m}_i$ for the observed field elements

$$\mathbf{A} = \left. \frac{\partial \mathbf{f}(m)}{\partial \mathbf{m}} \right|_{\mathbf{m}=\mathbf{m}_i} \tag{6.17}$$

These derivatives are obtained by summing the derivatives of the observed field elements with respect to all model parameters. Following previous workers,

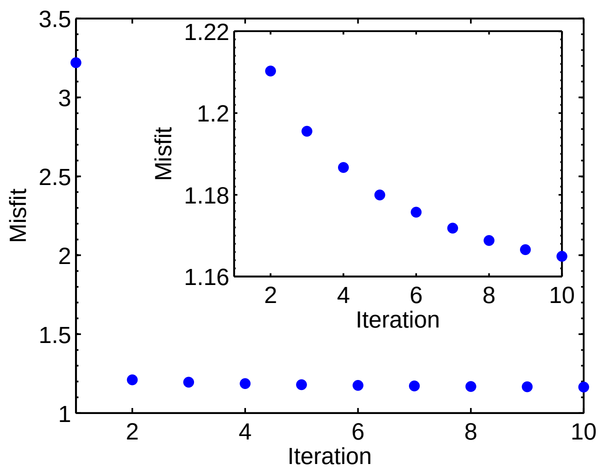

Figure 6.5: Convergence of the 1-norm measure of misfit for the model HFM-OL1.

the elements of the matrix **A** for the nonlinear geomagnetic components are derived using the chain rule:

$$dH = \frac{1}{H}(XdX + YdY) \tag{6.18}$$

$$dF = \frac{1}{F}(XdX + YdY + ZdZ) \tag{6.19}$$

$$dD = \frac{1}{X^2 + Y^2}(XdY - YdX) \tag{6.20}$$

$$dI = \frac{1}{X^2 + Y^2 + Z^2}(HdZ - ZdH) \tag{6.21}$$

To aid rapid convergence, the iterative model construction procedure is started from an initial model chosen to be CALS10k.1b (Korte et al., 2011) - a high quality field model covering the same time period. An example of convergence for model HFM-OL1 is present in Figs. 6.4 and 6.5. The rate of change in spatial and temporal norm is decreasing in the first 4-5 iterations and remains almost constant afterwards. After 10 iterations, the rate of change is below 3% in the spatial and around 11% in the temporal norm for the model HFM-OL1. The misfit is highest in the first iteration and it drops rapidly after the initial adjustment of calibration coefficients. In the case of HFM-OL1 (Fig. 6.5), the misfit continues to slightly decrease with further iterations. Again, when the inversion is performed using a cleaned dataset (5 sigma) and no data rejection, similar levels of convergence of the temporal and spatial norm changes are achieved as for the HFM models. Smaller misfits are however obtained due to the use of cleaned data. The presence of nearby incompatible data and certainly non-Gaussian errors may lead to problems in achieving better convergence of the norms.

6.4.3 Choice of spatial regularization

Quadratic regularization

In this chapter, three possible choices of norm measuring model spatial complexity are explored. The first is an approximation to the Ohmic dissipation norm on the CMB (Gubbins and Bloxham, 1985; Jackson et al., 2000):

$$\begin{aligned} R_S^O(\mathbf{m}) &= \int_{CMB} \frac{(\nabla \times \mathbf{B})^2}{\mu_0} dV \\ &= 4\pi \sum_{l=1}^{L} \left(\frac{a}{c}\right)^{2l+4} \frac{(l+1)(2l+1)(2l+3)}{l} \sum_{m=0}^{l} \left[(g_l^m)^2 + (h_l^m)^2\right] \end{aligned}$$

where μ_0 is magnetic permeability and $a = 6371.2$ km and $c = 3485$ km are the mean radius of the Earth and the radius of the CMB, respectively. The second is the integrated square of the radial field at the CMB:

$$\begin{aligned} R_S^B(\mathbf{m}) &= \int_{CMB} B_r^2 d\Omega \\ &= 4\pi \sum_{l=1}^{L} \left(\frac{a}{c}\right)^{2l+4} \frac{(l+1)^2}{(2l+1)} \sum_{m=0}^{l} \left[(g_l^m)^2 + (h_l^m)^2\right] \end{aligned}$$

Maximum entropy regularization

Maximum entropy regularization in space is also implemented for the first time in the context of millennial time scale field modelling. In contrast to the above quadratic norms that tend to penalize high field amplitudes or gradients, the maximum entropy technique permits a stable recovery of sharper field gradients, even in the presence of noisy or incomplete data (Gull and Daniell, 1978; Jackson et al., 2007). The information entropy S^* of a positive function m is defined as (e.g., Sivia and Skilling, 2006)

$$S^*[m, d_S] = \int_\Omega \left\{ m - d_S - m \ln\left[\frac{m}{d_S}\right] \right\} d\Omega \tag{6.22}$$

where Ω is a domain space and d_S is the default value of the model that is expected when no further constraints are available. The concept of information entropy has also been extended to the case of discrete functions that can take both positive and negative values (Gull and Skilling, 1990; Hobson and Lasenby, 1998). Here, we follow Gillet et al. (2007) and define the following quantity known as the negentropy S

$$S[m, d_S] = -4d_S \sum_{i=1}^{C} \left\{ \psi_i - 2d_S - m_i \ln\left[\frac{\psi_i + m_i}{2d_S}\right] \right\} \tag{6.23}$$

where $\psi_i = \sqrt{m_i^2 + 4d_S^2}$. Calculation of the negentropy associated with a field model is carried out in physical space using a spherical triangle tesselation (STT) (cf. Constable et al., 1993). The STT grid used here consists of 3242 nodes and 6480 cells (spherical triangles), and C in (6.23) denotes the number of cells. m_i is the radial magnetic field in the cells and it is linear function of the Gauss coefficients. The spatial norm derived from entropy considerations can therefore be written as

$$R_S^E(\mathbf{m}, d_S) = (\mathbf{m}, d_S) = \frac{-4d_S}{(t_e - t_s)} \int_{t_s}^{t_e} S\left[B_r(t), d_S\right] dt \qquad (6.24)$$

Further details of the implementation of entropy regularization for field modelling may be found in Jackson (2003); Jackson et al. (2007) and Gillet et al. (2007). Inversions have been carried out here for a range of values of the default parameter d_S, further details are presented in the Appendix B.

Insufficient data in the early part of the Holocene is found to result in an underestimation of the field intensity at these times if the entire field at the core surface is spatially regularized. In order to mitigate this effect, we follow Korte et al. (2009) and exclude the dipole term ($l = 1$, $m = 0, 1$) from the spatial and temporal regularizations both for the quadratic and the entropy choices of norm.

6.4.4 Implementation of relative paleointensity and relative declination observations in field modelling

Two of the three components derived from the sediment records are available only in relative form. Relative declination and paleointensity are related to absolute observations through a multiplication by a scaling factor (γ_F) for the relative paleointensity and addition of a constant (γ_D) for the relative declination for each record:

$$F_i(\theta, \varphi, r, t) = \gamma_F \cdot F_i^{rel}(\theta, \varphi, r, t) \qquad (6.25)$$

and

$$D_i(\theta, \varphi, r, t) = \gamma_D + D_i^{rel}(\theta, \varphi, r, t) \qquad (6.26)$$

In previous studies (e.g., Korte and Constable, 2006) relative intensity has been calibrated before being used as absolute intensity, while relative declination is usually included assuming a zero mean. In this study, we consider $N_F = 29$ RPI and $N_D = 70$ relative declination records.

In order to handle relative intensity and declination directly we extend the model vector to include $N_F + N_D$ additional calibration parameters γ_F and γ_D, each corresponding to a different sediment record, that are solved for during the inversion. The total number of model parameters is now $N = N_{spl} \cdot L(L+2) + N_F + N_D$.

$$\mathbf{m} = \left\{ g_1^0(t), g_1^1(t), h_1^1(t), \ldots, h_{10}^{10}(t), \gamma_{F_1}, \gamma_{F_2}, \ldots, \gamma_{F_{N_F}}, \gamma_{D_1}, \gamma_{D_2}, \ldots, \gamma_{D_{N_D}} \right\}$$

Implementation of the relative model parameters requires a modification of the matrix of Fréchet derivatives **A** (Eq. 6.17), which now also includes derivatives with respect to γ_F and γ_D as follows:

$$\begin{aligned}
\mathbf{A}^{F_i^{rel}} &= \frac{\partial \mathbf{f}(m)}{\mathbf{m}} \\
&= \left(\frac{\partial F_i^{rel}}{\partial g_1^0(t)} \; \frac{\partial F_i^{rel}}{\partial g_1^1(t)} \; \frac{\partial F_i^{rel}}{\partial h_1^1(t)} \cdots \frac{\partial F_i^{rel}}{\partial \gamma_{F_1}} \; \frac{\partial F_i^{rel}}{\partial \gamma_{F_2}} \cdots \frac{\partial F_i^{rel}}{\partial \gamma_{F_i}} \cdots \frac{\partial F_i^{rel}}{\partial \gamma_{D_{N_D}}} \right) \\
&= \gamma_{F_i} \left(\frac{\partial F_i}{\partial g_1^0(t)} \; \frac{\partial F_i}{\partial g_1^1(t)} \; \frac{\partial F_i}{\partial h_1^1(t)} \; \ldots \; 0 \; 0 \; \ldots \; \frac{F_i}{\gamma_{F_i}} \; \ldots \; 0 \right)
\end{aligned}$$

for the relative intensity records, and

$$\begin{aligned}
\mathbf{A}^{D_i^{rel}} &= \frac{\partial \mathbf{f}(m)}{\mathbf{m}} \\
&= \left(\frac{\partial D_i^{rel}}{\partial g_1^0(t)} \; \frac{\partial D_i^{rel}}{\partial g_1^1(t)} \; \frac{\partial D_i^{rel}}{\partial h_1^1(t)} \cdots \frac{\partial D_i^{rel}}{\partial \gamma_{F_1}} \cdots \frac{\partial D_i^{rel}}{\partial \gamma_{D_1}} \cdots \frac{\partial D_i^{rel}}{\partial \gamma_{D_i}} \cdots \frac{\partial D_i^{rel}}{\partial \gamma_{D_{N_D}}} \right) \\
&= \left(\frac{\partial D_i}{\partial g_1^0(t)} \; \frac{\partial D_i}{\partial g_1^1(t)} \; \frac{\partial D_i}{\partial h_1^1(t)} \; \ldots \; 0 \; \ldots \; 0 \; \ldots \; 1 \; \ldots \; 0 \right)
\end{aligned}$$

for the relative declination records. Here i represents the ith observation which has associated scaling or shifting parameters γ_{F_i} or γ_{D_i} for RPI and relative declination measurements respectively. Initial values for the new model parameters were chosen by comparing the relative records with the predictions of the CALS10k.1b model.

6.5 Results of the Holocene field modelling

Four models that have been constructed, using the different strategies that are outlined above, are presented. Comparisons are also made to the only previously published time-dependent Holocene field model CALS10k.1b (Korte et al., 2011). We refer to our new models as HFM-*, where HFM stands for Holocene Field Model and * describes the choice of misfit and regularization norm. Model HFM-BL1 uses an B_r^2 spatial norm and an L_1 measure of misfit, model HFM-OL1 uses the Ohmic heating norm and and L_1 norm measure of misfit, HMF-OL2 also uses and Ohmic heating spatial norm, but a L_2 measure of misfit, while HFM-EL1 uses entropy spatial regularization and an L_1 misfit measure. All models use the same second time derivative temporal norm as described in the previous section.

In order to find converged solutions, the first two iterations are always performed using the whole dataset due to the need to adjust the initial calibration coefficients. As a result of iterative scheme of data rejection, the final models are constrained by different numbers of data points (see Table 6.1).

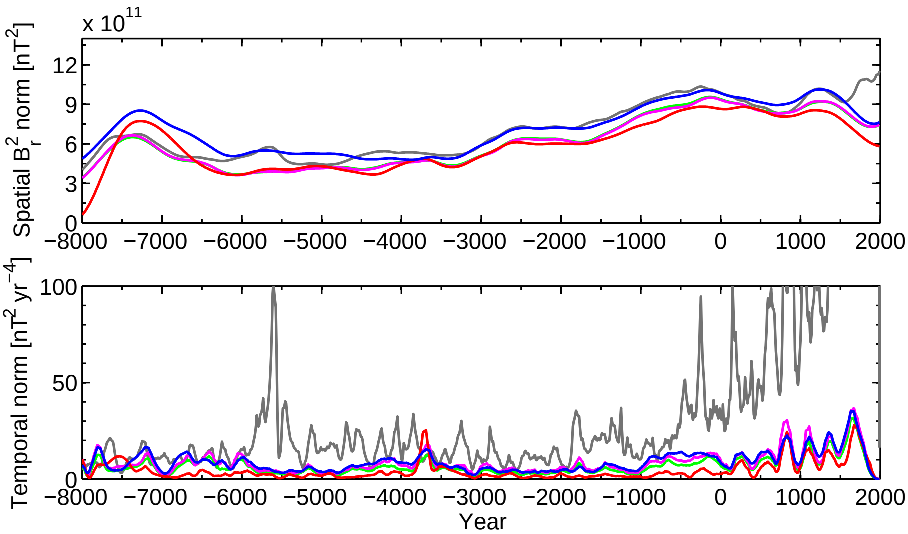

Figure 6.6: Comparison of the evolution of the spatial and temporal norms for all models. Models HFM-BL1 (green line), HFM-OL1 (pink line), HFM-OL2 (red line), HFM-EL1 (blue line) along with CALS10k.1b (grey line) are shown. Note that the vertical axis for the temporal norm is truncated at 100 $\mathrm{nT}^2\mathrm{yr}^{-4}$. The CALS10k.1b temporal norm grows up to the values of order of 10^5 for the most recent 400 years.

Trade-off curves to chose the damping parameters λ_s and λ_t are created with five iterations, while the final models are obtained after 10 iteration in order to achieve better convergence. Only the model based on L_2 measure of misfit HFM-OL2 does not converge well using this scheme, and higher damping parameters are required in this case in order to obtain a sensible model. The number of data used in the first two iterations (without rejection) and those used to produce the final models are listed in Table 6.1. In general about 3% of the data were rejected in the final models, with the maximum rejection for the HFM-OL2 and minimum for the HFM-EL1 model.

Table 6.2 presents the norms and misfits to the data of the new models and CALS10k.1b for comparison. Model HFM-EL1 has the smallest misfit and the highest spatial and temporal norm because the entropy norm allows higher amplitude, sharper, field structures. The time evolution of both the spatial B_r^2 and temporal norms are illustrated in Fig. 6.6. Overall, all models follow similar trend. The spatial norms show a general increase toward recent times which is likely due to increasing the number of data and better dating. This is also true for the temporal norm with one unexpected peak at around 3500 BC. Model HFM-OL2 exhibits the highest peak in its temporal norm at this time.

Spherical harmonic spectra at the CMB (cf. Lowes, 1974) are also pre-

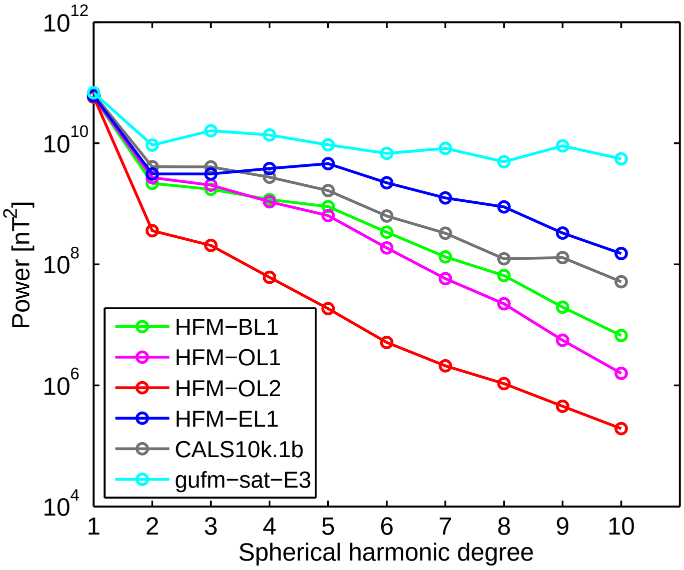

Figure 6.7: Comparison of the spherical harmonic spectra at the CMB for all models. Models HFM-BL1 (green line), HFM-OL1 (pink line), HFM-OL2 (red line), HFM-EL1 (blue line) along with CALS10k.1b (grey line) and *gufm-sat-E3* up to degree 10 (cyan line) are shown.

sented for comparison in Fig. 6.7. All spectra exhibit similar slopes above degree 4. But the quadratic regularized models decay faster between degrees 2 and 4 than entropy model HFM-EL1. HFM-OL1 and HFM-BL1 agree well up to degree 5 while the most rapid spectral decay is observed for the model HFM-OL2, which had to be damped more heavily in order to obtain satisfactory convergence. The spectrum for the model *gufm-sat-E3* (Finlay et al., 2012), constrained by satellite and observatory observations between 2000.0 to 2010.0 is also shown for reference. It exhibits a flatter power spectra up to degree 10. Except for HFM-OL2, all the HFM models possess spectra that agree well up to degree 2 with CALS10k1.b while they only approximately agree with *gufm-sat-E3* for degree 1. The entropy model HFM-EL1 does not show as rapid spectral decay as the other models, even an approximately constant power spectra is obtained for degrees 2 up 5 with the highest power (apart from the dipole term) in degree 5. In contrast, the highest power in the present day spectra from the model *gufm-sat-E3* is seen in degree 3 with less power in degree 5. The CALS10k.1b power spectrum shows slope similar to the models HFM-OL1, HFM-BL1 and HFM-EL1, with its power lying between the models HFM-EL1 and HFM-BL1.

Examples of the HFM models fits to the lake sediment data are given in Fig. 6.8, together with the CALS10k.1b model predictions and the robust spline

Table 6.2: Statistics of Holocene field models HFM derived in this thesis. The square of the second time derivative of the radial magnetic field integrated over the CMB and over time was used as the temporal regularization norm for all four models (Eq. 6.16). Spatial norm is calculated using the equation for the B_r^2 norm. The HFM-BL1 model has $\lambda_S = 1.25 \cdot 10^{-11} nT^{-2}$ and $\lambda_T = 2.4 \cdot 10^{-2} nT^{-2} yr^4$. Model HFM-OL1 model involves spatial regularization with $\lambda_S = 3.0 \cdot 10^{-13} nT^{-2}$ and temporal regularization with $\lambda_T = 1.75 \cdot 10^{-2} nT^{-2} yr^4$. The HFM-OL2 model has $\lambda_S = 3.15 \cdot 10^{-12} nT^{-2}$ and $\lambda_T = 2.25 \cdot 10^{-2} nT^{-2} yr^4$. The entropy model HFM-EL1 is constructed with default parameter $d_S = 9 \cdot 10^3 \mu T$, and the same spatial and temporal damping parameters as for the model HFM-BL1.

Model	Norm	Spatial regularization	Spatial B_r^2 norm $[nT^2]$	Temporal norm $[nT^2 yr^{-4}]$	Misfit (L_1) (normalized)
HFM-BL1	L_1	B_r^2	$5.30 \cdot 10^{11}$	6.15	1.17
HFM-OL1	L_1	Ohmic	$5.34 \cdot 10^{11}$	8.19	1.16
HFM-OL2	L_2	Ohmic	$4.96 \cdot 10^{11}$	4.80	1.29
HFM-EL1	L_1	Entropy	$6.44 \cdot 10^{11}$	8.26	1.13
CALS10k.1b	L_2	Ohmic	$6.39 \cdot 10^{11}$	$9.26 \cdot 10^2$	1.31

models for each record derived in Chapter 3. The noticeable differences in the recent 400 years are due to an additional constraint that has been applied to the CALS10k.1 model, forcing it to match the historical field model *gufm1*. Model HFM-OL2 shows variations which are not present in other models, probably because this model is still not sufficiently resolved, despite the large damping applied. Although in the first example, the Eifel Maars, Germany (Fig. 6.8a), all models along with the CALS10k.1b show good agreement with the predictions, at Lake Waiau, Hawaii (Fig. 6.8b), some offsets are observed in the predictions, especially in the inclination. The CALS10k.1b model predicted consistently lower inclination for the period from 8000 BC to 2500 BC, while the HFM models (except the HFM-OL2) better fit the data with higher mean inclination. For this particular record, inclination data have a mean of 27° which is lower than the GAD expectation for this location of 35° (Peng and King, 1992). Another approach to analysing the fit of the models to the data is to plot histograms of the residuals. Such a histograms are presented in Fig. 6.9 taking HFM-OL1 model as an example. Note that the distributions for all components and both archeomagnetic and lake sediment data are generally Laplacian.

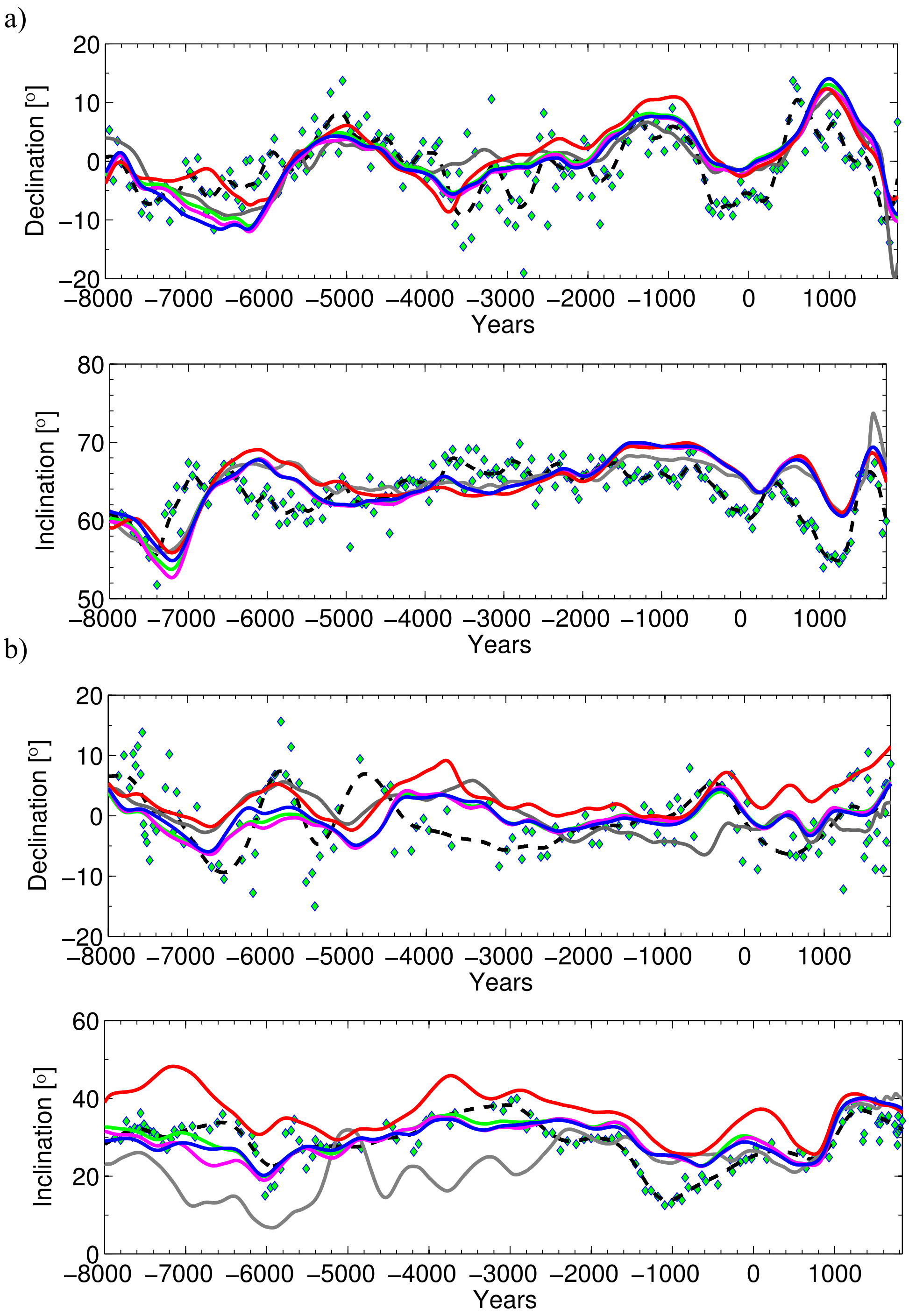

Figure 6.8: Example comparison of field model predictions: HFM-BL1 (green line), HFM-OL1 (pink line), HFM-OL2 (red line), and HFM-EL1 (blue line) with calibrated declination and inclination data of (a) Eifel Maars, Germany (Stockhausen, 1998) and (b) Lake Waiau, Hawaii (Peng and King, 1992). Lake sediment data are shown with green diamonds. The CALS10k.1b model (grey line) and the robust smoothing spline fit (dashed black line) are plotted for reference.

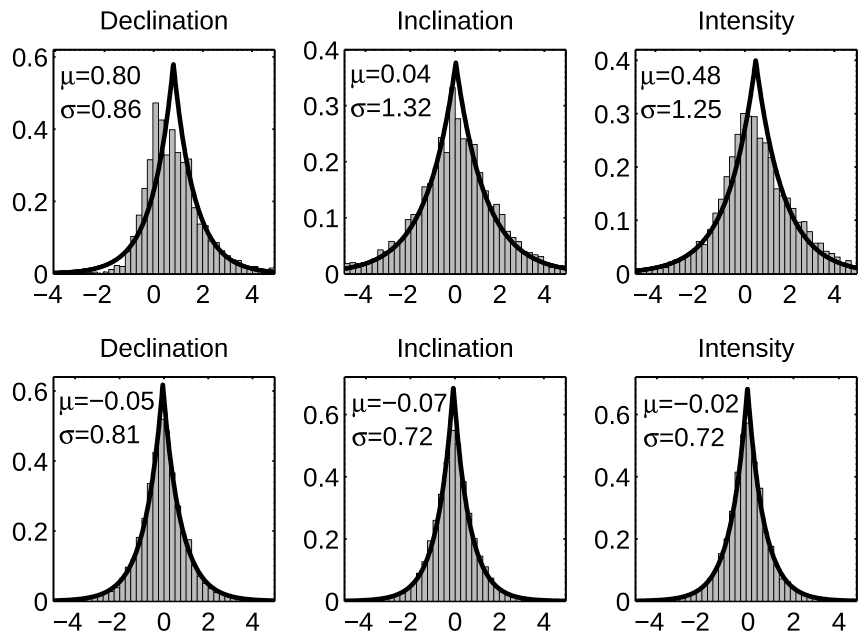

Figure 6.9: Example of histogram of normalised residuals between the HFM-OL1 model predictions and archeomagnetic data (upper panel) and lake sediment data (bottom panel). Histograms are normalized to unit area and a Laplacian distribution (black line) with mean (μ) and deviation (σ) calculated from the residuals is shown $\left[f(x) = \frac{1}{\sigma\sqrt{2}} exp\left(-\sqrt{2}\frac{|x-\mu|}{\sigma}\right)\right]$.

Maps of residuals as a function of location for declination, inclination and intensity from the HFM-OL1 model are given in Fig. D.3. Similar plots for the other three models are available in Appendix D. Declination high latitude records are shown to be less well fitted by the models. Inclination record from Lake Soppen (SoI) has the highest misfit to the models predictions due to shallower inclination values observed in this record (see Section 5.2), while the calibration of $SoII$ relative paleointensity record exhibited maximal values which have not been reached by the models.

Figs. 6.11 and 6.12 show a comparison of the evolution of the dipole and quadrupole coefficients for the HFM field models and CALS10k.1b. Due to the the fact that CALS10k.1b is forced to agree with the *gufm1* model for the most recent 400 years, and only from 1840 to 1990 for the axial dipole component, there is as expected a difference in this recent period with CALS10k.1b showing more temporal and spatial complexity than in HFM-BL1, HFM-OL1, and HFM-EL1 models. These differences are also visible in snapshots of the CMB field for the epoch 1990 AD presented in Fig. 6.15. Apart from this, the HFM model coefficients possess largely similar trends as those of

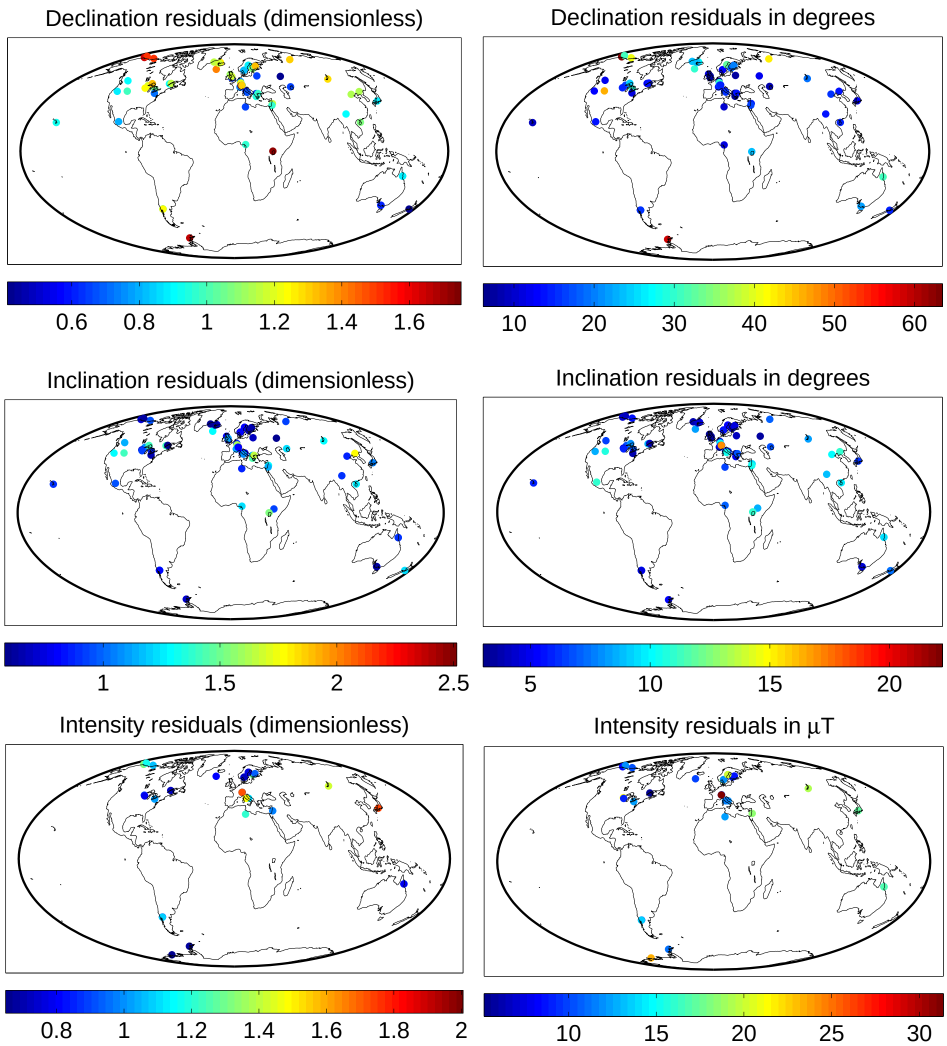

Figure 6.10: Map of residuals as a function of location from the HFM-OL1 model.

CALS10K.1b, although there is more consistency amongst the HFM models (except for HFM-OL2) than between them and CALS10k.1b. Overall, the dipole and quadrupole coefficients for all models fall within the error bars of the CALS10k.1b coefficients that are obtained by bootstrap sampling. The largest differences are a consistently higher axial dipole g_1^0 and a consistently lower g_2^2 coefficient in the HFM-L1 models.

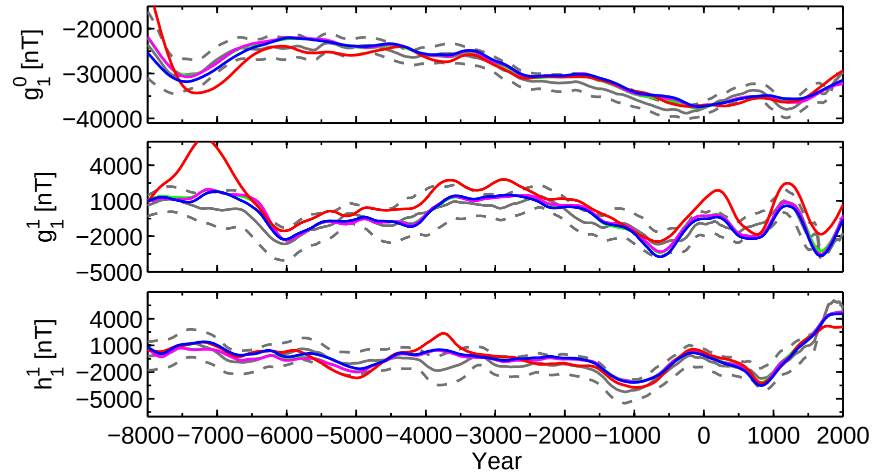

Figure 6.11: Evolution of dipole coefficients of the models HFM-BL1 (green line), HFM-OL1 (pink line), HFM-OL2 (red line), HFM-EL1 (blue line) along with CALS10k.1b (grey line). Dashed lines are bootstrap uncertainty estimates for the CALS10k.1b coefficients. Note that some lines overlap.

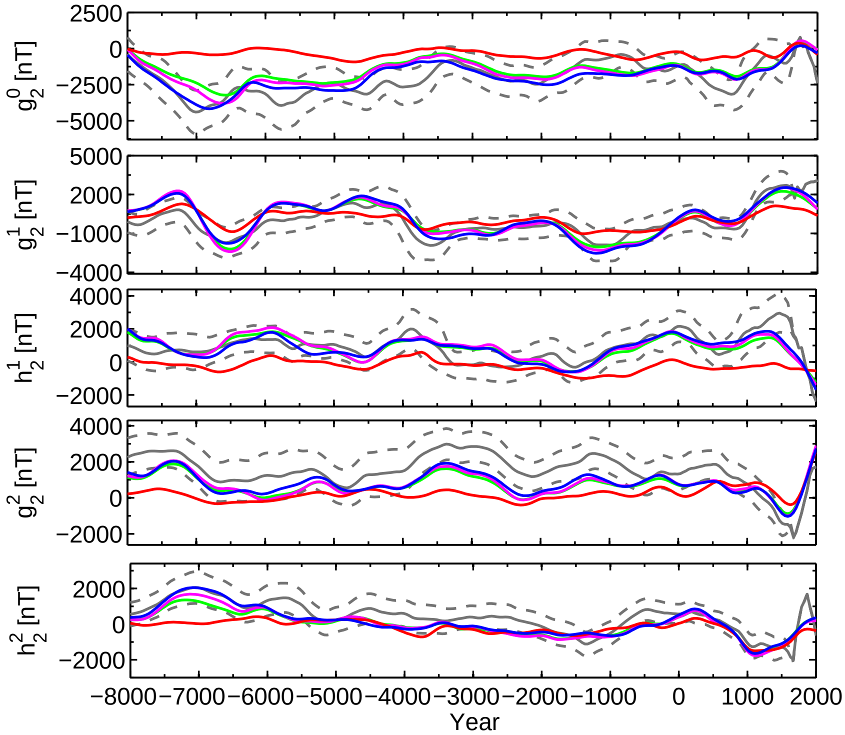

Figure 6.12: Evolution of quadrupole coefficients. An explanation of the labels is given in Fig. 6.11

6.5.1 Dipole moment evolution

The evolution of the geomagnetic dipole moment has been studied in the past on various time scales using global harmonic models or virtual axial dipole estimates (e.g., Yang et al., 2000; Korte and Constable, 2005b; Olson and Amit, 2006; Constable, 2007b; Genevey et al., 2008; Ziegler et al., 2011). It is also possible to reconstruct the dipole moment from cosmogenic radionuclides (^{10}Be and ^{14}C) (e.g., Knudsen et al., 2008). The magnetic dipole moment M is calculated with the following formula involving the Gaussian coefficients for the degree 1:

$$M(t) = \frac{4\pi a^3}{\mu_0}\sqrt{\left(g_1^0(t)\right)^2 + \left(g_1^1(t)\right)^2 + \left(h_1^1(t)\right)^2} \tag{6.27}$$

where $\mu_0 = 4 \cdot 10^{-7} NA^{-2}$ is the magnetic permeability of free space.

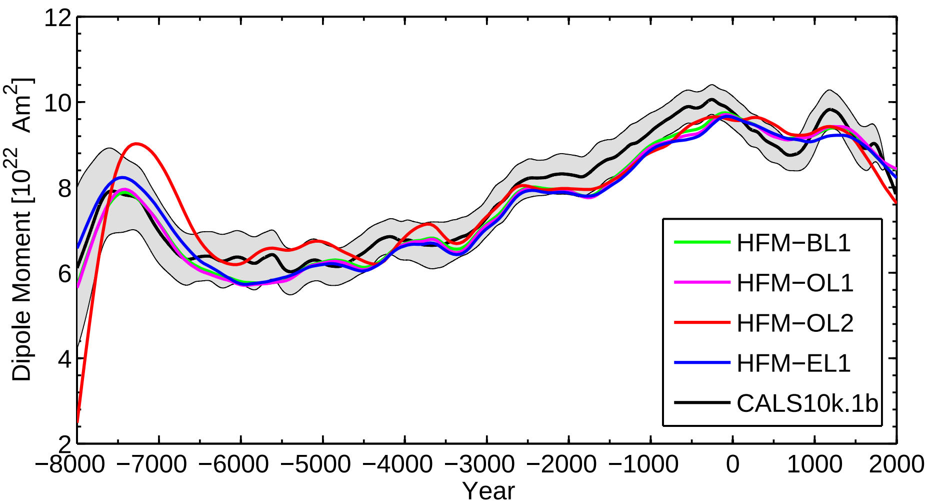

Figure 6.13: Evolution of the dipole moment for the models HFM-BL1 (green line), HFM-OL1 (pink line), HFM-OL2 (red line), HFM-EL1 (blue line) compared to the dipole moment from the CALS10k.1b model (black line). The grey area shows the error bounds of the CALS10k.1b dipole moment obtained by bootstrap sampling (Korte et al., 2011).

The dipole moment evolution for the models produced in this study are presented in Fig. 6.13. It is found that the dipole moment predicted by the entropy model HFM-EL1 is similar to the HFM-OL1 and HFM-BL1, with an exception of the first 2 kyrs where entropy model predicts a slightly higher moment than the quadratic ones. The HFM-OL2 will not be discussed further, due to its possible problems related to convergence. The other three HFM models follow the trend predicted by the CALS10k.1b but with lower amplitude variations during the recent 3 kyr and generally lower amplitude values before this time. HFM dipole moment estimates often fall within the bootstrap error bounds supplied with CALS10k.1b, which are designed to represent one standard deviation uncertainty estimates (Korte et al., 2011). The good agreement between the dipole moment estimates for the HFM with those for CALS10K.1b is reassuring, given that different model techniques have been used to construct the models. The average dipole moments of HFM-OL1 ($7.61 \cdot 10^{22} Am^2$) and HFM-EL1 model ($7.63 \cdot 10^{22} Am^2$) are also close to previously determined average values for the past 7 kyr ($7.4 \cdot 10^{22} Am^2$) (Korte and Constable, 2005b). For model HFM-OL1, the maximum value of the dipole moment ($9.71 \cdot 10^{22} Am^2$) is observed around 50 BC, whereas the minimum Holocene dipole moment ($5.72 \cdot 10^{22} Am^2$) is found at $\sim$ 6000 BC.

6.5.2 Field structure at the CMB: Time-average and patterns of evolution

Time-averaged geomagnetic field models (e.g, Johnson and Constable, 1995, 1997, 1998; Johnson and McFadden, 2007), provide information concerning the long-term structure and variability of the Earth's magnetic field. Recently, Korte and Holme (2010) tested the persistent structure of 7-kyr field model constrained by the time-averaged field models from *gufm1* and CALS3k.3. Their result showed that small-scale features appearing in the shorter time-average fields are not present in the long-time scale averages. Identification of persistent high intensity flux concentrations at the CMB are very important for understanding the geodynamo processes.

Fig. 6.14 shows the time-averaged radial magnetic field at the CMB from models compared to the CALS10k.1b model, while Fig. 6.15 presents snapshots of the same quantity at 2000 year intervals for models HFM-OL1, HFM-EL1 and CALS10k.1b. It is obvious that much of the higher degree features are averaged out when averages over 10 kyrs are considered. For the HFM-OL2 model, all non-dipolar influence is averaged out and the magnetic field is close to dipolar; this illustrates the effect of very strong damping in such models, as was applied in this case to try to aid convergence. Their is a pronounced difference between the quadratic regularized models, HFM-BL1 and HFM-OL1, and the entropy model HFM-EL1, with the northern hemisphere flux lobes (Canadian and Eurasian) more visible and separate in HFM-EL1. These two flux lobes along with one high intensity flux patch in the Southern Ocean are present for almost the entire Holocene. Distinct flux patches do not appear in the southern hemisphere of the HFM-OL1 model. For the time period from 7000 BC to 4000 BC, the southern hemisphere lobe is split up into two patches of lower intensity, because of the appearance of reverse flux under Antarctica. This feature is also present in the CALS10k.1b model but with lower intensity. In HFM-EL1, there is strong flux patch present south of South America that spreads out in the Indian Ocean and Australia and is of generally weaker intensity.

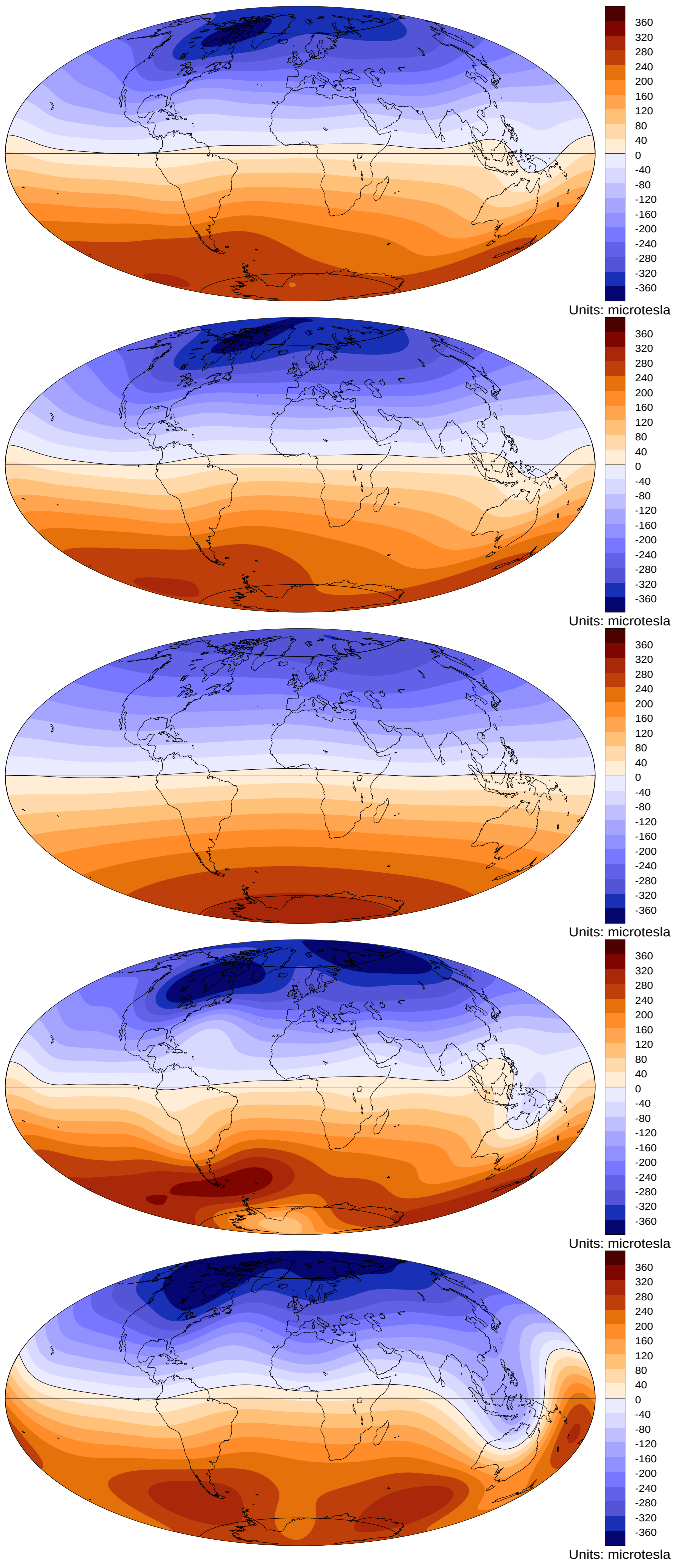

Figure 6.14: Time average of the models HFM-BL1, HFM-OL1, HFM-OL2, HFM-EL1, and CALS10k.1b (from up to down) for the radial component of the field at the CMB.

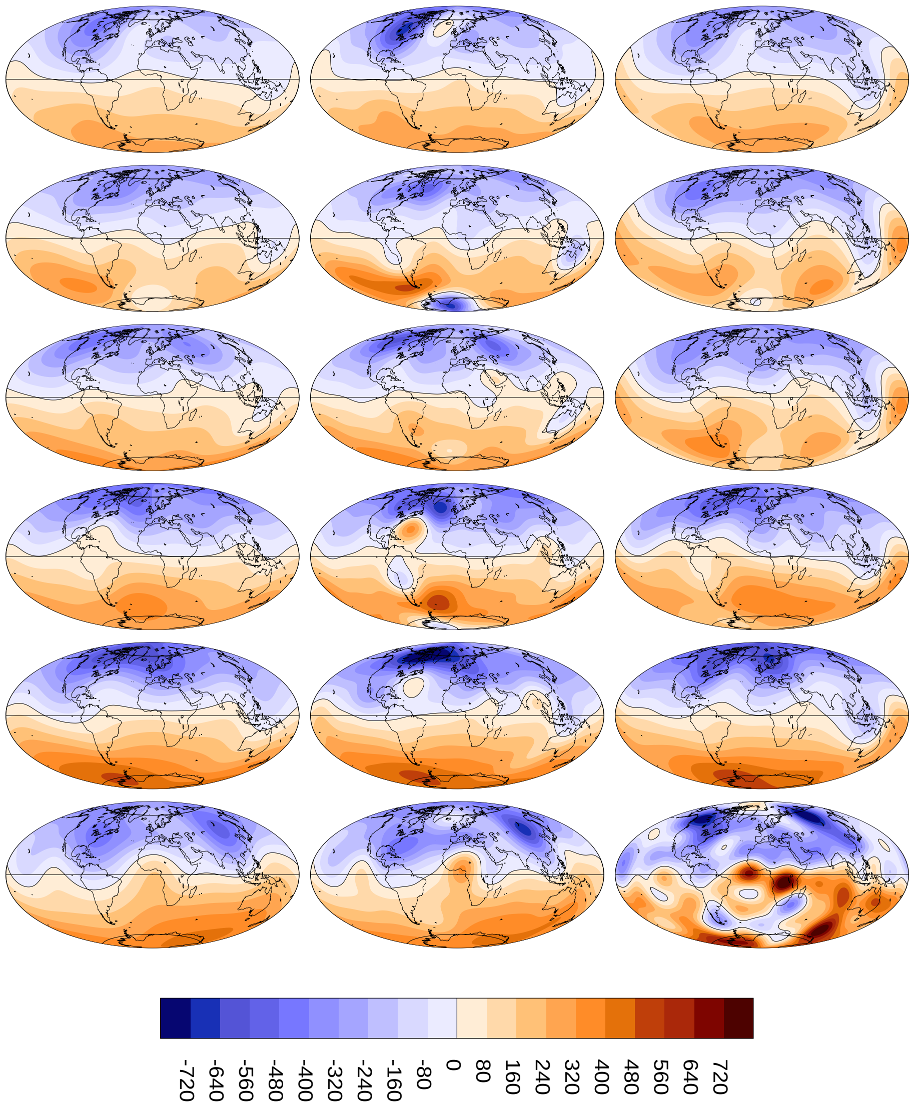

Figure 6.15: Comparison of the radial component of the field at the CMB (in μT) from the models HFM-OL1 (left column), HFM-EL1 (middle), and CALS10k.1b (right), for the time interval 8000 BC to 1990 AD (from top to bottom at 2000-year intervals).

The two high flux regions in the Southern hemisphere in the CALS10k.1b model, compatible with the historical model *gufm1*, are not so obvious in the HFM-OL1 and HFM-EL1 models. A reverse flux patch that appears under Antarctica in the HFM-EL1 model contributes to the weaker flux in the corresponding time-averaged field for this model. An intriguing characteristic of all the average models is the undulation of the magnetic equator close to Indonesia and Northern Australia that is also seen in historical and satellite era field models. Although it is not so pronounced in the HFM-BL1 and HFM-OL1, it is observed in all models throughout the timespan of the models. Similar feature of deflection of the magnetic equator is appearing over western part of South America for the periods from 6000 BC to 5000 BC and again from 3500 BC to 1000 BC. Sporadically over the same period, reversed flux patch is coming out over the South America in the HFM-EL1 model. Another reverse flux is occurring over the Atlantic Ocean for an interval of 500 years (1000 AD to 1500 AD), whereas the CALS10k.1b model shows the lower intensity over this region.

The negative flux lobes observed in the entropy model HFM-EL1 under Antarctica should be interpreted with caution. It is constrained only by the Palmer Deep (PAD) record (Brachfeld et al., 2000) and moreover, the entropy regularization with no dipole terms penalized can produce localized, high amplitude flux patches. Additional tests, preferably with new data sources, are requires to probe the reliability of this feature.

6.6 Discussion and conclusions

Four new geomagnetic field models approximately covering the Holocene (8000 BC to 1990 AD), based on paleomagnetic sediment and archeomagnetic data, have been constructed. A distinction between absolute archeomagnetic and relative sediment measurements has been made and different techniques have been adopted to include these data within the modelling framework. Relative declination and RPI from lake sediment records are included with extra calibration coefficients solved for during the inversion. The average change of the calibration coefficients, considering the models HFM-BL1, HFM-OL1 and HFM-EL1, starting from the CALS10k.1b to the final models after 10 iterations, is 8% for all RPI records, with almost no change for some of the coefficients and a maximum change of 25%. There is, however, very little change in calibration coefficients of relative declination with the average change being only 1°. Table 6.3 reports the RPI calibration factors in two HFM-OL1 models derived from different starting point, the axial dipole model and the CALS10k.1b, using the same spatial and temporal damping parameters. In general, the CALS10k.1b calibration coefficients are bigger than those calculated from an axial dipole, both initial and final values. The average difference between the calibration coefficients obtained by different starting models is about 10%, with a maximum difference of 25% for the LEB record.

The HFM models minimize different measures of spatial complexity at the CMB and either L_1 or L_2 measure of misfit. Maximum entropy regularization, is used here for the first time in millennial time scale field modelling. Model HFM-EL1, derived using this approach, possesses the highest spatial and temporal norms of the models constructed here. Its power spectra is also closer to a typical satellite era field model *gufm-sat-E3* (Finlay et al., 2012).

Table 6.3: Changes in the RPI calibration coefficients (γ_F) obtained from the HFM-OL1 model starting from the axial dipole model and the CALS10k.1b. RPI records are calibrated in units of μT. The relative change is $\Delta\gamma_F = |\text{initial}\gamma_F - \text{final}\gamma_F|/\text{initial}\gamma_F \cdot 100$. δ_{γ_F} defines the ratio between the final calibration coefficients obtained with the axial dipole starting model and the CALS10k.1b model. δ_{γ_F} bigger than 1 shows an axial dipole calibration coefficient bigger than the CALS10k1.b.

Code	RPI calibration coefficients (γ_F)						
	Starting model: Axial dipole			Starting model: CALS10k.1b			
	initial γ_F	final γ_F	$\Delta\gamma_F$	initial γ_F	final γ_F	$\Delta\gamma_F$	δ_{γ_F}
AAM	4530.7	4507.9	0.5	4417.8	4381.9	0.8	1.03
AD1	2.1	2.1	0.0	2.1	2.1	0.0	0.99
BAI	52.4	54.5	4.0	53.2	53.6	0.8	1.02
BAR	60.7	58.5	3.6	51.4	52.1	1.4	1.12
BEA	80.2	83.4	4.0	100.0	98.4	1.6	0.85
BI2	372.8	364.6	2.2	344.5	354.9	3.0	1.03
BIR	44.2	47.6	7.7	52.3	53.5	2.3	0.89
CHU	133.6	134.9	1.0	139.8	141.2	1.0	0.96
EAC	58.3	58.3	0.0	64.1	62.6	2.3	0.93
ESC	48.1	47.9	0.4	47.3	48.2	1.9	0.99
FRG	14.0	14.0	0.0	14.6	14.7	0.7	0.95
FUR	24.7	24.7	0.0	28.2	27.2	3.5	0.91
GAR	14407.8	14940.0	3.7	15890.7	16136.8	1.5	0.93
GHI	40.9	41.6	1.7	43.6	44.7	2.6	0.93
LEB	114.8	121.3	5.7	153.0	152.6	0.3	0.80
LSC	174.8	178.6	2.2	226.9	211.6	6.7	0.84
MEZ	47.3	49.9	5.5	57.6	58.1	0.9	0.86
MOT	18.2	18.1	0.5	19.0	18.9	0.5	0.96
NAU	58.9	61.1	3.7	63.7	64.8	1.7	0.94
PAD	63.8	61.2	4.1	55.6	56.1	0.9	1.09
PEP	146.0	147.2	0.8	176.6	172.0	2.6	0.86
POH	55.4	62.7	13.2	71.4	72.8	2.0	0.86
SAR	34.3	33.6	2.0	33.7	32.5	3.6	1.04
STL	48.0	47.5	1.0	52.0	52.2	0.4	0.91
TRE	54.0	49.3	8.7	49.7	50.4	1.4	0.98
WAS	273.5	267.5	2.2	225.9	246.6	9.2	1.08
Ba	89.9	94.8	5.5	106.3	107.0	0.6	0.89
SoI	42.6	45.1	5.9	51.4	52.1	1.4	0.87
SoII	360.1	382.8	6.3	459.0	453.0	1.3	0.85

The HFM-OL2 model requires very high damping in order to try to force convergence, so it contains much less power in all spherical harmonic degrees except the first, which is not explicitly damped in the method employed here. All the diagnostics results indicate that the L_2 norm is not a suitable choice for modelling the paleomagnetic and archeomagnetic data, using rather weak (five sigma) error rejection, relative to a prior uncertainty estimates. The models HFM-OL1 and HFM-BL1 possess very similar spatial and temporal norms evolutions and comparable model fits to the observations. Therefore, choosing either the R_S^B or R_S^O leads to the construction of very similar models.

Comparison with the CALS10k.1b model (Fig. 6.6) reveals that its spatial norm is similar to that of the HFM-EL1 model and generally higher than the other three HFM models during most of the Holocene period. Comparison of the temporal norms shows that CALS10k.1b possess significantly more time variations than the HFM models, especially in the recent 500 years, when it has been forced to agree with the historical field model *gufm1*. Regularisation parameters for CALS10k models have been chosen in a different way than the trade-off curve based approach presented here. Instead Korte et al. (2011) chose their damping parameters on the basis of a comparison of average main field and secular variation power spectra to those of the models IGRF (the International Geomagnetic Reference Field for epoch 2000) (e.g., Maus et al., 2005) and *gufm1* for the first three to four degrees. Other differences between the approach presented here and that taken in the construction of CALS10k.1b, which may contribute to its higher temporal norm, are that we have used generally larger uncertainty estimates for the lake sediment records (see Chapter 3) and it should also be remembered that CALS10k.1b is actually the mean of an ensemble of bootstrap models, so was not in itself constructed to minimize a norm measuring temporal complexity.

Predictions at individual lake locations from the HFM models (excluding HFM-OL2) and CALS10k.1b (Fig. 6.8) do not show dramatic differences. Dipole and quadrupole Gauss coefficients from the HFM models are generally within the error bars provided for CALS10k.1b.

One notable difference between models HFM-OL1, HFM-BL1 and HFM-EL1 compared to model CALS10k.1b is that the the HFM model possess much lower amplitude (outside the error bars for CALS10k.1b) for the g_2^2 coefficients, especially from 8000 BC to 1000 AD. Since the HFM models fit the data as well as CALS10k.1b it may be questionable whether the high power in the CALS10k.1b g_2^2 coefficient (a non-zonal, sectoral harmonic) is trustworthy.

With respect to the dipole moment, in the HFM models we find that the dipole moment has decayed for the past 2000 years (Fig. 6.13). The maxima at around 250 BC and 1200 AD, and minimum in between ($\sim$700 AD) in the dipole moment of the CALS10k.1b are not well reproduced in the HFM models. These variations are more pronounced in the archeomagnetic data than in the lake sediments. The HFM models are constrained primarily by lake sediment observations, which have been consistently allocated error estimates. These models are based on much heavier regularization and fit better lake sediment records, resulting in an acceptable global misfit as there are more lake sediment data than archeomagnetic data. They are designed to robustly model the evolution of the dipole moment over the entire 10 kyr interval of model validity. In general, there is an agreement between the models on the

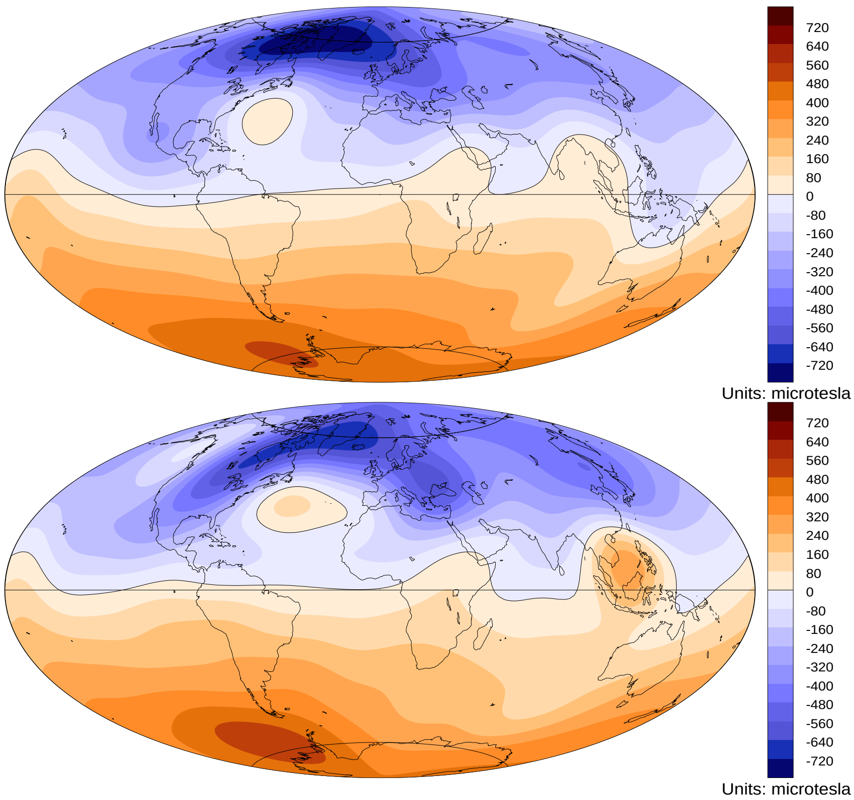

Figure 6.16: Changes in the CMB morphology occurring moving from a strong to declining dipole moment. Time-averaged field at the CMB for the interval from 300 BC to 200 AD for the HFM-EL1 model when the maximum dipole moment is observed (left) and time-averaged field at the CMB for the interval from 600 AD to 1100 AD for the same model when the dipole moment is declining (right). Note the difference in the amplitude of the high latitude flux patch over North America.

low dipole moment at ∼6000 BC, the increase towards ∼500 BC, followed by the decrease towards present.

In order to study changes in the CMB morphology that signal the start of present decline of the dipole moment, we plot in Fig. 6.16 the time-averaged field at the CMB of the HFM-EL1 model for the interval from 300 BC to 200 AD to capture the epoch of strongest dipole moment at 50 BC, and also the time-averaged field for the interval from 600 AD to 1100 AD of a weaker decreasing dipole moment. It is found that a very strong high latitude flux patch under North America is connected with the strong dipole moment around 50 BC. This flux patch has noticeably decreased in intensity by the epoch centred on 850 AD. Note that the averaging kernels suggest good data coverage over the North American region during this period. The dipole moment decay may also be affected by an increase in the intensity of the low-latitude flux patch below Indonesia. There also appears to be a slight growth in the area and intensity of a reverse flux patch below the north-western Atlantic.

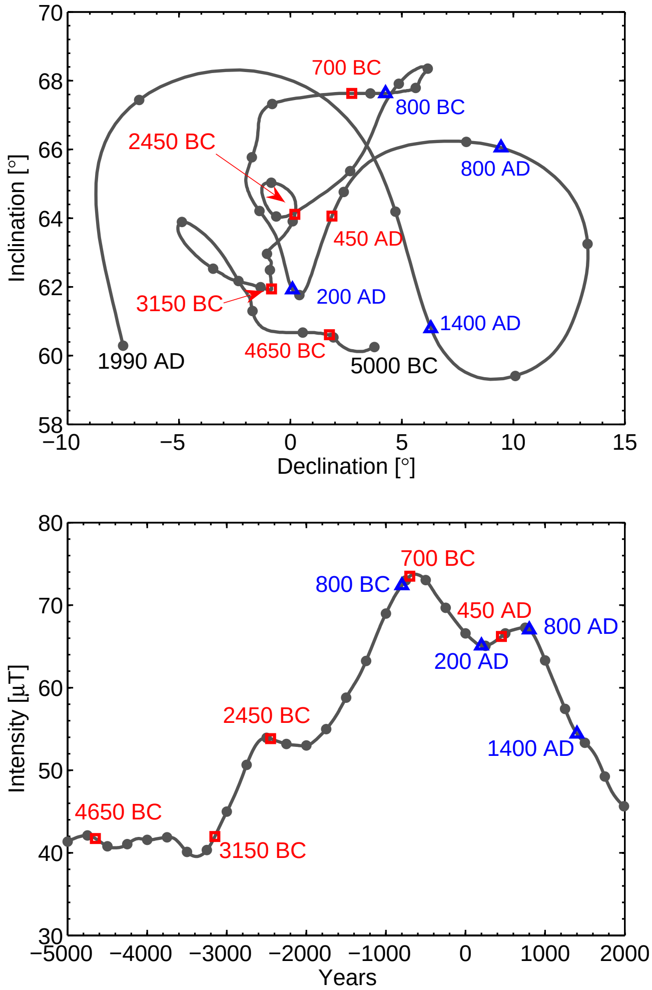

Figure 6.17: Directional and intensity variations of the geomagnetic field at 48° latitude and 9° longitude (Central Europe) obtained from the HFM-EL1 model (grey line). Tie points (grey circles) are plotted at every 250 years. Times of occurrence of archeomagnetic jerks found in archeomagnetic data from Western Europe (Gallet et al., 2003) (blue triangles) and archeomagnetic jerks in our *SoBa* records (Section 5.7) (red squares) are marked. The HFM-EL1 model predictions are shown only for the last 7 kyrs when known events are available for comparisons in Central Europe.

It is also of interest to consider whether or not sudden changes in directions (related to archeomagnetic jerks - see Chapter 1) can be resolved by the HFM models. Fig. 6.17 shows the directional variations obtained by the HFM-EL1 model at one point in Central Europe (48°N and 9°E). One of the most intense jerks events discussed by Gallet et al. (2003) that occurs in 200 AD is in fact well resolved by the HFM-EL1 model. Two further events close to each other, at 700 BC and 800 BC in the *SoBa* record and French archeomagnetic data respectively, are found to be close to a period when there is changes in directions in the HFM-EL1 model. The most recent jerks events are however not captured by the HFM-EL1 model. The slow directional variations that the HFM models are capable of resolving in the recent period are not able to capture these rapid field changes. This illustrates that the HFM models are not suitable for studying archeomagnetic jerks events occurring on time scales of less than a century. If however the jerks events are of sufficiently long duration, on time scale of ∼200-400 years, and reveal a significant change in the directions, then it is possible for models of the HFM type to diagnose their existence.

Chapter 7

Conclusions and outlook for future studies

7.1 Overview of thesis

This thesis presents the results of new approaches to model global scale Holocene geomagnetic field evolution. A comprehensive statistical analysis of the available database of Holocene magnetic records has been carried out in order to obtain improved uncertainty estimates. As a by-product, this analysis also enabled the study of periodicities and the spectrum of temporal variations for Holocene magnetic variations. Time-dependent, spherical harmonic, field models were constructed testing different misfit and regularization measures in an effort to find the most effective combination for extracting as much reliable information as possible from the often scattered and noisy paleomagnetic and archeomagnetic observations.

The process of natural magnetization is of fundamental importance when assessing the reliability of paleomagnetic and archeomagnetic data. Different experimental protocols are used, for example, to determine intensity estimates from the thermoremanent magnetization. Moreover, the procedures used to account for the effects of TRM including the magnetic alterations, TRM anisotropy and cooling rate corrections, are not consider in a systematic way by all authors. Depositional remanent magnetization acquired by sediment magnetic grains can influence the data reliability on a different manner. Smoothing of the geomagnetic signal due to time period needed for magnetization to lock-in, always affects the sediment magnetic records. The other source of uncertainties is related to the process of dating. Age determinations are mostly based on radiocarbon dating, but varve counting, pollen analysis, and tephra are also used. All these methods provide different precisions and dating errors associated with the dated points. Moreover, the age-depth model for the sediment records, created by a linear interpolation between the points under assumption of a constant sedimentation rate, contributes likely an additional dating error.

Holocene lake sediment records were studied in Chapter 3 and the random variability characterized using a robust smoothing spline modelling technique, developed specifically for the purposes of this thesis. Random errors in the records were found to range from 0.5° to 11.6° (median value: 2.7°; interquartile range: 1.8° to 4.4°) for inclination, 1.2° to 45.6° (median value: 7.5°; interquartile range: 5.1° to 13.2°) for declination, and 0.2 to 1.0 (median value: 0.5; interquartile range: 0.3 to 0.6) for standardised RPI. Comparisons between the magnetic sediment data and nearby archeomagnetic data, other nearby sediment records, the historical field model *gufm1* in the time periods of overlap, and the archeomagnetic field model ARCH3k.1 when nearby archeomagnetic data are available, provided an independent uncertainty estimates including random and systematic sources. Inclination data showed much better agreement than declination for all comparisons undertaken. Final uncertainty estimates were obtained by comparison with archeomagnetic estimates when possible, or using a combination of robust smoothing spline results and the average of those comparisons to archeomagnetic estimates that were possible. Taking into account possible systematic errors, a larger spread of uncertainties was finally obtained, ranging from 2.5° to 11.2° (median: 5.9°; interquartile range: 5.4° to 7.2°) for inclination, 4.1° to 46.9° (median: 13.4°; interquartile range: 11.4° to 18.9°) for relative declination, and 0.59 to 1.32 (median: 0.93; interquartile range: 0.86 to 1.01) for standardized relative paleointensity. Age uncertainties were not separately assessed but they contribute to the uncertainties inferred in the comparisons with archeomagnetic estimates. The wide range of uncertainty estimates obtained highlights the need of treating each component of each record individually. Holocene sediment magnetic records were not found to show evidence for inclination shallowing. The temporal resolution of the records was found to have an interquartile range of 80 to 250 years.

Three different time series analysis techniques, multitaper spectral estimation, wavelet analysis and empirical mode decomposition, were applied to the robust spline fits to the Holocene sediment data compilation. They revealed the presence of broadband variations of the geomagnetic field on millennial time scales and no evidence for discrete periodicities. A mean power law exponent of -2.3 ± 0.6 is found for the period range from $300 - 4000$ years. This result agrees well with the spectrum of the dipole moment obtained by Constable and Johnson (2005), and with the spectrum obtained from geodynamo simulations studied by Olson et al. (2012). A slope of -2 in the temporal spectrum of the magnetic energy is consistent with the hypothesis of chaotic convection in the core producing a white spectrum of flow variations (Tanriverdi and Tilgner, 2011).

Three new lake sediment records, *SoI* and *SoII* from Lake Soppen, and *Ba* from Lake Baldegg, were analysed in order to compile a Holocene secular variation master curve for Switzerland. Additionally, uncertainty estimates are assigned to each record and the composite. These new Swiss records were also used in the construction of new Holocene global field models derived in this thesis. Comparisons between the *SoBa* record and nearby lakes (EIF, MOR, BOU, FEN and MEZ), archeomagnetic data and independent global field models (ARCH3k.1, SCHA.DIF.8k and CALS10k.1b) reveal a generally good agreement, but with an age offset of about $250 - 300$ years for the first 3000 years, which may be related to shortcomings of the age models for the cores. Analysis of the change in curvature and RPI from the *SoBa* records pointed to the existence of two well constrained rapid field change events in approximately 700 BC and 450 AD, and three less defined at 4650 BC, 3150 BC, and 2450 BC. Archeomagnetic jerks found in the *SoBa* records were compared to similar events found in French, Peruvian and Korean archeomagnetic data, and Swedish lake sediment records.

In the final part of the thesis four new time-dependent Holocene geomagnetic field models spanning the period from 8000 BC and 1990 AD were constructed. These are designed to capture the robust aspects of large scale field evolution at the CMB during the Holocene. The modelling directly utilizes declination and paleointensity in relative form for the first time, without prior calibration of the records. Use is also made of the new uncertainty estimates for lake sediment records derived earlier in the thesis. An absolute deviation (L_1) measure of misfit was found to yield well converged models with satisfactory global misfits, while the L_2 norm was found to require more data rejection or stronger damping. Models constructed with Ohmic heating and B_r^2 spatial norms were found to be very similar in terms of their spatial and temporal norms and their fit to the observations. On the other hand, a model constructed using maximum entropy regularization has a spherical harmonic spectrum closer to that found from satellite and observatory observations for the the present field, as well as geomagnetic field changes with higher amplitude than other models constructed here.

Comparisons with the CALS10k.1b model showed that the new models constructed using the L_1 misfit, fit the observations to a similar level and have dipole and quadrupole coefficients generally within the error bars of the CALS10k.1b coefficients (as obtained by bootstrap sampling). All these models also display persistent non-zonal contributions to the time-averaged Holocene field at the CMB, especially the Northern hemisphere high latitude flux patches and an oscillatory feature in the magnetic equator in the Indonesian region. Study of the CMB field morphology at the times of strong dipole moment and when it subsequently start to decay, reveal that a weakening of a strong high latitude flux patch beneath North America is primarily responsible. Sudden directional changes are not well resolved with the new field models and they can therefore only be used to study the longest duration and most intense archeomagnetic jerk events.

7.2 Outlook for future studies

The approach developed for deriving uncertainty estimates for Holocene lake sediments provides a useful improvement on earlier approaches, but it should be updated and improved in future. One possible shortcoming is the reliance on comparisons with archeomagnetic data. Since these are restricted mostly to the Northern hemisphere imperfect results may result when applied to the Southern hemisphere. In order to avoid outliers in archeomagnetic data, the ARCH3k.1 model predictions were also used, but this means the time scale for comparisons was also restricted to the past 3 kyrs. When comparisons are not possible, the average comparison value is used in the equation for the final uncertainty. The best way to improve this situation is for more archeomagnetic data to be collected in the Southern hemisphere and at earlier times, to allow better testing and quantification of the uncertainties in the sediment records. Selection of the smoothing parameter in the robust spline models, in cases when the cross validation method fails, rely on prior knowledge of the sedimentation rate and lock-in depth. The assumption of a constant sedimentation rate is made because detailed information concerning the age-depth models and changes in accumulation rate are often not available. The assumed lock-in depth of 10 cm is also based on relatively few previous studies. It would therefore be very useful if information about the changes in the sedimentation rate and lock-in depth were provided in future lake sediment studies. For the sediment records that were included in the data compilation in pre-smoothed form, consistently lower value for the random uncertainties were obtained sometimes resulting in unrealistically small final uncertainty estimates. A clear recommendation is therefore that future records should be provided in raw form because it is important for modellers to retain the information on the original fidelity of the records. Much larger uncertainty estimates were typically assigned to the multiple cores records, especially in the cases of significant offset in the data. Prior to field modelling, it is probably preferable to reject those cores that are incompatible with data from other sources (e.g., archeomagnetic data, nearby lake records or other cores from the same lake). For this reason, individual cores should be separately included in databases along with their own depth-age model.

Turning to the paleosecular variation master curve for Switzerland derived from Lake Soppen and Lake Baldegg, curves for the three components showed that some incompatibilities in the records and not perfectly aligned features cause many variations, especially in declination, to be cancelled out. In order to obtain a more reliable and detailed master curve, further Swiss sediment records should be included. A more sophisticated procedure allow shifting and stretching of records to take into account imperfections in the age-depth model should also be considered.

Although the number of paleomagnetic data spanning the Holocene is constantly increasing, more data are still needed to address the serious deficiencies of coverage in the Southern hemisphere. Promising results are now appearing from Indonesia, Lake Matano and Lake Towuti in the central part of Sulawesi (S. Bijaksana, pers. communication). These will be very interesting to further constrain the history of the oscillation of the magnetic equator observed in this region. Moreover, new archeomagnetic studies from the African continent, in particular from Tunisia and Morocco, (Gómez-Paccard et al., 2012), will soon better constrain the evolution of the geomagnetic field during recent times. It is clear that further efforts are essential on the data collection side in order to enable more detailed knowledge of the mechanisms of secular variation on millennial time scales.

Regarding the field modelling methods developed in this thesis, one short coming is the absence of model uncertainties. In the future, statistical bootstraping similar to that carried out in the construction of the CALS10k.1b model could be carried out, taking into account the new uncertainty estimates for the sediment magnetic records. Such error estimates will prove very helpful for future hypothesis testing, although the role played by the choice of regularization parameter still needs to be resolved. Another possible improvement of the modelling procedure could be to consider the lake sediment data as time averages, and not as a single point in time, as has been done in this thesis and all previous studies. Due to the DRM acquisition process, which occurs over decades to centuries depending on the sedimentation rate, the measured data is actually an averaged version of the true signal.

More generally, the statistical analyses and field modelling methods developed in the thesis can also be applied on longer time scales than the Holocene (e.g., 100 kyrs). One of the objectives in paleomagnetism is to better characterize and understand large directional and intensity changes (excursions and reversals) through reconstruction of CMB field structure. Characterization of the reliability of various contributing records, a consistent combination of sediment and lava data, and use of L_1 and maximum entropy field modelling approaches could make a useful improvement in this regard. However, the accuracy of independent dating becomes more and more of a challenging issue for very long timescales modelling.

Appendix A

Holocene data compilation

Table A.1: Archeomagnetic directional data. Declination and inclination data of one age and location are counted as one data point.

Code	Country or Region	Lat Min	Lat Max	Long Min	Long Max	Age Range	Nb.
AFR	Morocco, Canary Isl.	28.3	35.5	-17.8	-6.0	200 BC to 1971 AD	26
ARK	Arkansas	33.1	40.2	-93.8	-88.7	150 AD to 1725 AD	61
AUS	Australia, New Zealand	-36.8	-33.5	143.0	174.9	5000 BC to 1845 AD	28
BUL	Bulgaria	41.2	45.2	17.5	28.6	5875 BC to 1894 AD	242
CAU	Azerbaijan, Georgia	40.0	43.2	40.3	50.0	3250 BC to 1993 AD	192
CHA	China, Mongolia, Baikal	28	48	102	119.1	4495 BC to 1966 AD	101
EEU	Eastern Europe	50	59.8	20	30.5	350 AD to 1910 AD	160
EUR	Europe	38.3	55.6	-3.4	43.5	2200 BC to 1658 AD	50
FRA	France	43.0	50.8	-4.3	9.5	775 BC to 1830 AD	184
GBA	Great Britain	45.8	57.9	-6.3	1.6	3250 BC to 1987 AD	438
GER	Germany	47.4	53.9	6.3	14.7	4900 BC to 1805 AD	125
HAW	Hawaii	19.1	19.8	-156.1	-154.8	3058 BC to 1960 AD	201
HUN	Hungary	45.9	48.3	1.7	22.5	1900 BC to 1850 AD	179
JAP	Japan	33.0	38.6	128.9	140.9	440 AD to 1950 AD	78
MAM	Meso-America	13.3	22.1	-99.3	-61.2	200 BC to 1905 AD	102
NEA	Egypt, Iraq, Israel	24.0	35.6	30.6	44.6	2150 BC to 1795 AD	34
NWA	Northwest America	33.7	55.2	-129.1	-105.9	7230 BC to 1980 AD	57
RUS	Russia	46.5	59.6	36.1	73.3	1350 BC to 1924 AD	487
SEU	Greece, Italy	35.1	45.2	7.1	35.4	1450 BC to 1960 AD	161
SIB	Siberia	48.5	56.6	85.0	135.0	1710 AD to 1914 AD	94
SWU	Southwest USA	31.8	42.8	-112.6	-103.6	595 AD to 1994 AD	273
UKR	Ukraine, Moldova	44.0	59.5	20.4	45.5	3450 BC to 1925 AD	380
UZB	Uzbekistan	38.0	42.0	64.3	76.0	900 AD to 1914 AD	134

Table A.2: Archeomagnetic intensity data.

Code	Country or Region	Lat Min	Lat Max	Long Min	Long Max	Age Range	Nb.
AUI	Australia	-35.9	-33.5	143.0	146.1	4114 BC to 1532 AD	20
BUI	Bulgaria	41.2	45.2	17.5	28.6	4870 BC to 1894 AD	253
CAI	Azerbaijan, Georgia	40.0	50.3	20.5	50.5	5000 BC to 1970 AD	415
CHI	China, Mongolia	23.0	57.0	76.0	126.9	5000 BC to 1966 AD	314
FRI	France, Spain	39.5	50.6	-2.2	8.3	4730 BC to 1750 AD	91
GBI	Great Britain	50.7	53.8	-5.8	1.0	150 AD to 1900 AD	47
HAI	Hawaii	19.1	19.7	-155.6	-154.8	4468 BC to 1960 AD	24
HUI	Hungary	47.0	52.0	13.3	21.0	4800 BC to 1873 AD	72
INI	India	9.2	31.0	70.5	79.9	2752 BC to 1984 AD	71
JAI	Japan	31.6	38.9	125.9	141.3	4645 BC to 1950 AD	165
MEI	Mexico	14.7	23.7	-105.3	-89.8	3380 BC to 1971 AD	62
NAI	North America	27.8	46.1	-122.2	78.9	4830 BC to 1978 AD	161
NEI	Near East	24.0	36.4	13.1	54.8	5000 BC to 1990 AD	304
RUI	Russia, Ukraine	43.0	59.5	20.4	46.0	3860 BC to 1890 AD	344
SAI	South America	-22.2	-1.8	-115.2	-68.3	3050 BC to 1800 AD	147
SCI	Scandinavia	55.1	65.7	-21.8	25.7	4360 BC to 1980 AD	56
SEI	Southern Europe	34.7	45.8	10.4	33.8	4869 BC to 1983 AD	330
UZI	Uzbekistan, Turkmenistan	37.0	41.3	58.0	72.0	4935 BC to 1971 AD	330

Table A.3: Sediment magnetic records. The number of data are given as declination/inclination/intensity for the whole time span.

Code	Location	Lat	Long	SR	Age Range	N(D/I/F)	Ref.
AAM	Alaskan Margin, Arctic Sea	71.63	-156.86	1.93	6010 BC to 172 AD	994/994/994	1
AD1	Adriatic Sea, Italy	42.6	14.5	0.54	10428 BC to 1606 AD	0/170/168	2
AD2	Adriatic Sea, Italy	42.7	14.6	0.17	10609 BC to 1655 AD	0/88/88	2
ANN	Lac d' Annecy, France	45.8	6.2	1.8	350 BC to 1810 AD	167/167/0	3
ARA	Lake Aral, Kazakhstan	46.0	59.2	10.2	525 AD to 1675 AD	47/47/0	4
ASL	Lake Aslikul, Russia	54.4	54.1	0.75	2110 BC to 1445 AD	437/437/0	5
BAI	Lake Baikal, Russia	52.2	106.5	0.14	23679 BC to 1575 AD	166/162/73	6
BAM	Lake Barombi Mbo, Cameroun	4.5	9.5	1.8	23828 BC to 689 AD	375/370/0	7
BAR	Lake Barrine, Australia	-17.2	145.6	0.75	10331 BC to 925 AD	1149/1149/387	8, 9
BEA	Beaufort Sea, Arctic Ocean	70.63	-135.88	1.35	2629 BC to 1556 AD	561/556/561	10
BEG	Lake Begoritis, Greece	40.8	21.8	1.0	3280 BC to 1950 AD	628/628/0	11
BI2	Lake Biwa 2, Japan	35.25	136.06	0.4	37681 BC to 112 BC	141/141/137	12
BIR	Birkat Ram, Israel	33.3	35.7	1.6	4403 BC to 1942 AD	208/208/202	13, 14
BIW	Lake Biwa, Japan	35.3	136.0	1.21	7767 BC to 1683 AD	508/508/0	15
BLM	Lake Bullenmerri, Australia	-38.2	143.1	0.88	9352 BC to 1742 AD	98/98/0	16
BOU	Lac du Bourget, France	45.7	5.9	3.75	250 AD to 1930 AD	146/146/0	3
BYA	Byestadssjön, Sweden	57.4	15.3	0.56	8895 BC to 1500 AD	247/247/247	27, 64
CAM	Brazo Campanario, Argentina	-41.0	-71.5	0.77	5585 BC to 1361 AD	306/306/0	17
CHU	Chukchi Sea, Arctic Ocean	72.86	-158.87	1.3	7561 BC to 336 AD	1070/1070/1070	10
DES	Dead Sea, Israel	32.0	35.0	2.0	5021 BC to 1662 AD	782/782/0	18
EAC	Lake Eacham, Australia	-17.3	145.6	1.1	3747 BC to 1476 AD	738/738/369	8, 9
EIF	Eifel maars, Germany	50.12	6.83	1.02	11050 BC to 1850 AD	234/234/0	19

Continued on next page

Table A.3 – continued from previous page

Code	Location	Lat	Long	SR	Age Range	N(D/I/F)	Ref.
ERH	Erhai Lake, China	25.82	100.17	0.9	4664 BC to 1922 AD	134/134/0	20
ERL	Erlongwan Lake, China	42.3	126.37	0.27	36050 BC to 550 AD	106/106/0	21
ESC	Lake Escondido, Argentina	-41.0	-71.3	0.3	15657 BC to 776 AD	250/250/302	22, 23
FAN	Lake Fangshan, China	40.2	116.0	0.5	16844 BC to 1454 AD	245/245/0	24
FIN	Finnish Lakes, Finland	63.62	29.02	0.64	7950 BC to 1970 AD	993/993/0	25
FIS	Fish Lake, USA	42.5	-118.9	0.8	9451 BC to 1803 AD	253/253/0	26
FRG	Frängsjön, Sweden	64.0	19.7	0.4	6670 BC to 1621 AD	285/285/298	27, 28
FUR	Furskogstjärnet, Sweden	59.4	12.1	0.41	7462 BC to 1721 AD	242/242/237	27, 29
GAR	Gardar Drift, North Atlantic	60.4	-23.6	0.3	6910 BC to 1955 AD	204/204/204	30
GEI	Llyn Geirionydd, UK	53.0	-3.0	0.31	5150 BC to 1839 AD	176/176/0	31
GHI	Cape Ghir, NW Afr. Margin	30.9	-10.3	0.6	5411 BC to 1849 AD	176/176/176	32
GNO	Lake Gnotuk, Australia	-38.2	142.9	0.39	9421 BC to 831 AD	344/344/0	16
GRE	Greenland, North Atlantic	67.1	-30.8	1.0	9772 BC to 748 AD	2324/2324/0	33
HUR	Lake Huron, USA	44.0	-82.0	0.63	14021 BC to 1460 AD	1013/1013/0	34
ICE	Iceland, North Atlantic	66.6	-20.9	2.0	9583 BC to 1560 AD	2217/2217/0	33
JON	Ionian Sea, Italy	36.7	15.9	0.09	14224 BC to 604 BC	91/101/0	2
KEI	Lake Keilambete, Australia	-38.2	142.9	0.31	10327 BC to 1912 AD	795/795/0	16
KYL	Kylen Lake, Minnesota	47.0	-91.8	0.8	6034 BC to 2293 BC	95/95/0	35
LAM	Lake Lama, Russia	69.5	90.2	0.59	17334 BC to 1664 AD	731/787/0	36
LAR	Larsen Ice Shelf, Antarctic Pen.	-64.8	-60.4	0.16	4950 BC to 1950 AD	91/91/91	65
LEB	Lake LeBoeuf, USA	41.0	-80.0	2.1	2773 BC to 1830 AD	42/42/365	37
LOM	Loch Lomond, UK	56.0	-5.0	0.31	4885 BC to 1838 AD	170/170/0	38
LOU	Louis Lake, USA	42.6	-108.85	0.2	17433 BC to 1471 AD	38/36/0	39
LSC	Lake St.Croix, USA	45.0	-93.0	2.5	8674 BC to 1859 AD	289/289/342	35

Continued on next page

Table A.3 – continued from previous page

Code	Location	Lat	Long	SR	Age Range	N(D/I/F)	Ref.
MAR	Mara Lake, Canada	50.8	-119.0	1.22	3529 BC to 1861 AD	231/231/0	40
MEE	Meerfelder Maar, Germany	49.0	7.0	1.0	15050 BC to 1843 AD	1273/1273/0	41
MEZ	Lago di Mezzano, Italy	42.6	11.9	0.9	4105 BC to 1774 AD	244/258/214	42
MNT	Lago Morenito, Argentina	-41.0	-71.5	0.3	10331 BC to 1424 AD	500/500/0	17
MOR	Lac Morat, Switzerland	46.9	7.1	0.9	110 BC to 1590 AD	153/153/0	3
MOT	Mötterudstjärnet, Sweden	59.7	12.7	0.41	7764 BC to 1811 AD	253/253/253	27, 29
NAR	Lake Naroch, Belorussia	54.8	26.6	0.64	9970 BC to 902 AD	244/244/0	43
NAU	Nautajärvi, Finland	61.8	24.7	0.6	7900 BC to 1980 AD	253/253/253	27, 44
NEM	Lake Nemi, Italy	41.7	12.9	1.1	8969 BC to 1930 AD	269/283/0	2
PAD	Palmer Deep, Antarctic Pen.	-64.9	-64.2	2.5	7333 BC to 1755 AD	1932/1932/1872	45
PEP	Lake Pepin, USA	44.4	-92.1	1.5	6196 BC to 1964 AD	0/954/954	46
POH	Pohjajärvi, Finland	62.8	28.0	1.04	1291 BC to 1950 AD	109/109/109	47
POU	Lake Pounui, New Zealand	-41.1	175.0	0.96	600 BC to 1759 AD	47/47/0	48
SAG	Saguenay Fjord, Canada	48.3	-70.26	1.5	5214 BC to 1799 AD	1095/1114/0	49
SAN	Hoya de San Nicolas, Mexico	20.39	-101.26	0.38	9730 BC to 860 BC	176/176/0	50
SAR	Sarsjön, Sweden	64.0	19.6	0.4	7000 BC to 1600 AD	252/252/252	27, 28
SAV	Savijärvi, Finland	61.8	24.7	0.42	8250 BC to 1000 AD	132/132/0	27, 51
SCL	Lake Shuangchiling, China	19.94	110.19	2.2	6981 BC to 1747 AD	637/647/0	52
STL	St. Lawrence Est., Canada	48.6	-68.6	1.5	6555 BC to 1197 AD	1215/1199/1236	53
SUP	Lake Superior, USA	48.5	-89.0	1.08	11908 BC to 1850 AD	598/598/0	54
TRE	Laguna El Trébol, Argentina	-41.1	-71.5	0.4	35457 BC to 1639 AD	409/409/328	55, 56
TRI	Lake Trikhonis, Greece	38.6	21.5	1.0	4687 BC to 1899 AD	905/905/0	11
TUR	Lake Turkana, Kenya	2.6	36.6	1.9	743 BC to 1969 AD	0/100/0	57
TY1	Tyrrhenian Sea, Italy	42.6	9.9	0.1	3015 BC to 1886 AD	60/60/0	2

Continued on next page

Table A.3 – continued from previous page

Code	Location	Lat	Long	SR	Age Range	N(D/I/F)	Ref.
TY2	Tyrrhenian Sea, Italy	42.9	9.9	0.1	3604 BC to 1874 AD	76/78/0	2
VAT	Vatndalsvatn, Iceland	66.0	-23.0	0.78	4837 BC to 1377 AD	345/346/0	58
VIC	Lake Victoria, Uganda	0.0	32.4	1.0	5637 BC to 1850 AD	209/215/0	59
VOL	Lake Volvi, Greece	40.8	23.5	2.5	539 BC to 1877 AD	821/821/0	11
VUK	Vukonjärvi, Finland	63.4	29.1	0.5	4995 BC to 1763 AD	106/126/0	60
WAI	Lake Waiau, Hawaii	19.8	-155.5	0.4	13111 BC to 1836 AD	205/205/0	61
WAS	West Amundsen Sea	-73.73	-116.84	0.2	22593 BC to 1526 AD	0/0/86	62
WIN	Lake Windermere, UK	54.3	-3.0	0.5	9596 BC to 611 AD	216/216/0	31
WPA	West Pacific	24.8	122.5	3.9	7473 BC to 1934 AD	0/3351/3387	63

References: 1, Lisé-Pronovost et al. (2009); 2, Vigliotti (2006); 3, Hogg (1978); 4, Nourgaliev et al. (2003); 5, Nourgaliev et al. (1996); 6, Peck et al. (1996); 7, Thouveny and Williamson (1988); 8, Constable and McElhinny (1985); 9, Constable (1985); 10, Barletta et al. (2008); 11, Creer et al. (1981); 12, Hayashida et al. (2007); 13, Frank et al. (2002b); 14, Frank et al. (2003); 15, Ali et al. (1999); 16, Barton and McElhinny (1981); 17, Creer et al. (1983); 18, Frank et al. (2007); 19, Stockhausen (1998); 20, Hyodo et al. (1999); 21, Frank (2007); 22, Gogorza et al. (2002); 23, Gogorza et al. (2004); 24, Zhu et al. (1994); 25, Haltia-Hovi et al. (2010); 26, Verosub et al. (1986); 27, Snowball et al. (2007); 28, Snowball and Sandgren (2002); 29, Zillén (2003); 30, Channell et al. (1997); 31, Turner and Thompson (1981); 32, Bleil and Dillon (2008); 33, Stoner et al. (2007); 34, Mothersill (1981); 35, Lund and Banerjee (1985); 36, Frank et al. (2002a); 37, King (1983); 38, Turner and Thompson (1979); 39, Geiss et al. (2007); 40, Turner (1987); 41, Brown (1991); 42, Brandt et al. (1999); 43, Nourgaliev et al. (2005); 44, Ojala and Saarinen (2002); 45, Brachfeld et al. (2000); 46, Brachfeld and Banerjee (2000); 47, Saarinen (1998); 48, Turner and Lillis (1994); 49, St-Onge et al. (2004); 50, Chaparro et al. (2008); 51, Ojala and Tiljander (2003); 52, Yang et al. (2009); 53, St-Onge et al. (2003); 54, Mothersill (1979); 55, Irurzun et al. (2006); 56, Gogorza et al. (2006); 57, Barton and Torgersen (1988); 58, Thompson and Turner (1985); 59, Mothersill (1996); 60, Huttunen and Stober (1980); 61, Peng and King (1992); 62, Hillenbrand et al. (2010); 63, Richter et al. (2006); 64, Snowball and Sandgren (2004) and 65, Brachfeld et al. (2003).

Appendix B

Selection of the default parameter for the entropy models

The default parameter d_S is varied in order to obtain a suitably sharp image of the radial field at the CMB. Fig. B.1 presents how the B_r^2 norm changes as the default entropy parameter (d_S) is varied. The evolution of the B_r^2 spatial norms and power spectra for the same models are given in Fig. B.2. For large values of d_S, the maximum entropy regularization converges as expected towards the solution obtained from quadratic regularization (e.g., Gillet et al., 2007). For smaller values of d_S, the spatial norm (Fig. B.1) and at temporal evolution (Fig. B.2), starts to increase, producing models with higher amplitude than in the quadratic case, with only small changes in the misfit. Snapshots of the CMB field reveal that more intense flux patches are present in the entropy models with $d_S \leq 5 \cdot 10^5$. It is a challenging task to select the default parameter d_S (see for example Jackson et al., 2007). The entropy model presented in the thesis (HFM-EL1) is with $d_S = 9 \cdot 10^3$. This value is found to be low enough so that the field amplitudes are significantly higher than in the quadratic models and yet few additional reverse flux patches are introduced.

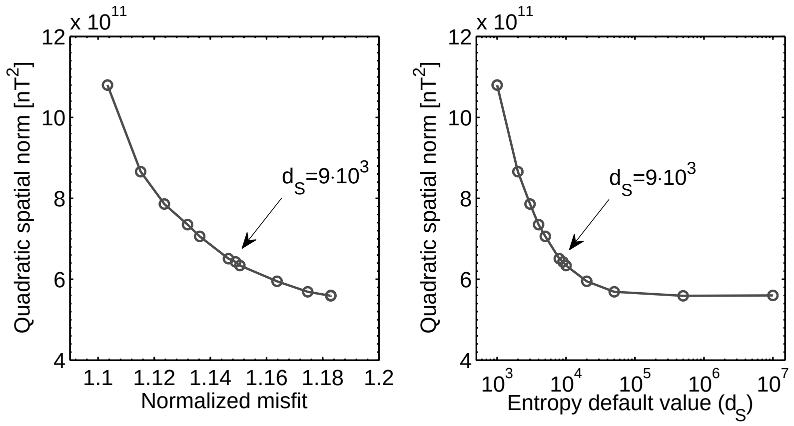

Figure B.1: (left) Trade-off curve of the quadratic B_r^2 spatial norm vs. misfit for entropy models with different values of the entropy default parameter (d_S) and (right) change of the quadratic B_r^2 spatial norm vs. d_S.

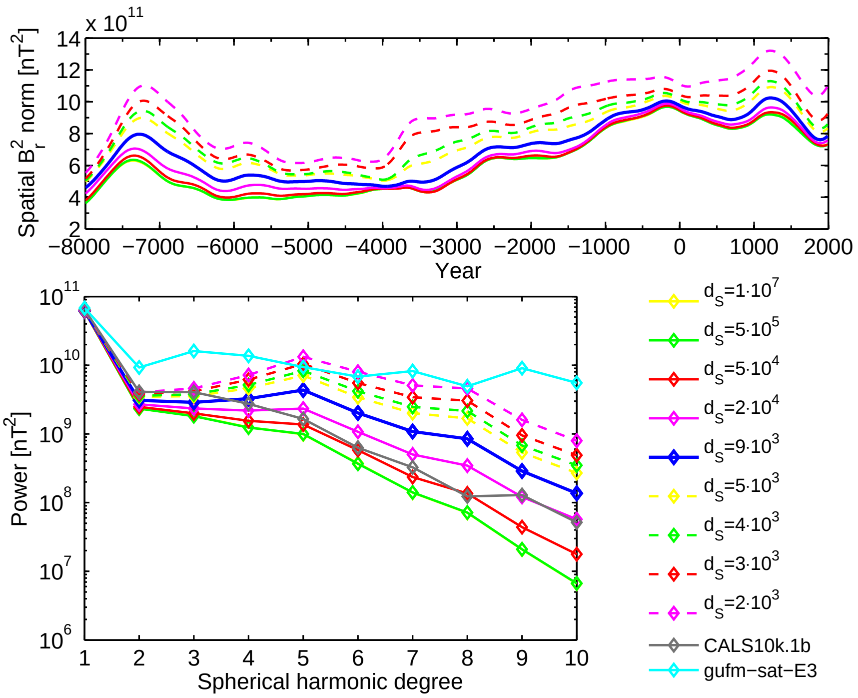

Figure B.2: Quadratic B_r^2 spatial norm and spherical harmonic spectrum for B_r for different values of the entropy default parameter (d_S). The B_r^2 norm is increasing when d_S is decreasing. For large values of d_S, the power spectra are overlapped and similar to the quadratic B_r^2 model's spectrum. CALS10k.1b (grey line) and gufm-sat-E3 (cyan line) spherical harmonic spectra are shown for reference.

Appendix C

Models misfits to all sediment magnetic records

The following four tables summarise the L_2 misfit of the four models in Chapter 6 to all the lake sediment records, denoted as RMS. Additionally, the dimensional misfits, RMSdim, are given in unit of degrees for the declination and inclination, and in μT for the paleointensity. Dash stands for the absence of a particular component.

Table C.1: L_2 misfit of the model HFM-BL1.

Code	Declination		Inclination		Intensity	
	RMS	RMSdim [°]	RMS	RMSdim [°]	RMS	RMSdim [μT]
AAM	1.65	63.52	0.71	4.26	1.33	8.36
AD1	-	-	0.79	6.20	1.16	12.67
ANN	0.71	15.20	0.77	7.29	-	-
ARA	0.66	8.06	1.24	6.74	-	-
ASL	0.45	12.08	0.61	3.55	-	-
BAI	1.42	21.47	1.38	8.76	1.50	20.38
BAM	0.97	11.06	1.21	7.23	-	-
BAR	0.93	35.31	0.92	10.07	1.06	13.70
BEA	1.51	40.73	0.95	5.63	1.06	10.42
BEG	0.63	6.41	1.16	3.15	-	-
BI2	0.83	10.94	1.06	6.22	1.82	17.97
BIR	1.14	15.05	1.28	9.55	0.98	18.22
BLM	0.61	21.02	1.01	6.59	-	-
BOU	0.74	13.75	1.11	4.08	-	-
CAM	0.72	8.99	0.75	4.63	-	-
CHU	1.51	30.75	0.64	3.97	1.18	12.15
DES	0.97	16.49	1.15	10.34	-	-
EAC	0.89	31.49	0.90	9.41	0.79	16.86
EIF	0.71	6.09	0.85	4.07	-	-
ERH	0.91	13.65	0.91	8.73	-	-
ERL	1.05	12.48	1.74	10.91	-	-
Continued on next page						

Table C.1 – continued from previous page

Code	Declination		Inclination		Intensity	
	RMS	RMSdim [°]	RMS	RMSdim [°]	RMS	RMSdim [μT]
ESC	1.05	22.35	1.02	6.71	0.94	10.17
FAN	1.14	15.25	0.95	10.78	-	-
FIN	0.63	7.35	0.77	4.47	-	-
FIS	0.88	13.10	1.29	8.21	-	-
FRG	1.06	17.29	0.59	3.85	0.75	10.05
FUR	0.75	11.80	0.60	3.79	0.81	17.60
GAR	1.41	29.86	1.28	8.29	0.80	9.89
GEI	0.63	6.00	0.57	2.93	-	-
GHI	0.64	9.93	0.85	6.36	1.21	12.25
GNO	0.61	20.94	0.78	6.18	-	-
GRE	1.20	24.49	0.63	3.91	-	-
HUR	1.04	29.76	0.86	6.95	-	-
ICE	1.27	27.45	0.70	4.53	-	-
KEI	0.62	21.31	0.62	4.30	-	-
KYL	1.20	16.06	1.08	6.60	-	-
LAM	1.34	43.59	0.91	7.10	-	-
LEB	0.71	10.54	0.62	3.85	1.01	12.27
LOM	1.10	10.66	0.79	3.29	-	-
LOU	0.98	45.70	1.39	10.72	-	-
LSC	1.24	15.10	0.69	4.47	0.87	21.47
MAR	0.88	12.34	1.14	6.25	-	-
MEE	1.30	32.03	1.62	10.00	-	-
MEZ	0.52	13.57	0.81	6.30	1.49	11.51
MNT	1.06	13.53	0.93	6.07	-	-
MOR	1.75	16.88	1.15	5.73	-	-
MOT	0.83	13.03	0.82	5.59	0.72	12.03
NAR	0.65	7.65	0.68	3.94	-	-
NAU	0.99	12.56	0.71	6.02	1.26	9.05
NEM	0.66	15.68	1.08	10.59	-	-
PAD	1.71	60.18	0.72	5.23	0.68	11.34
PEP	-	-	0.91	5.76	0.78	8.96
POH	1.08	14.15	1.40	8.55	0.94	8.52
POU	0.41	13.91	1.22	7.43	-	-
SAG	0.89	11.62	1.41	8.56	-	-
SAN	0.83	13.80	0.94	10.63	-	-
SAR	0.88	32.49	0.81	5.14	0.75	19.38
SAV	1.08	17.92	0.66	4.00	-	-
SCL	1.07	14.67	1.27	9.87	-	-
STL	1.14	13.91	0.61	3.75	0.73	5.19
SUP	1.31	24.52	1.39	8.07	-	-
TRE	1.20	15.12	0.77	4.47	1.14	14.23
TRI	0.95	6.77	1.43	4.98	-	-
TUR	-	-	0.95	8.65	-	-
VAT	1.19	23.83	0.63	4.30	-	-
VIC	1.72	23.67	1.50	10.72	-	-

Continued on next page

Table C.1 – continued from previous page

Code	Declination		Inclination		Intensity	
	RMS	RMSdim [°]	RMS	RMSdim [°]	RMS	RMSdim [μT]
VOL	0.96	13.78	1.66	6.79	-	-
VUK	1.32	20.56	0.65	4.42	-	-
WAI	0.95	9.34	0.83	5.47	-	-
WAS	-	-	-	-	0.68	24.87
WIN	1.06	7.35	1.07	3.40	-	-
Ba	0.93	11.78	2.53	6.62	1.99	10.22
SoI	0.67	15.72	1.02	22.21	1.00	9.86
SoII	1.31	14.45	0.80	17.07	1.73	31.32

Table C.2: L_2 misfit of the model HFM-OL1.

Code	Declination		Inclination		Intensity	
	RMS	RMSdim [°]	RMS	RMSdim [°]	RMS	RMSdim [μT]
AAM	1.64	63.49	0.71	4.25	1.32	8.33
AD1	-	-	0.77	6.03	1.11	12.10
ANN	0.71	15.15	0.77	7.27	-	-
ARA	0.66	8.06	1.24	6.74	-	-
ASL	0.43	12.32	0.61	3.60	-	-
BAI	1.29	19.40	1.29	8.38	1.43	19.11
BAM	0.96	11.04	1.22	7.06	-	-
BAR	0.94	36.23	0.96	10.59	1.01	13.00
BEA	1.52	40.95	0.96	5.71	1.07	10.44
BEG	0.62	6.53	1.16	3.15	-	-
BI2	0.90	12.76	1.05	6.14	1.74	17.18
BIR	1.15	14.93	1.30	9.61	0.98	18.30
BLM	0.59	21.19	1.00	6.53	-	-
BOU	0.75	13.77	1.12	4.05	-	-
CAM	0.75	9.34	0.78	4.84	-	-
CHU	1.52	31.08	0.63	3.92	1.17	12.05
DES	0.97	16.45	1.15	10.33	-	-
EAC	0.88	31.03	0.90	9.41	0.79	16.83
EIF	0.75	6.43	0.86	4.24	-	-
ERH	0.91	13.75	0.90	8.73	-	-
ERL	1.12	13.54	1.77	11.03	-	-
ESC	1.00	21.97	1.07	6.79	0.88	9.50
FAN	1.13	15.81	0.87	9.96	-	-
FIN	0.63	7.54	0.77	4.43	-	-
FIS	0.89	13.12	1.30	8.45	-	-
FRG	1.07	17.49	0.59	3.85	0.75	10.12
FUR	0.75	11.70	0.59	3.81	0.82	17.75
GAR	1.41	29.83	1.28	8.26	0.80	10.00
GEI	0.62	6.15	0.58	3.02	-	-
GHI	0.64	10.09	0.85	6.43	0.21	12.27
GNO	0.61	21.86	0.78	6.11	-	-
GRE	1.15	23.80	0.59	3.70	-	-

Continued on next page

Table C.2 – continued from previous page

Code	Declination		Inclination		Intensity	
	RMS	RMSdim [°]	RMS	RMSdim [°]	RMS	RMSdim [μT]
HUR	1.05	30.03	0.85	6.92	-	-
ICE	1.27	27.49	0.71	4.56	-	-
KEI	0.61	21.94	0.62	4.33	-	-
KYL	1.20	16.20	1.08	6.86	-	-
LAM	1.31	42.58	0.91	7.16	-	-
LEB	0.71	11.11	0.64	3.75	1.02	12.30
LOM	1.12	10.74	0.80	3.29	-	-
LOU	0.99	46.06	1.40	10.63	-	-
LSC	1.23	14.94	0.70	4.48	0.87	21.44
MAR	0.90	12.39	1.15	6.37	-	-
MEE	1.21	29.65	1.64	10.10	-	-
MEZ	0.53	13.48	0.81	6.29	1.49	11.52
MNT	1.10	14.06	0.98	6.40	-	-
MOR	1.75	16.85	1.16	5.71	-	-
MOT	0.83	13.08	0.81	5.56	0.72	12.11
NAR	0.65	7.71	0.69	3.98	-	-
NAU	0.99	12.56	0.71	6.01	1.27	9.05
NEM	0.66	15.72	1.07	10.49	-	-
PAD	1.66	58.25	0.71	5.21	0.67	11.04
PEP	-	-	0.92	5.79	0.78	8.89
POH	1.08	14.90	1.39	8.54	0.93	8.52
POU	0.41	14.95	1.23	7.43	-	-
SAG	0.89	11.77	1.41	8.56	-	-
SAN	0.79	13.81	0.96	11.07	-	-
SAR	0.88	32.68	0.81	5.18	0.76	20.06
SAV	1.08	17.93	0.67	4.10	-	-
SCL	1.07	14.67	1.25	9.78	-	-
STL	1.15	14.00	0.61	3.72	0.73	5.18
SUP	1.32	24.57	1.40	8.06	-	-
TRE	1.25	15.92	0.82	4.62	1.08	13.53
TRI	0.95	6.83	1.43	5.01	-	-
TUR	-	-	0.94	8.61	-	-
VAT	1.18	23.65	0.63	4.22	-	-
VIC	1.72	23.70	1.54	11.04	-	-
VOL	0.96	13.75	1.66	6.79	-	-
VUK	1.31	20.41	0.65	4.57	-	-
WAI	0.92	9.07	0.88	5.84	-	-
WAS	-	-	-	-	0.65	23.49
WIN	1.19	7.65	1.11	3.57	-	-
Ba	0.93	11.91	2.51	6.57	2.00	10.26
SoI	0.67	15.92	1.02	22.21	0.99	9.85
SoII	1.30	14.53	0.80	17.07	1.73	31.37

Table C.3: L_2 misfit of the model HFM-BL1.

Code	Declination		Inclination		Intensity	
	RMS	RMSdim [°]	RMS	RMSdim [°]	RMS	RMSdim [μT]
AAM	1.57	47.33	0.79	4.79	1.37	8.99
AD1	-	-	0.90	6.89	1.42	14.78
ANN	0.67	19.60	0.75	7.04	-	-
ARA	0.76	19.64	1.70	9.31	-	-
ASL	0.52	8.30	0.84	4.37	-	-
BAI	1.27	18.90	1.25	7.94	1.33	18.87
BAM	0.99	11.15	1.40	7.75	-	-
BAR	0.98	26.29	1.06	11.57	1.26	16.76
BEA	1.61	43.38	0.98	5.91	1.17	10.59
BEG	0.66	13.09	1.27	3.47	-	-
BI2	0.78	9.37	1.76	9.55	2.07	22.90
BIR	1.14	16.54	1.38	10.38	0.95	15.92
BLM	0.92	11.34	1.05	6.84	-	-
BOU	0.75	18.50	1.21	4.05	-	-
CAM	0.65	8.76	0.85	5.24	-	-
CHU	1.50	33.57	0.89	5.51	1.04	10.67
DES	0.99	18.70	1.28	11.45	-	-
EAC	0.91	26.78	0.93	9.92	0.78	16.36
EIF	0.85	12.08	1.08	4.82	-	-
ERH	0.85	12.82	1.11	10.44	-	-
ERL	0.88	17.91	2.28	14.08	-	-
ESC	1.04	26.41	1.04	6.29	1.37	14.90
FAN	1.28	16.49	1.00	11.48	-	-
FIN	0.75	17.97	0.88	4.88	-	-
FIS	0.98	12.31	1.04	6.88	-	-
FRG	1.18	21.29	0.64	4.24	0.74	9.70
FUR	0.75	17.64	0.66	4.26	0.88	19.69
GAR	1.48	30.96	1.32	8.50	0.83	9.57
GEI	0.59	12.18	0.59	3.32	-	-
GHI	0.65	12.99	0.90	6.63	1.15	11.95
GNO	0.86	11.21	0.97	7.37	-	-
GRE	1.50	32.70	1.13	6.84	-	-
HUR	1.15	32.95	0.95	7.84	-	-
ICE	1.43	31.52	1.02	6.43	-	-
KEI	0.72	9.70	0.85	5.76	-	-
KYL	1.12	16.07	1.13	6.96	-	-
LAM	1.45	47.22	1.11	8.47	-	-
LEB	0.70	9.48	0.73	4.05	1.00	10.60
LOM	1.17	15.72	0.77	2.88	-	-
LOU	0.98	48.13	1.55	11.81	-	-
LSC	1.16	15.32	0.70	4.50	0.93	20.11
MAR	0.98	12.25	1.12	5.98	-	-
MEE	1.18	31.94	1.73	10.65	-	-
MEZ	0.51	16.58	0.83	6.46	1.45	10.88
MNT	1.00	12.80	1.05	6.85	-	-

Continued on next page

Table C.3 – continued from previous page

Code	Declination		Inclination		Intensity	
	RMS	RMSdim [°]	RMS	RMSdim [°]	RMS	RMSdim [μT]
MOR	1.70	19.44	1.20	5.88	-	-
MOT	0.82	17.48	0.89	6.06	0.77	12.76
NAR	0.72	14.34	0.68	3.91	-	-
NAU	0.98	18.98	0.76	6.49	1.23	8.75
NEM	0.68	19.13	1.12	10.92	-	-
PAD	2.16	75.91	0.78	5.70	0.86	15.18
PEP	-	-	0.93	5.94	0.85	8.81
POH	1.10	23.54	1.42	8.52	0.88	7.46
POU	0.55	6.47	0.91	4.94	-	-
SAG	0.92	11.81	1.53	9.10	-	-
SAN	0.96	16.33	1.04	12.15	-	-
SAR	0.89	34.94	0.79	4.84	0.81	19.20
SAV	1.14	22.69	0.60	3.78	-	-
SCL	1.14	15.39	1.64	12.73	-	-
STL	1.16	14.17	0.74	4.64	0.76	4.80
SUP	1.29	24.27	1.56	8.95	-	-
TRE	1.16	14.59	0.72	4.36	1.39	17.22
TRI	0.99	12.92	1.46	5.12	-	-
TUR	-	-	0.86	8.04	-	-
VAT	1.17	23.22	0.62	4.35	-	-
VIC	1.66	22.92	1.56	10.93	-	-
VOL	0.94	16.66	1.70	6.95	-	-
VUK	1.44	26.49	0.67	4.54	-	-
WAI	0.96	6.64	1.50	9.54	-	-
WAS	-	-	-	-	0.82	35.03
WIN	0.89	8.09	1.29	4.25	-	-
Ba	0.89	16.54	2.47	6.45	1.93	9.60
SoI	0.67	19.18	1.02	22.11	0.95	9.22
SoII	1.27	17.25	0.79	16.78	1.71	24.84

Table C.4: L_2 misfit of the model HFM-BL1.

Code	Declination		Inclination		Intensity	
	RMS	RMSdim [°]	RMS	RMSdim [°]	RMS	RMSdim [μT]
AAM	1.62	64.35	0.69	4.19	1.41	8.86
AD1	-	-	0.73	5.76	0.89	9.73
ANN	0.72	15.84	0.78	7.27	-	-
ARA	0.68	8.06	1.22	6.74	-	-
ASL	0.43	12.56	0.61	3.57	-	-
BAI	1.29	19.44	1.28	8.44	1.10	14.69
BAM	0.94	10.72	1.09	6.15	-	-
BAR	0.91	37.56	0.90	9.94	0.84	10.82
BEA	1.45	42.05	0.91	5.28	1.02	9.95
BEG	0.62	6.24	1.14	3.13	-	-
BI2	0.81	11.86	1.04	5.65	1.27	12.50

Continued on next page

Table C.4 – continued from previous page

Code	Declination		Inclination		Intensity	
	RMS	RMSdim [°]	RMS	RMSdim [°]	RMS	RMSdim [μT]
BIR	1.14	14.92	1.27	9.39	0.98	18.24
BLM	0.56	22.39	1.12	7.02	-	-
BOU	0.75	14.66	1.09	4.08	-	-
CAM	0.76	9.48	0.62	3.94	-	-
CHU	1.42	29.18	0.59	3.74	0.99	10.17
DES	0.95	16.02	1.13	10.09	-	-
EAC	0.87	33.13	0.89	9.26	0.79	16.96
EIF	0.71	6.00	0.81	3.96	-	-
ERH	0.93	13.89	0.88	8.62	-	-
ERL	1.13	13.82	1.68	10.19	-	-
ESC	1.04	22.21	0.95	6.10	0.81	8.70
FAN	1.08	15.34	0.85	9.75	-	-
FIN	0.60	7.11	0.76	4.41	-	-
FIS	0.91	14.45	1.27	8.25	-	-
FRG	1.06	16.55	0.58	3.93	0.76	10.33
FUR	0.76	11.79	0.60	3.81	0.82	17.82
GAR	1.43	30.12	1.29	8.35	0.80	9.89
GEI	0.66	6.35	0.60	3.14	-	-
GHI	0.64	9.79	0.84	6.29	1.21	12.16
GNO	0.59	22.45	0.79	6.22	-	-
GRE	1.13	23.64	0.57	3.56	-	-
HUR	1.08	31.02	0.87	7.02	-	-
ICE	1.24	27.09	0.71	4.62	-	-
KEI	0.60	23.32	0.60	4.18	-	-
KYL	1.17	15.85	1.08	6.75	-	-
LAM	1.33	43.15	0.97	7.57	-	-
LEB	0.69	11.93	0.64	4.15	1.05	12.81
LOM	1.05	10.12	0.83	3.40	-	-
LOU	1.00	47.11	1.38	10.72	-	-
LSC	1.25	15.33	0.68	4.34	0.86	21.37
MAR	0.84	13.56	1.13	6.22	-	-
MEE	0.98	23.98	1.57	9.69	-	-
MEZ	0.53	13.66	0.81	6.19	1.49	11.58
MNT	0.94	12.09	0.87	5.86	-	-
MOR	1.73	17.57	1.12	5.67	-	-
MOT	0.84	13.28	0.81	5.63	0.72	12.27
NAR	0.67	7.92	0.67	3.97	-	-
NAU	1.00	12.58	0.70	5.94	1.23	8.75
NEM	0.67	15.82	1.09	10.72	-	-
PAD	1.42	50.52	0.69	5.11	0.62	9.94
PEP	-	-	0.89	5.63	0.75	8.66
POH	1.05	14.30	1.41	8.41	0.96	8.89
POU	0.36	15.57	1.30	7.43	-	-
SAG	0.86	11.84	1.31	7.89	-	-
SAN	0.81	14.18	0.93	10.44	-	-

Continued on next page

Table C.4 – continued from previous page

Code	Declination		Inclination		Intensity	
	RMS	RMSdim [°]	RMS	RMSdim [°]	RMS	RMSdim [μT]
SAR	0.88	32.71	0.79	5.13	0.75	19.60
SAV	1.07	17.69	0.66	3.94	-	-
SCL	1.05	14.58	1.15	9.09	-	-
STL	1.11	13.46	0.61	3.76	0.72	5.15
SUP	1.31	24.49	1.41	8.15	-	-
TRE	1.12	13.86	0.72	4.26	0.96	12.01
TRI	0.93	6.62	1.43	4.99	-	-
TUR	-	-	0.96	9.22	-	-
VAT	1.21	24.58	0.64	4.42	-	-
VIC	1.70	23.31	1.45	10.28	-	-
VOL	0.95	13.68	1.66	6.79	-	-
VUK	1.30	19.83	0.65	4.59	-	-
WAI	0.90	9.51	0.85	5.68	-	-
WAS	-	-	-	-	0.50	17.55
WIN	1.22	8.03	1.04	3.28	-	-
Ba	0.93	12.01	2.52	6.61	2.01	10.27
SoI	0.68	16.02	1.02	22.18	1.00	9.96
SoII	1.32	15.06	0.80	16.96	1.71	31.14

Appendix D

Spatial distribution of residuals

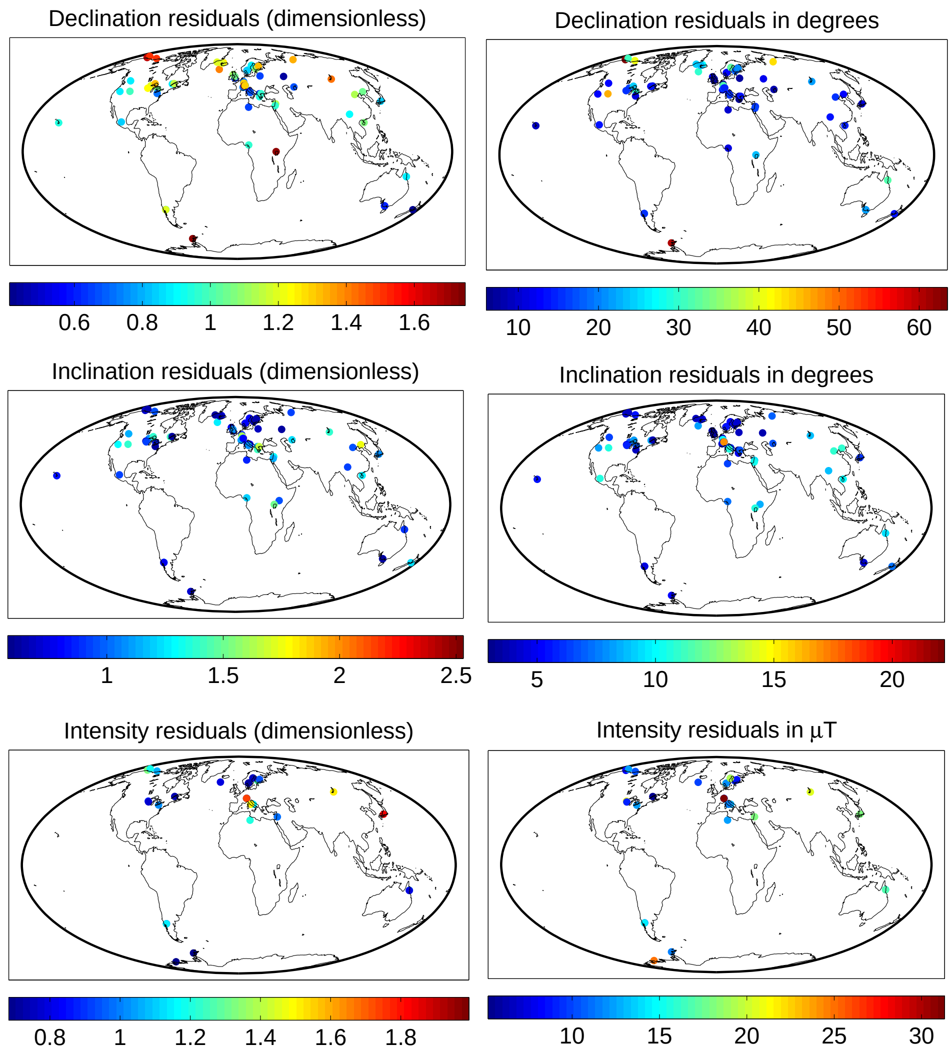

Figure D.1: Residuals as a function of location from the HFM-BL1 model.

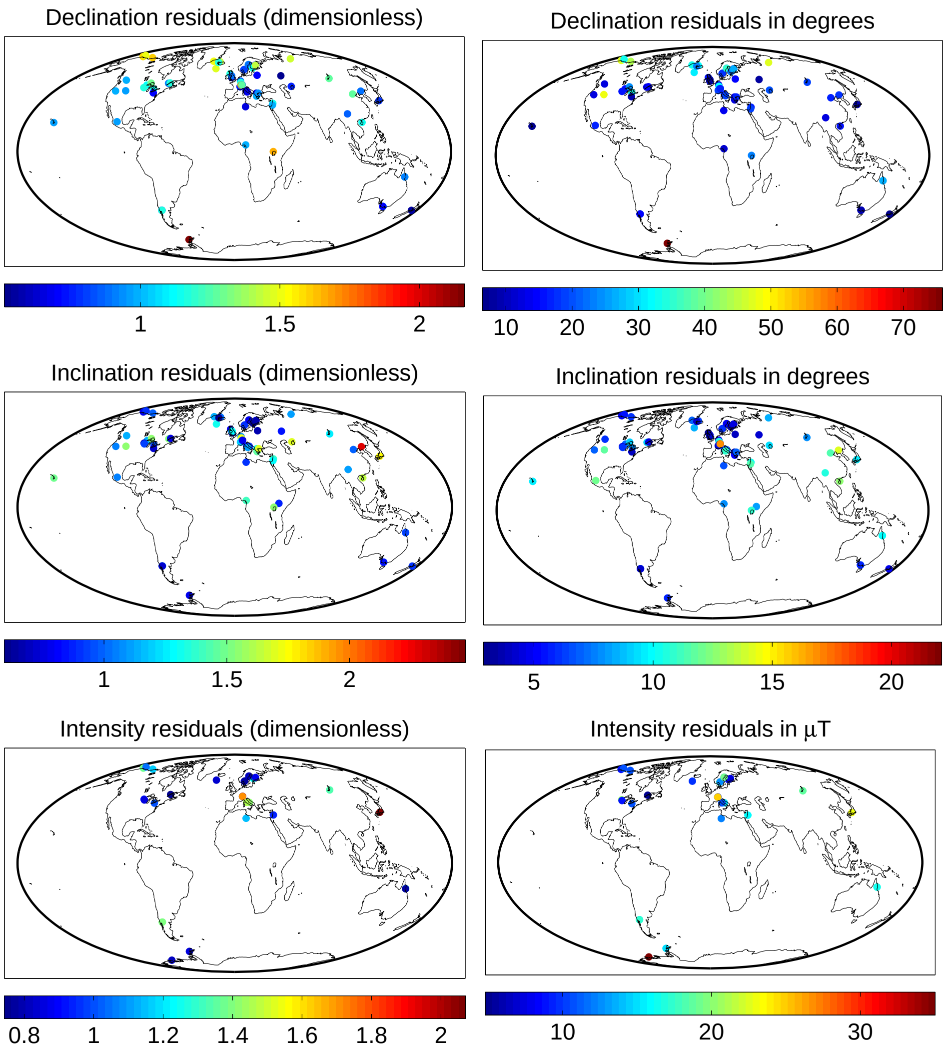

Figure D.2: Residuals as a function of location from the HFM-OL2 model.

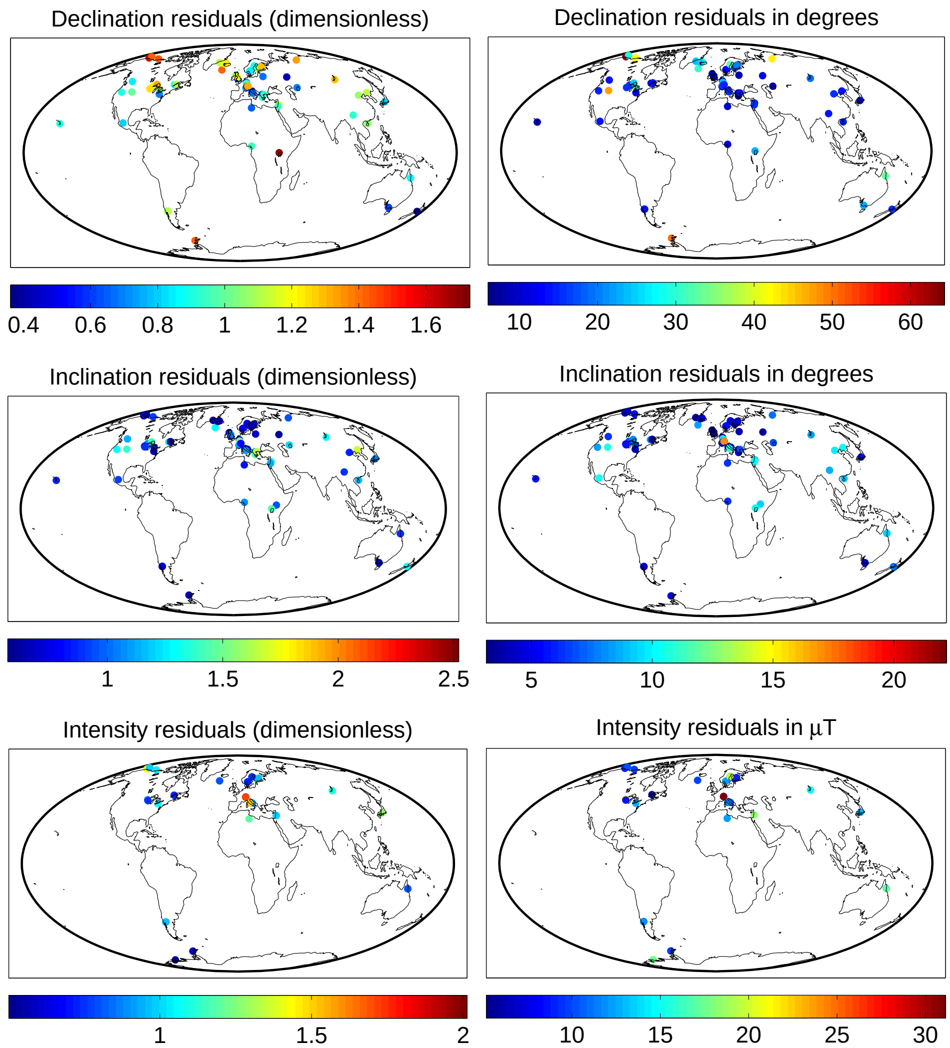

Figure D.3: Residuals as a function of location from the HFM-EL1 model.

Appendix E

Models predictions to all sediment magnetic records

Comparison of field model predictions to all lake sediment records: HFM-BL1 (green line), HFM-OL1 (pink curve), HFM-OL2 (red line), and HFM-EL1 (blue line). The CALS10k.1b model prediction (grey line) is plotted for reference. Lake sediment data are shown with green diamonds. Relative components, declination and paleointensity, have been calibrated prior to plotting.

AAM – Alaskan Margin, Arctic Sea: Declination

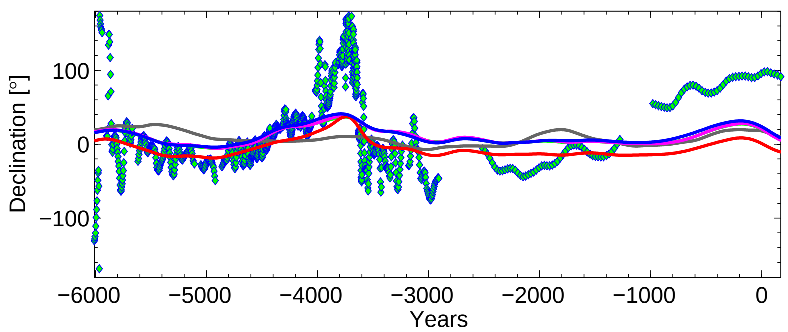

AAM – Alaskan Margin, Arctic Sea: Inclination

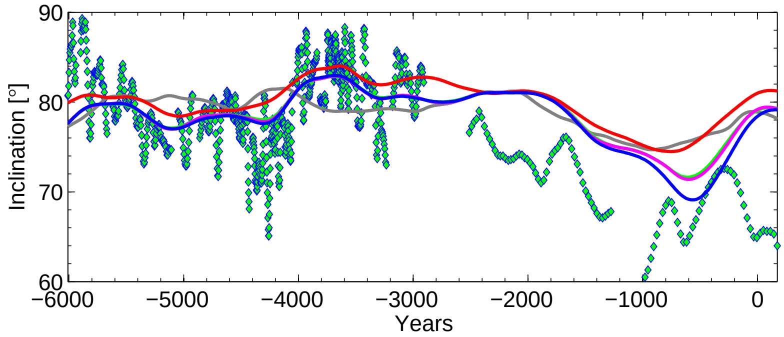

AAM – Alaskan Margin, Arctic Sea: Intensity

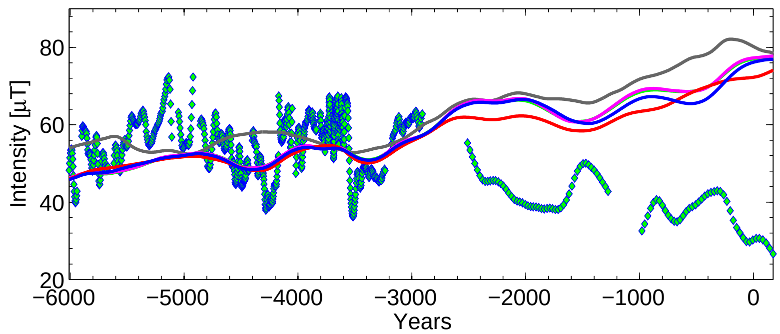

AD1 – Adriatic Sea, Italy: Inclination

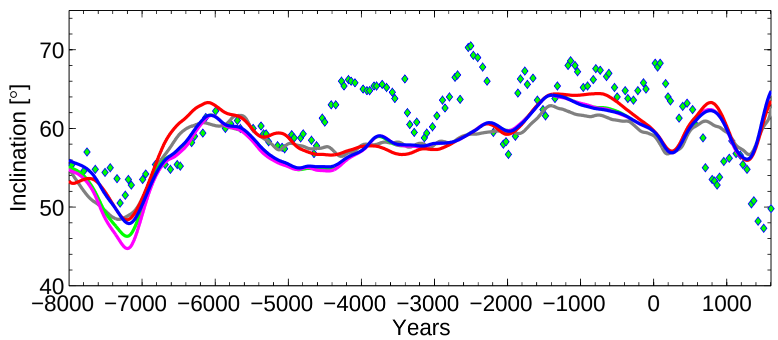

AD1 – Adriatic Sea, Italy: Intensity

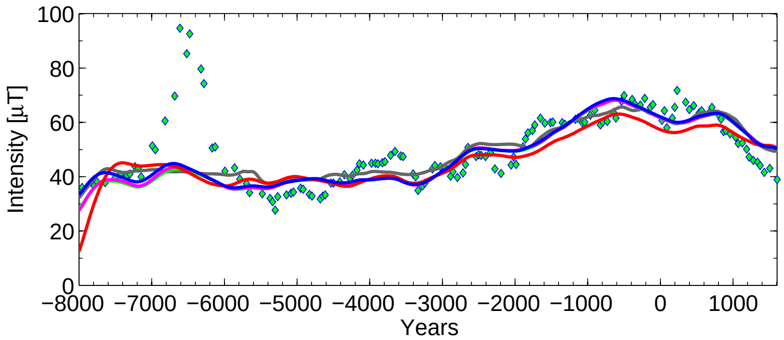

ANN – Lac d' Annecy, France: Declination

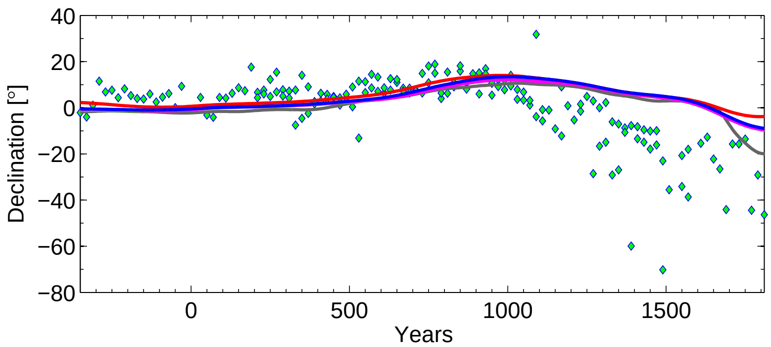

ANN – Lac d' Annecy, France: Inclination

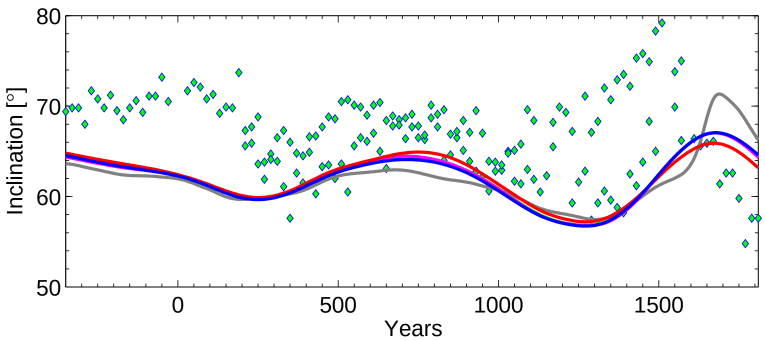

ARA – Lake Aral, Kazakhstan: Declination

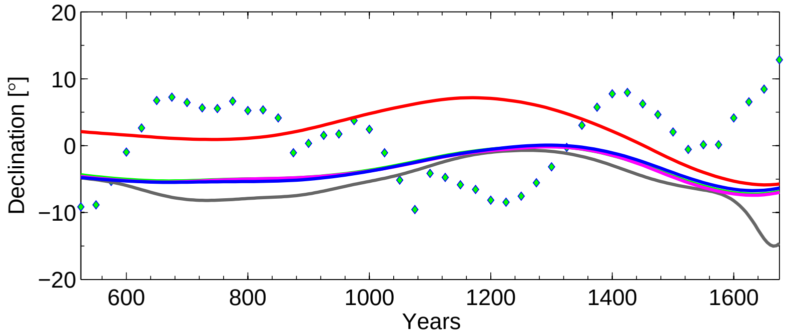

ARA – Lake Aral, Kazakhstan: Inclination

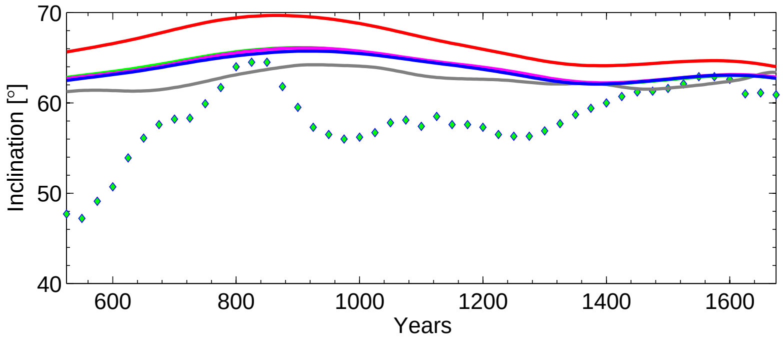

ASL – Lake Aslikul, Russia: Declination

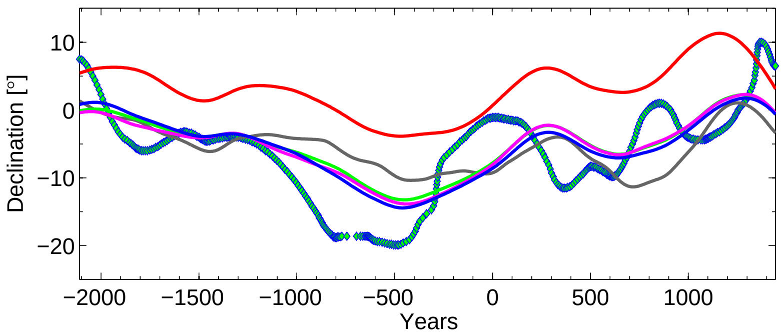

ASL – Lake Aslikul, Russia: Inclination

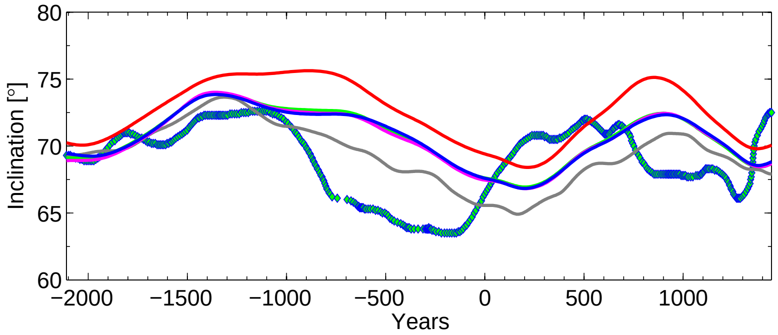

BAI – Lake Baikal, Russia: Declination

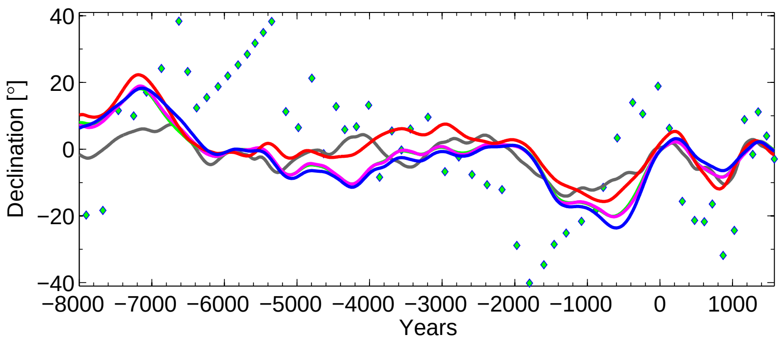

BAI – Lake Baikal, Russia: Inclination

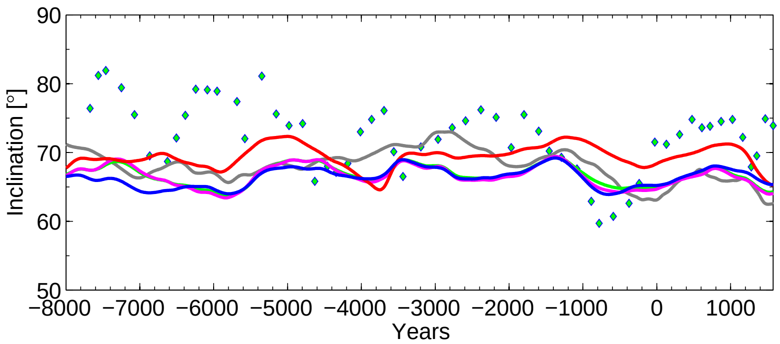

BAI – Lake Baikal, Russia: Intensity

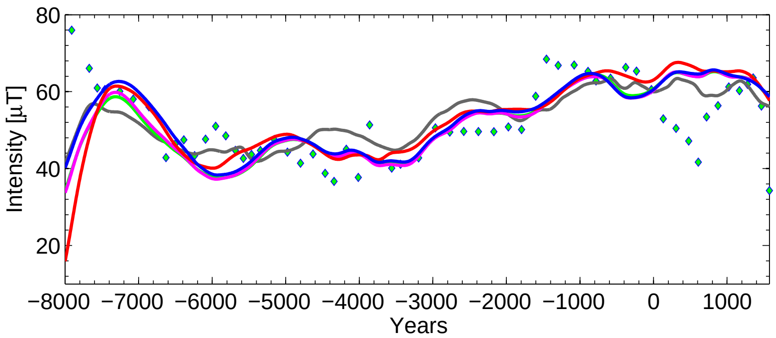

BAM – Lake Barombi Mbo, Cameroun: Declination

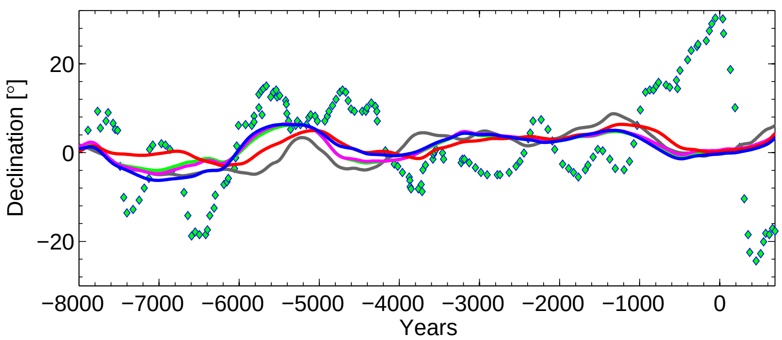

BAM – Lake Barombi Mbo, Cameroun: Inclination

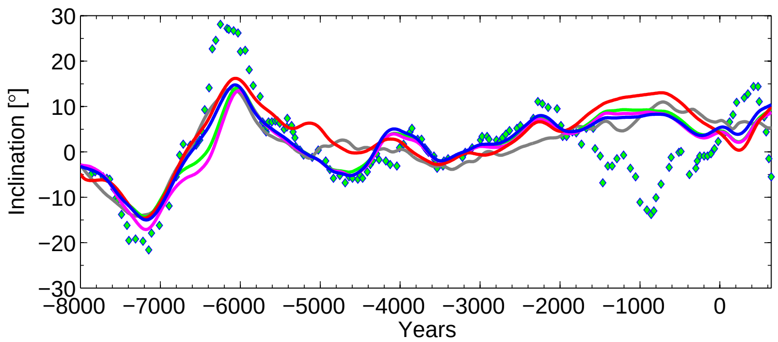

BAR – Lake Barrine, Australia: Declination

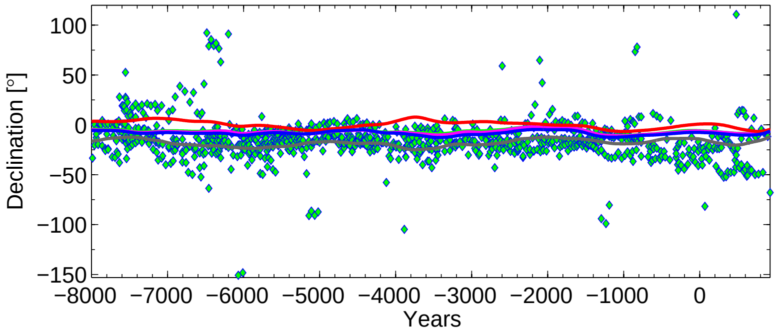

BAR – Lake Barrine, Australia: Inclination

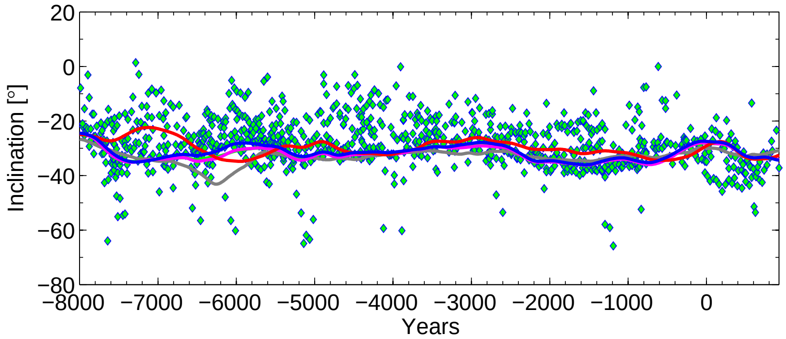

BAR – Lake Barrine, Australia: Intensity

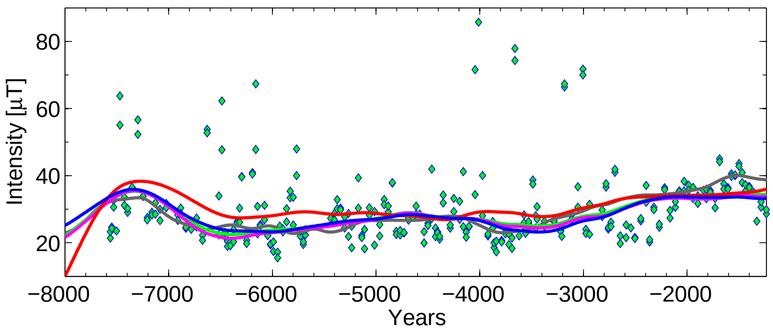

BEA – Beaufort Sea, Arctic Ocean: Declination

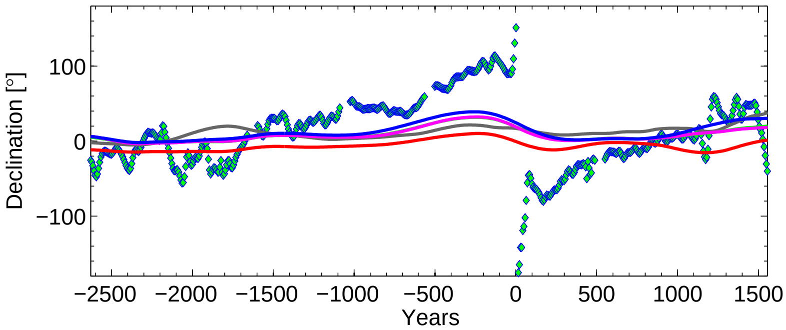

BEA – Beaufort Sea, Arctic Ocean: Inclination

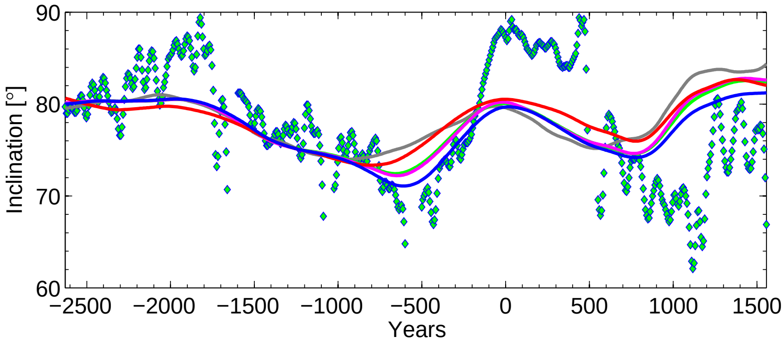

BEA – Beaufort Sea, Arctic Ocean: Intensity

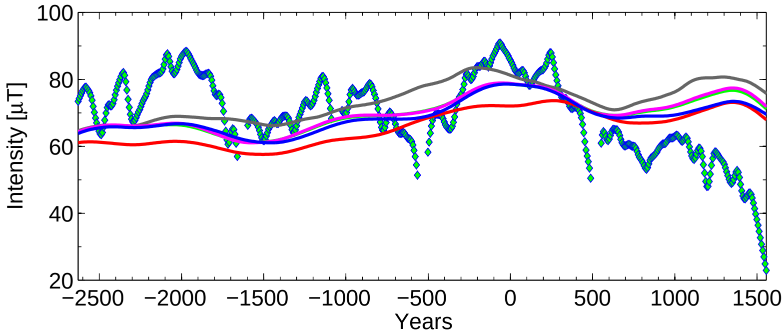

BEG – Lake Begoritis, Greece: Declination

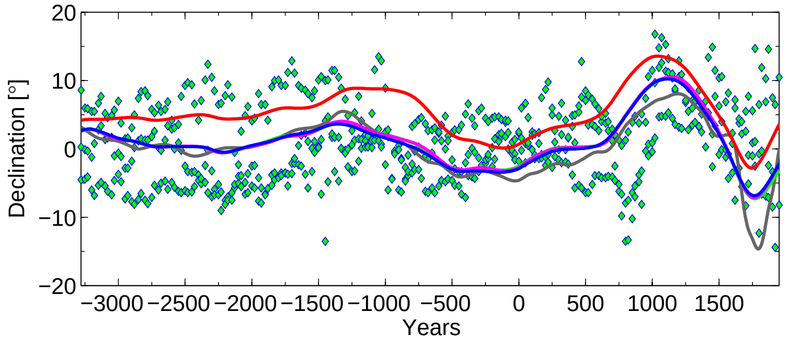

BEG – Lake Begoritis, Greece: Inclination

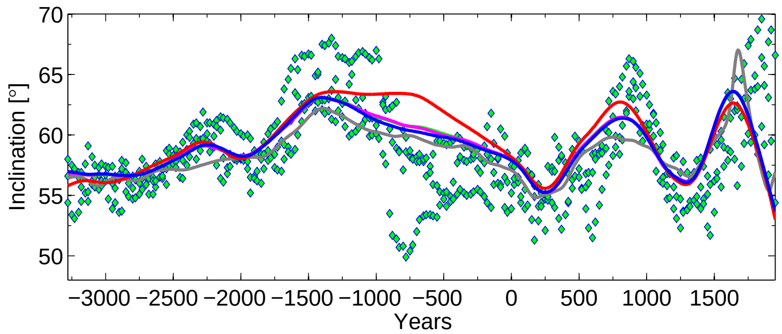

BI2 – Lake Biwa 2, Japan: Declination

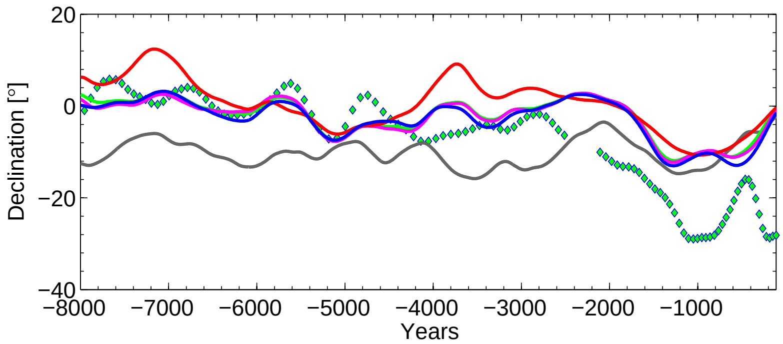

BI2 – Lake Biwa 2, Japan: Inclination

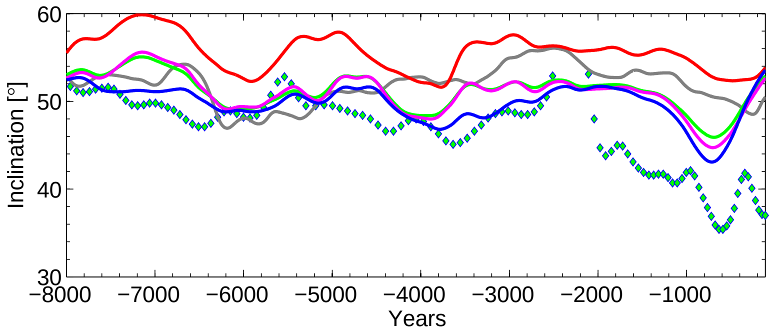

BI2 – Lake Biwa 2, Japan: Intensity

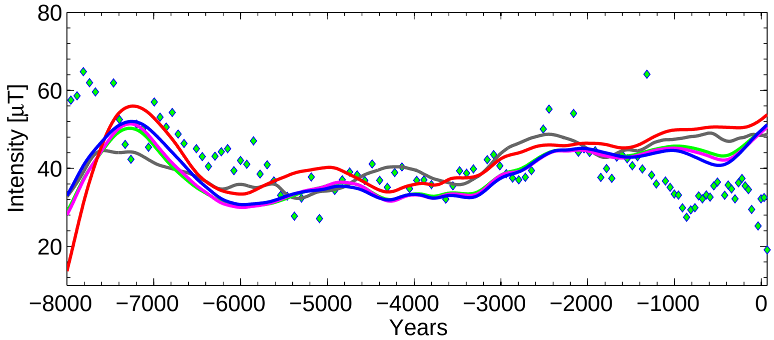

BIR – Birkat Ram, Israel: Declination

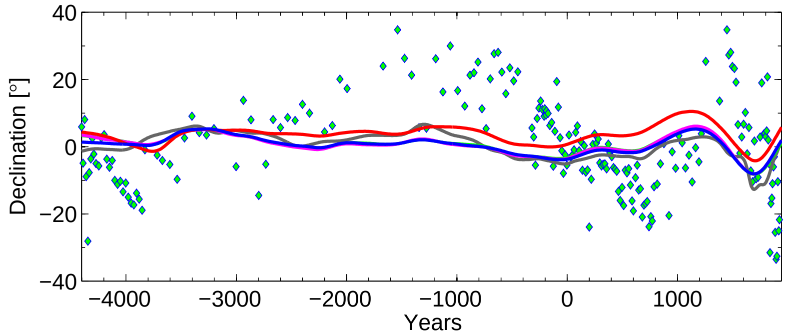

BIR – Birkat Ram, Israel: Inclination

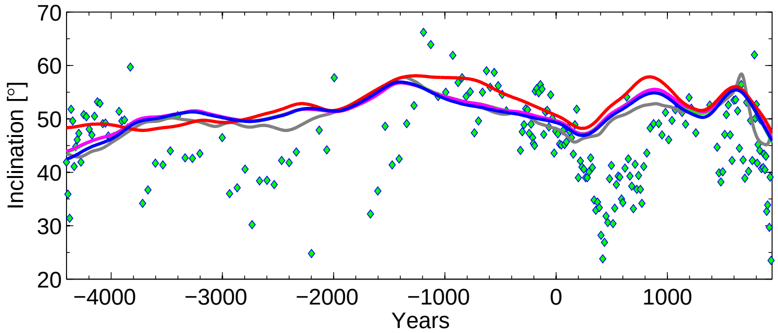

BIR – Birkat Ram, Israel: Intensity

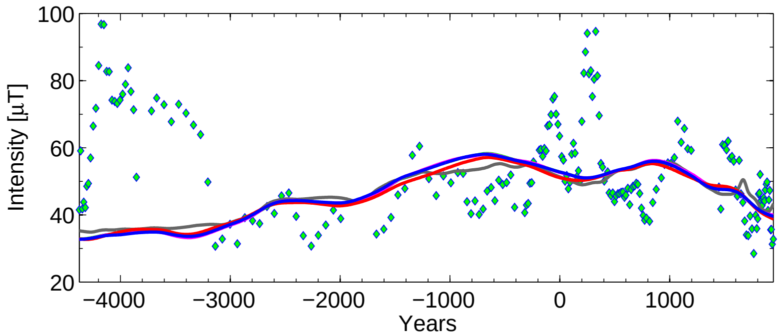

BLM – Lake Bullenmerri, Australia: Declination

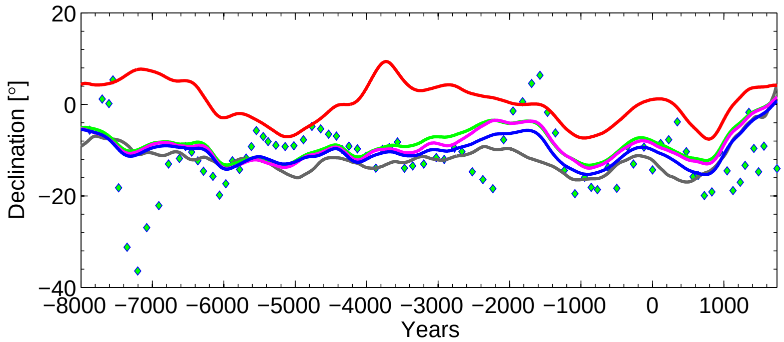

BLM – Lake Bullenmerri, Australia: Inclination

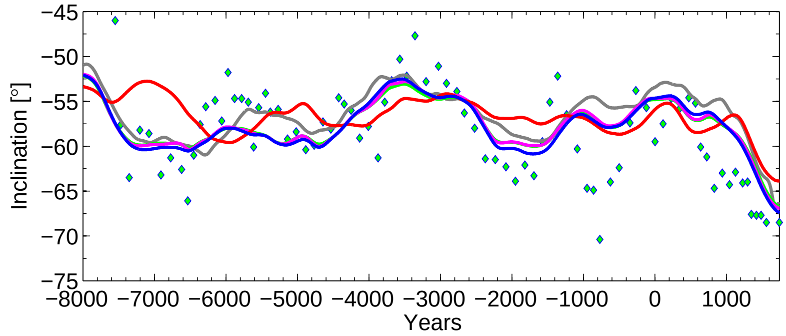

BOU – Lac du Bourget, France: Declination

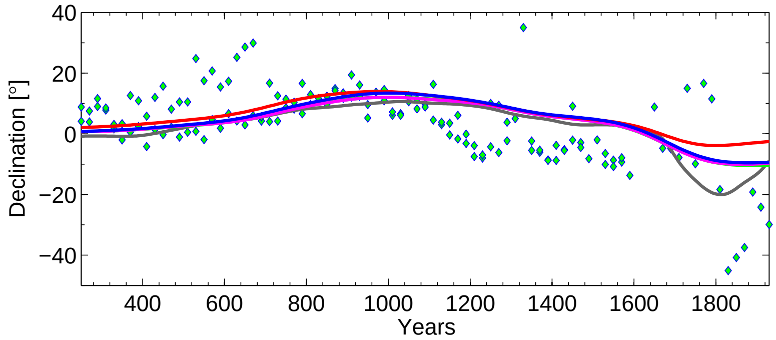

BOU – Lac du Bourget, France: Inclination

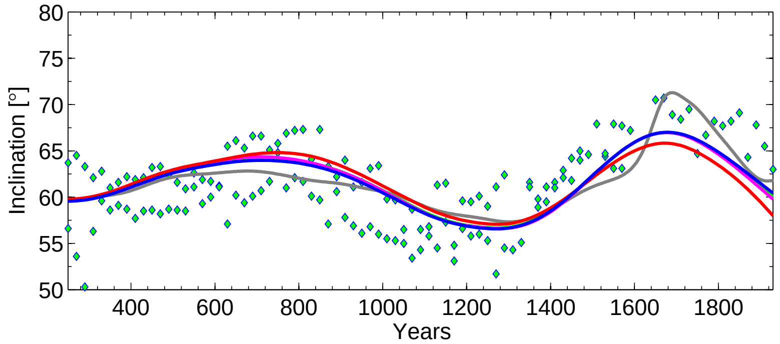

CAM – Brazo Campanario, Argentina: Declination

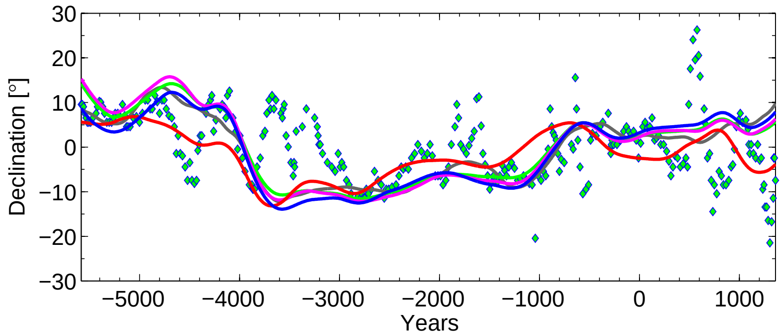

CAM – Brazo Campanario, Argentina: Inclination

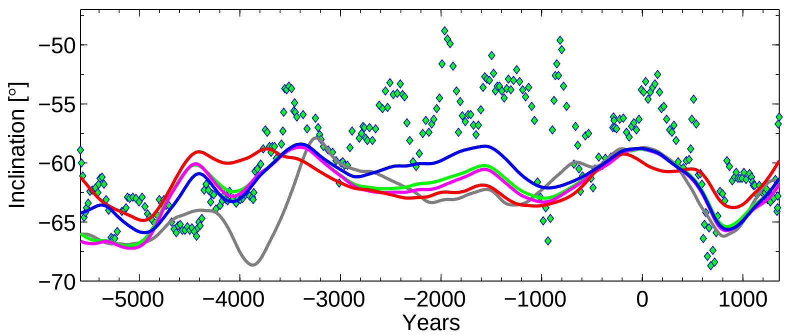

CHU – Chukchi Sea, Arctic Ocean: Declination

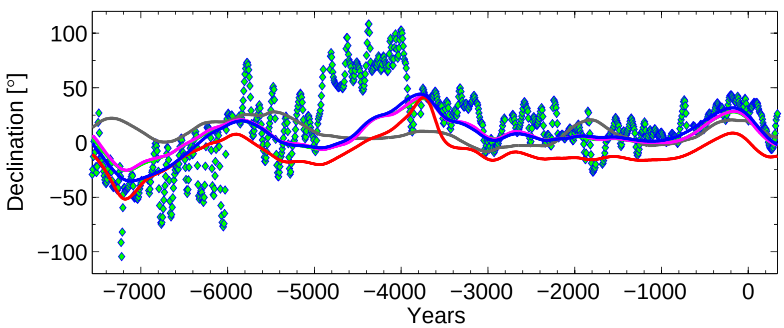

CHU – Chukchi Sea, Arctic Ocean: Inclination

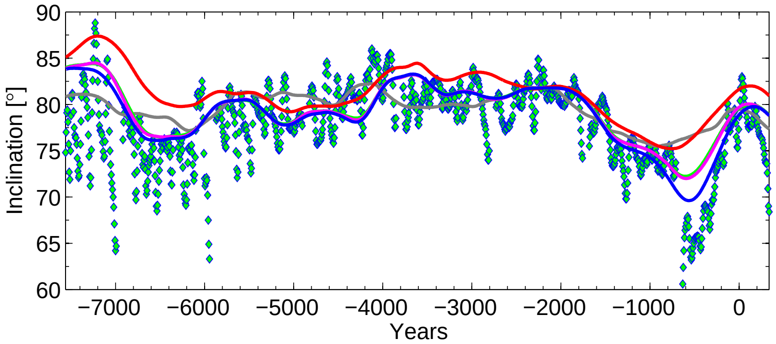

CHU – Chukchi Sea, Arctic Ocean: Intensity

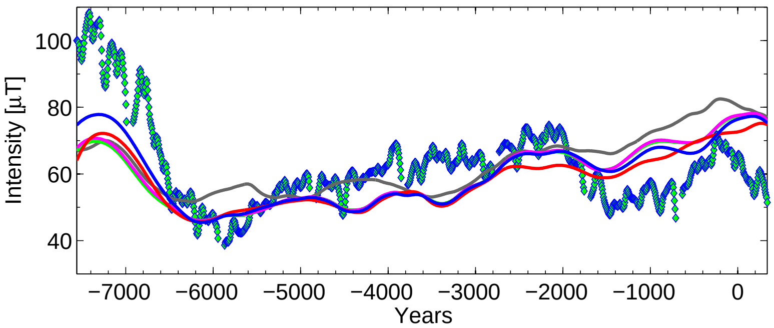

DES – Dead Sea, Israel: Declination

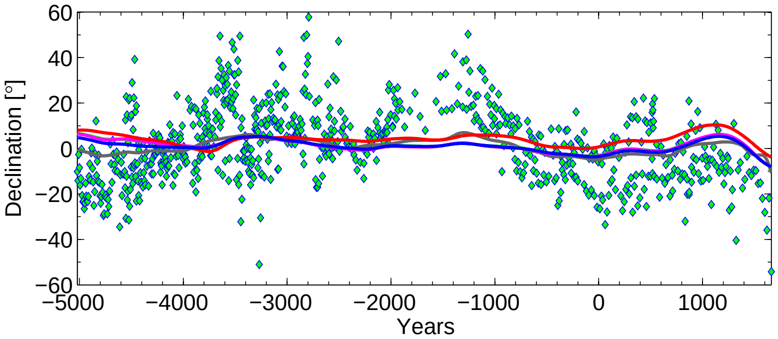

DES – Dead Sea, Israel: Inclination

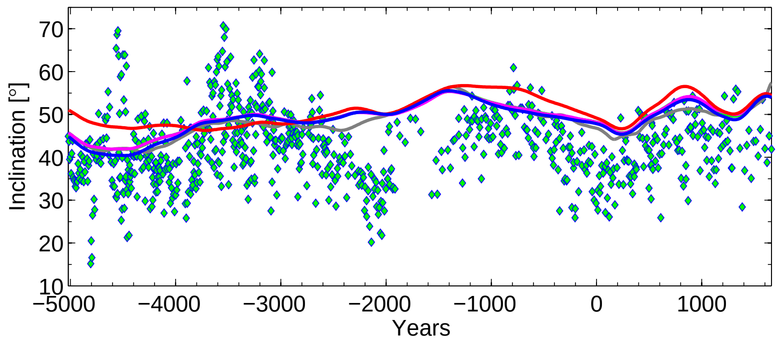

EAC – Lake Eacham, Australia: Declination

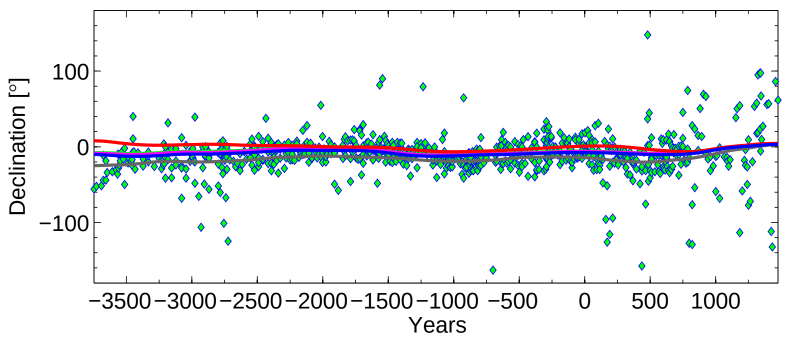

EAC – Lake Eacham, Australia: Inclination

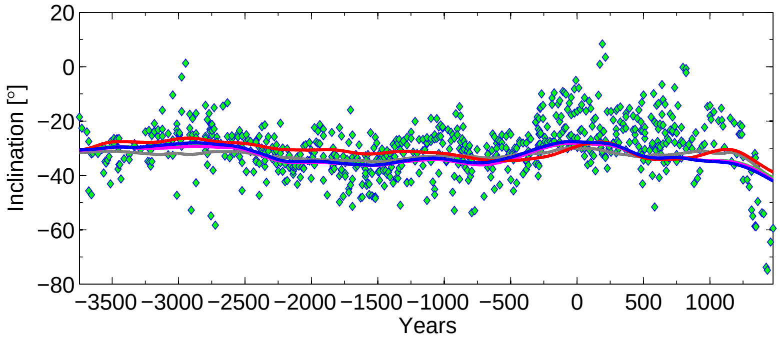

EAC – Lake Eacham, Australia: Intensity

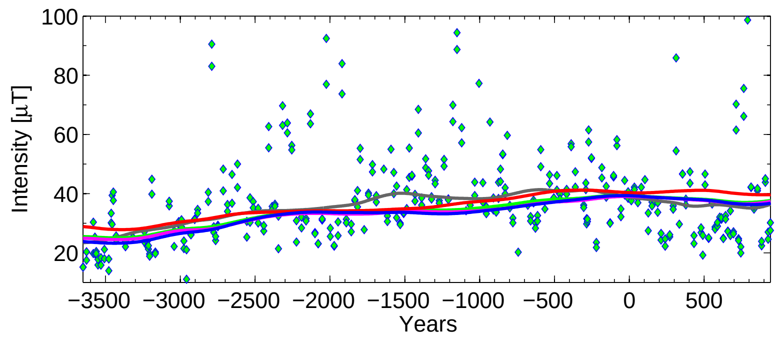

EIF – Eifel maars, Germany: Declination

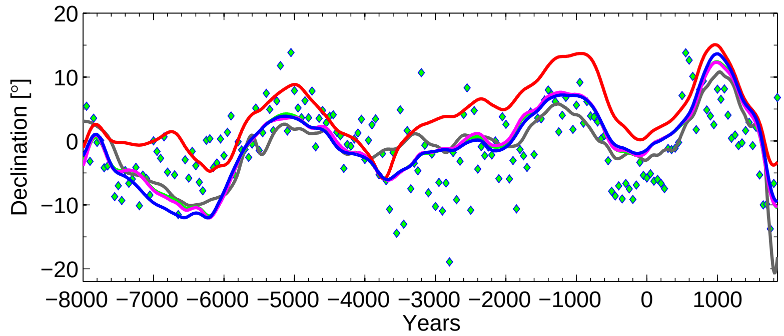

EIF – Eifel maars, Germany: Inclination

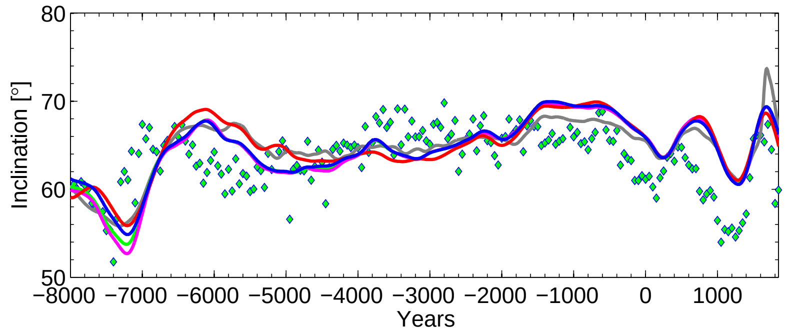

ERH – Erhai Lake, China: Declination

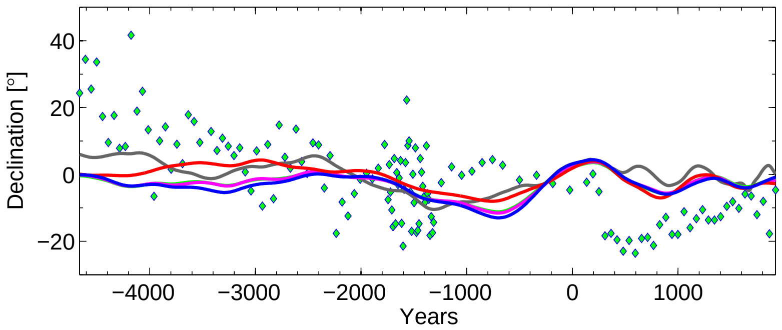

ERH – Erhai Lake, China: Inclination

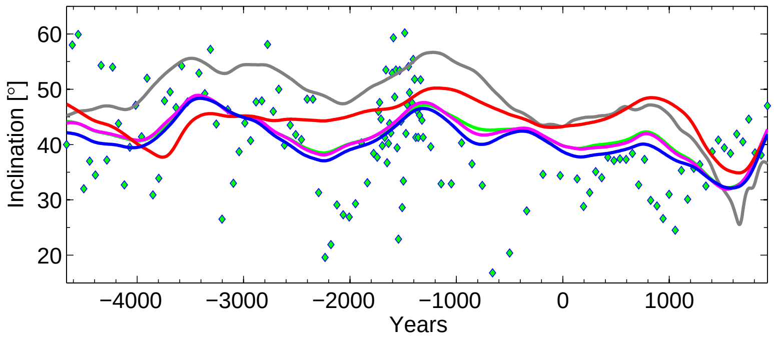

ERL – Erlongwan Lake, China: Declination

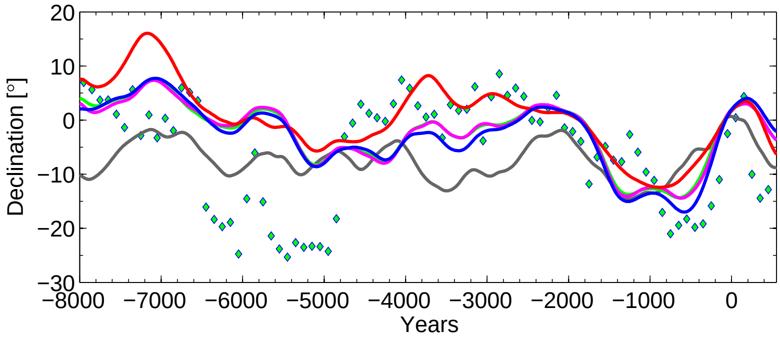

ERL – Erlongwan Lake, China: Inclination

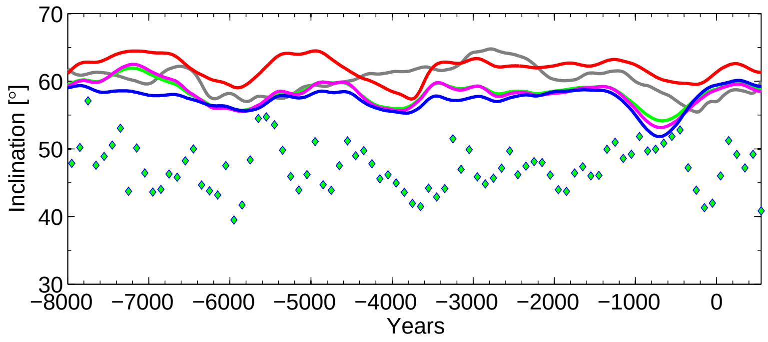

ESC – Lake Escondido, Argentina: Declination

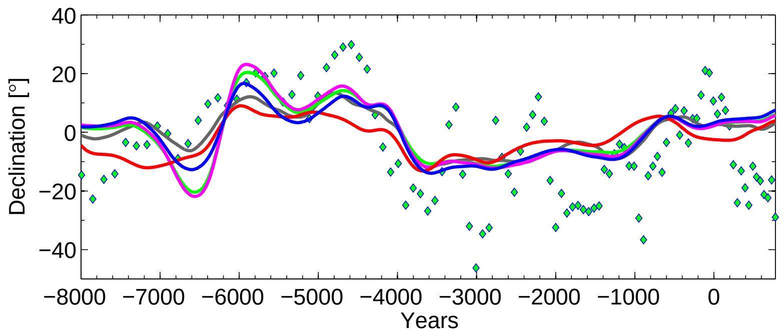

ESC – Lake Escondido, Argentina: Inclination

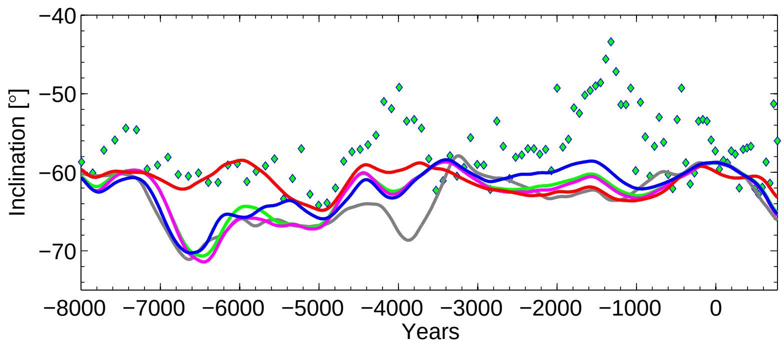

ESC – Lake Escondido, Argentina: Intensity

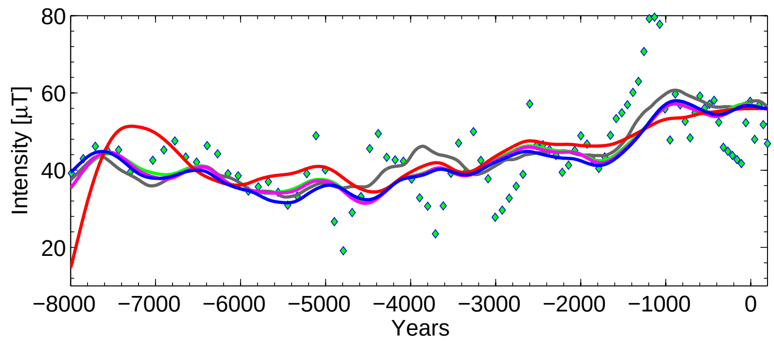

FAN – Lake Fangshan, China: Declination

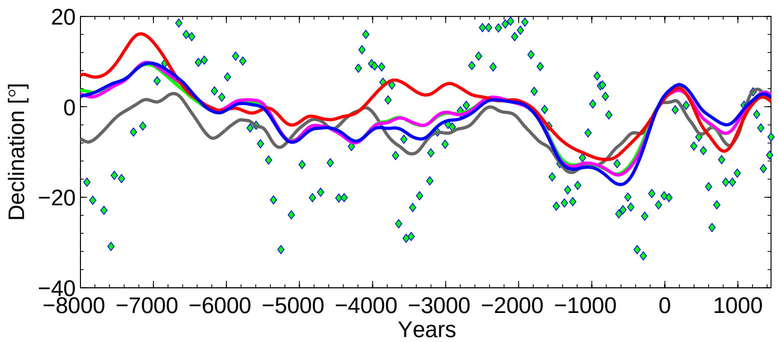

FAN – Lake Fangshan, China: Inclination

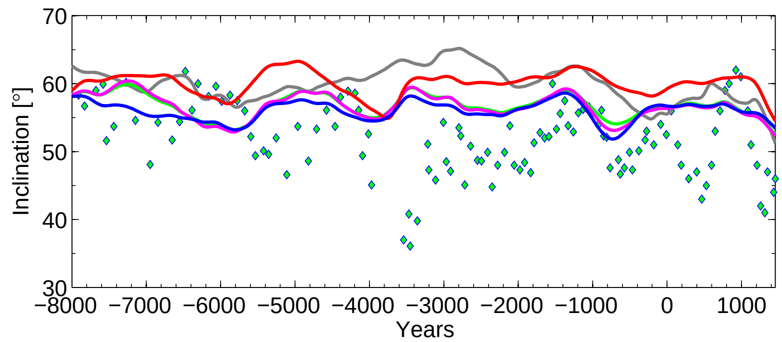

FIN – Finnish Lakes, Finland: Declination

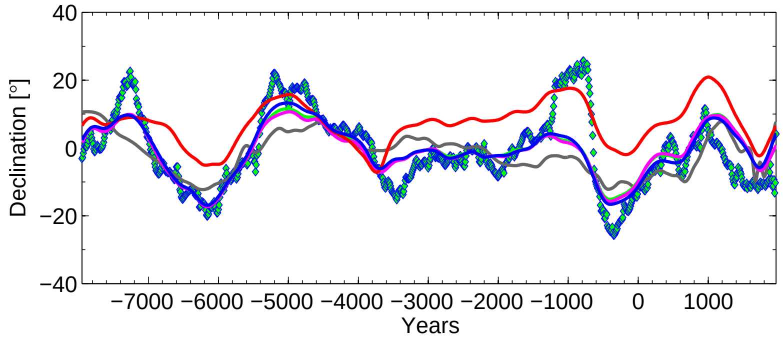

FIN – Finnish Lakes, Finland: Inclination

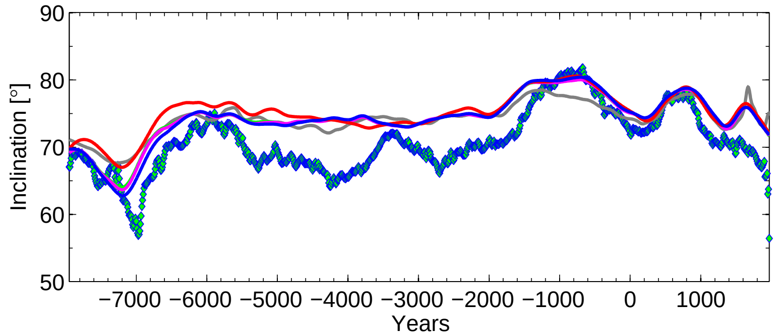

FIS – Fish Lake, USA: Declination

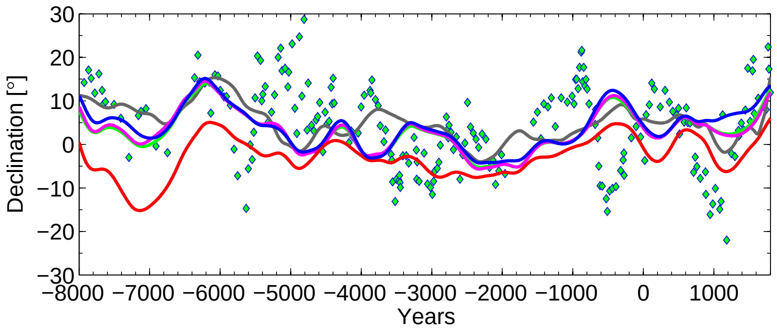

FIS – Fish Lake, USA: Inclination

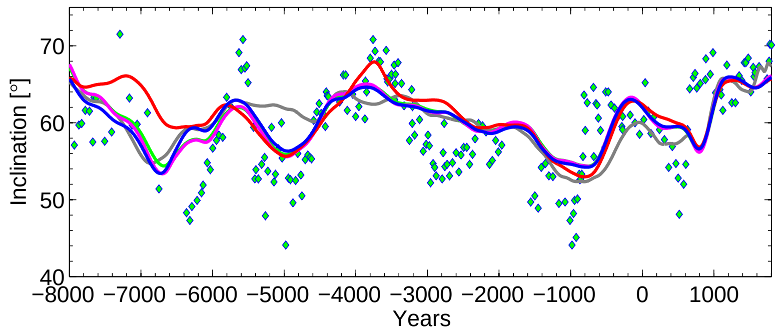

FRG – Frängsjön, Sweden: Declination

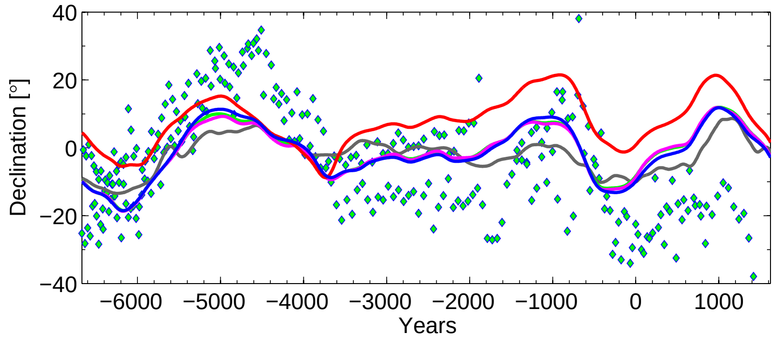

FRG – Frängsjön, Sweden: Inclination

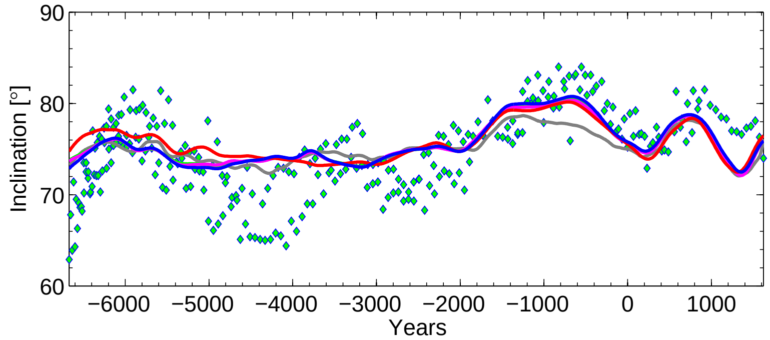

FRG – Frängsjön, Sweden: Intensity

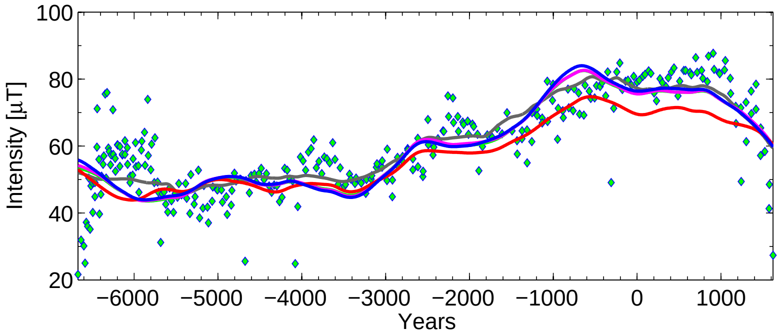

FUR – Furskogstjärnet, Sweden: Declination

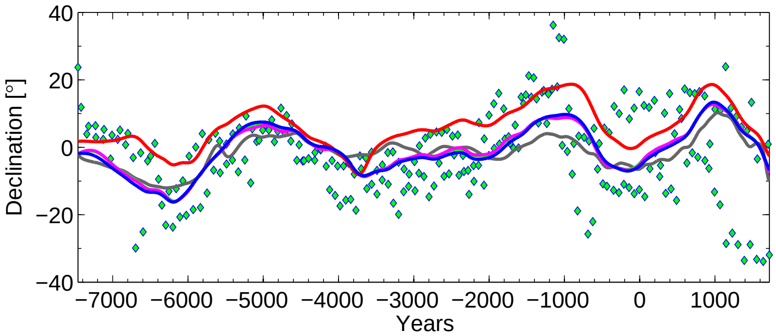

FUR – Furskogstjärnet, Sweden: Inclination

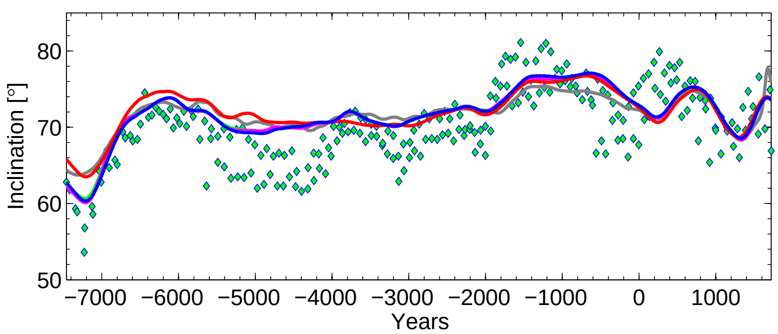

FUR – Furskogstjärnet, Sweden: Intensity

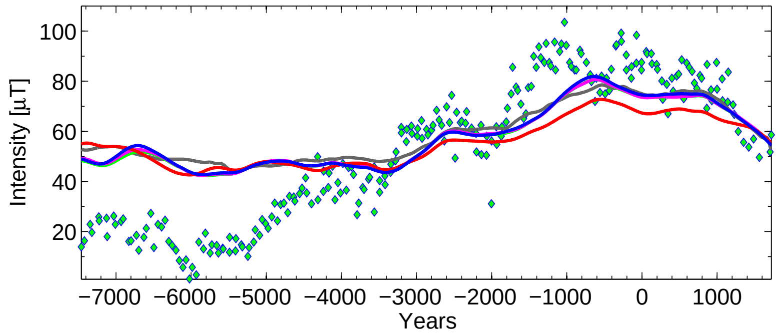

GAR – Gardar Drift, North Atlantic: Declination

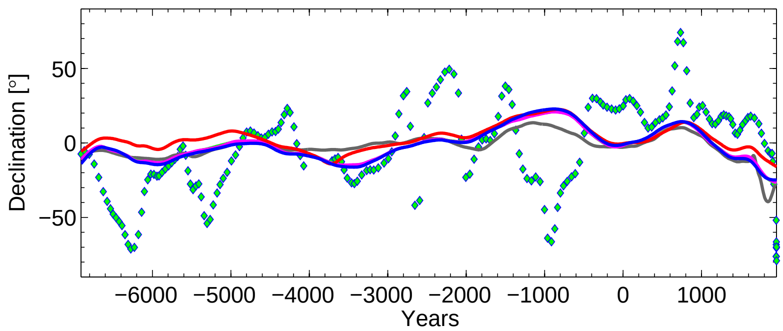

GAR – Gardar Drift, North Atlantic: Inclination

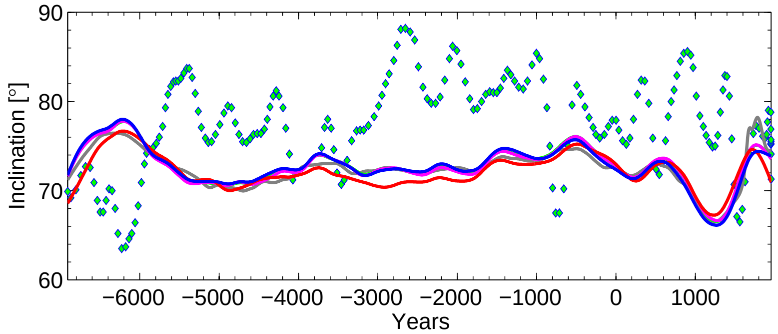

GAR – Gardar Drift, North Atlantic: Intensity

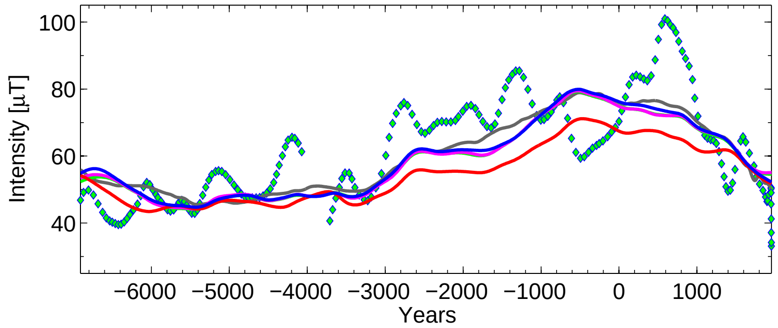

GEI – Llyn Geirionydd, UK: Declination

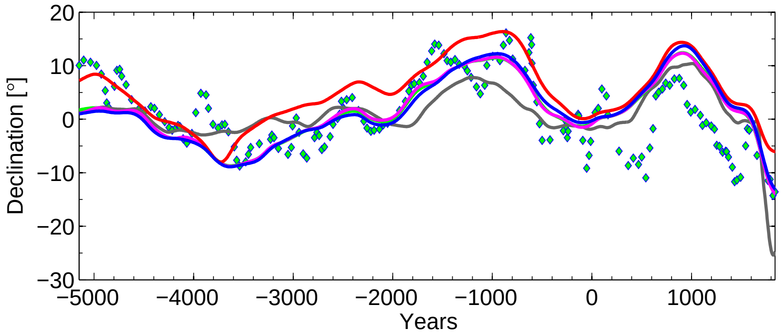

GEI – Llyn Geirionydd, UK: Inclination

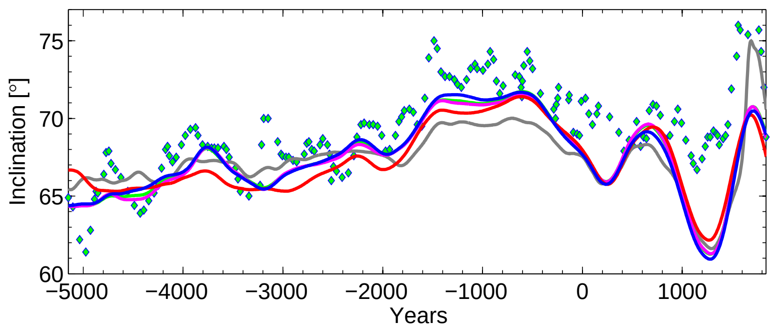

GHI – Cape Ghir, NW Afr. Margin: Declination

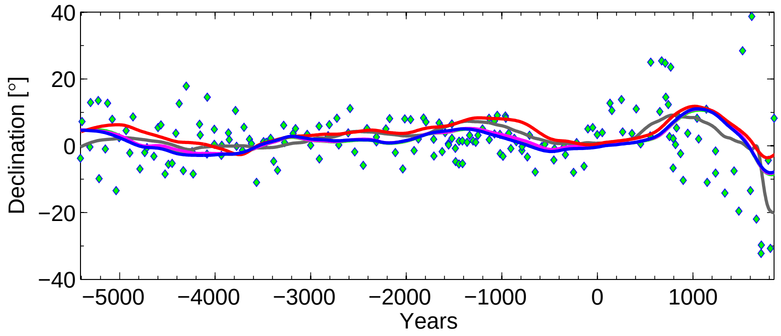

GHI – Cape Ghir, NW Afr. Margin: Inclination

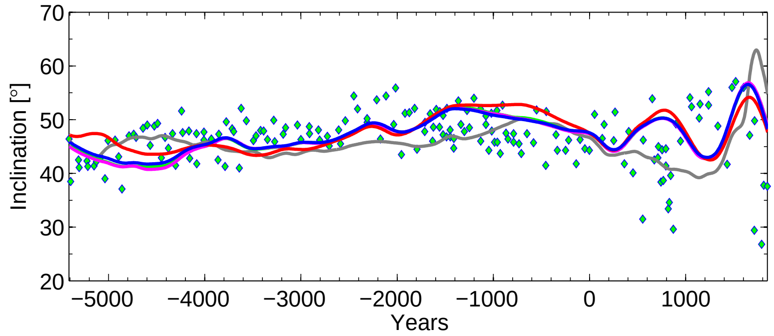

GHI – Cape Ghir, NW Afr. Margin: Intensity

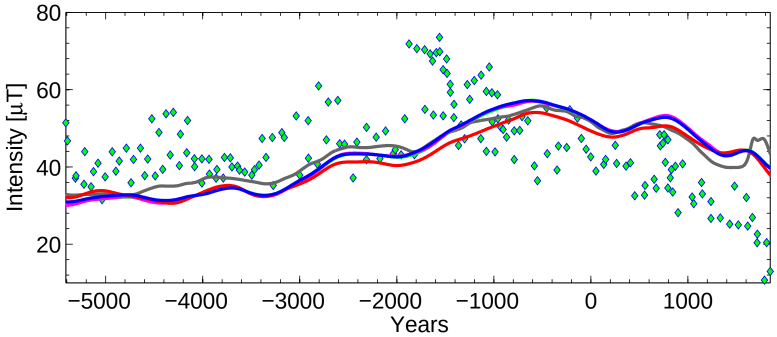

GNO – Lake Gnotuk, Australia: Declination

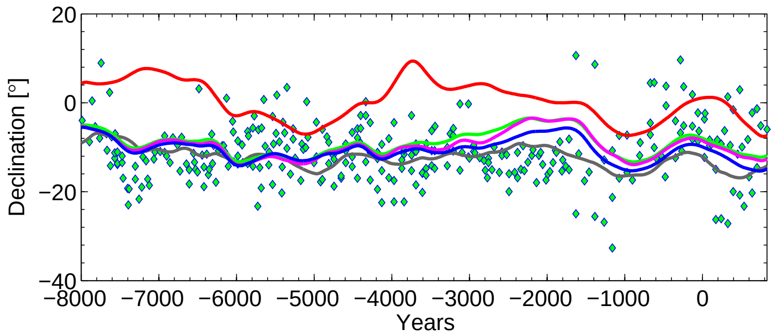

GNO – Lake Gnotuk, Australia: Inclination

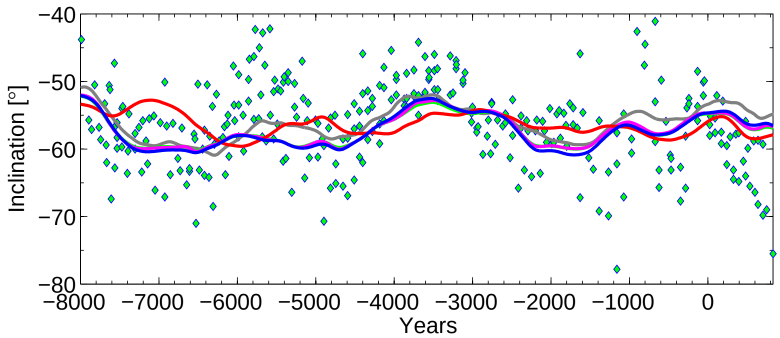

GRE – Greenland, North Atlantic: Declination

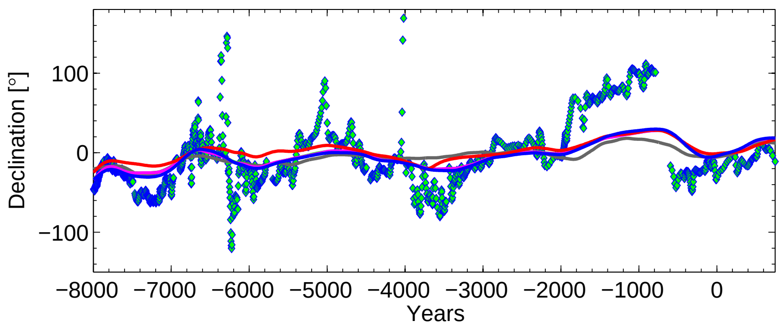

GRE – Greenland, North Atlantic: Inclination

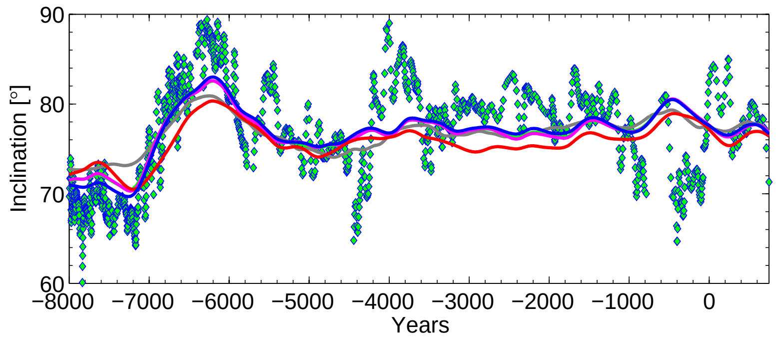

HUR – Lake Huron, USA: Declination

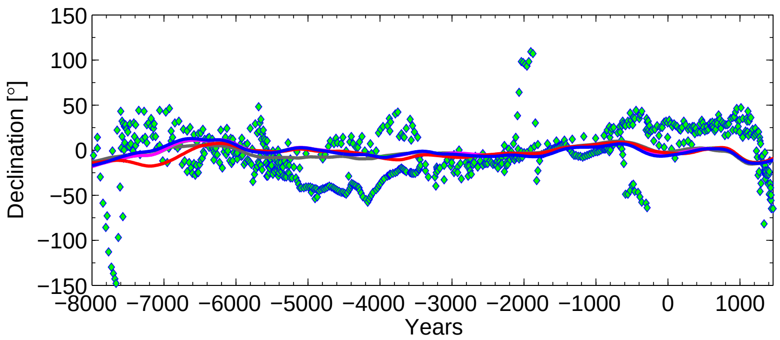

HUR – Lake Huron, USA: Inclination

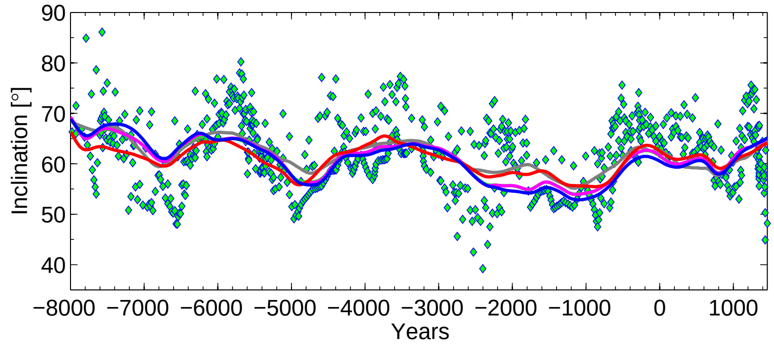

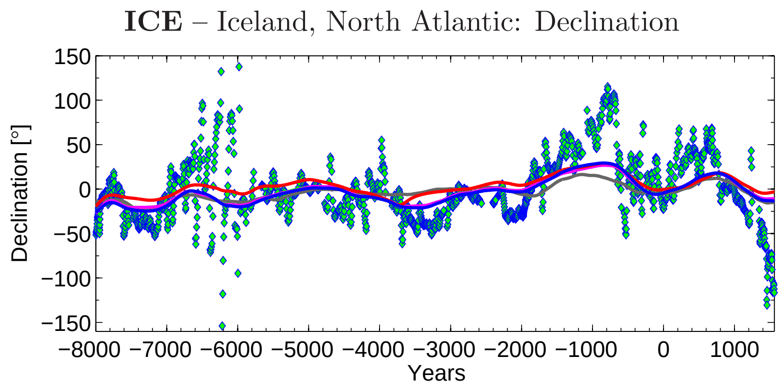
ICE – Iceland, North Atlantic: Declination
Declination [°]
Years

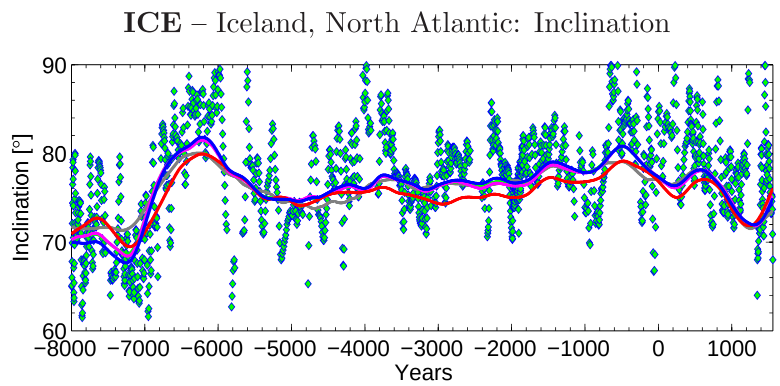
ICE – Iceland, North Atlantic: Inclination
Inclination [°]
Years

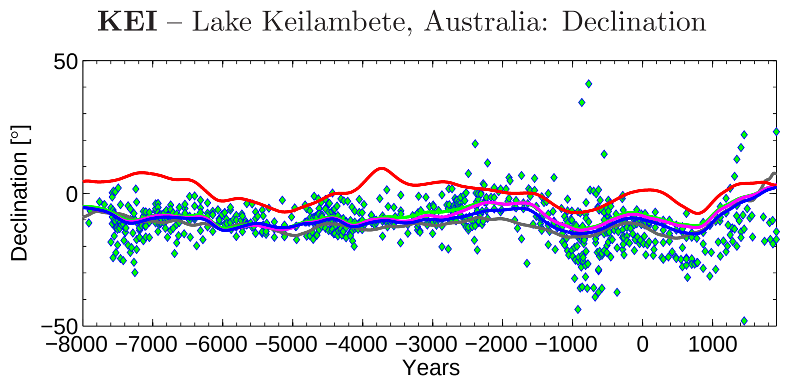
KEI – Lake Keilambete, Australia: Declination
Declination [°]
Years

KEI – Lake Keilambete, Australia: Inclination

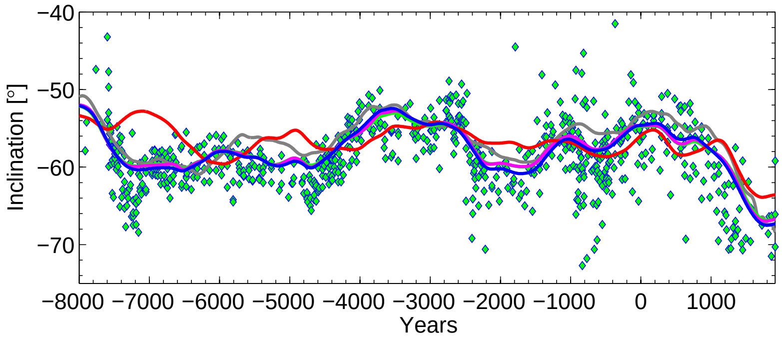

KYL – Kylen Lake, Minnesota: Declination

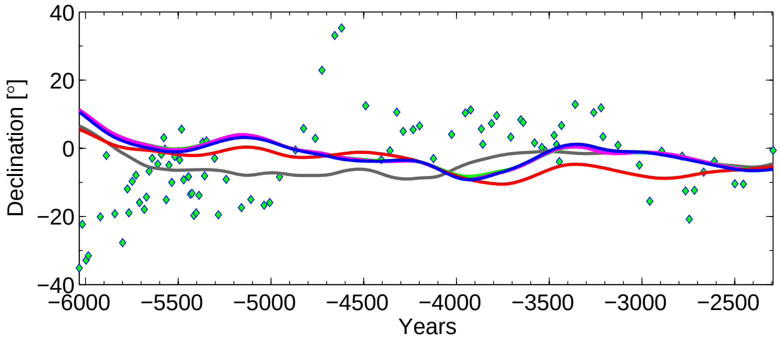

KYL – Kylen Lake, Minnesota: Inclination

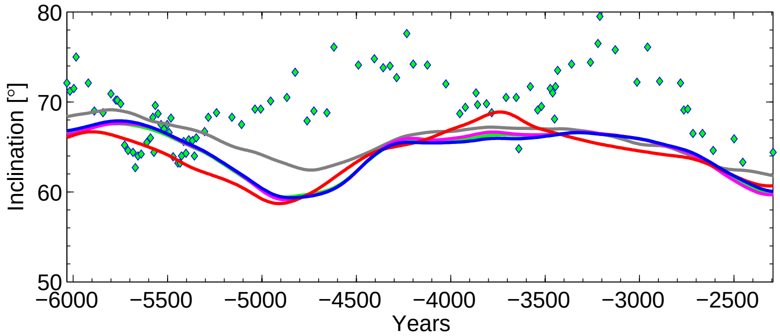

LAM – Lake Lama, Russia: Declination

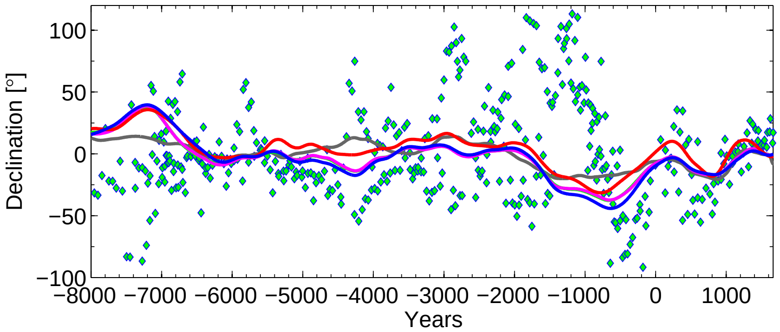

LAM – Lake Lama, Russia: Inclination

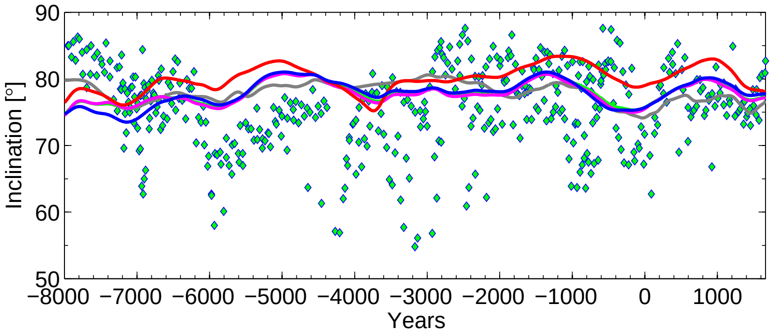

LEB – Lake LeBoeuf, USA: Declination

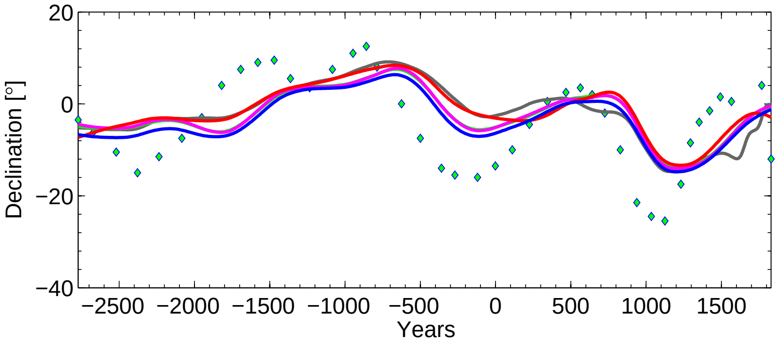

LEB – Lake LeBoeuf, USA: Inclination

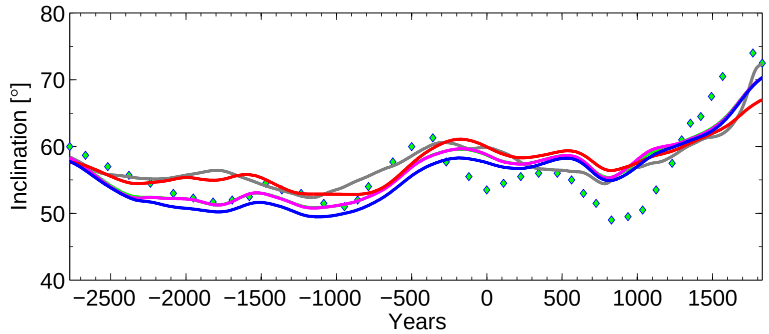

LEB – Lake LeBoeuf, USA: Intensity

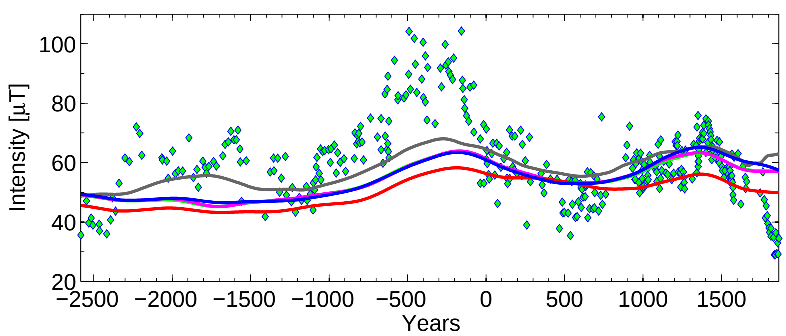

LOM – Loch Lomond, UK: Declination

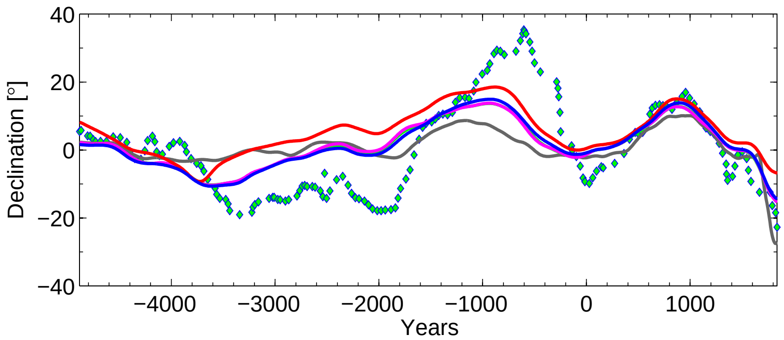

LOM – Loch Lomond, UK: Inclination

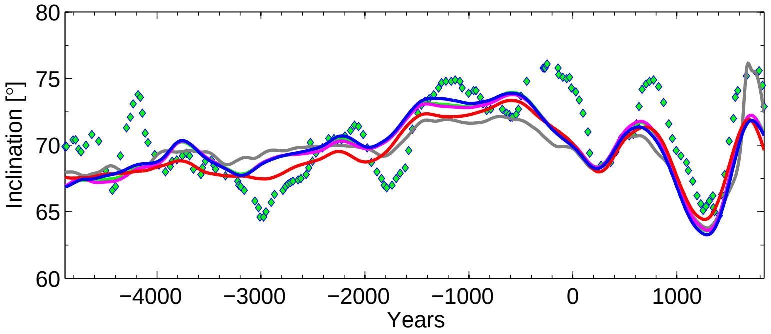

LOU – Louis Lake, USA: Declination

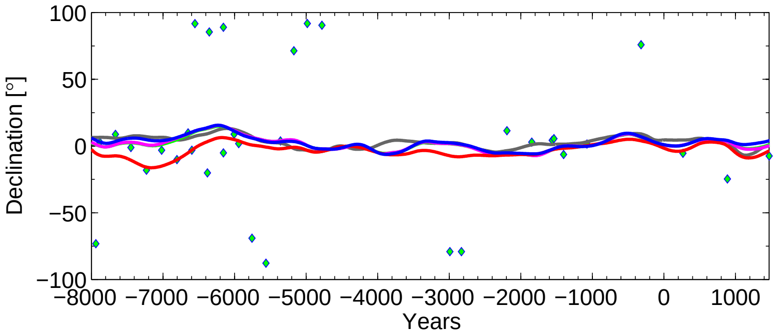

LOU – Louis Lake, USA: Inclination

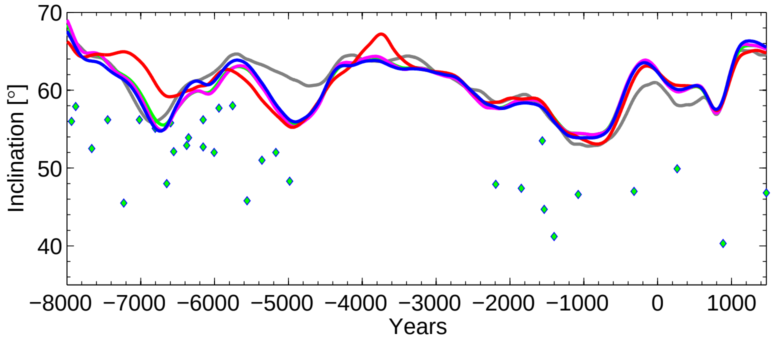

LSC – Lake St.Croix, USA: Declination

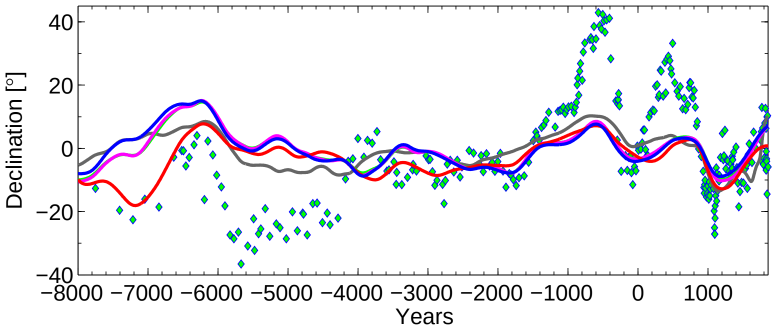

LSC – Lake St.Croix, USA: Inclination

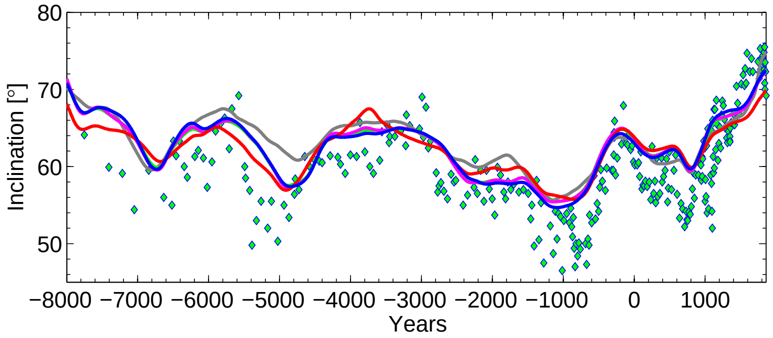

LSC – Lake St.Croix, USA: Intensity

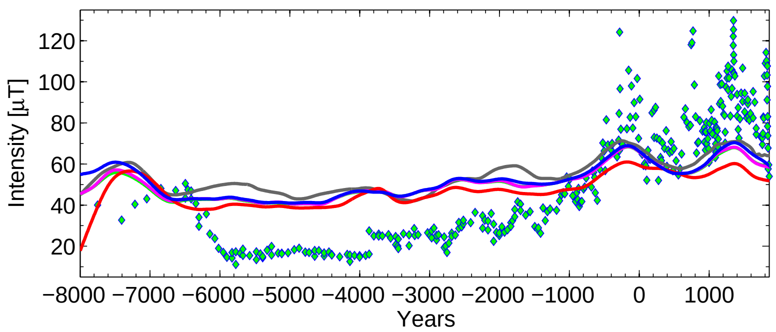

MAR – Mara Lake, Canada: Declination

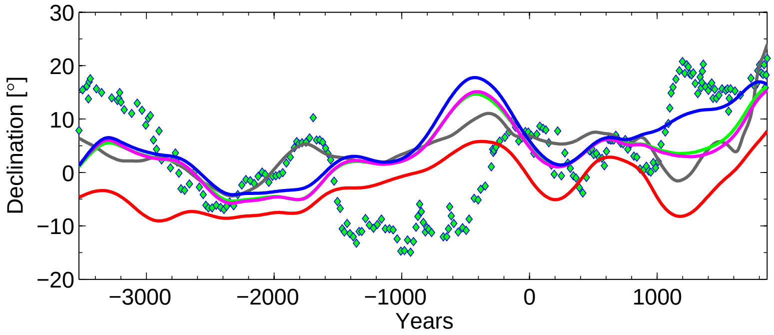

MAR – Mara Lake, Canada: Inclination

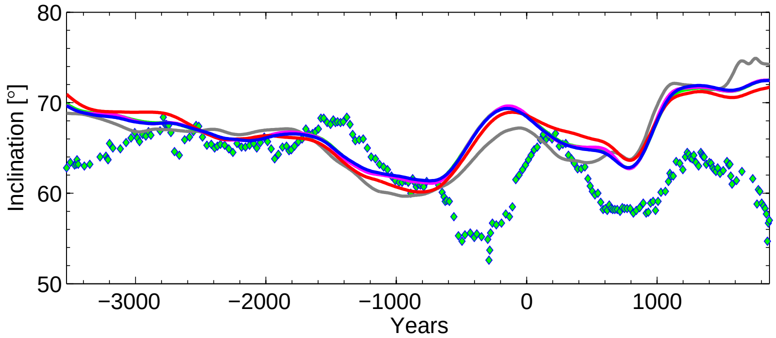

MEE – Meerfelder Maar, Germany: Declination

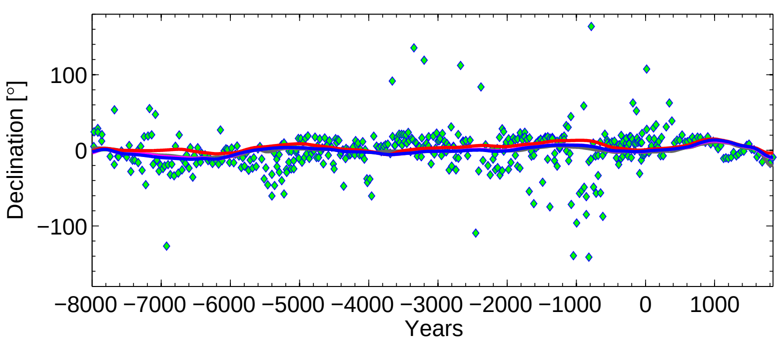

MEE – Meerfelder Maar, Germany: Inclination

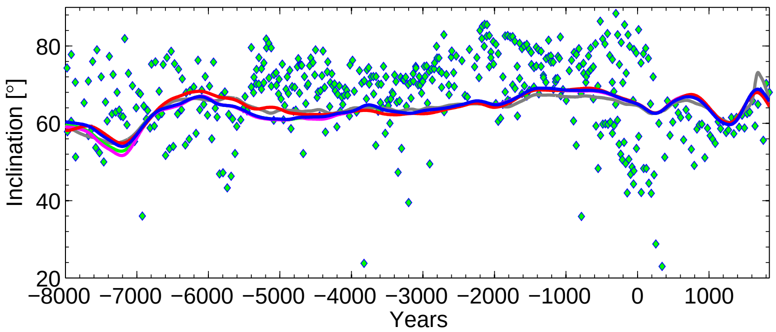

MEZ – Lago di Mezzano, Italy: Declination

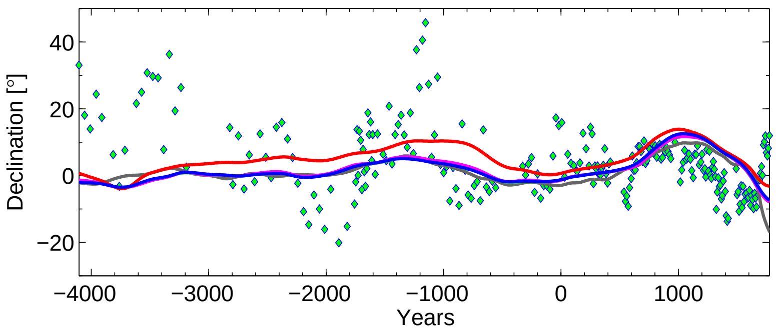

MEZ – Lago di Mezzano, Italy: Inclination

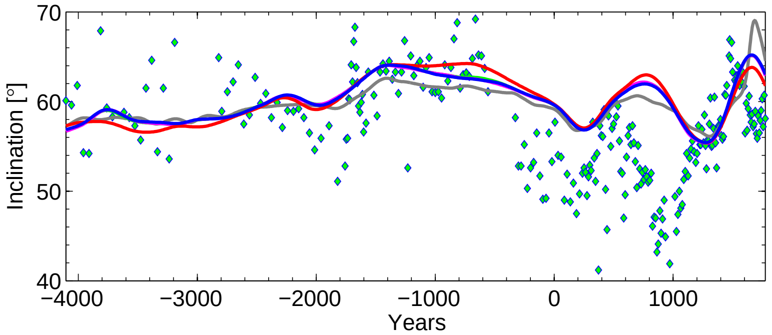

MEZ – Lago di Mezzano, Italy: Intensity

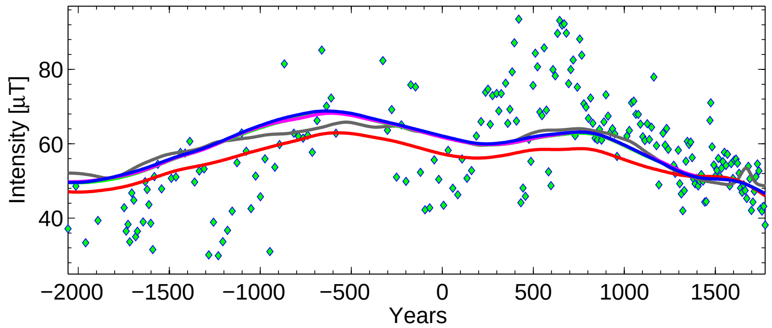

MNT – Lago Morenito, Argentina: Declination

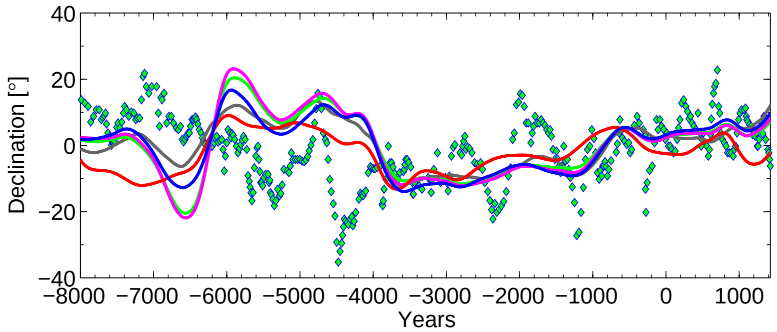

MNT – Lago Morenito, Argentina: Inclination

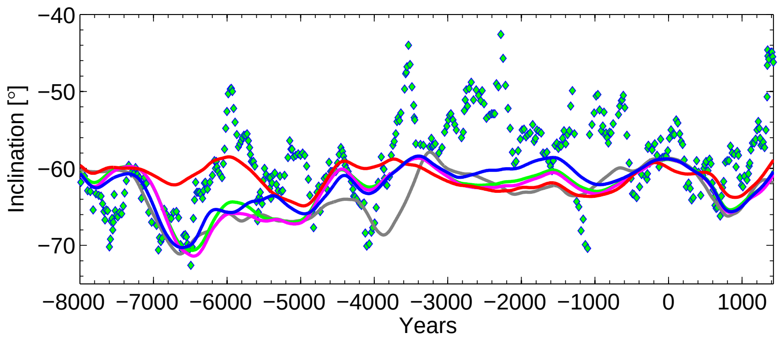

MOR – Lac Morat, Switzerland: Declination

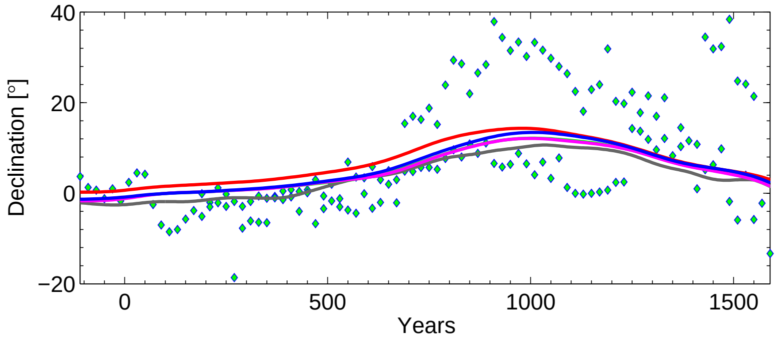

MOR – Lac Morat, Switzerland: Inclination

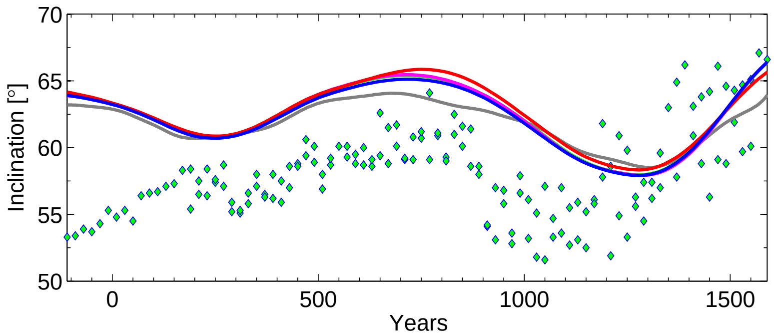

MOT – Mötterudstjärnet, Sweden: Declination

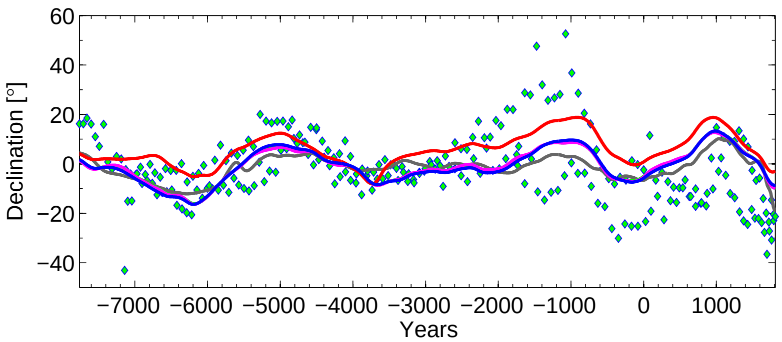

MOT – Mötterudstjärnet, Sweden: Inclination

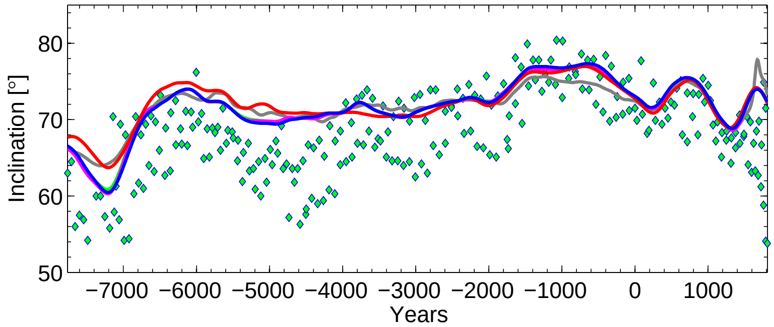

MOT – Mötterudstjärnet, Sweden: Intensity

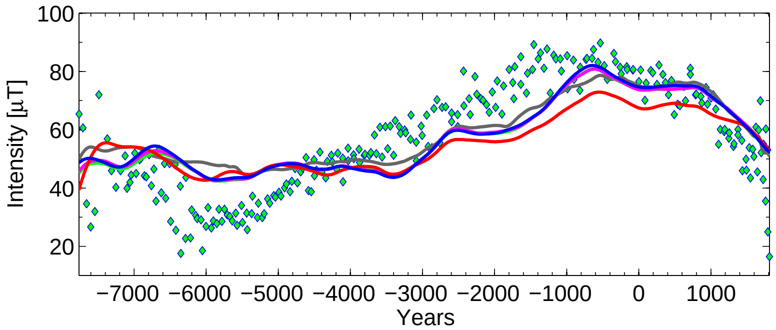

NAR – Lake Naroch, Belorussia: Declination

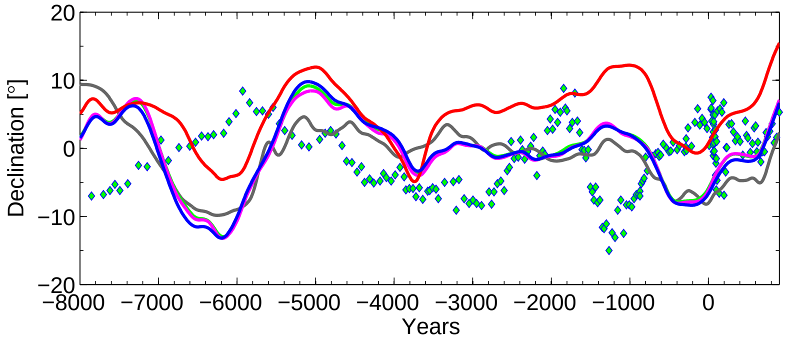

NAR – Lake Naroch, Belorussia: Inclination

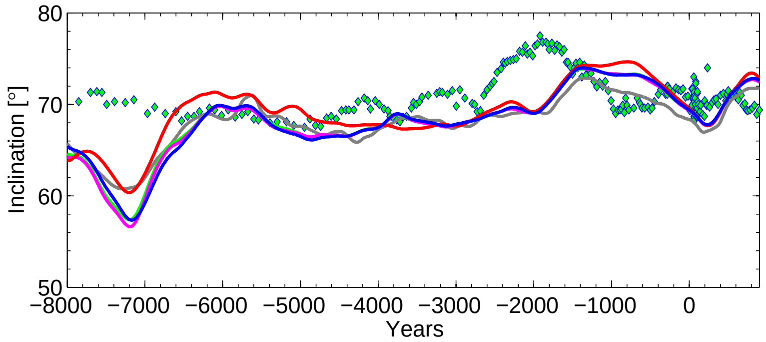

NAU – Nautajärvi, Finland: Declination

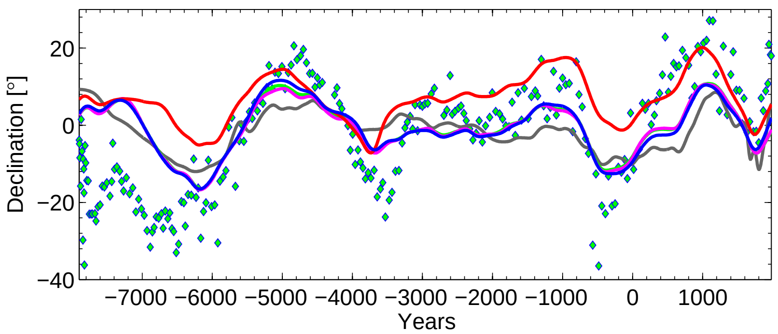

NAU – Nautajärvi, Finland: Inclination

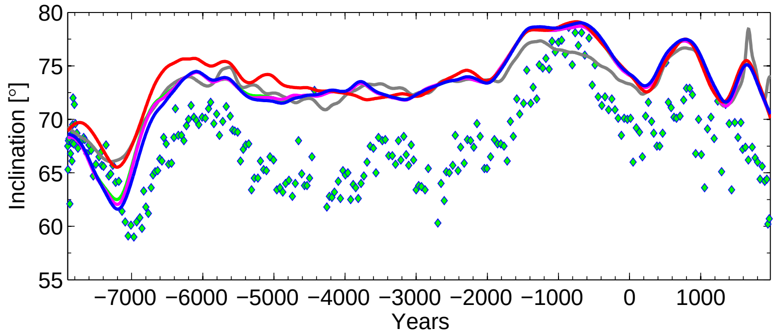

NAU – Nautajärvi, Finland: Intensity

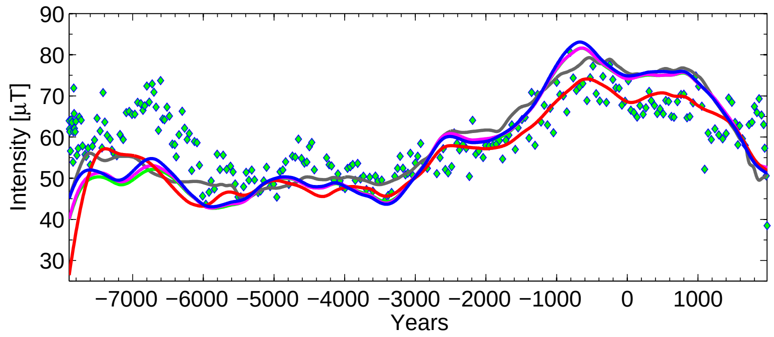

NEM – Lake Nemi, Italy: Declination

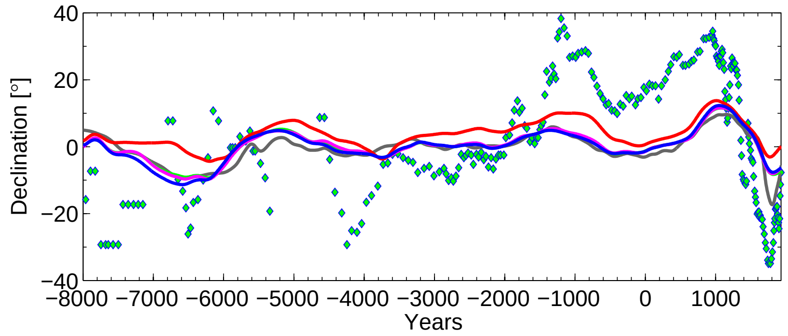

NEM – Lake Nemi, Italy: Inclination

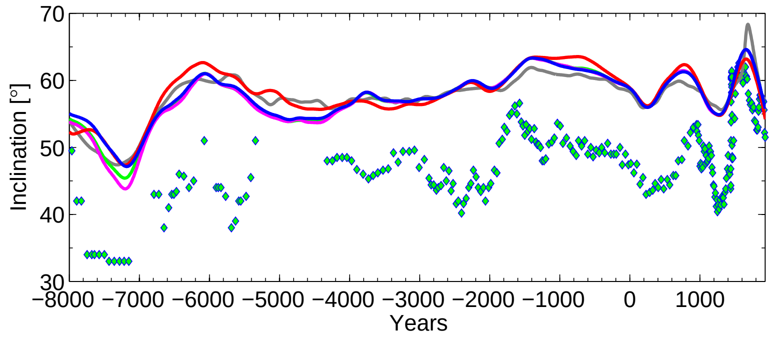

PAD – Palmer Deep, Antarctic Pen.: Declination

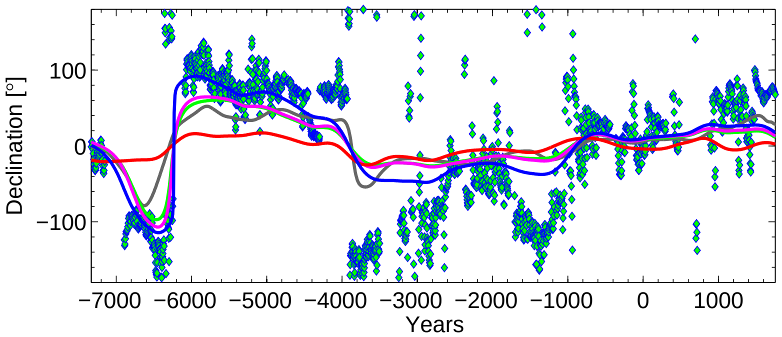

PAD – Palmer Deep, Antarctic Pen.: Inclination

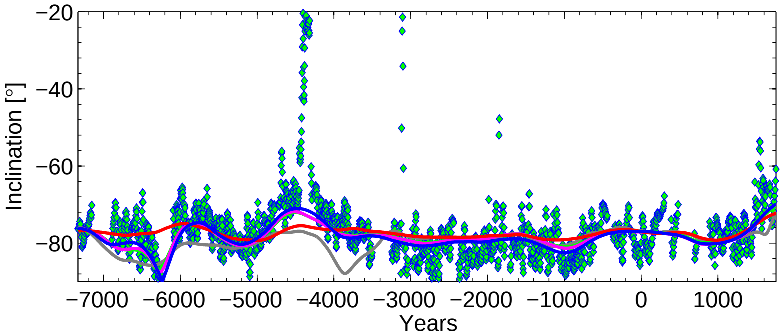

PAD – Palmer Deep, Antarctic Pen.: Intensity

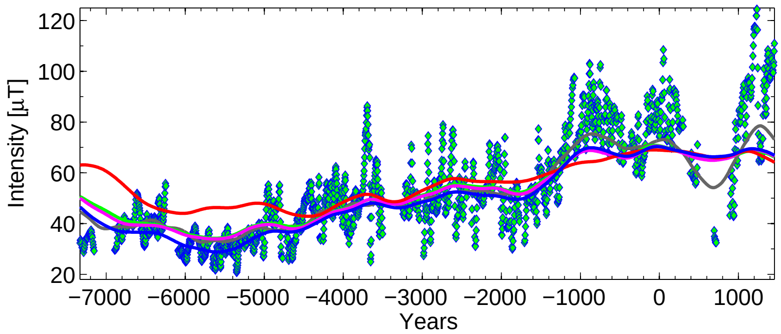

PEP – Lake Pepin, USA: Inclination

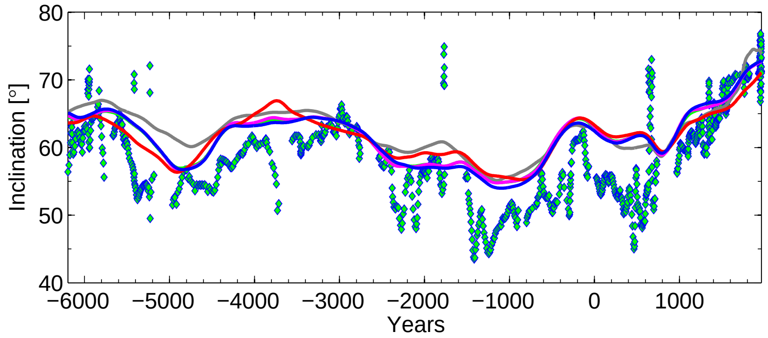

PEP – Lake Pepin, USA: Intensity

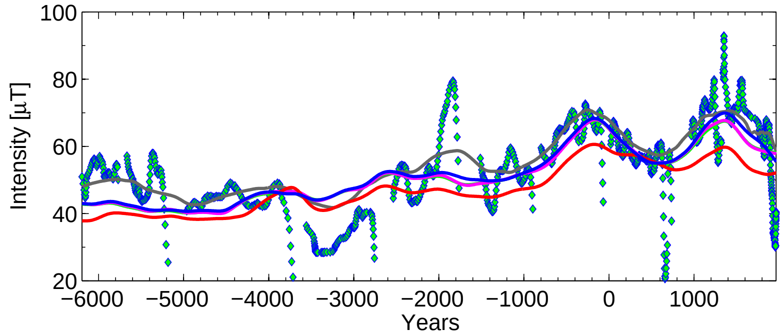

POH – Pohjajärvi, Finland: Declination

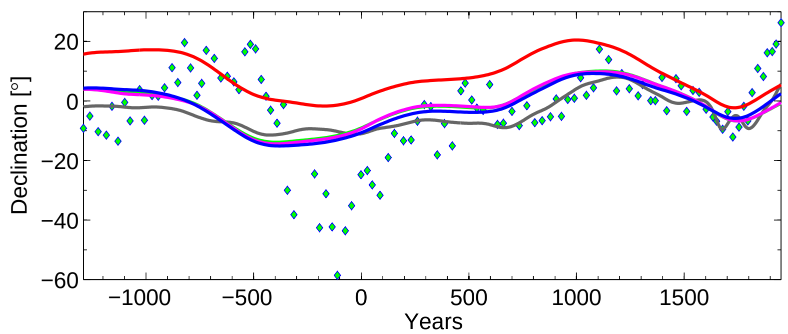

POH – Pohjajärvi, Finland: Inclination

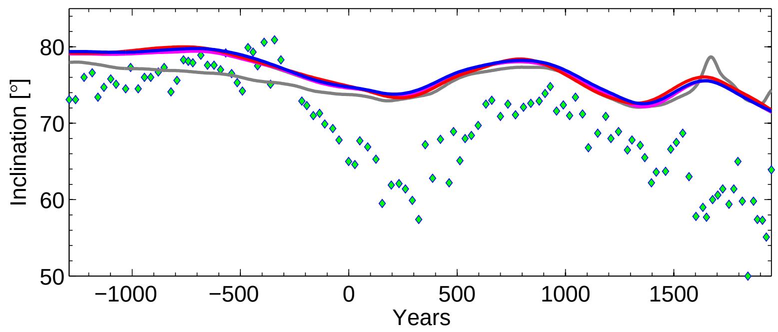

POH – Pohjajärvi, Finland: Intensity

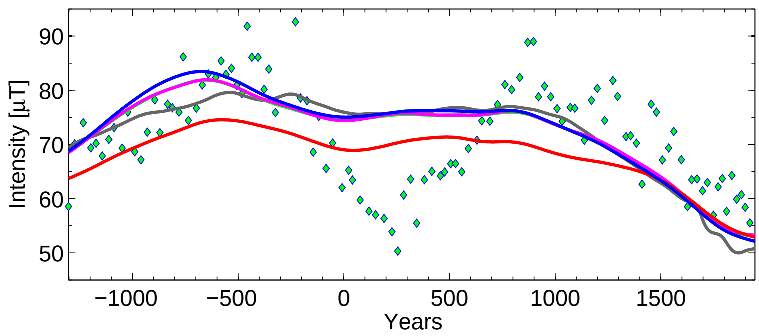

POU – Lake Pounui, New Zealand: Declination

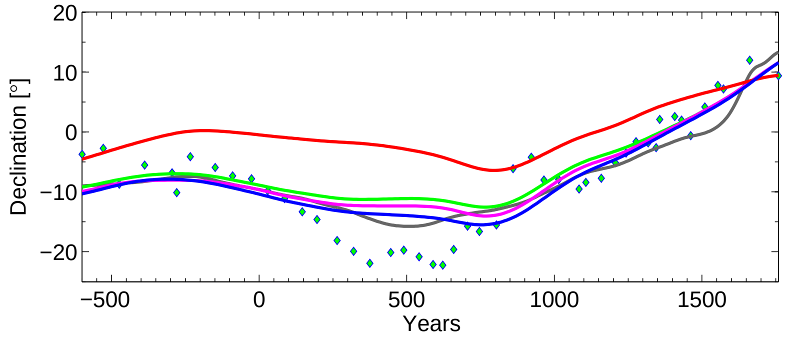

POU – Lake Pounui, New Zealand: Inclination

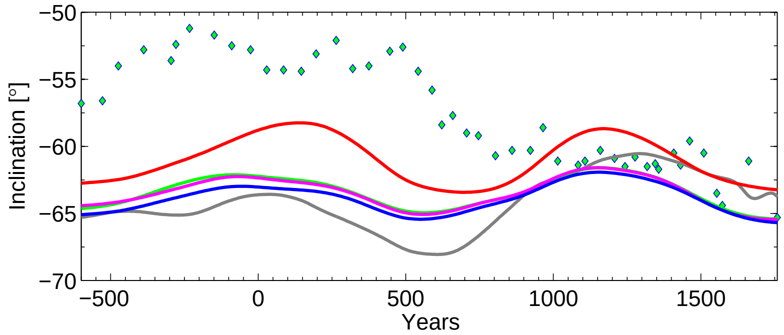

SAG – Saguenay Fjord, Canada: Declination

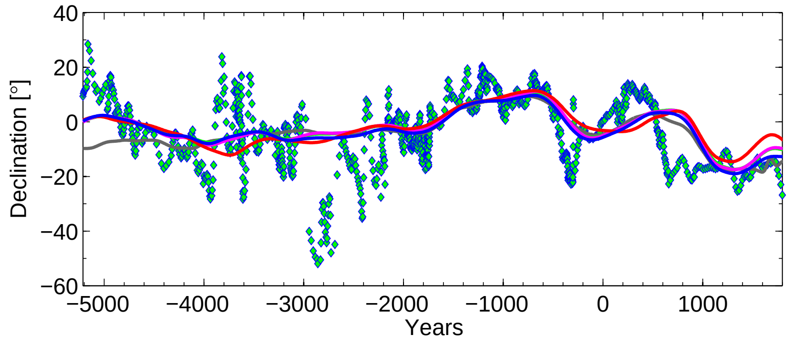

SAG – Saguenay Fjord, Canada: Inclination

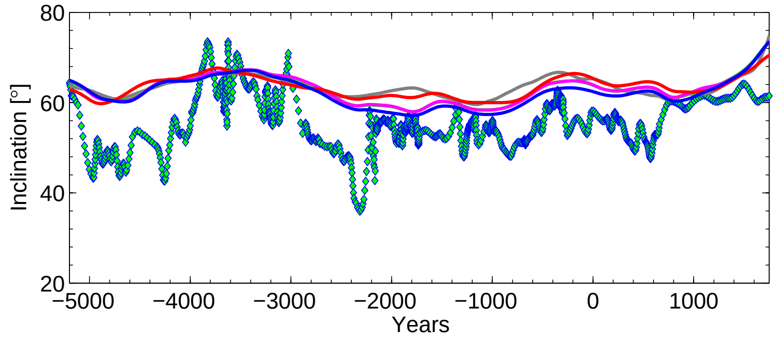

SAN – Hoya de San Nicolas, Mexico: Declination

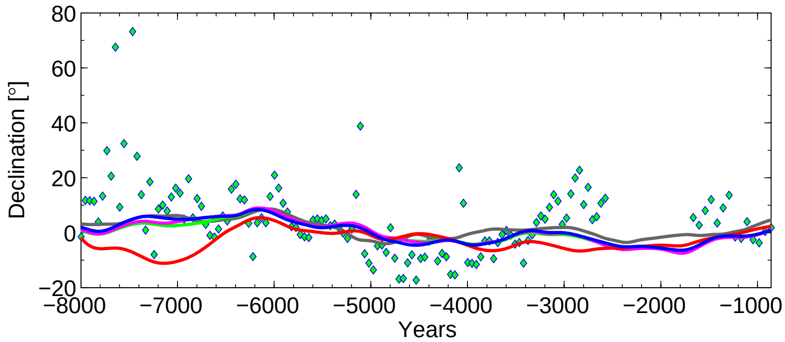

SAN – Hoya de San Nicolas, Mexico: Inclination

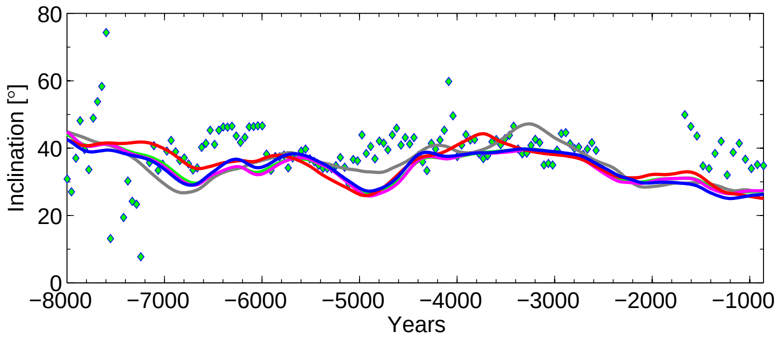

SAR – Sarsjön, Sweden: Declination

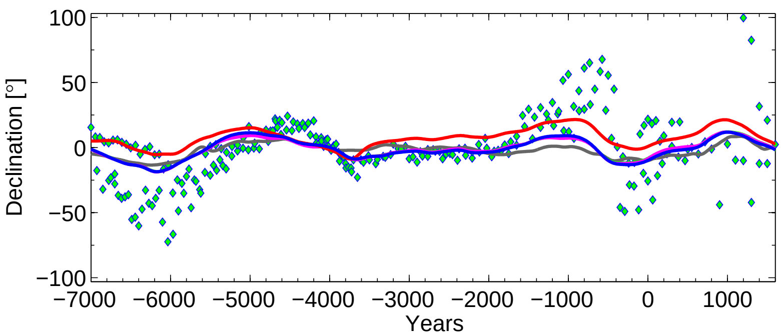

SAR – Sarsjön, Sweden: Inclination

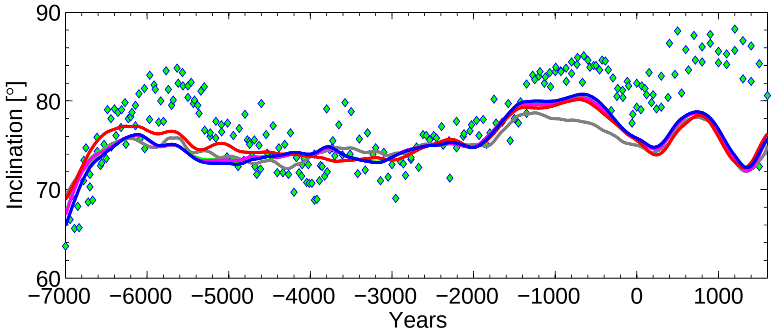

SAR – Sarsjön, Sweden: Intensity

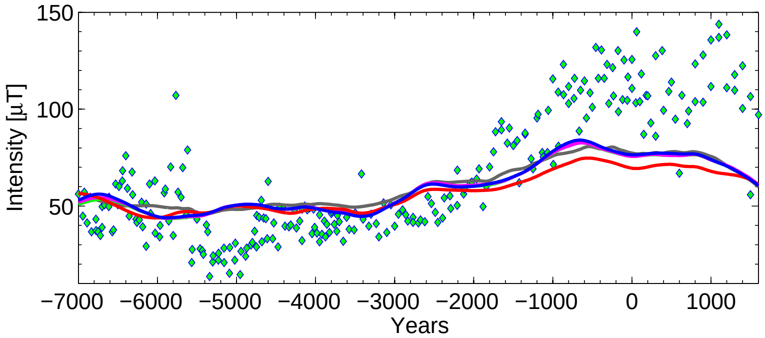

SAV – Savijärvi, Finland: Declination

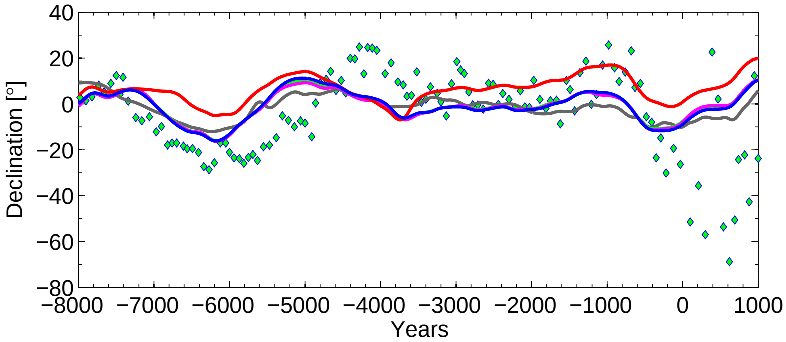

SAV – Savijärvi, Finland: Inclination

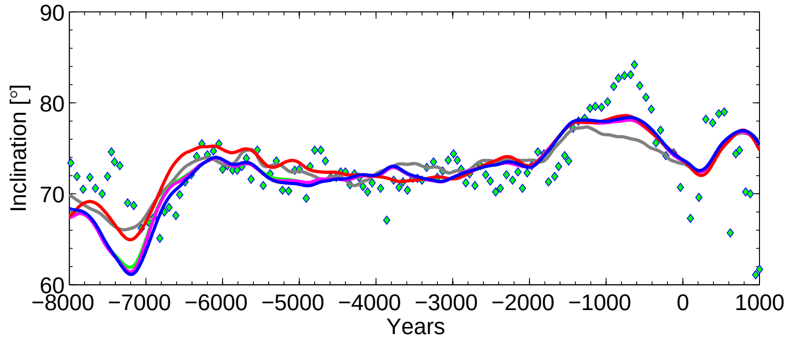

SCL – Lake Shuangchiling, China: Declination

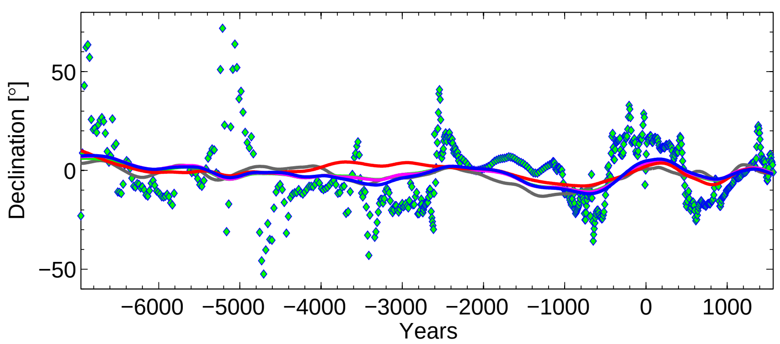

SCL – Lake Shuangchiling, China: Inclination

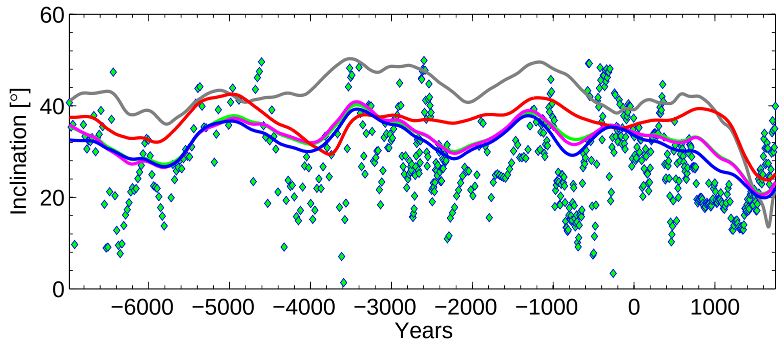

STL – St. Lawrence Est., Canada: Declination

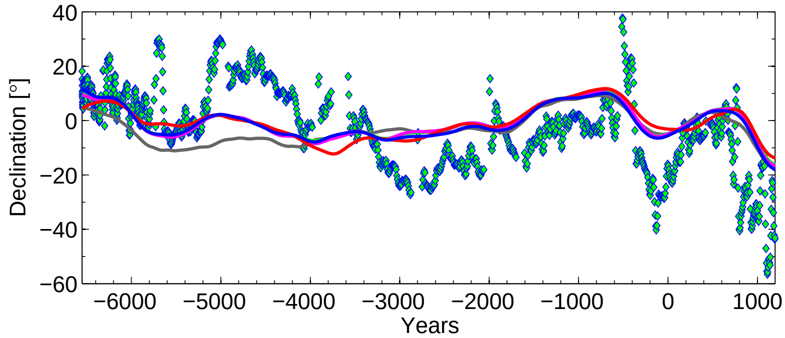

STL – St. Lawrence Est., Canada: Inclination

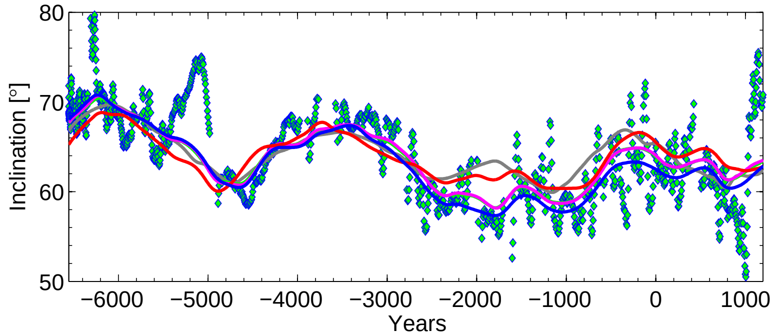

STL – St. Lawrence Est., Canada: Intensity

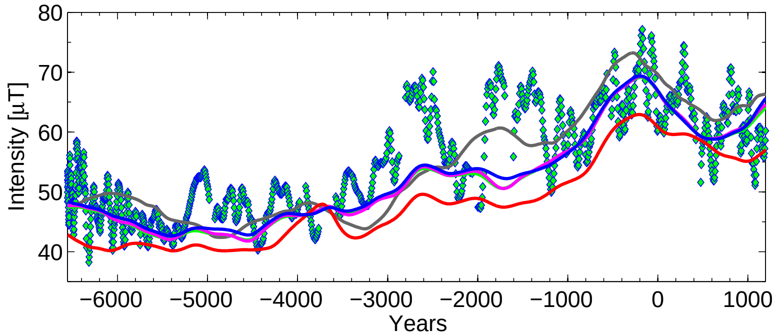

SUP – Lake Superior, USA: Declination

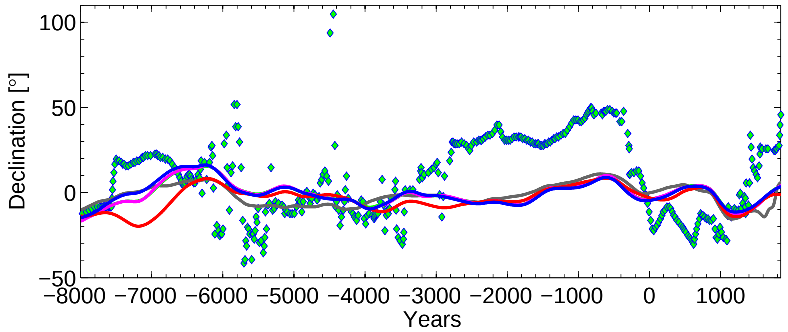

SUP – Lake Superior, USA: Inclination

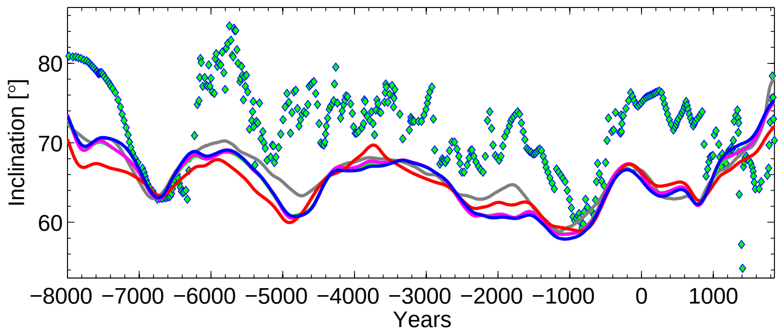

TRE – Laguna El Trébol, Argentina: Declination

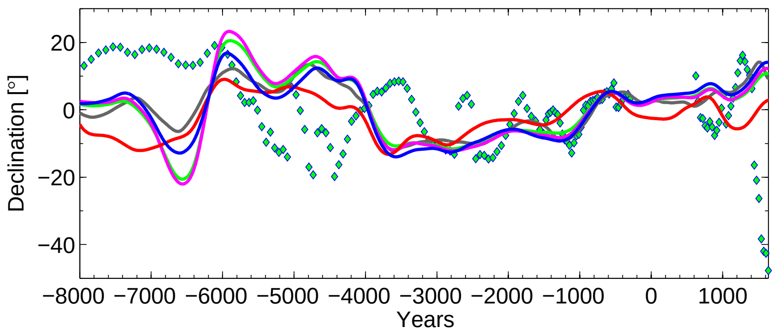

TRE – Laguna El Trébol, Argentina: Inclination

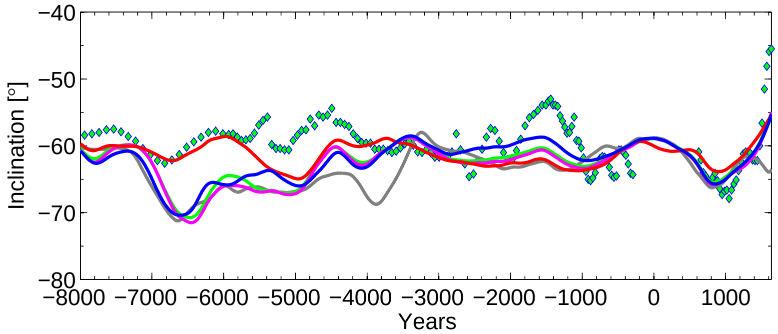

TRE – Laguna El Trébol, Argentina: Intensity

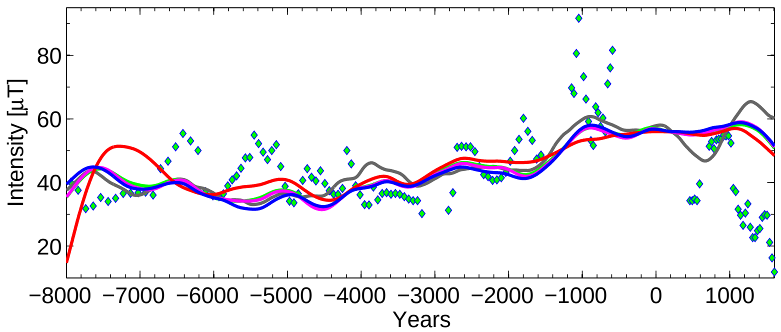

TRI – Lake Trikhonis, Greece: Declination

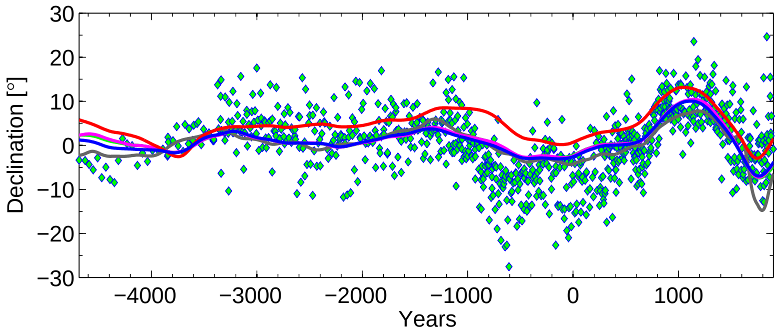

TRI – Lake Trikhonis, Greece: Inclination

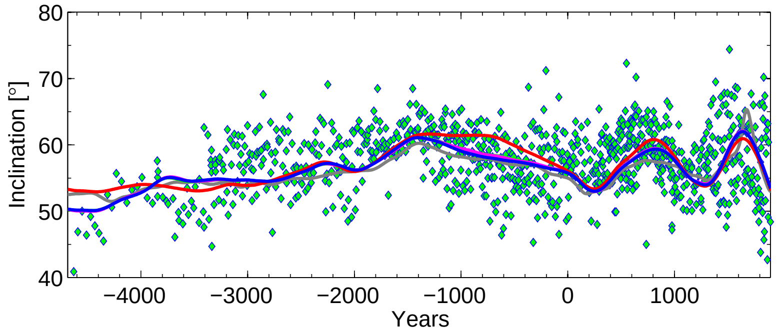

TUR – Lake Turkana, Kenya: Inclination

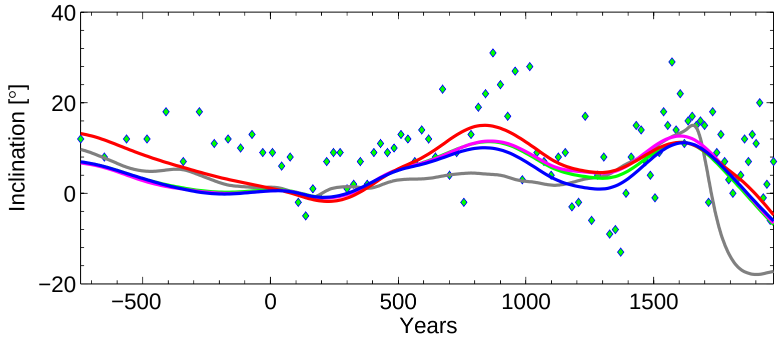

VAT – Vatndalsvatn, Iceland: Declination

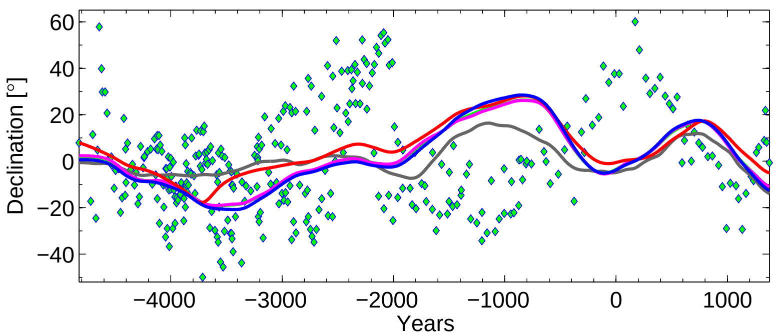

VAT – Vatndalsvatn, Iceland: Inclination

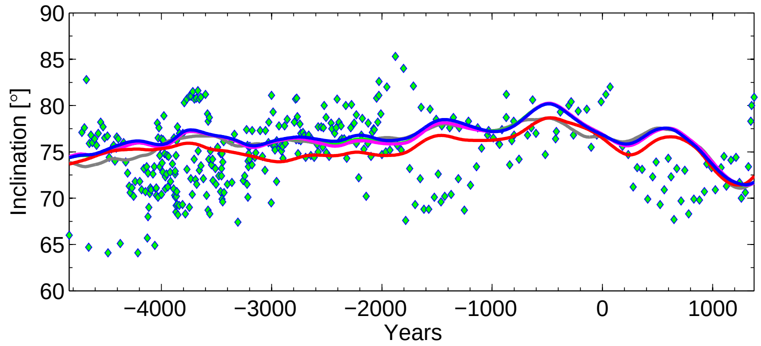

VIC – Lake Victoria, Uganda: Declination

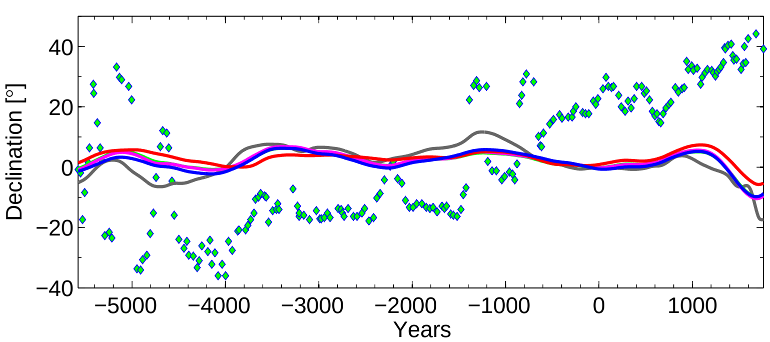

VIC – Lake Victoria, Uganda: Inclination

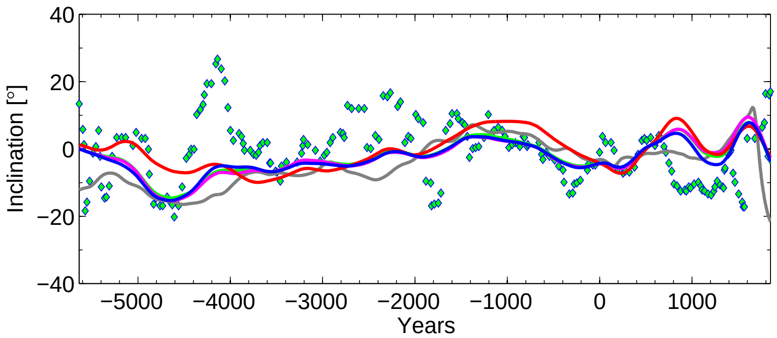

VOL – Lake Volvi, Greece: Declination

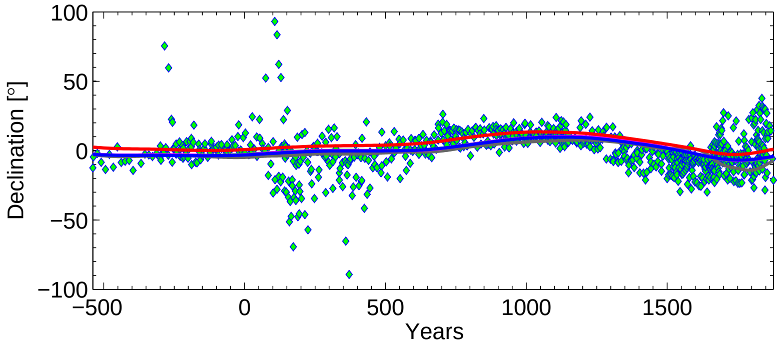

VOL – Lake Volvi, Greece: Inclination

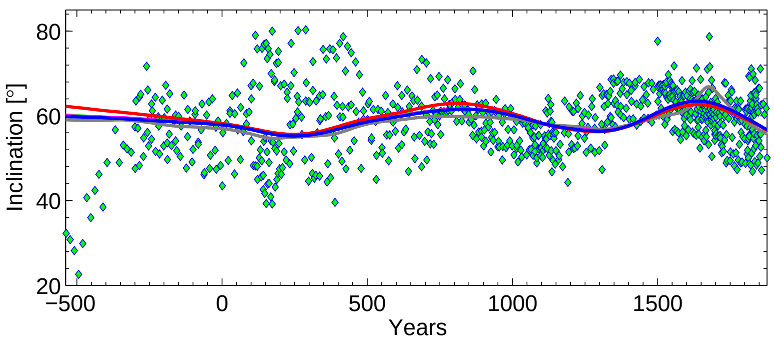

VUK – Vukonjärvi, Finland: Declination

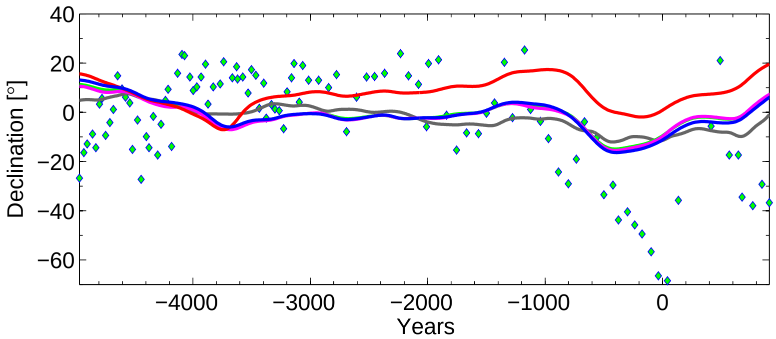

VUK – Vukonjärvi, Finland: Inclination

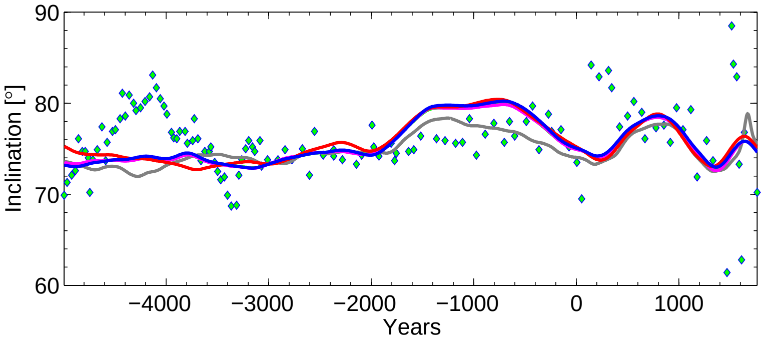

WAI – Lake Waiau, Hawaii: Declination

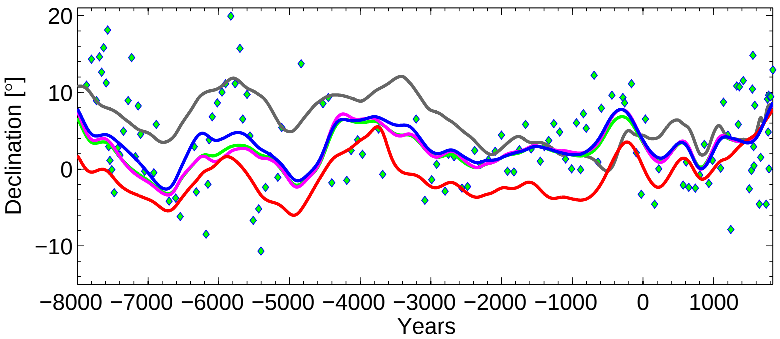

WAI – Lake Waiau, Hawaii: Inclination

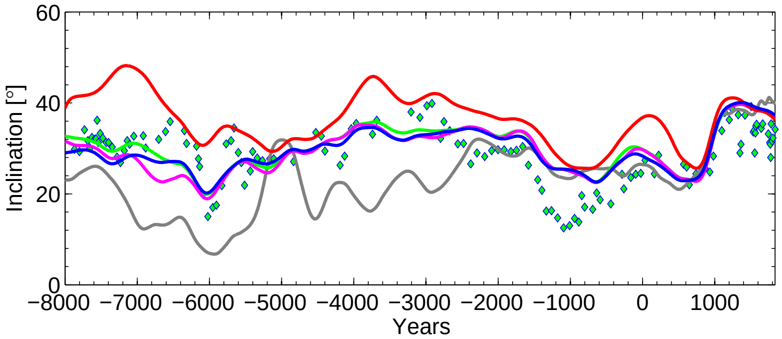

WAS – West Amundsen Sea: Intensity

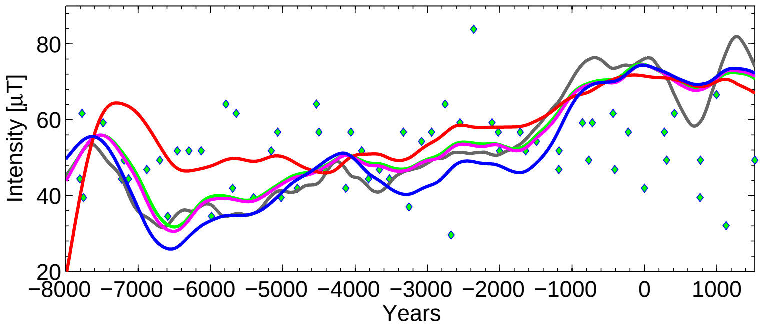

WIN – Lake Windermere, UK: Declination

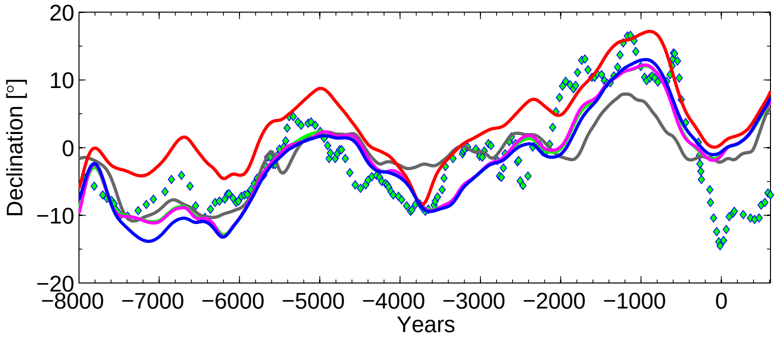

WIN – Lake Windermere, UK: Inclination

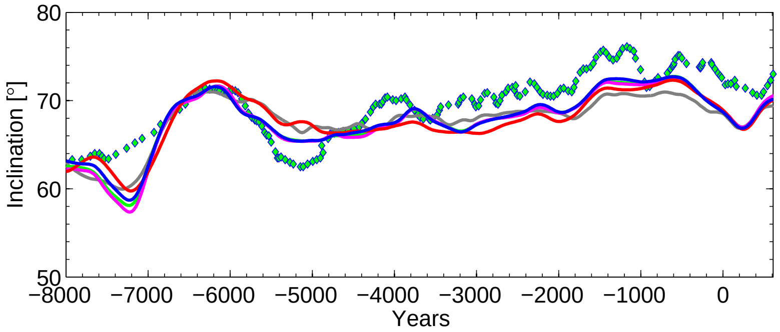

Ba – Lake Baldegg, Switzerland: Declination

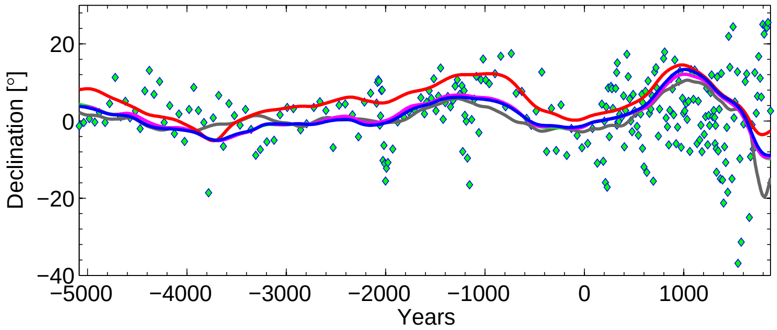

Ba – Lake Baldegg, Switzerland: Inclination

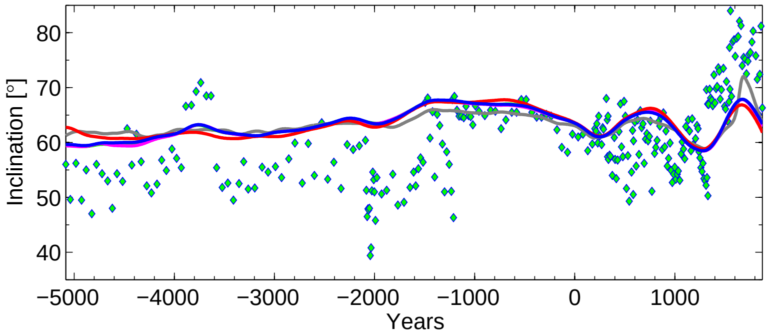

Ba – Lake Baldegg, Switzerland: Intensity

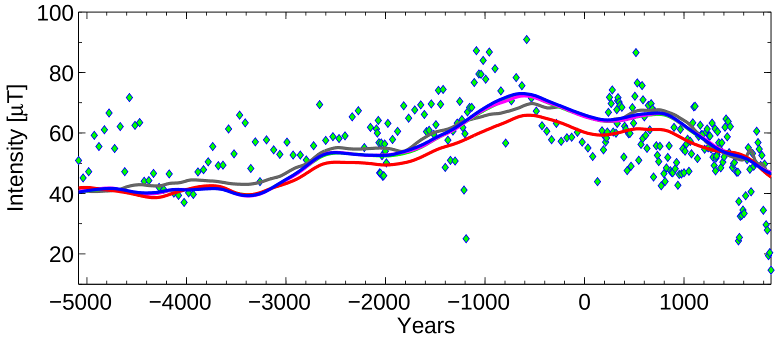

SoI – Lake Soppen I, Switzerland: Declination

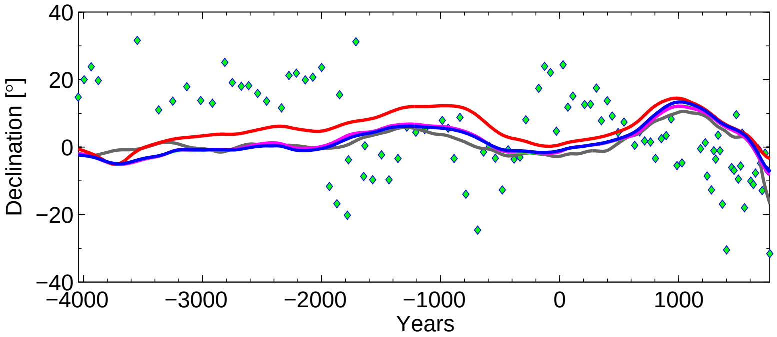

SoI – Lake Soppen I, Switzerland: Inclination

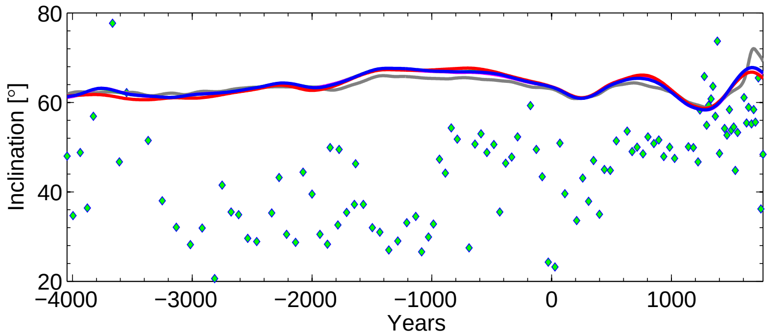

SoI – Lake Soppen I, Switzerland: Intensity

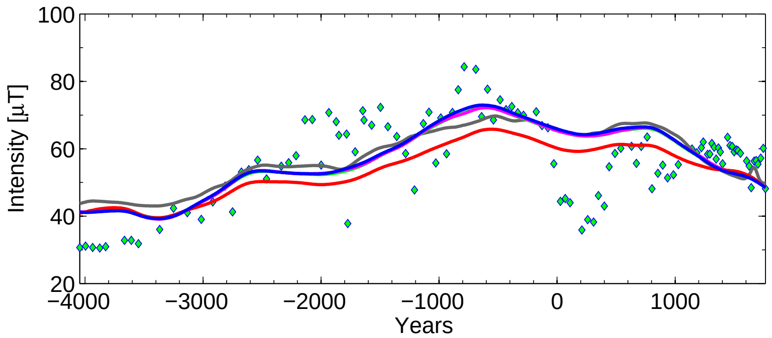

SoII – Lake Soppen II, Switzerland: Declination

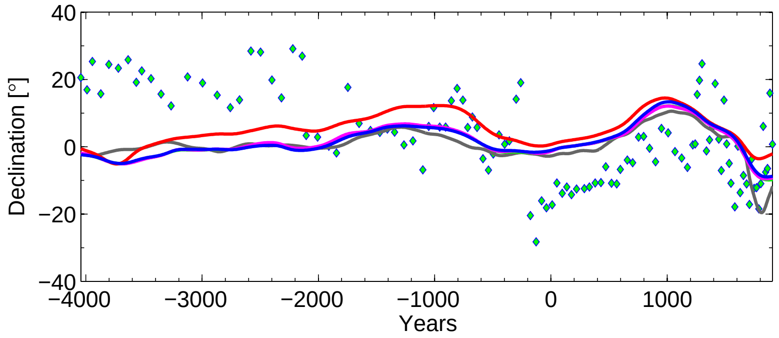

SoII – Lake Soppen II, Switzerland: Inclination

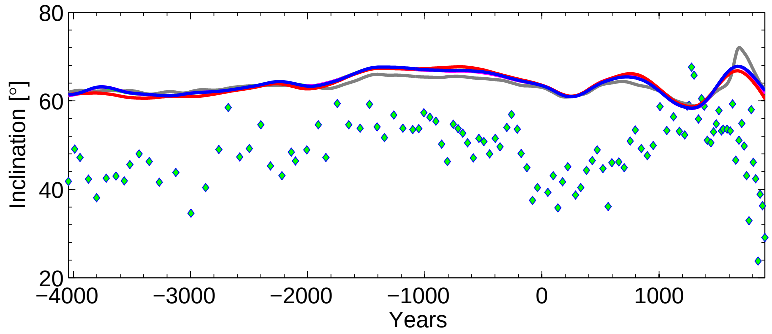

SoII – Lake Soppen II, Switzerland: Intensity

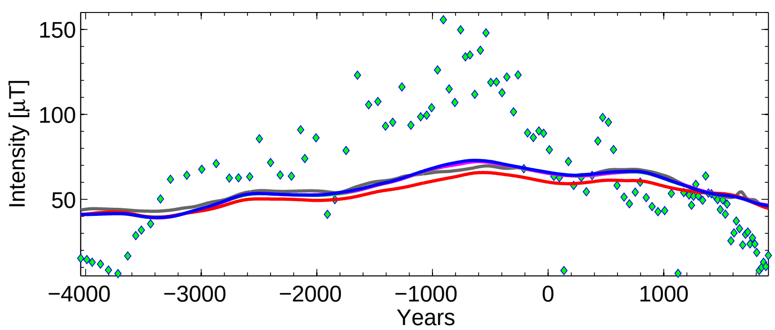

Bibliography

Aitken, M.J., Allsop, A.L., Bussell, G.D., and Winter, M.B. Determination of the intensity of the Earth's magnetic field during archeological times: Reliability of the Thellier technique. *Rev. Geophys.*, 26, 3–12, 1988.

Alexandrescu, M., Gibert, D., Hulot, G., Le Mouël, J.-L., and Saracco, G. Worldwide wavelet analysis of geomagnetic jerks. *J. Geophys. Res.*, 101, 21975–21994, 1996.

Ali, M., Oda, H., Hayashida, A., Takemura, K., and Torii, M. Holocene palaeomagnetic secular variation at Lake Biwa, central Japan. *Geophys. J. Int.*, 136, 218–228, 1999.

Amit, H., Aubert, J., and Hulot, G. Stationary, oscillating or drifting mantle-driven geomagnetic flux patches. *J. Geophys. Res.*, 115, B07108, 2010.

Amit, H., Korte, M., Aubert, J., Constable, C.G., and Hulot, G. The time-dependence of intense archeomagnetic flux patches. *J. Geophys. Res.*, 116, B12106, 2011.

Amit, H. and Olson, P. Geomagnetic dipole tilt changes induced by core flow. *Phys. Earth Planet. Inter.*, 166, 226–238, 2008.

Anson, G.L. and Kodama, K.P. Compaction-induced inclination shallowing of the post-depositional remanent magnetization in a synthetic sediment. *Geophys. J. Roy. Astron. Soc.*, 88, 673–692, 1987.

Arason, P. and Levi, S. Models of inclination shallowing during sediment compaction. *J. Geophys. Res.*, 95, 4481–4499, 1990.

Aster, R.C., Borchers, B., and Thurber, C.H. *Parameter Estimation and Inverse Problems.* Elsevier Academic Press, Amsterdam, 2005.

Backus, G., Parker, R.L., and Constable, C.G. *Foundations of Geomagnetism.* Cambridge University Press, New York, 1996.

Bard, Y. *Nonlinear Parameter Estimation.* Academic Press, New York, 1974.

Barletta, F., St-Onge, G., Channell, J.E.T., Rochon, A., Polyak, L., and Darby, D. High–resolution paleomagnetic secular variation and relative paleointensity records from the western Canadian Arctic: Implication for Holocene stratigraphy and geomagnetic field behaviour. *Can. J. Earth Sci.*, 45, 1265–1281, 2008.

Barton, C.E. Spectral analysis of palaeomagnetic time series and the geomagnetic spectrum. *Phil. Trans. R. Soc. Lond. A*, 306, 203–209, 1982.

Barton, C.E. Analysis of palaeomagnetic time series - Technique and applications. *Geophys. Surv.*, 5, 335–368, 1983.

Barton, C.E. and McElhinny, M.W. A 10000 years geomagnetic secular variation record from three Australian maars. *Geophys. J. Roy. Astron. Soc.*, 67, 465–485, 1981.

Barton, C.E. and Torgersen, T. Palaeomagnetic and ^{210}Pb estimates of sedimentation in Lake Turkana, East Afrika. *Paleogeogr. Plaeocl.*, 68, 53–60, 1988.

Beer, J., Muscheler, R., Wagner, G., Laj, C., Kissel, C., Kubik, P.W., and Synal, H.-A. Cosmogenic nuclides during Isotope Stages 2 and 3. *Quaternary Science Rev.*, 21, 1129–1139, 2002.

Ben-Yozef, E., Tauxe, L., Levy, T.E., Shaar, R., Ron, H., and Najjar, M. Geomagnetic intensity spike recorded in high resolution slag deposit in Southern Jordan. *Earth Planet. Sci. Lett.*, 287, 529–539, 2009.

Birks, H.H., Gulliksen, S., Haflidason, H., Mangerud, J., and Possnert, G. New radiocarbon dates for the Vedde ash and the Saksunarvatn ash from Western Norway. *Quatern. Res.*, 45, 119–127, 1996.

Bleil, U. and Dillon, M. Holocene Earth's magnetic field variations recorded in marine sediments of the NW African continental margin. *Stud. Geophys. Geod.*, 52, 133–155, 2008.

Blockley, S.P.E., Ramsey, C.B., Lane, C.S., and Lotter, A.F. Improved age modelling approaches as exemplified by the revised chronology for the Central European varved lake Soppensee. *Quaternary Sci. Rev.*, 27, 61–71, 2008.

Bloxham, J., Gubbins, D., and Jackson, A. Geomagnetic secular variation. *Phil. Trans. R. Soc. Lond. A.*, 329, 415–502, 1989.

Bloxham, J. and Jackson, A. Time-dependent mapping of the magnetic field at the core-mantle boundary. *J. Geophys. Res.*, 97, 19537–19563, 1992.

Boudreau, B.P. Is burial velocity a master parameter for bioturbation? *Geochim. Cosmochim. Acta*, 58, 1243–1249, 1994.

Boudreau, B.P. Mean mixed depth of sediments: The wherefore and the why. *Limnol. Oceanogr.*, 43, 524–526, 1998.

Bouligand, C., Hulot, G., Khokhlov, A., and Glatzmaier, G.A. Statistical paleomagnetic field modelling and dynamo numerical simulation. *Geophys. J. Int.*, 161, 603–626, 2005.

Brachfeld, S., Acton, G.D., Guyodo, Y., and Banerjee, S.K. High-resolution paleomagnetic records from Holocene sediments from the Palmer Deep, Western Antartic Peninsula. *Earth Planet. Sci. Lett.*, 181, 429–441, 2000.

Brachfeld, S., Domack, E., Kissel, C., Laj, C., Leventer, A., Ishman, S., Gilbert, R., Camerlenghi, A., and Eglinton, L.B. Holocene history of the Larsen-A Ice Shelf constrained by geomagnetic paleointensity dating. *Geol.*, 31(9), 749–752, 2003.

Brachfeld, S.A. and Banerjee, S.K. A new high-resolution geomagnetic relative paleointensity record for the North American Holocene: A comparison of sedimentary and absolute intensity data. *J. Geophys. Res.*, 105(B1), 821–834, 2000.

Braginsky, S.I. Analytic description of the geomagnetic field of past epochs and determination of the spectrum of magnetic waves in the core of the Earth I. *Geomagnetism and Aeronomy*, 12, 947–957, 1972.

Braginsky, S.I. Analytic description of the geomagnetic field of past epochs and determination of the spectrum of magnetic waves in the core of the Earth II. *Geomagnetism and Aeronomy*, 14, 441–447, 1974.

Brandt, U., Nowaczyk, N.R., Ramrath, A., Brauer, A., Mingram, J., Wulf, S., and Negendank, J.F.W. Palaeomagnetism of Holocene and Late Pleistocene sediments from Lago di Mezzano and Lago Grande di Monticchio (Italy): Initial results. *Quaternary Sci. Rev.*, 18, 961–976, 1999.

Brown, H.A. *A Palaeomagnetic, Geochronological and Palaeoenvironmental Investigation of Late and Post Glacial Maar Lake Sediments from NW-Europe*. PhD thesis, University of Edinburgh, Edinburgh, 1991.

Busse, F.H. Convective flows in rapidly rotating spheres and their dynamo action. *Phys. Fluids*, 14, 1301–1314, 2002.

Butler, R.F. *Paleomagnetism: Magnetic Domains to Geologic Terranes*. Blackwell Scientific Publications, 1992.

Channell, J.E.T. and Guyodo, Y. The Matuyama Chronozone at ODP Site 982 (Rockall Bank): Evidence for decimeter-scale magnetization lock-in depths. In Channell, J.E.T., Kent, D.V., Lowrie, W., and Meert, J.G., editors, *Timescales of the Paleomagnetic Field*, Volume 145, pages 205–219. AGU Geophysical Monograph, 2004.

Channell, J.E.T., Hodell, D.A., and Lehman, B. Relative geomagnetic paleointensity and δ^{18}O at ODP Site 983 (Gardar Drift, North Atlantic) since 350 ka. *Earth Planet. Sci. Lett.*, 153, 103–118, 1997.

Chaparro, M. A. E., Böhnel, H. N., Byrne, R., Nowaczyk, N. R., Molina-Garza, R. S., Park, J., and Negendank, J. F. W. Palaeomagnetic secular variation and rock–magnetic studies of Holocene sediments from a maar lake (Hoya de San Nicolas) in Central Mexico. *Geophys. J. Int.*, 175, 462–476, 2008.

Chapman, S. and Bartels, J. *Geomagnetism*. Clarendon, Oxford, England, 1940.

Chui, C.K. *Introduction to Wavelets*. Academic Press, San Diego, 1992.

Claerbout, J.F. and Muir, F. Robust modeling with erratic data. *Geophysics*, 38, 826–844, 1973.

Coe, R.S. Paleo-intensity of the Earth's magnetic field determined from Tertiary and Quaternary rocks. *J. Geophys. Res.*, 72, 3247–3262, 1967.

Coe, R.S., Grommé, S., and Mankinen, E. Geomagnetic paleointensities from radiocarbon-dated lava flows on Hawaii and the question of the Pacific Nondipole Low. *J. Geophys. Res.*, 83, 1740–1756, 1978.

Constable, C.G. Eastern Australian geomagnetic field intensity over the past 14000 yr. *Geophys. J. Roy. Astron. Soc.*, 81, 121–130, 1985.

Constable, C.G. Parameter-estimation in non-gaussian noise. *Geophys. J.*, 94, 131–142, 1988.

Constable, C.G. Centennial- to millennial-scale geomagnetic field variations. In Kono, M., editor, *Treatise of Geophysics, Geomagnetism*, Volume 5, pages 337–372. Elsevier, 2007a.

Constable, C.G. Dipole moment variation. In Gubbins, D.G. and Herrero-Bervera, E., editors, *Encyclopedia of Geomagnetism and Paleomagnetism*, pages 159–161. Springer, 2007b.

Constable, C.G. Non-dipole field. In Gubbins, D.G. and Herrero-Bervera, E., editors, *Encyclopedia of Geomagnetism and Paleomagnetism*, pages 701–704. Springer, 2007c.

Constable, C.G. Modelling the geomagnetic field from syntheses of paleomagnetic data. *Phys. Earth Planet. Inter.*, 187, 109–117, 2011.

Constable, C.G. and Johnson, C.L. A paleomagnetic power spectrum. *Phys. Earth Planet. Inter.*, 153, 61–73, 2005.

Constable, C.G., Johnson, C.L., and Lund, S.P. Global geomagnetic field models for the past 3000 years: Transient or permanent flux lobes. *Phil. Trans. R. Soc. Lond. A*, 358, 991–1008, 2000.

Constable, C.G. and McElhinny, M.W. Holocene geomagnetic secular variation records from north-eastern Australian lake sediments. *Geophys. J. Roy. Astron. Soc.*, 81, 103–120, 1985.

Constable, C.G. and Parker, R.L. Smoothing, splines and smoothing splines; Their application in geomagnetism. *J. Comput. Phys.*, 78, 493–508, 1988.

Constable, C.G., Parker, R.L., and Stark, P.B. Geomagnetic field models incorporating frozen-flux constraints. *Geophys. J. Int.*, 113, 419–433, 1993.

Cottrell, R.D. and Tarduno, J.A. Geomagnetic paleointensity derived from single plagioclase crystals. *Earth Planet. Sci. Lett.*, 169, 1–5, 1999.

Courtillot, V. and Le Mouël, J-L. Time variations of the Earth's magnetic field: from daily to secular. *Ann. Rev. Earth Planet. Sci.*, 16, 389–476, 1988.

Creer, K.M., Hogg, T.E., Readman, P.W., and Reynaud, C. Palaeomagnetic secular variation curves extending back to 13,400 years B.P. recorded by sediments deposited in Lac de Joux, Switzerland. *J. Geophys.*, 48, 139–147, 1980.

Creer, K.M., Molyneux, L., Vernet, J.P., and Wagner, J.J. Palaeomagnetic dating of 1-metre cores of sediments from Lake Geneva. *Earth Planet. Sci. Lett.*, 28, 127–132, 1975.

Creer, K.M., Readman, P.W., and Papamarinopoulos, S. Geomagnetic secular variation in Greece through the last 6000 years obtained from lake sediment studies. *Geophys. J. Roy. Astron. Soc.*, 66, 193–219, 1981.

Creer, K.M., Valencio, D.A., Sinito, A.M., Tucholka, P., and Vilas, J.F.A. Geomagnetic secular variations 0-14 000 yr BP as recorded by lake sediments from Argentina. *Geophys. J. Roy. Astron. Soc.*, 74, 199–221, 1983.

Currie, R.G. Geomagnetic spectrum of internal origin and lower mantle conductivity. *J. Geophys. Res.*, 73, 2779–2790, 1968.

Daly, L. and Le Goff, M. An updated and homogeneous world secular variation data base. 1. Smoothing of the archeomagnetic results. *Phys. Earth Planet. Inter.*, 93, 159–190, 1996.

De Boor, C. *A Practical Guide to Splines*. Springer, New York, 2001.

Dekkers, M.J. and Böhnel, H.N. Reliable absolute palaeointensities independent of magnetic domain state. *Earth Planet. Sci. Lett.*, 248, 508–517, 2006.

Donadini, F., Korhonen, K., Riisager, P., and Pesonen, L. Database for Holocene geomagnetic intensity information. *EOS, Trans. Am. Geophys. Union*, 87(14), 137–143, 2006.

Donadini, F., Korte, M., and Constable, C.G. Geomagnetic field for 0-3 ka: 1. New data sets for global modelling. *Geochem. Geophys. Geosys.*, 10, Q06007, 2009.

Dumberry, M. and Bloxham, J. Azimuthal flows in the Earth's core and changes in length of day on millennial timescales. *Geophys. J. Int.*, 165, 32–46, 2006.

Dumberry, M. and Finlay, C.C. Eastward and westward drift of the Earth's magnetic field for the last three millennia. *Earth Planet. Sci. Lett.*, 254, 146–157, 2007.

Dunlop, D. and Özdemir, Ö. *Rock Magnetism: Fundamentals and Frontiers*. Cambridge University Press, Cambridge, 1997.

Egli, R. Characterization of individual rock magnetic components by analysis of remanence curves. 3. Bacterial magnetite and natural processes in lakes. *Phys. Chem. Earth*, 29, 869–884, 2004.

Elsasser, W., Ney, E.P., and Winckler, J.R. Cosmic ray intensity and geomagnetism. *Nature*, 178, 1226–1227, 1956.

Farquharson, C.G. and Oldenburg, D.W. Non-linear inversion using general measures of data misfit and model structure. *Geophys. J. Int.*, 134, 213–227, 1998.

Finlay, C.C., Jackson, A., Gillet, N., and Olsen, N. Core surface magnetic field evolution 2000-2010. *Geophys. J. Int.*, 189, 761–781, 2012.

Fisher, R.A. Dispersion on a sphere. *Proc. R. Soc. Lon. A*, 217, 295–305, 1953.

Flandrin, P. Empirical mode decomposition, 2009. http://perso.ens-lyon.fr/patrick.flandrin/software2.html.

Foufoula-Georgiou, E. and Kumar, P. *Wavelets in Geophysics*. Academic Press, San Diego, 1994.

Frank, U. Palaeomagnetic investigations on lake sediments from NE China: A new record of geomagnetic secular variations for the last 37 ka. *Geophys. J. Int.*, 169, 29–40, 2007.

Frank, U., Nowaczyk, N.R., and Negendank, J.F.W. Palaeomagnetism of greigite bearing sediments from the Dead Sea, Israel. *Geophys. J. Int.*, 168, 904–920, 2007.

Frank, U., Nowaczyk, N.R., Negendank, J.F.W., and Melles, M. A paleomagnetic record from Lake Lama, northern Central Siberia. *Phys. Earth Planet. Inter.*, 133, 3–20, 2002a.

Frank, U., Schwab, M.J., and Negendank, J.F.W. A lacustrine record of paleomagnetic secular variations from Birkat Ram, Golan Heights (Israel) for the last 4400 years. *Phys. Earth Planet. Inter.*, 133, 21–34, 2002b.

Frank, U., Schwab, M.J., and Negendank, J.F.W. Results of rock magnetic investigations and relative paleointensity determinations on lacustrine sediments from Birkat Ram, Golan Heights (Israel). *J. Geophys. Res.*, 108(B8), 2379–2394, 2003.

Gallet, Y., Genevey, A., and Courtillot, V. On the possible occurrence of 'archeomagnetic jerks' in the geomagnetic field over the past three millennia. *Earth Planet. Sci. Lett.*, 214, 237–242, 2003.

Gallet, Y., Hulot, G., Chulliat, A., and Genevey, A. Geomagnetic field hemispheric asymmetry and archeomagnetic jerks. *Earth Planet. Sci. Lett.*, 284, 179–186, 2009.

Geiss, C.E., Dorale, J.A., and Dahms, D. A rockmagnetic and palaeomagnetic record of two glacial lakes in the Wind River Range, Wyoming, U.S.A. *EOS Trans. Am. Geophys. Union*, 88(52), Abstract GP53B–1216, 2007.

Genevey, A. and Gallet, Y. Intensity of the geomagnetic field in western Europe over the past 2000 years: New data from ancient French pottery. *J. Geophys. Res.*, 107(B11), 2285, 2002.

Genevey, A., Gallet, Y., Constable, C.G., Korte, M., and Hulot, G. Archeoint: An upgraded compilation of geomagnetic field intensity data for the past ten millennia and its application to the recovery of the past dipole moment. *Geochem. Geophys. Geosys.*, 9, Q04038, 2008.

Gillet, N., Jackson, A., and Finlay, C.C. Maximum entropy regularization of time-dependent geomagnetic field models. *Geophys. J. Int.*, 171, 1005–1016, 2007.

Gogorza, C.S.G., Irurzun, M.A., Chaparro, M.A.E., Lirio, J.M., Nuñez, H., Bercoff, P.G., and Sinito, A.M. Relative paleointensity of the geomagnetic field over the last 21,000 years BP from sediment cores, Lake El Trébol (Patagonia, Argentina). *Earth Planets Space*, 58, 1323–1332, 2006.

Gogorza, C.S.G., Lirio, J.M., Nuñez, H., Chaparro, M., Bertorello, H.R., and Sinito, A.M. Paleointensity studies on Holocene–Pleistocene sediments from Lake Escondido, Argentina. *Phys. Earth Planet. Inter.*, 145, 219–238, 2004.

Gogorza, C.S.G., Sinito, A.M., Di Tommaso, I., Vilas, J.F., Creer, K.M., and Nuñez, H. Holocene geomagnetic secular variations recorded by sediments from Escondido Lake (South Argentina). *Earth Planets Space*, 51, 93–106, 1999.

Gogorza, C.S.G., Sinito, A.M., Lirio, J.M., Nuñez, H., Chaparro, M., and Vilas, J.F. Paleosecular variations 0–19,000 years recorded by sediments from Escondido Lake (Argentina). *Phys. Earth Planet. Inter.*, 133, 35–55, 2002.

Gómez-Paccard, M., McIntosh, G., Chauvin, A., Beamud, E., Pavón-Carrasco, F.J., and Thiriot, J. Archaeomagnetic and rock magnetic study of six kilns from North Africa (Tunisia and Morocco). *Geophys. J. Int.*, 189, 169–786, 2012.

Green, P.J. and Silverman, B.W. *Nonparametric Regression and Generalized Linear Models, A Roughness Penalty Approach*. CRC Press, London, 1994.

Griffiths, D.H. The remanent magnetism of varved clays from Sweden. *Monthly Notices, Roy. Astro. Soc., Supplement 7*, 7, 103–114, 1955.

Gubbins, D. *Time Series Analysis and Inverse Theory for Geophysicists*. Cambridge University Press, London, 2004.

Gubbins, D. and Bloxham, J. Geomagnetic field analysis - III. Magnetic fields on the core-mantle boundary. *Geophys. J. Roy. Astron. Soc.*, 80, 695–713, 1985.

Gubbins, D. and Roberts, N. Use of the frozen flux approximation in the interpretation of archaeomagnetic and paleomagnetic data. *Geophys. J. Roy. Astron. Soc.*, 73, 675–687, 1983.

Gull, S. and Skilling, J. *The MEMSYS5 User's Manual*. Maximum Entropy Data Consultants Ltd., Royston, 1990.

Gull, S.F. and Daniell, G.J. Image reconstruction from incomplete and noisy data. *Nature*, 272, 686–690, 1978.

Gurarii, G.Z. and Aleksyutin, M.V. Wavelet analysis of paleomagnetic data: 3. Wavelet analysis of the basic series of archaeomagnetic data on the geomagnetic field intensity for the past 7500 years. *Izvestiya, Phys. Solid Earth*, 45, 527–538, 2009.

Guyodo, Y., Gaillot, P., and Channell, J.E.T. Wavelet analysis of relative geomagnetic paleointensity at ODP Site 983. *Earth Planet. Sci. Lett.*, 184, 109–123, 2000.

Hajdas, I., Bonani, G., and Zolitschka, B. Radiocarbon dating of varve chronologies: Soppensee and Holzmaar lakes after ten years. *Radiocarbon*, 42, 349–353, 2000.

Hajdas, I., Ivy, S.D., Beer, J., Bonani, G., Imboden, D., Lotter, A.F., Sturm, M., and Suter, M. AMS radiocarbon dating and varve chronology of Lake Soppensee: 6000 to 12000 ^{14}C years BP. *Climate Dynamics*, 9, 107–116, 1993.

Hajdas, I. and Michczyński, A. Age-depth model of Lake Soppensee (Switzerland) based on the high-resolution ^{14}C chronology compared with varve chronology. *Radiocarbon*, 52, 1027–1040, 2010.

Haltia-Hovi, E., Nowaczyk, N., and Saarinen, T. Holocene palaeomagnetic secular variation recorded in multiple lake sediment cores from eastern Finland. *Geophys. J. Int.*, 180, 609–622, 2010.

Hayashida, A., Ali, M., Kuniko, Y., Kitagawa, H., Torii, M., and Takemura, K. Environmental magnetic record and paleosecular variation data for the last 40 kyrs from the Lake Biwa sediments, Central Japan. *Earth Planets Space*, 59, 807–814, 2007.

Hillenbrand, C.-D., Smith, J.A., Kuhn, G., Esper, O., Gersonde, R., Larter, R.D., Maher, B., Moreton, S.G., Shimmield, T.M., and Korte, M. Age assignment of a diatomaceous ooze deposited in the western Amundsen Sea Embayment after the Last Glacial Maximum. *J. Quatern. Sci.*, 25(3), 280–295, 2010.

Hirt, A., Jackson, A., Haug, G., Beer, J., Finlay, C., and Gilli, A. Lacustrine sediments: High resolution archives for geomagnetic field behavior and paleoclimate. *ETH CHIRP*, 2008.

Hirt, A.M., Stoeckli, A., and Lotter, A.F. A 600 year magnetic record from Lake Hallwil, Switzerland. *Geophys. Res. Abstr.*, 5, 08552, 2003.

Hobson, M.P. and Lasenby, A.N. The entropic prior for distributions with positive and negative values. *Mon. Not. R. Astron. Soc.*, 298, 905–908, 1998.

Hoffman, K.A. and Biggin, A.J. A rapid multiple-sample approach to the determination of absolute paleointensity. *J. Geophys. Res.*, 110, B12108, 2005.

Hogg, E. *The Holocene Geomagnetic Field in Europe.* PhD thesis, University of Edinburgh, Edinburgh, UK, 1978.

Hongre, L., Hulot, G., and Khokhlov, A. An analysis of the geomagnetic field over the past 2000 years. *Phys. Earth Planet. Inter.*, 106, 311–335, 1998.

Huang, N.E., Shen, Z., Long, S.R., Wu, M.L., Shih, H.H., Zheng, Q., Yen, N.C., Tung, C.C., and Liu, H.H. The empirical mode decomposition and Hilbert spectrum for nonlinear and nonstationary time series analysis. *Proc. R. Soc. Lon. A*, 454, 903–995, 1998.

Huttunen, P. and Stober, J. Dating of palaeomagnetic records from Finnish lake sediment cores using pollen analysis. *Boreas*, 9, 193–202, 1980.

Hyodo, M. Possibility of reconstruction of the past geomagnetic field from homogeneous sediments. *J. Geomagn. Geoelectr.*, 36, 45–62, 1984.

Hyodo, M., Yoshihara, A., Kashiwaya, K., Okimura, T., Masuzawa, T., Nomura, R., Tanaka, S., Xing, T.B., Qing, L.S., and Jian, L.S. A Late Holocene geomagnetic secular variation record from Erhai Lake, southwest China. *Geophys. J. Int.*, 136, 784–790, 1999.

Irurzun, M.A., Gogorza, C.S.G., Chaparro, M.A.E., Lirio, J.M., Nuñez, H., Vilas, J.F., and Sinito, A.M. Paleosecular variations recorded by Holocene-Pleistocene sediments from Lake El Trébol (Patagonia, Argentina). *Phys. Earth Planet. Inter.*, 154, 1–17, 2006.

Irving, E. and Major, A. Post-depositional detrital remanent magnetization in a synthetic sediment. *Sedimentol.*, 3, 135–143, 1964.

Jackson, A. Intense equatorial flux spots on the surface of the Earth's core. *Nature*, 424, 760–763, 2003.

Jackson, A., Constable, C.G., and Gillet, N. Maximum entropy regularization of the geomagnetic core field inverse problem. *Geophys. J. Int.*, 171, 995–1004, 2007.

Jackson, A. and Finlay, C.C. Geomagnetic secular variation and its applications to the core. In Kono, M., editor, *Treatise of Geophysics, Geomagnetism*, Volume 5, pages 147–193. Elsevier, 2007.

Jackson, A., Jonkers, A.R.T., and Walker, M.R. Four centuries of geomagnetic secular variation from historical records. *Phil. Trans. R. Soc. Lond. A*, 358, 957–990, 2000.

Jackson, L.P. and Mound, J.E. Geomagnetic variation on decadal time scales: What can we learn from Empirical Mode Decomposition? *Geophys. Res. Lett.*, 37, L14307, 2010.

Johnson, C.L. and Constable, C.G. The time-averaged geomagnetic field as recorded by lava flows over the past 5 Myr. *Geophys. J. Int.*, 122, 489–519, 1995.

Johnson, C.L. and Constable, C.G. The time-averaged geomagnetic field: Global and regional biases for 0-5 Ma. *Geophys. J. Int.*, 131, 643–666, 1997.

Johnson, C.L. and Constable, C.G. Persistently anomalous Pacific geomagnetic fields. *Geophys. Res. Lett.*, 25, 1011–1014, 1998.

Johnson, C.L. and McFadden, P. Time-averaged field and paleosecular variation. In Kono, M., editor, *Treatise of Geophysics, Geomagnetism*, Volume 5, pages 417–453. Elsevier, 2007.

Johnson, E.A., Murphy, T., and Torreson, O.W. Pre-history of the Earth's magnetic field. *Terr. Mag. and Atm. Elec.*, 53, 349–372, 1948.

Kind, J. *Ferromagnetic resonance spectroscopy and Holocene Earth's magnetic field variations in sediments from Swiss lakes.* PhD thesis, ETH Zürich, Switzerland, 2012.

Kind, J., Gehring, A.U., Winklhofer, M., and Hirt, A.M. Combined use of magnetometry and spectroscopy for identifying magnetofossils in sediments. *Geochem. Geophys. Geosys.*, 12, Q08008, 2011.

King, J.W. *Geomagnetic Secular Variation Curves for Northeastern North America for the Last 9000 Years B.P.* PhD thesis, University of Minnesota, Minneapolis, 1983.

King, J.W., Banerjee, S.K., and Marvin, J. A new rock-magnetic approach to selecting sediments for geomagnetic paleointensity studies: Application to paleointensity for the last 4000 years. *J. Geophys. Res.*, 88(B7), 5911–5921, 1983.

King, R.F. The remanent magnetism of artificially deposited sediments. *Mon. Not. R. Astron. Soc.*, 7, 115–134, 1955.

Kirschvink, J.L. The least-squares line and plane and the analysis of palaeomagnetic data. *Geophys. J. R. astr. Soc.*, 62, 699–718, 1980.

Knudsen, M.F., Riisager, P., Donadini, F., Snowball, I., Muscheler, R., Korhonen, K., and Pesonen, L.J. Variations in the geomagnetic dipole moment during the Holocene and the past 50 kyr. *Earth Planet. Sci. Lett.*, 272, 319–329, 2008.

Kodama, K.P. and Sun, W.W. Magnetic anisotropy as a correction for compaction-caused palaeomagnetic inclination shallowing. *Geophys. J. Int.*, 111, 465–469, 1992.

Kono, M. and Roberts, P.H. Recent geodynamo simulations and observations of the geomagnetic field. *Rev. Geophys.*, 40(4), 2002.

Kono, M. and Ueno, N. Paleointensity determination by a modified Thellier method. *Phys. Earth Planet. Inter.*, 13, 305–314, 1977.

Korhonen, K., Donadini, F., Riisager, P., and Pesonen, L.J. Geomagia50: An archeointensity database with PHP and MySQL. *Geochem. Geophys. Geosys.*, 9, Q04029, 2008.

Korte, M. and Constable, C.G. Continuous global geomagnetic field models for the past 3000 years. *Phys. Earth Planet. Inter.*, 140, 73–89, 2003.

Korte, M. and Constable, C.G. Continuous geomagnetic field models for the past 7 millennia: 2. CALS7K. *Geochem. Geophys. Geosys.*, 6, Q02H16, 2005a.

Korte, M. and Constable, C.G. The geomagnetic dipole moment over the last 7000 years-new results from a global model. *Earth Planet. Sci. Lett.*, 236, 348–358, 2005b.

Korte, M. and Constable, C.G. On the use of calibrated relative paleointensity records to improve millennial–scale geomagnetic field models. *Geochem. Geophys. Geosys.*, 7, Q09004, 2006.

Korte, M. and Constable, C.G. Spatial and temporal resolution of millennial scale geomagnetic field models. *Adv. Space Res.*, 41, 57–69, 2008.

Korte, M. and Constable, C.G. Improving geomagnetic field reconstructions for 0-3 ka. *Phys. Earth Planet. Inter.*, 188, 247–259, 2011.

Korte, M., Constable, C.G., Donadini, F., and Holme, R. Reconstructing the Holocene geomagnetic field. *Earth Planet. Sci. Lett.*, 312, 497–505, 2011.

Korte, M., Donadini, F., and Constable, C.G. Geomagnetic field for 0-3 ka: 2. A new series of time–varying global models. *Geochem. Geophys. Geosys.*, 10, Q06008, 2009.

Korte, M., Genevey, A., Constable, C.G., Frank, U., and Schnepp, E. Continuous geomagnetic field models for the past 7 millennia: 1. A new global data compilation. *Geochem. Geophys. Geosys.*, 6, Q02H15, 2005.

Korte, M. and Holme, R. On the persistence of geomagnetic flux lobes in global Holocene field models. *Phys. Earth Planet. Inter.*, 182, 179–186, 2010.

Langel, R.A. *The Main Field*, pages 249–512. Academic Press, London, 1987.

Lanos, P., Le Goff, M., Kovacheva, M., and Schnepp, E. Hierarchical modelling of archaeomagnetic data and curve estimation by moving average technique. *Geophys. J. Int.*, 160, 440–476, 2005.

Latham, A.G., Schwarcz, H.P., and Ford, D.C. The paleomagnetism and U-Th dating of Mexican stalagmite, DAS2. *Earth Planet. Sci. Lett.*, 79, 195–207, 1986.

Leonhardt, R. Analyzing rock magnetic measurements: The RockMagAnalyzer 1.0 software. *Comp. Geosci.*, 32, 1420–1431, 2006.

Leonhardt, R., Matzka, J., Nichol, A., and Dingwell, D.B. Cooling rate correction of paleointensity determination for volcanic glasses by relaxation geospeedometry. *Earth Planet. Sci. Lett.*, 243, 282–292, 2006.

Lesur, V., Wardinski, I., Rother, M., and Mandea, M. GRIMM: the GFZ Reference Internal Magnetic Model based on vector satellite and observatory data. *Geophys. J. Int.*, 173, 382–394, 2008.

Lisé-Pronovost, A., St-Onge, G., Brachfeld, S., Barletta, F., and Darby, D. Paleomagnetic constrains on the Holocene stratigraphy of the Arctic Alaskan margin. *Global Planet. Change*, 68, 85–99, 2009.

Lotter, A.F. Evidence of annual layering in Holocene sediments of Soppensee, Switzerland. *Aquat. Sci.*, 51/1, 19–30, 1989.

Lotter, A.F. Absolute dating of the late-glacial period in Switzerland using annually laminated sediments. *Quatern. Res.*, 35, 321–330, 1991.

Lowes, F.J. Spatial power spectrum of the main geomagnetic field. *Geophys. J. R. astr. Soc*, 36, 717–730, 1974.

Lowrie, W. *Fundamentals of Geophysics*. Cambridge University Press, New York, 2007.

Lund, S.P. and Banerjee, S.K. Late Quaternary paleomagnetic field secular variation from two Minnesota lakes. *J. Geophys. Res.*, 90(B1), 803–825, 1985.

Lund, S.P. and Keigwin, L. Measurement of the degree of smoothing in sediment paleomagnetic secular variation records: an example from Late Quaternary deep–sea sediments of the Bermuda Rise, western North Atlantic ocean. *Earth Planet. Sci. Lett.*, 122, 317–330, 1994.

Masarik, J. and Beer, J. Simulation of particle fluxes and cosmogenic nuclide production in the Earth's atmosphere. *J. Geophys. Res.*, 104(D10), 12009–12111, 1999.

Maus, S., Macmillan, S., Chernova, T., Choi, S., Dater, D., Golovkov, V., Lesur, V., Lowes, F., Lühr, H., Mai, W., McLean, S., Olsen, N., Rother, M., Sabaka, T., Thomson, A., and Zvereva, T. The 10th generation international geomagnetic reference field. *Geophys. J. Int.*, 161, 561–565, 2005.

McElhinny, M.W. and Lock, J. IAGA paleomagnetic databases with Access. *Surv. Geophys.*, 17, 575–591, 1996.

McElhinny, M.W. and McFadden, P.L. Palaeosecular variation over the past 5 Myr based on a new generalized database. *Geophys. J. Int.*, 131, 240–252, 1997.

McMillan, D.G., Constable, C.G., Parker, R.L., and Glatzmaier, G.A. A statistical analysis of magnetic fields from some geodynamo simulations. *Geochem. Geophys. Geosys.*, 2, 2000GC000130, 2001.

Menke, W. *Geophysical Data Analysis: Discrete Inverse Theory.* Acadamic Press, San Diego, 1989.

Monecke, K., Anselmetti, F.S., Becker, A., Sturm, M., and Giardini, D. The record of historic earthquakes in lake sediments of Central Switzerland. *Tectonophysics*, 394, 21–40, 2004.

Mothersill, J.S. The paleomagnetic record of the late Quaternary sediments of Thunder Bay. *Can. J. Earth Sci.*, 16, 1016–1023, 1979.

Mothersill, J.S. Late Quaternary record of the Goderich Basin, Lake Huron. *Can. J. Earth Sci.*, 18, 448–456, 1981.

Mothersill, J.S. Paleomagnetic results from lakes Victoria and Albert, Uganda. *Stud. Geophys. Geod.*, 40, 25–35, 1996.

Nilsson, A., Muscheler, R., and Snowball, I. Millennial scale cyclicity in the geodynamo inferred from a dipole tilt reconstruction. *Earth Planet. Sci. Lett.*, 311, 299–305, 2011.

Nilsson, A., Snowball, I., Muscheler, R., and Uvo, C. B. Holocene geocentric dipole tilt model constrained by sedimentary paleomagnetic data. *Geochem. Geophys. Geosys.*, 11, Q08018, 2010.

Nourgaliev, D.K., Borisov, A.S., Heller, F., Burov, B.V., Jasonov, P.G., Khasanov, D.I., and Ibragimov, S.Z. Geomagnetic secular variation through the last 3500 years as recorded by Lake Aslikul sediments from eastern Europe (Russia). *Geophys. Res. Lett.*, 23(4), 375–378, 1996.

Nourgaliev, D.K., Heller, F., Borisov, A.C., Yasonov, P.G., Chernova, I.Y., and Hajdas, I. Principal features (master curve) of geomagnetic field variations in Belorussia during the last 12 thousand years. *Russ. J. Earth Sci.*, 7, 1–16, 2005.

Nourgaliev, D.K., Heller, F., Borisov, A.S., Hajdas, I., Bonani, G., Iassonov, P.G., and Oberhänsli, H. Very high resolution paleosecular variation record for the last ∼1200 years from the Aral Sea. *Geophys. Res. Lett.*, 30, 4–7, 2003.

Ojala, A. and Saarinen, T. Palaeosecular variation of the Earth's magnetic field during the last 10000 years based on the annually laminated sediment of Lake Nautajärvi, central Finland. *Holocene*, 12(4), 391–400, 2002.

Ojala, A. and Tiljander, M. Testing the fidelity of sediment chronology: Comparison of varve and paleomagnetic results from Holocene lake sediments from central Finland. *Quaternary Sci. Rev.*, 22, 1787–1803, 2003.

Oldfield, F., Crooks, P. R. J., Harkness, D. D., and Petterson, G. AMS radiocarbon dating of organic fractions from varved lake sediments: an empirical test of reliability. *J. Paleolimnol.*, 18, 87–91, 1997.

Olson, P.L. and Amit, H. Changes in earth's dipole. *Naturwissenschaften*, 93, 519–542, 2006.

Olson, P.L., Christensen, U.R., and Driscoll, P.E. From superchrons to secular variation: A broadband dynamo frequency spectrum for the geomagnetic dipole. *Earth Planet. Sci. Lett.*, 319-320, 75–82, 2012.

Panovska, S., Finlay, C.C., Donadini, F., and Hirt, A.M. Spline analysis of Holocene sediment magnetic records: Uncertainty estimates for field modelling. *J. Geophys. Res.*, 117, B02101, 2012.

Parker, R.L. *Geophysical Inverse Theory.* Princeton University Press, Princeton, 1994.

Pavón-Carrasco, F.J., Osete, M.L., and Torta, J.M. Regional modeling of the geomagnetic field in Europe from 6000 to 1000 B.C. *Geochem. Geophys. Geosys.*, 11, Q11008, 2010.

Pavón-Carrasco, F.J., Osete, M.L., Torta, J.M., and Gaya-Piqué, L.R. A regional archeomagnetic model for Europe for the last 3000 years, SCHA.DIF.3K: Applications to archeomagnetic dating. *Geochem. Geophys. Geosys.*, 10, Q03013, 2009.

Pavón-Carrasco, F.J., Osete, M.L., Torta, J.M., Gaya-Piqué, L.R., and Lanos, P. Initial SCHA.DI.00 regional archaeomagnetic model for Europe for the last 2000 years. *Phys. Chem. Earth*, 33, 596–608, 2008.

Peck, J.A., King, J.W., Colman, S.M., and Kravchinsky, V.A. An 84-kyr paleomagnetic record from the sediments of Lake Bailkal, Siberia. *J. Geophys. Res.*, 101(B5), 11365–11385, 1996.

Peng, L. and King, J.W. A late Quaternary geomagnetic secular variation record from Lake Waiau, Hawaii, and the question of the Pacific nondipole low. *J. Geophys. Res.*, 97(B4), 4407–4424, 1992.

Percival, D.B. and Walden, A.T. *Spectral Analysis for Physical Applications: Multitaper and Conventional Univariate Techniques*. Cambridge, New York, NY, 1998.

Piper, J.D.A. *Palaeomagnetism*, Volume 3. Academic Press, 1989.

Press, W.H., Teukolsky, S.A., Vetterling, W.T., and Flannery, B.P. *Numerical Recipes in Fortran*. Cambridge University Press, London, 1992.

Prieto, G.A., Parker, R.L., Thomson, D.J., Vernon, F.L., and Graham, R.L. Reducing the bias of multitaper spectrum estimates. *Geophys. J. Int.*, 171, 1269–1281, 2007.

Prieto, G.A., Parker, R.L., and Vernon, F.L. A Fortran 90 library for multitaper spectrum analysis. *Comp. Geosci.*, 35, 1701–1710, 2009.

Rice, J. A. *Mathematical Statistics and Data Analysis*. Duxbury Press, Belmont, Calif., 1995.

Richter, C., Venuti, A., Verosub, K.L., and Wei, K.-Y. Variations of the geomagnetic field during the Holocene: Relative palaeointensity and inclination record from the West Pacific (ODP Hole 1202B). *Phys. Earth Planet. Inter.*, 156, 179–193, 2006.

Riedel, K.S. and Sidorenko, A. Minimum bias multiple taper spectrum estimation. *IEEE T. Signal Proces.*, 43(1), 188–195, 1995.

Riley, K.F., Hobson, M.P., and Bence, S.J. *Mathematical Methods for Physics and Engineering*. Cambridge University Press, 2002.

Rilling, G., Flandrin, P., and Gonçalvès, P. On Empirical Mode Decomposition and Its Algorithms. In *IEEE-EURASIP Workshop Nonlinear Signal Image Processing (NSIP)*, 2003.

Roberts, A.P. and Winklhofer, M. Why are geomagnetic excursion not always recorded in sediments? Constraints from post–depositional remanent magnetization lock–in modeling. *Earth Planet. Sci. Lett.*, 227, 345–359, 2004.

Roberts, P.H. and Glatzmaier, G. Geodynamo theory and simulations. *Rev. Mod. Phys.*, 72, 1081–1123, 2000.

Roberts, P.H., Yu, Z.J., and Russell, C.T. On the 60–year signal from the core. *Geophys. Astrophys. Fluid Dyn.*, 101, 11–35, 2007.

Saarinen, T. High-resolution palaeosecular variation in northern Europe during the last 3200 years. *Phys. Earth Planet. Inter.*, 106, 299–309, 1998.

Sakuraba, A. and Hamano, Y. Turbulent structure in Earth's fluid core inferred from time series of geomagnetic dipole moment. *Geophys. Res. Lett.*, 34, L15308, 2007.

Scales, J.A., Gersztenkorn, A., and Treitel, S. Fast l_p solution of large, sparse, linear systems: Application to seismic travel time tomography. *J. Comput. Phys.*, 75(2), 314–333, 1988.

Schlossmacher, E.J. An iterative technique for absolute deviations curve fitting. *J. Am. Stat. Assoc.*, 68, 857–859, 1973.

Schnepp, E., Pucher, R., Reinders, J., Hambach, U., Soffel, H., and Hedley, I. A German catalogue of archaeomagnetic data. *Geophys. J. Int.*, 157, 64–78, 2004.

Selkin, P.A. and Tauxe, L. Long-term variations in palaeointensity. *Phil. Trans. R. Soc. Lond. A*, 358, 1065–1088, 2000.

Senanayake, W.E., McElhinny, M.W., and McFadden, P.L. Comparison between the Thellier's and Shaw's paleointensity methods using basalts less than 5 million years old. *J. Geomag. Geoelectr.*, 34, 141–161, 1982.

Shaw, J. A new method of determining the magnitude of the palaeomagnetic field: Application to five historic lavas and five archaeological samples. *Geophys. J. R. astr. Soc.*, 39, 133–141, 1974.

Shure, L., Parker, R.L., and Backus, G.E. Harmonic splines for geomagnetic modelling. *Phys. Earth Planet. Inter.*, 28(3), 215–229, 1982.

Sivia, D.S. and Skilling, J. *Data Analysis. A Bayesian Tutorial.* Oxford University Press, Oxford, 2006.

Slepian, D. Prolate spheroidal wave functions. Fourier analysis, and uncertainty. V: the discrete case. *AT&T Tech. J.*, 57, 1371–1430, 1978.

Smith-Boughner, L.T. and Constable, C.G. Spectral estimation for geophysical time-series with inconvenient gaps. *Geophys. J. Int.*, 190, 1404–1422, 2012.

Smith-Boughner, L.T., Ziegler, L.B., and Constable, C.G. Changing spectrum of geomagnetic intensity variations in a fragmented 12 My sediment record from the Oligocene. *Phys. Earth Planet. Inter.*, 188(3-4), 260–269, 2011.

Snowball, I. and Sandgren, P. Geomagnetic field variations in northern Sweden during the Holocene quantified from varved lake sediments and their implications for cosmogenic nuclide production rates. *Holocene*, 12(5), 517–530, 2002.

Snowball, I. and Sandgren, P. Geomagnetic field intensity changes in Sweden between 9000 and 450 cal BP: Extending the record of ‘archaeomagnetic jerks’ by means of lake sediments and the pseudo-Thellier technique. *Earth Planet. Sci. Lett.*, 227, 361–376, 2004.

Snowball, I., Zillén, L., Ojala, A., Saarinen, T., and Sandgren, P. FENNOSTACK and FENNORPIS: Varve dated Holocene palaeomagnetic secular variation and relative palaeointensity stacks for Fennoscandia. *Earth Planet. Sci. Lett.*, 255, 106–116, 2007.

Solanki, S.K., Usoskin, I.G., Kromer, B., Schüssler, M., and Beer, J. Unusual activity of the Sun during recent decades compared to the previous 11,000 years. *Nature*, 431, 1084–1087, 2004.

St-Onge, G., Piper, T. Mulder D.J.W., Hillaire-Marcel, C., and Stoner, J.S. Earthquake and flood–induced turbidites in the Saguenay Fjord (Québec): A Holocene paleoseismicity record. *Quaternary Sci. Rev.*, 23, 283–294, 2004.

St-Onge, G., Stoner, J.S., and Hillaire-Marcel, C. Holocene paleomagnetic records from the St. Lawrence Estuary, eastern Canada: Centennial- to millennial-scale geomagnetic modulation of cosmogenic isotopes. *Earth Planet. Sci. Lett.*, 209, 113–130, 2003.

Stanton, T., Snowball, I., Zillén, L., and Wastegård, S. Validating a Swedish varve chronology using radiocarbon, palaeomagnetic secular variation, lead pollution history and statistical correlation. *Quat. Geochronology*, 5, 611–624, 2010.

Stark, F., Leonhardt, R., Fassbinder, J.W.E., and Reindel, M. The field of sherds: Reconstructing geomagnetic field variations from Peruvian potsherds. In Reindel, M. and Wagner, G.A., editors, *New Technologies for Archaeology*, pages 103–116. Springer, 2009.

Stockhausen, H. Geomagnetic paleosecular variation (0–13 000 yr BP) as recorded in sediments from the three maar lakes from the West Eifel (Germany). *Geophys. J. Int.*, 135, 898–910, 1998.

Stoner, J.S., Jennings, A., Kristjánsdóttir, G.B., Dunhill, G., Andrews, J.T., and Hardardóttir, J. A paleomagnetic approach toward refining Holocene radiocarbon-based chronologies: Paleoceanographic records from the north Iceland (MD99-2269) and east Greenland (MD99-2322) margins. *Paleoceanography*, 22, 1–23, 2007.

Strang, G. and Nguyen, T. *Wavelets and Filter Banks*. Wellesley-Cambridge Press, Wellesley, Mass., 1996.

Stuiver, M. and Reimer, P. J. Extended ^{14}C data base and revised CALIB 3.0 ^{14}C age calibration program. *Radiocarbon*, 35, 215–230, 1993.

Stuiver, M., Reimer, P. J., and Braziunas, T. F. High-precision radiocarbon age calibration for terrestrial and marine samples. *Radiocarbon*, 40, 1127–1151, 1998.

Suganuma, Y., Okuno, J., Heslop, D., Roberts, A.P., Yamazaki, T., and Yokoyama, Y. Post-depositional remanent magnetization lock-in for marine sediments deduced from ^{10}Be and paleomagnetic records through the Matuyama-Brunhes boundary. *Earth Planet. Sci. Lett.*, 311, 39–52, 2011.

Suttie, N., Holme, R., Hill, M.J., and Shaw, J. Consistent treatment of errors in archaeointensity implies rapid decay of the dipole prior to 1840. *Earth Planet. Sci. Lett.*, 304, 13–21, 2011.

Tanriverdi, V. and Tilgner, A. Global fluctuations in magnetohydrodynamics dynamos. *New J. Phys.*, 13, 033019, 2011.

Tarantola, A. *Inverse Problem Theory and Methods for Model Parameter Estimation*. Soc. Ind. Appl. Math., Philadelphia, Pa, 2005.

Tauxe, L. Sedimentary records of relative paleointensity of the geomagnetic field: Theory and practice. *Rev. Geophys.*, 31(3), 319–354, 1993.

Tauxe, L. *Paleomagnetic Principles and Practice*. Kluwer Academic Publishers, Dordrecht, 2002.

Tauxe, L. Inclination flattening and the geocentric axial dipole hypothesis. *Earth Planet. Sci. Lett.*, 233, 247–261, 2005.

Tauxe, L., Kodama, K.P., and Kent, D.V. Testing corrections for paleomagnetic inclination error in sedimentary rocks: A comparative approach. *Phys. Earth Planet. Inter.*, 169, 152–165, 2008.

Tauxe, L. and Yamazaki, T. Paleointensities. In Kono, M., editor, *Treatise of Geophysics, Geomagnetism*, pages 509–563. Elsevier, 2007.

Thellier, E. and Thellier, O. Sur l'intensité du champ magnétique terrestre dans le passé historique et géologique. *Ann. Geophys.*, 15, 285–376, 1959.

Thompson, R. and Kelts, K. Holocene sediments and magnetic stratigraphy from lakes Zug and Zurich, Switzerland. *Sedimentology*, 21, 577–596, 1974.

Thompson, R. and Turner, G.M. Icelandic Holocene palaeolimnomagnetism. *Phys. Earth Planet. Inter.*, 38, 250–261, 1985.

Thomson, D.J. Spectrum estimation and harmonic analysis. *Proc. IEEE*, 70(9), 1055–1096, 1982.

Thomson, D.J. and Chave, A.D. Jackknifed error estimates for spectra, coherences, and transfer functions. In Haykin, S., editor, *Advances in Spectrum Analysis and Array Processing*, Volume 1, pages 58–113. Prentice Hall, Englewood Cliffs, NJ, 1991.

Thouveny, N. and Williamson, D. Palaeomagnetic study of the Holocene and Upper Pleistocene sediments from Lake Barombi Mbo, Cameroun: First results. *Phys. Earth Planet. Inter.*, 52, 193–206, 1988.

Trauth, M.H. *Matlab Recipes for Earth Sciences*. Springer, Berlin-Heidelberg, Third edition, 2010.

Trefethen, L.N. and Bau, D. *Numerical Linear Algebra*. Soc. Ind. Appl. Math., Philadelphia, Pa, 1997.

Turner, G.M. A 5000 year geomagnetic palaeosecular variation record from western Canada. *Geophys. J. Roy. Astron. Soc.*, 91, 103–121, 1987.

Turner, G.M. and Lillis, D.A. A palaeomagnetic secular variation record for New Zealand during the past 2500 years. *Phys. Earth Planet. Inter.*, 83, 265–282, 1994.

Turner, G.M. and Thompson, R. Behaviour of the Earth's magnetic field as recorded in the sediment of Loch Lomond. *Earth Planet. Sci. Lett.*, 42, 412–426, 1979.

Turner, G.M. and Thompson, R. Lake sediment record of the geomagnetic secular variation in Britain during Holocene times. *Geophys. J. Roy. Astron. Soc.*, 65, 703–725, 1981.

Usoskin, I.G., Korte, M., and Kovaltsov, G.A. Role of centennial geomagnetic changes in local atmospheric ionization. *Geophys. Res. Lett.*, 35, L05811, 2008.

Usoskin, I.G., Mironova, I.A., Korte, M., and Kovaltsov, G.A. Regional millennial trend in the cosmic ray induced ionization of the troposphere. *J. Atmos. Solar-Terr. Phys.*, 72, 19–25, 2010.

Usoskin, I.G., Solanki, S.K., and Korte, M. Solar activity reconstructed over the last 7000 years: The influence of geomagnetic field changes. *Geophys. Res. Lett.*, 33, L08103, 2006.

Valet, J.-P. Time variations in geomagnetic intensity. *Rev. Geophys.*, 41(1), 1004, 2003.

Valet, J.-P., Meynadier, L., and Guyodo, Y. Geomagnetic dipole strength and reversal rate over the past two million years. *Nature*, 435, 802–805, 2005.

Verosub, K.L. Depositional and postdipositional processes in the magnetization of sediments. *Rev. Geophys. Space Phys.*, 15, 129–143, 1977.

Verosub, K.L., Mehringer, P.J., and Waterstraat, P. Holocene secular variation in western North America: Paleomagnetic record from Fish Lake, Harney County, Oregon. *J. Geophys. Res.*, 91(B3), 3609–3623, 1986.

Vigliotti, L. Secular variation record of the Earth's magnetic field in Italy during the Holocene: Constraints for the construction of a master curve. *Geophys. J. Int.*, 165, 414–429, 2006.

Wahba, G. *Spline Models for Observational Data*. Soc. Ind. Appl. Math., Philadelphia, Pa, 1990.

Walden, A.T., McCoy, E.J., and Percival, D.B. The effective bandwidth of a multitaper spectral estimator. *Biometrika*, 82(1), 201–214, 1995.

Walker, M.R. and Jackson, A. Robust modelling of the Earth's magnetic field. *Geophys. J. Int.*, 143, 799–808, 2000.

Walton, D., Shaw, J., Share, J., and Hakes, J. Microwave demagnetization. *J. Appl. Phys.*, 71, 1549–1551, 1992.

Wardinski, I. and Korte, M. The evolution of the core-surface flow over the last seven thousands years. *J. Geophys. Res.*, 113, B05101, 2008.

Weiss, B.P., Lima, E.A., Fong, L.E., and Baudenbacher, F.J. Paleointensity of the earth's magnetic field using SQUID microscopy. *Earth Planet. Sci. Lett.*, 264, 61–71, 2007.

Wilson, R.L. Palaeomagnetism in Northern Ireland: Part I. The thermal demagnetization of natural magnetic moments in rocks. *Geophys. J. R. astr. Soc.*, 5, 45–58, 1961.

Yamazaki, T. Thickness of the lock-in zone of post-depositional remanent magnetization in deep-sea silicious clay. *Rock Magn. Paleogeophys.*, 11, 85–90, 1984.

Yang, S., Odah, H., and Shaw, J. Variations in the geomagnetic dipole moment over the last 12 000 years. *Geophys. J. Int.*, 140, 158–162, 2000.

Yang, X., Heller, F., Yang, J., and Su, Z. Paleosecular variations since ∼9000 yr BP as recorded by sediments from maar lake Shuangchiling, Hainan, South China. *Earth Planet. Sci. Lett.*, 288, 1–9, 2009.

Yu, Y., Doh, S.-J., Kim, W., Park, Y.-H., Lee, H.-J., Yim, Y., Cho, S.-G., Oh, Y.-S., Lee, D.-S., Lee, H.-H., Gong, M.-G., Hyun, D.-H., Cho, J.-K., Sin, Y.-S., and Do, M.-S. Archeomagnetic secular variation from Korea: Implication for the occurrence of global archeomagnetic jerks. *Earth Planet. Sci. Lett.*, 294, 173–181, 2010.

Yu, Y., Tauxe, L., and Genevey, A. Toward an optimal geomagnetic field intensity determination technique. *Geochem. Geophys. Geosyst.*, 5, Q02H07, 2004.

Zeiler, A., Faltermeier, R., Keck, I.R., Tomé, A.M., Puntonet, C.G., and Lang, E.W. Empirical Mode Decomposition - an introduction. In *IEEE WCCI-IJCNN*, pages 1–8, 2010.

Zhu, R., Gu, Z., Huang, B., Jin, Z., Wei, X., and Li, C. Geomagnetic secular variations and climate changes since 15,000 a B.P., Beijing region. *Sci. China, Ser. B.*, 37(8), 984–990, 1994.

Ziegler, L.B., Constable, C.G., Johnson, C.L., and Tauxe, L. PADM2M: a penalized maximum likelihood model of the 0-2 Ma palaeomagnetic axial dipole moment. *Geophys. J. Int.*, 184, 1069–1089, 2011.

Zijderveld, J.D.A. A.C. demagnetization of rocks: Analysis of results. In Collinson, D.W., Creer, K.M., and Runcorn, S.K., editors, *Methods in Palaeomagnetism*, pages 256–286. Elsevier, 1967.

Zillén, L. *Setting the Holocene Clock Using Varved Lake Lediments in Sweden*. PhD thesis, Lund University, Sweden, 2003.

Acknowledgements

I would like first to acknowledge Dr. Chris Finlay for supervising my PhD research over the past three and a half years. I really appreciate all the time he spent with me on scientific discussions of books and papers. He has always provided advice concerning my work and helped me with all my questions. Without his support during modelling and writing, this thesis would not have been possible.

I sincerely thank Prof. Andy Jackson for giving me the chance to work in this challenging and interesting field as part of the Earth and Planetary Magnetism group at ETH Zürich, for reviewing this manuscript and for his support.

Special thanks to Prof. Ann Hirt, for her encouragement, help and constructive criticism. She introduced me to the field of paleomagnetism and rock magnetism, and always supported my work. I'm grateful to her for reading and revising my manuscripts and this thesis.

I thank Dr. Monika Korte for making her database of Holocene sediment magnetic records and CALS models available, which were essential to this thesis. Her invitation to visit GFZ, Potsdam for discussions was also much appreciated.

Dr. Fabio Donadini has given me great help concerning the archeomagnetic data. He has also made an important contribution to my papers through many suggestions and corrections.

I would like to thank Jessica Kind for all her personal and scientific support during my PhD studies, for the unforgettable summer in Macedonia and for teaching me to measure in the paleomagnetic laboratory. I would also like to acknowledge Dr. Adrian Gilli and Ulrike van Raden for the opportunity to join the Swiss lake sediment drilling campaign and for discussions on paleoclimate topics.

Thanks to my former and current office mates: Andrey Sheyko, Katharina Vogt, Diana Dymkova, Tobias Rolf, Thibault Durez, Lisa Kapper and Stephan Koch for the wonderful time and the encouragement. I would like to mention my former flatmate Katia Pinheiro for her friendship and for making my first two months in Zürich easily adaptable and enjoyable. To my German classmate Monika Welch - thanks for her friendship and for making the German class funny and interesting.

I would like to thank my working colleagues from the EPM group for interesting discussions and seminars: Prof. William Lowrie, P.D. Dr. Alexei Kuvshinov, Dr. Andreas Gehring, Dr. Jérôme Noir, Dr. Elisabeth Canet, Dr. Bjarne Almqvist, Dr. Stijn Vantieghem, Dr. Jose Abreu, Dr. Peter Scarfe, Dr. David Cébron, Hans-Peter Hächler, Andrea Biedermann, Jenneke Bakker, Zacharias Stelzer, Friedemann Samrock, Kuan Li, Monika Kumari, Christoph Püthe, Yufeng Lin and Michalis Charilaou.

I thank Prof. Todor Delipetrov for introducing me into the world of geomagnetism during my BSc and MSc studies. His broad knowledge in geophysics have guided me in the right direction.

A special acknowledgement to Prof. Angelo De Santis for his help on modelling using Spherical Cap Harmonic Analysis and the important contribution to my MSc thesis.

I wish to make a special acknowledgement to my family and in-laws: Goce and Irena Panovski, Dominik, Irena and Vlatko Jankovski, Joze Cekovski, Danka and Peter Haupt and Trajan Cekovski for all the support, help, care and all the happy moments. I wish to express my deep gratitude to my dear parents, Velika and Mitko Panovski who, even from Macedonia, were always present in my life. Their care and love were very valuable and always a source of strength and encouragement to me.

I am infinitely grateful to my loving husband Aleksandar, who has been next to me the whole time. It means the world to me that he believed in me since the beginning of our journey.

This thesis was supported by the CHIRP1 project of ETH (CH1-02-08-2).

Curriculum vitae

Sanja Panovska

Personal

Birth date: 13.09.1980
Citizenship: Republic of Macedonia

Education

2009-2012 PhD, ETH Zürich, Institute of Geophysics, Earth and Planetary Magnetism Group. Thesis title "Modelling Holocene geomagnetic field evolution"

2005-2007 MSc, Department of Geology and Geophysics, Faculty of Mining, Geology and Polytechnics, University Ss. Cyril and Methodius, Skopje, Macedonia. Thesis title "Geomagnetic model of the central part of the Balkan Peninsula with special attention of the Republic of Macedonia"

1999-2004 BSc, Institute of Physics, Faculty of Natural Sciences and Mathematics, University Ss. Cyril and Methodius, Skopje, Macedonia. Thesis title "Model of the geomagnetic field of the Earth - IGRF"

List of Publications

- Panovska S., Delipetrov T. Analysis of geomagnetic field data from measurements during 2003 in Macedonia. - In J.L. Rasson and T. Delipetrov (eds.), Geomagnetics for Aeronautical Safety, 325-346, 2006

- Panovska, S. Finlay, C.C., Donadini, F., and Hirt, A.M. Spline analysis of Holocene sediment magnetic records: Uncertainty estimates for field modelling. J. Geophys. Res. 117, B02101, 2012

Conference proceedings

- Panovska. S., Delipetrov T., (2005). Analyzing geomagnetic field data from the measurements in 2002 - 2004 in Macedonia. ARW NATO Programme Security Through Science: New data for the magnetic field in the Republic of Macedonia for enhanced flying and airport safety, Ohrid, Macedonia

- Panovska S., Delipetrov T., Delipetrov B., (2006). Correlation between IGRF2000 model and measured geomagnetic data on the territory of the Republic of Macedonia from measurements in 2003 and 2004. XIIth IAGA Workshop on geomagnetic observatory instruments, data acquisition and processing, Belsk, Poland

- Panovska S., Delipetrov M., Delipetrov T., Delipetrov B., (2008). Models of the geomagnetic field of the territory of the Republic of Macedonia. XIIIth IAGA Workshop on geomagnetic observatory instruments, data acquisition and processing, Golden, Colorado, USA

- Panovska S., Delipetrov M., Delipetrov T., (2008). Geophysical investigations with VLF method. First Congress of Geologists of the Republic of Macedonia, Ohrid, Macedonia

- Panovska S., Finlay C.C., (2010). Smoothing spline analysis and error assessment of Holocene lake sediments magnetic records. 12 Castle Meeting on Paleo, Rock and Environmental Magnetism, Castle of Nove Hrady, Czech Republic

- Panovska S., Finlay C.C., (2011). Analysis of Holocene lake sediment magnetic records: Evidence for periodicities and error estimates for field modelling. XXV IUGG General Assembly, Melbourne, Australia

- Panovska S. (2012). Modelling Holocene geomagnetic field evolution. AGU Fall Meeting, San Francisco, USA